From Radio-Frequency sources to particle beam: optimisation of RF power transfer for accelerating cavities

Juliette Plouin

▶ **To cite this version:**

Juliette Plouin. From Radio-Frequency sources to particle beam: optimisation of RF power transfer for accelerating cavities. Accelerator Physics [physics.acc-ph]. université paris saclay, 2024. tel-04565940

HAL Id: tel-04565940
https://hal.science/tel-04565940v1

Submitted on 2 May 2024

HAL is a multi-disciplinary open access archive for the deposit and dissemination of scientific research documents, whether they are published or not. The documents may come from teaching and research institutions in France or abroad, or from public or private research centers.

L'archive ouverte pluridisciplinaire **HAL**, est destinée au dépôt et à la diffusion de documents scientifiques de niveau recherche, publiés ou non, émanant des établissements d'enseignement et de recherche français ou étrangers, des laboratoires publics ou privés.

université
PARIS-SACLAY

From Radio-Frequency sources to particle beam: optimisation of RF power transfer for accelerating cavities

Des sources Radio Fréquence au faisceau de particules : optimisation du transfert de puissance RF pour les cavités accélératrices

Habilitation à diriger des recherches
de l'Université Paris-Saclay

présentée et soutenue à Saclay,
le 10 janvier 2024, par

Juliette PLOUIN

Composition du jury

Graeme Burt Professeur, Université de Lancaster (Royaume-Uni)	Rapporteur
Jens Knobloch Professeur, Université de Siegen (Allemagne)	Rapporteur
Walter Wuensch Expert senior, CERN (Suisse)	Rapporteur
Marie-Emmanuelle Couprie Chercheuse, Synchrotron Soleil	Présidente du jury
Bertrand Baudouy Ingénieur Chercheur, CEA Saclay	Examinateur
Sophie Kazamias Professeure, Université Paris Saclay	Examinatrice

Habilitation à diriger des recherches

Contents

LHC	Large Hadron Collider
ESS	European Spallation Source
XFEL	X-ray Free-Electron Laser
SARAF	Soreq Applied Research Accelerator Facility
IFMIF	International Fusion Materials Irradiation Facility
DONES	Demo Oriented Neutron Source
DEMO	Demonstration Power Plant
PIP-II	Proton Improvement Plan II
MuCol	Muon Collider
CARE	Coordinated Accelerator Research in Europe
HIPPI	High Intensity Pulsed Proton Injector
EuCARD	European Coordination for Accelerator Research Development
ARIES	Accelerator Research and Innovation for European Science and Society
WPENS	Work Package Early Neutron Source
TYL-FJPPL	"Toshiko Yuasa" France Japan Particle Physics Laboratory
FCC	Future Circular Collider
ILC	International Linear Collider
CLIC	Compact LInear Collider

Table 1: List of the projects and programs acronyms used in the document.

Acknowledgment

I would like to thank Graeme Burt, Jens Knobloch and Walter Wuensch for having accepted to be referees for my Habilitation à Diriger des Recherches, Bertrand Baudouy and Sophie Kazamias for being part of my examination board and Marie-Emmanuelle Couprie for her board president role.

During the writing of this dissertation, I have received the valuable support of my Laboratory and Department, which helped me a lot. A special thank to Claude Marchand and Pierre Bosland for their review of the manuscript.

Obviously, all the work described here is a team work, gathering many people at CEA and in many laboratories and companies including technicians, engineers, researchers, and also many students. I have tried to cite all of them hereafter, and I hope the ones I could have forgotten will forgive me. From all of them I have learnt a lot, scientifically, technically and on a human level.

Overview

My research activity started with a PhD on the improvement of output power in Traveling Wave Tubes (TWT) and went on as a researcher/engineer on Radio Frequency (RF) structures for particle accelerators. The interaction and energy transfer between a particle beam and an electromagnetic field has always been a key point of my activity, the transfer being in favor of the RF field, in TWTs and klystrons, or in favor of the particle beam, in accelerating cavities.

Alongside research activities, I have regularly contributed to science transmission. For many years now, I am teaching electromagnetism and radio frequency sources principles at the university, and I have given some courses on superconducting cavities. I have supervised one PhD student and a dozen of technical and master students.

In this document, I give an overview of some efforts carried out to improve efficiency and performance of particle accelerating RF structures.

The first chapter is an introduction presenting the background of research and development on particle accelerators.

The second chapter describes how to go from an RF design, adapted to the beam dynamics requirements, to the fabrication, preparation and test of cavities. Two examples of superconducting cavities are detailed, the first one, the high beta elliptical cavity for ESS being in series construction phase, and the second one, the high beta half wave resonator for IFMIF/DONES being in prototyping phase. Besides further developments on superconducting cavities, we are starting a new activity on normal conducting cavities for muon collider. In the frame of the MuCol European program, we are planning experimental studies on the influence of material, frequency, design and temperature on breakdown phenomena.

The third chapter details how to control and limit the magnetic flux trapping in superconducting niobium, from magnetic shield design and fabrication to magnetic environment management. Besides the development of shielding for future accelerators, a large effort is ongoing for minimizing magnetic fields likely to radiate inside cryomodules. In particular, we plan to install and test a degaussing setup to mitigate residual magnetic field around cavities. On the other hand, we will explore the relationship between flux trapping amplitude and cavity performance during cavity tests.

The fourth chapter gives an overview of methods and technologies to improve RF sources efficiency. The example of second harmonic injection in TWTs is presented, and new techniques for increasing klystron efficiency have been investigated. This last point is crucial for limiting electricity consumption in future large particle accelerators. Today's computing power allows the use of new optimization tools for the design, an example of a genetic algorithm being presented in this document. Then, our experience on high efficiency klystron fabrication has underlined the need to guarantee RF parameters accuracy and new solutions are envisaged.

The fifth chapter presents sensors developments used for cavity diagnostics in cryostats and cryomodules. It underlines the need of an improvement in diagnostics implementation, for assuring accelerators projects achievement, as well as for developing research activities in laboratories.

Chapter 1

Introduction

I have been working on particle accelerators since I joined CEA in 2006, as a research engineer in the radiofrequency domain in the Accelerators, Cryogenics and Magnetism Division (DACM) of the Institute of Research into the Fundamental Laws of the Universe (Irfu). The mission of the DACM is to develop and produce particle accelerators, ion sources, accelerator cavities, cryogenic systems and superconducting magnets for Irfu's scientific programs. The DACM participates to the major accelerator projects and scientific programs in Europe and around the world, thanks to the expertise of its five laboratories detailed in Figure 1.1. I am member of the Accelerator and Hyper frequency Systems Engineering Laboratory (LISAH) which represents DACM's expertise in the design and construction of high frequency electromagnetic structures and their implementation through the use of appropriate instrumentation.

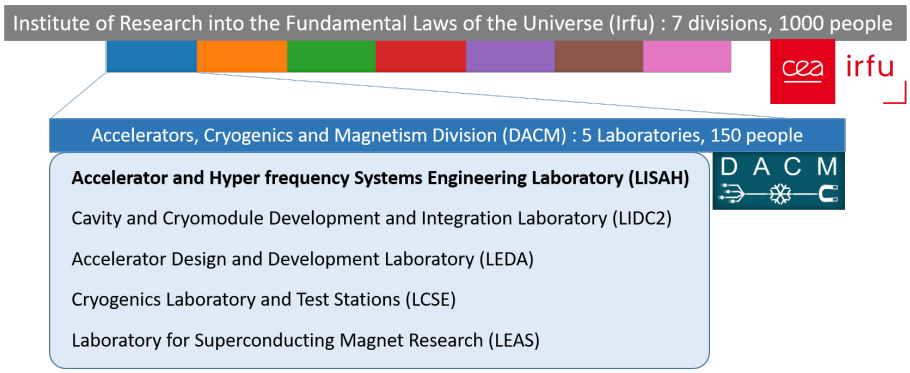

Figure 1.1: The Accelerators, Cryogenics and Magnetism Division organization.

The principle of particles accelerators consists into the transfer of energy from the electricity power grid to a particle beam. The aim of the research and development on accelerators finally consists into the optimization of this transfer. The work presented in this document will concentrate on the following points:

1. How to develop superconducting cavity design, fabrication and preparation to optimize the RF power transfer from coupler to accelerating field. This chapter details two cavity developments: ESS high beta elliptical cavity and IFMIF/DONES high beta half wave resonator.

2. How to optimize the magnetic environment of cavities to guarantee cavity performance. This chapter focuses on magnetic shielding development, magnetic hygiene and magnetic sensors.

3. How to optimize RF power sources efficiency. This chapter starts with the output power improvement in traveling wave tubes and then focuses on the efficiency optimization in klystrons.

These three points are illustrated in Figure 1.2 in the example of the ESS accelerator.

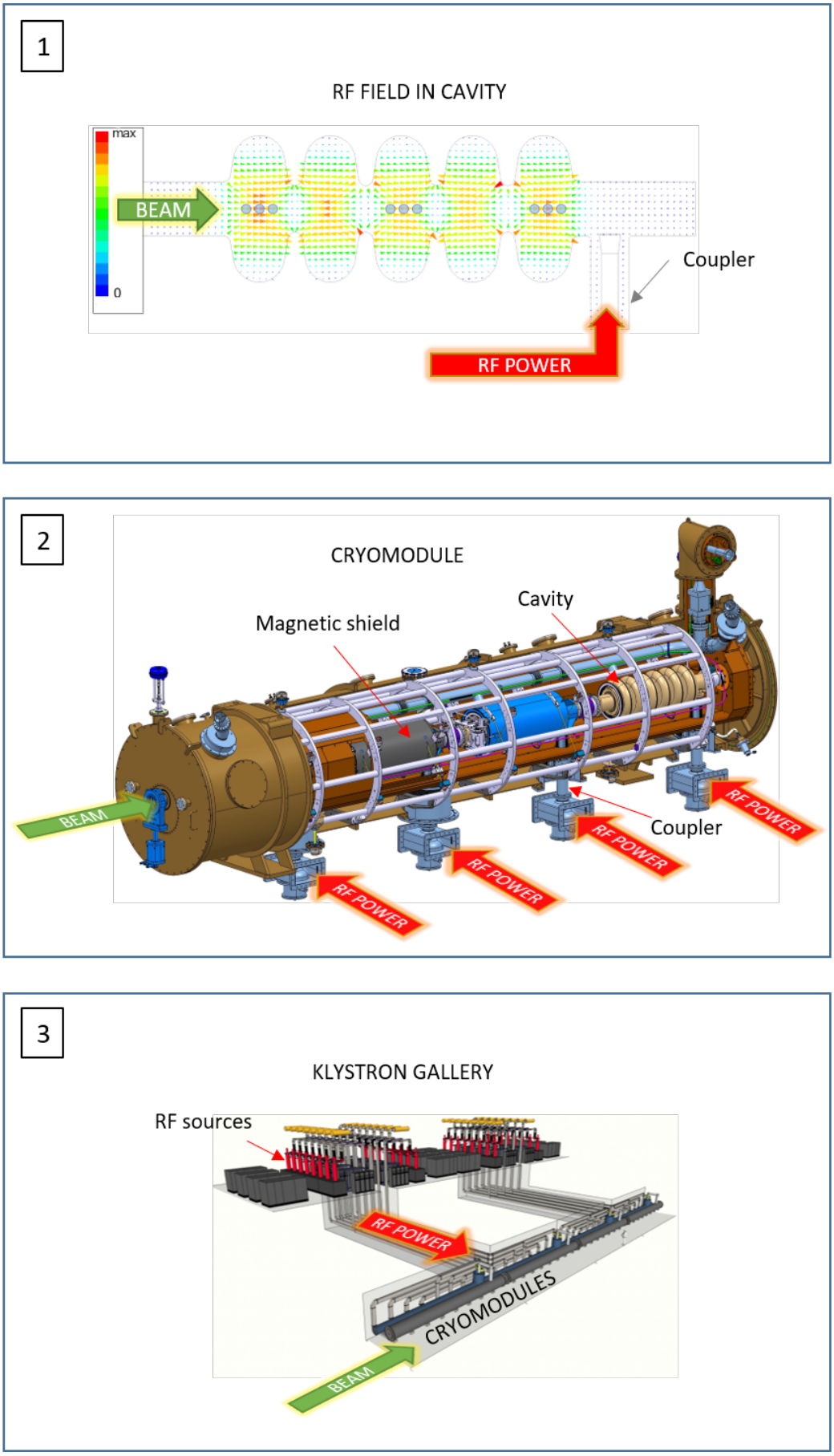

Figure 1.2: Illustration of the energy transfer to the beam in the ESS accelerator

1.1 Particle accelerators

1.1.1 Particle accelerators projects

Particle accelerators use electric and magnetic fields to bring charged particles to high speed and energy while keeping them into a focused beam. They are used in a wide range of applications, from industry, medical domain to fundamental research. The largest and most well known is the Large Hadron Collider at CERN in Switzerland, which accelerates proton beams to generate collisions, generating high energy particles like the Higgs Boson. New accelerators projects are foreseen by CERN, to succeed LHC after 2040: the Futur Circular Collider, the Compact Linear Collider or the Muon Collider.

Large particle accelerators are in different phases of exploitation, construction or study all around the world. In the following, I will focus on the facilities involving our laboratories at CEA-Irfu, and to which I have directly contributed.

The Figure 1.3 represents the accelerator schemes for all these accelerators.

In operation since 2017 in Hamburg (Germany), the European XFEL generates ultrashort intense X-rays flashes to explore matter. An electron beam is accelerated to very high energy, and guided by periodic arrangements of magnets (undulators) resulting in synchronized X-ray radiation. The CEA-Irfu has been in charge of the assembly of the hundred cryomodules constituting the 1.7 km long linear electron accelerator. I have participated to the procurement of the magnetic shields assembled around the superconducting cavities.

The European Spallation Source (ESS) is under construction since 2014 in Lund (Sweden). A proton beam will be accelerated up to 2 GeV and hit a tungsten target, resulting in a spallation process and neutron generation for scientific experiments across multiple disciplines. The CEA-Irfu is currently in charge of the cryomodule assembly for the high energy acceleration section. I was in charge of the RF and mechanical design of the high beta elliptical cavities, and was involved in the design of the medium beta cavities (see Chapter 2). Moreover I am the magnetic expert for the procurement and assembly of the magnetic shields.

The Israeli SARAF project will provide a source of fast neutrons and radioactive nuclei generated by the interaction between a proton or deuteron beam with specific targets. CEA-Irfu is in charge of the fabrication of the whole protons/deuterons accelerator. I have been the magnetic expert for the procurement of the magnetic shields, and have carried out measurements on flux trapping in the half wave resonator (see Chapter 3).

The Demo-Oriented early Neutron Source for the International Fusion Materials Irradiation Facility (IFMIF/DONES) project in Granada (Spain) originates from the need of a fusion-like neutron source for the qualification of the materials to be used in a DEMO reactor and future fusion power plant [Kró+21]. The facility will consist into a high intensity deuteron accelerator aimed to impact a liquid lithium target for neutron production. An accelerator prototype, the IFMIF/Lipac, is currently being assembled in Japan, representative of the low energy section. CEA-Irfu has provided the injector and low beta cryomodule. IFMIF/DONES is now in a study phase, and CEA-Irfu's contribution concerns the beam dynamics and the cryomodules. For the IFMIF/Linac, I have participated to the RF design of the half wave resonators, I have been in charge of the design and procurement of the magnetic shield for the cryomodule, and I have contributed to the effort on limiting flux trapping in cavities (see Chapter 3). At present, I am responsible of the design, fabrication and tests of the high beta half wave resonator prototype for IFMIF/DONES (see Chapter 2), in the frame of the EUROfusion program (see section 1.1.2).

The Proton Improvement Plan II, or PIP-II, project is an essential upgrade to the Fermilab's accelerator complex in Batavia (USA) to enable intense beam of high-energy neutrinos

generation. A proton beam will be accelerated up to 800 MeV and the CEA-Irfu is in charge of the production of the low beta cryomodules for elliptical cavities. I am the magnetic expert for the magnetic shield and magnetic hygiene in the cryomodules.

Finally, CEA-Irfu is now involved in the European collaboration MuCol, working on a Design Study for a Muon Collider complex at 10 TeV center of mass. The elements of a muon beam generation and acceleration are the following (Figure 1.4): a proton driver forms intense and short proton bunches; a front end, made of a pion production target able to withstand the high proton beam, for muon generation beam shaping; a cooling channel aimed to reduce the 6D phase space occupied by the beam by up to five orders of magnitude; a series of muon acceleration stages to take the muon beams to the relevant energy before injection in the muon collider ring.

In the cooling stage process, the muon beam loses both longitudinal and transverse momentum. RF cavities are needed to restore the longitudinal momentum. CEA-Irfu is involved into the development of such cavities.

1.1.2 Transverse R&D activities for particle accelerators

Different programs exist among the accelerators community to carry on research and development activities in the field of particle accelerators, and CEA-Irfu is part of most of them. In particular, we have participated to the the R&D programs developed by the European Community to generate a structured and integrated European area in the field of accelerator research and related R&D, within the Frameworks Programs 6, 7, 8 (Horizon 2020) and 9 (Horizon Europe).

- ⋆ 2004-2008: CARE (Coordinated Accelerator Research in Europe). We have participated to the integrated developments of normal and superconducting structures for the acceleration of very high-intensity proton beams, HIPPI, (High Intensity Pulsed Proton Injector) and achieved the design, the fabrication and the characterization of a superconducting cavity prototype at 704 MHz and beta = 0.47 for pulsed proton linac [Bos+07; Dev+08a; Dev+08b].
- ⋆ 2008-2012: EuCARD (European Coordination for Accelerator Research Development). In the Work Package 10 *Superconducting RF technology for proton accelerators and electron linear accelerators* we have achieved the design, the fabrication and the characterization of a beta = 1 cavity for pulsed proton linac [PDC11]. The experience gained during CARE and EuCARD was later applied to the design development of the elliptical ESS cavities.
- ⋆ 2013-2017: EuCARD2. In the Work Package 12, *Innovative Radio Frequency Technologies (RF)*, we have carried out the design, fabrication and test of a 5 GHz high efficiency klystron with the kladistron method, which will be detailed in Chapter 4. I was deputy of the WP12 leader during the program.
- ⋆ 2017-2022: ARIES (Accelerator Research and Innovation for European Science and Society), co-funded under the European Commission's Horizon 2020 Research and Innovation programme. We have provided the design of a 12 GHz efficient klystron (see Chapter 4).
- ⋆ 2021-2027: EUROfusion Workpackage WPENS (Work Package Early Neutron Source) in the Horizon Europe program. CEA-Irfu is developing the design of the cryomodules for the superconducting linac of the IFMIF/DONES accelerator. I am responsible of the development of the prototype of a high beta cavity.
- ⋆ 2023-2027: MuCol (International Muon Collider Collaboration), aimed to produce a coherent description of a novel particle accelerator complex that will collide muons of opposite charge at the energy frontier in the frame of Horizon Europe. In the Work Package 6

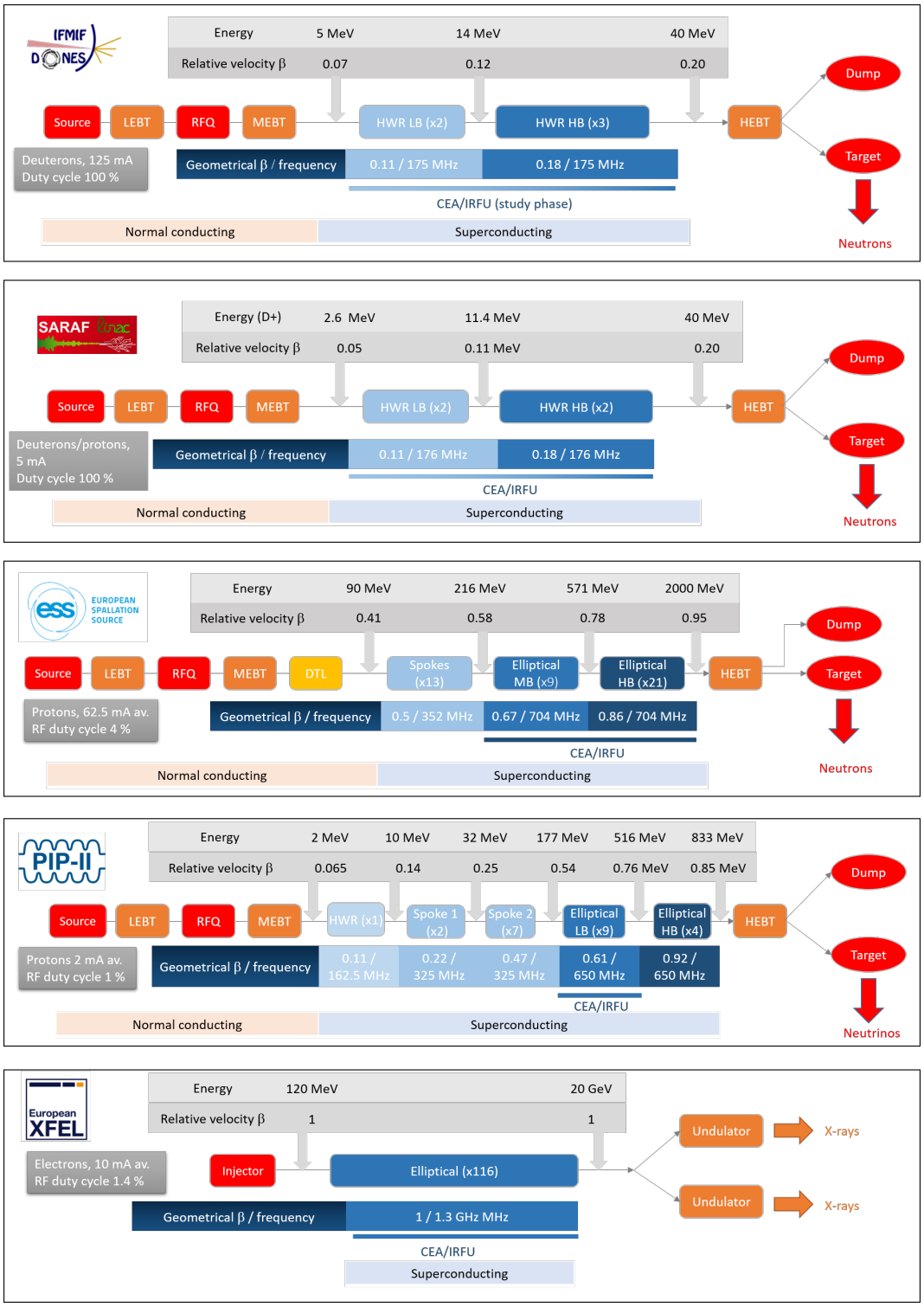

Figure 1.3: Acceleration scheme for IFMIF/DONES, SARAF, ESS, PIP-II and XFEL.

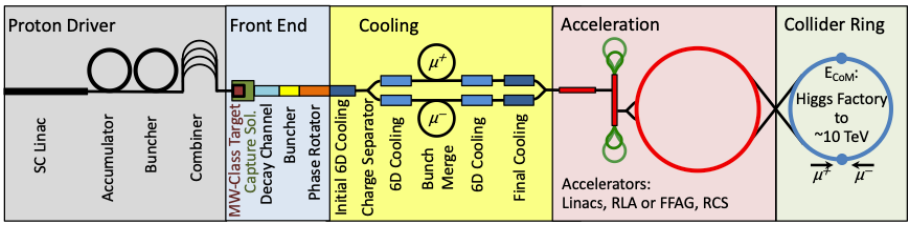

Figure 1.4: Schematic layouts of Muon Collider complex.

we are in charge of studying the cavities destined to the muon cooling complex, and in particular the breakdown mitigation in presence of high DC magnetic field (see Chapter 2). I am deputy of the WP6 leader.

Finally, we are part of the TYL-FJPPL ("Toshiko Yuasa" France Japan Particle Physics Laboratory) created in 2006 to promote collaboration between French and Japanese teams of researchers working in subatomic physics and related areas. I am member of the steering committee in this laboratory, as CEA representative. We have developed and share experience about magnetic shields and magnetic sensors in the frame of this collaboration see Chapter 3).

1.2 Particle acceleration

The principle of accelerating charged particles with RF cavities has been developed in an article published in the French journal *Techniques de l'ingénieur* in 2013 [AP14]. This paper has been written by Claire Antoine and by myself, and is named *Cavités supraconductrices pour les accélérateurs de particules* (Superconducting cavities for particle accelerators). In addition to this publication for non initiated people, I have assured a course in Paris Saclay University on Superconducting cavities.

1.2.1 Accelerating charged particles

Accelerated particles can be represented by their velocity v or relative velocity $\beta = v/c$ (c being the light velocity), or by their total energy, equal to $E_{tot} = \gamma mc^2$, γ being the Lorentz factor for particles in motion:

$$\gamma = \frac{1}{\sqrt{1-\beta^2}} \tag{1.1}$$

Accelerating particles requires providing kinetic energy E_c, which is the difference between the total and the rest energy $E_0 = mc^2$:

$$E_c = (\gamma - 1)mc^2 \tag{1.2}$$

A particle with charge q and velocity $\vec{v}$ in an electromagnetic field $(\vec{E}, \vec{B})$ is subjected to the Lorentz force:

$$\vec{F} = q\vec{E} + q\vec{v} \wedge \vec{B} \tag{1.3}$$

The energy supplied by this field to the particle represents the work of this force, and only the term corresponding to the electric field is non-zero. In a particle accelerator, the electric field provides energy to the beam while the magnetic field provides focusing and bending.

In electrostatic accelerators, particles are subjected to a constant field and their kinetic energy is directly related to the potential ΔV between input and output : $E_c = q\Delta V$. Electrostatic accelerators are limited by the maximal reachable DC voltage, and do not exceed some megaelectronvolts (MeV). They are restricted to low energy ion acceleration.

1.2.2 Radiofrequency acceleration

Radiofrequency (RF) acceleration consists in generating intense electromagnetic fields able to provide energy to the beam. Particles are traveling along the axis of a resonant cavity, loaded with a stationary RF field of frequency f. The field has an electric component on the cavity axis. The particles have been previously bunched so that each bunch always experiences an accelerating field. This principle is illustrated in Figure 1.5 in a four gap cavity : two particle bunches with positive charge, represented by red dots, are traveling through a multicell cavity loaded with a stationary π mode at frequency $f = 1/T$. L is the distance between two consecutive cells. The particles are accelerated when the field is positive, ie in cells 1 and 3 at time t_0, and cells 2 and 4 at time $t_0 + T/2$. Thus, RF acceleration requires synchronization between the distance L, the frequency f and the particle relative velocity β. When cavities are used in the π mode, the following condition must be verified, λ being the vacuum wavelength corresponding to f:

$$L = \frac{\beta\lambda}{2} \tag{1.4}$$

A cavity is characterized by a *geometrical* β defined in the previous example by $\beta_g = 2L/\lambda$.

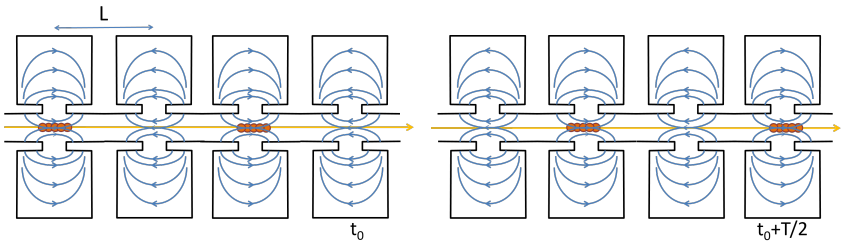

Figure 1.5: RF acceleration principle in a 4 gaps cavity.

In a linear accelerator, the beam energy increases during propagation through the RF cavities. For heavy particles, like ions and protons, the relative velocity increases and the geometrical β of the successive cavities must be adapted to optimize acceleration. This is illustrated in Figure 1.3 for IFMIF/DONES (deuterons), SARAF (deuterons and protons), ESS and PIP-II (protons): a succession of cavity types, identified by their geometric β, are installed in the linac. On the other hand, electrons are so light that they reach $\beta = 1$ at the first acceleration stages and requires only one cavity type (Fig. 1.3, XFEL).

In principle, the bunches enter the cavity in phase with the cavity voltage, when the voltage is maximal (Fig. 1.6, left). However, a particle bunch is subjected to perturbations that produce variations in the arrival times in the cavity. Then, for bunch stability reasons it is better to introduce a phase Φ_s so that the bunch enters the cavity when the voltage is increasing (Fig. 1.6, right). The particles arriving earlier than the bunch center receive less energy, while the particles arriving late receive a higher kick, resulting to bunch stability. The phase Φ_s is called the synchronous phase.

1.2.3 Cavity frequencies and types

Radio-frequency cavities used in accelerators have frequencies in the 100 MHz-1GHz range, and can have very different shapes. All of them have an electric field component on the beam axis, with oscillation synchronized to the beam. The length of a cavity gap is fixed by the *geometrical*

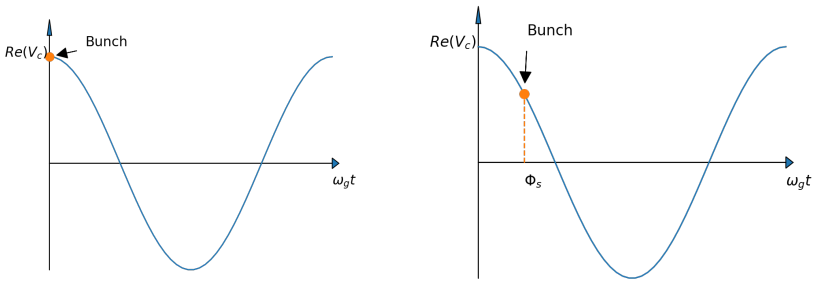

Figure 1.6: Position of a particle bunch in a varying cavity voltage V_{cav}, when the bunch enters the cavity in phase with the voltage (left) or out of phase with Φ_s (right).

β, this latter being determined by the global accelerating scheme:

$$L_{gap} = \frac{\beta\lambda}{2} = \frac{\beta c}{2f} \tag{1.5}$$

Low beta cavities must have lower frequencies to keep reasonable gap length. Cavities with a transverse electro-magnetic mode (TEM) are well adapted to these applications. The gap length being fixed, the resonance frequency is adjusted by the cavity height (close to λ). The frequency and shape choices are a trade-off between cavity fabrication process (low beta cavities are bigger, thus more expensive to produce), beam tube aperture possibilities, and RF efficiency. IFMIF/DONES and SARAF linacs are aimed to accelerate deuterons, with β lower than 0.2. Both use the frequency 175 MHz, and half wave resonators (HWR). ESS and PIP-II protons linacs use spoke cavities around 300 MHz for a medium stage of acceleration ($\beta < 0.5/0.6$). HWR and spokes are both TEM cavities, the outer conductor being coaxial with the inner conductor for the HWR and coaxial with the beam axis for the spokes (Fig. 1.7 (a,b)).

For high β, the standard shape comes from simple pill-box cavities, where cell shape has been rounded to limit peak field on the walls and multipacting, resulting in elliptical shapes, as for the ESS high beta cavities (Fig. 1.7 (c)).

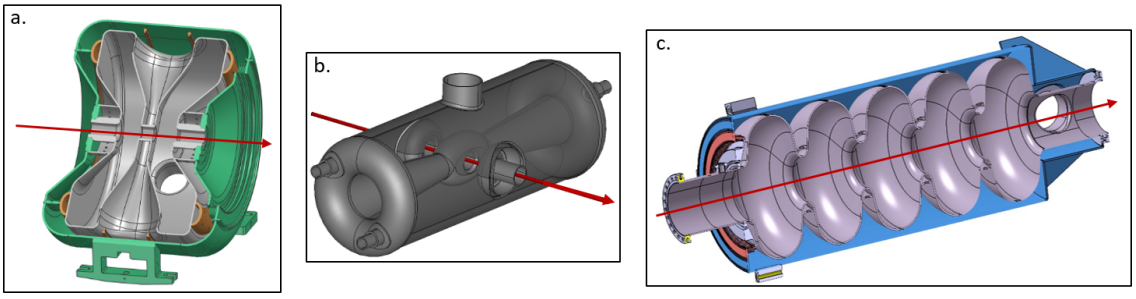

Figure 1.7: (a) PIP-II Single spoke resonator type 1, 325 MHz, β=0.22 [Nar+22], (b) high beta IFMIF/DONES half wave resonator, 175 MHz, β=0.18, (c) ESS high beta elliptical cavity, 704 MHz, β=0.86. The read arrows represent the beam axis.

The electric field pattern is represented in Figure 1.8 in a pill-box, an ESS high beta cavity and the IFMIF/DONES high beta HWR.

1.2.4 Cavity performance

The performance of an accelerating cavity is measured by its ability to provide maximum energy per unit length to a beam at a minimal cost, ie while minimizing the thermal losses. It is described by two main parameters :

⋆ The accelerating field E_{acc} represents the amount of energy ΔU likely to be provided to the beam per length unit (L_{acc} is the accelerating length, in principle equal to $n\beta\lambda/2$, n being the number of cavity gaps).

$$E_{acc} = \frac{|\Delta U|}{qL_{acc}}$$

⋆ The quality factor Q_0 measures the RF losses P_{cav} into the cavity walls for a given stored energy W.

$$Q_0 = \frac{\omega W}{P_{cav}} \qquad P_{cav} = \frac{1}{2}\iint_S R_s H^2 dS$$

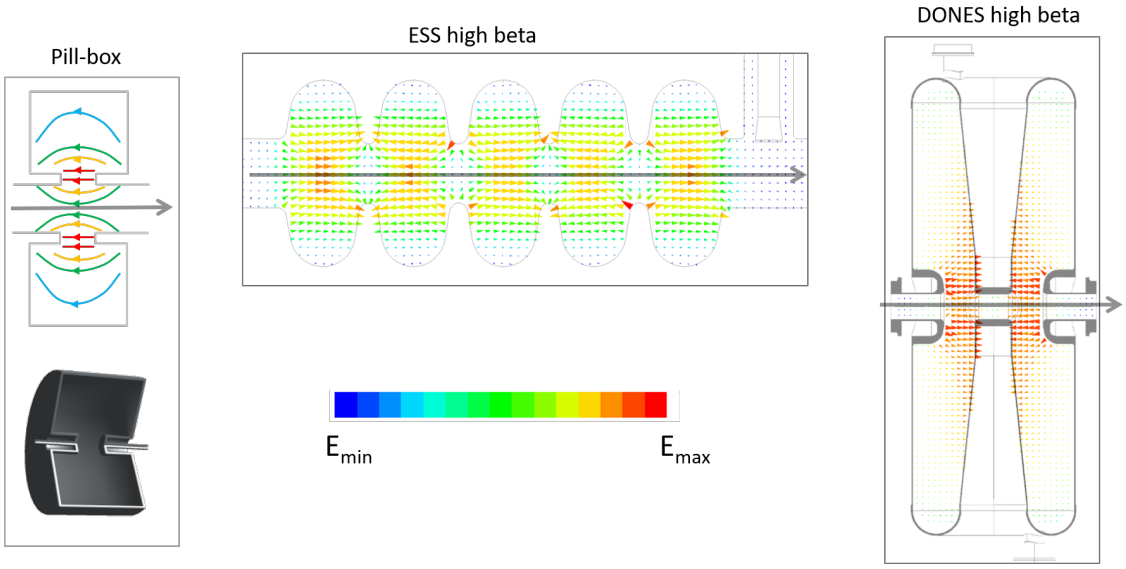

Figure 1.8: Electric field in cavities: pill-box, ESS high beta cavity and IFMIF/DONES high beta HWR. The grey arrows represent the beam axis.

The RF losses in a metal are due to the Joule effect, and are proportional to the metal surface resistance R_s and to the square of the RF magnetic field H along the cavity surface S. Large RF losses reduce the efficiency of beam acceleration, because they represent a fraction of the RF power provided to the cavities which is transformed into metal heating instead of being transferred to the beam. The heat produced in the cavity wall has to be evacuated to protect cavity and ancillaries integrity. The ability of a cavity to reach high accelerating field with low RF losses is estimated during the design phase. It requires providing appropriate material for the cavity fabrication and specific preparation steps for the cavity. This will detailed in the following sections.

Some geometrical parameters are also useful to characterize the cavity:

⋆ the shunt impedance to quality factor ratio r/Q represents the cavity ability to provide high accelerating field for a given amount of stored energy W

$$\frac{r}{Q} = \frac{(E_{acc}.L_{acc})^2}{\omega W}$$

⋆ the geometrical factor $G = Q_0.R_s$

Both parameters only depend on the cavity geometry, irrespective of the cavity material. They are optimized during the design phase.

The cavity resonates at its design frequency f within a range equal to a few bandwidths $\Delta f = f/Q_l$. Here, Q_l is the loaded cavity factor, containing both RF losses P_{cav} and power exchange with outside P_{ext} (more details in section 1.4.1):

$$\frac{1}{Q_l} = \frac{1}{Q_0} + \frac{1}{Q_{ext}} = \frac{\omega W}{P_{cav}} + \frac{\omega W}{P_{ext}} \tag{1.6}$$

The goal cavity frequency is set up during the cavity fabrication and preparation steps (see section 2.3). A mechanical frequency tuning, based on cavity shape plastic deformation, is performed after cavity fabrication. When the cavity is in operation in an accelerator, a fine frequency tuning is obtained by the implementation of a motorized frequency tuning system. The principle is to deform the RF field pattern, either by inserting a movable plunger in the cavity, or by applying a deformation on the cavity shape (in the elastic domain). This latter solution is illustrated in Figure 1.9 where a tuning system applies a force between the cavity and its helium vessel. The role of this vessel is to allow a superconducting cavity to be immersed in liquid helium.

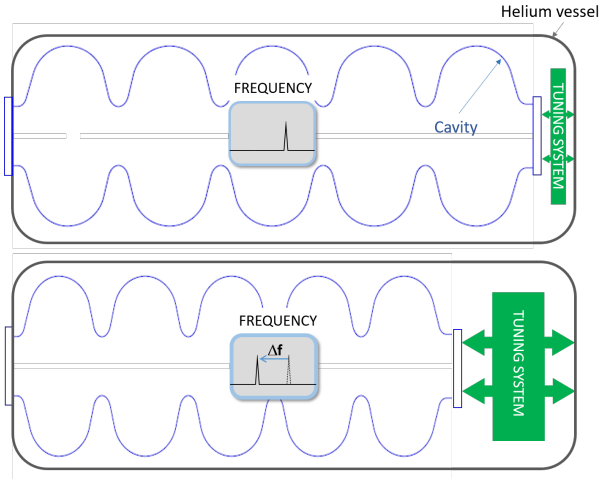

Figure 1.9: Principle of a frequency tuning system based on cavity shape deformation.

1.3 Normal versus superconducting cavities

Historically, accelerating cavities were made of copper, however due to the high level of RF losses, the accelerating field was limited to a few megavolts per meter, and for very short pulses. Otherwise, the copper was definitely damaged. For many decades now, superconducting niobium is used for the fabrication of accelerating cavities, with the advantage of a dramatically decrease of the RF losses. The accelerating fields can reach tens of megavolts per meter and be used in long pulses and even in continuous mode.

Today, many accelerators includes superconducting cavities. Among the projects planned for the future particle physics strategy, the Future Circular Collider (FCC, CERN), and the International Linear Collider (ILC, Japan), include superconducting cavities. On the other hand, the Compact linear collider (CLIC, CERN) should be made of copper cavities operating at 12 GHz. These cavities will work in very low duty cycle, around 1 per million, to prevent copper overheating, and aim to reach challenging gradients at 100 MV/m.

This section presents formulas and phenomena characteristic of superconducting cavities, which are detailed by H. Padamsee, J. Knobloch and T. Hays in the book *RF Superconductivity for Accelerators* [PKH08].

1.3.1 Surface resistance and RF losses

The niobium is the natural superconducting element whose transition temperature is the highest. It has the property of becoming superconductor when cooled down under its transition temperature T_c, equal to 9.2 K. While the resistance of a superconductor is zero for a continuous electric field, it is small but non zero in the presence of a radiofrequency field. This is explained by the two fluids model describing the electrons in a superconductor under T_c. One fluid is a superfluid of paired electrons (called the Cooper pairs) and the other is a normal fluid of free electrons. The paired electrons move coherently and carry a supercurrent with zero resistance. Since this supercurrent flows without resistance, it can carry the entire current, while the normal electrons do not move. This is why the resistance in a DC field is strictly zero. However, the Cooper pairs move without friction but with inertia. Then, in a variable electric field, they do not move fast enough to carry the entire current, leaving a fraction of this current carried by normal electrons, and the surface resistance is not exactly zero, even if very low.

The variation of the surface resistance of superconducting metals is described by a model called the BCS resistance, noted R_{BCS}, described by the BCS theory [PKH08]. This resistance (in Ω) depends on the temperature (T in K) and on the square of the RF frequency (f in GHz) with the formula [PKH08]:

$$R_{BCS}(T) = \frac{2.10^{-4}}{T}\left(\frac{f}{1.5}\right)^2 e^{-17.67/T} \tag{1.7}$$

However, at very low temperature, the observed surface resistance reaches a limit, non described by the BCS model. This term, independant of the temperature, is the residual resistance R_{res}, and the overall surface resistance is described by:

$$R_S = R_{BCS}(T) + R_{res} \tag{1.8}$$

The residual resistance may be caused by the presence of defects, hydrides, oxidized layer on the surface, or welding imperfections. A fraction of the residual resistance is generated by the trapping of magnetic flux in the superconductor, and this effect will be studied in more details in Section 3.1.

The comparison between the surface resistance of superconducting niobium and copper illustrates the huge advantage of using niobium for accelerating cavities. This comparison is shown in the left part of Figure 1.10; the niobium surface resistance is the sum of R_{BCS} calculated from equation 1.7, and R_{res} arbitrary fixed to a common value of 10 $n\Omega$.

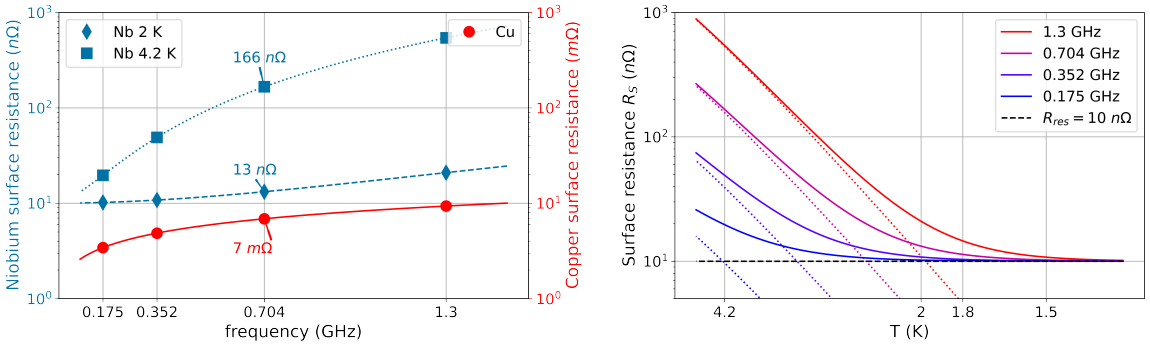

Figure 1.10: Left: comparison of the surface resistance of niobium (in $n\Omega$) and copper (in $m\Omega$). Numerical values are shown for 704 MHz. Right: evolution of the niobium surface resistance with temperature for different frequencies. The dotted lines are the BCS resistances. The residual resistance is fixed at 10 $n\Omega$ for both graphs.

One can see how the surface resistance in niobium is divided by around five orders of magnitude, compared with copper at room temperature. It is this huge reduction in surface resistance that justifies the preferred use of superconducting niobium over copper in many particle accelerators.

Indeed, because of their high surface resistance, copper cavities can only support short pulses above a certain power to allow the material to cool down. On the contrary, superconducting cavities can be operated with an accelerator field of tens of megavolts per meter at high duty cycle, i.e. by injecting the beam and radio-frequency power with long pulses, or even continuously. The efficiency of niobium cavities is also much better, since the heat dissipation in the walls is decreased, so that practically all the power injected into the cavity is transmitted to the beam. In copper cavities, on the other hand, much of the power injected is lost through heating, efficiency is low, and high-power radio-frequency power sources are required to drive the cavities.

The $1/T$ dependency of the niobium BCS resistance tends to encourage lowering the operation temperature of cavities. The right part of Figure 1.10 shows the surface resistance variation with temperature for typical cavity frequencies. The residual resistance has been fixed to a standard value of 10 $n\Omega$ and the R_{BCS} resistance has been calculated with formula 1.7. For the lowest frequencies the surface resistance approaches the residual resistance at 4.2 K. However, the BCS resistance for high frequencies keeps high at 4.2 K, and becomes lower than a few $n\Omega$ at 2 K. For this reason, high frequencies cavities ($>$ 500 MHz) are generally cooled down with superfluid helium around 2 K. Referring to the accelerators described in Figure 1.3, IFMIF/DONES and SARAF, working at 175 MHz, are cooled down at 4.2 K while the elliptical cavities of ESS, PIP-II and XFEL, with operation frequencies above 600 MHz, are cooled down at 2 K.

As an illustration we have calculated the surface resistance corresponding to the design parameters of a high beta ESS cavity working at 704 MHz, considering copper and niobium at 4.2 and 2 K. The surface resistance values come from Figure 1.10. The quality factor is calculated from $G = Q_0.Rs$, with $G = 241\ \Omega$ (see Table 2.1). The peak dissipated power P_{diss} is given by the following relation[PKH08] with the cavity nominal gradient $E_{acc} = 19.9\ MV/m$, the accelerating length $L_{acc} = 0.916\ m$ and $r/Q = 477\ \Omega$ (see Table 2.1). The average dissipated power $< P_{diss} >$ takes the duty cycle, equal to 4 %, into account:

$$P_{diss} = \frac{(E_{acc}.L_{acc})^2}{r/Q.Q_0} \tag{1.9}$$

The results are shown in Table 1.1. Using copper for the cavities would result in 20 MW peak power losses (800 kW in average), while those cavities are aimed to provide 1 MW peak power to the beam. By comparison, the power peak losses in niobium would be some tens of watts in average, four order of magnitude lower.

	R_s	Q_0	P_{diss}	$< P_{diss} >$
Copper	7 mΩ	3.5e4	20 MW	800 kW
Niobium 4.2 K	166 nΩ	1.5e9	480 W	19 W
Niobium 2 K	13 nΩ	1.8e10	38 W	1.5 W

Table 1.1: Estimated surface resistance, quality factor, peak and average RF losses for an ESS high beta cavity working at 4% duty cycle.

Table 1.1 also shows that the RF losses in niobium are decreased by one order of magnitude by working at 2 K instead of 4.2 K. Note that this table only gives orders of magnitude. In reality, the heat load for an ESS high beta cavity has been estimated to 5 W at 2 K, and the measured values were mostly between 1 and 3 W [Piq+23].

However, working at cryogenic temperature requires energy, as well as dedicated installation, which of course has to be taken into account when one wants to estimate the energy cost of an accelerator. This will be discussed in section 1.5.

1.3.2 Performance limitations for cavities

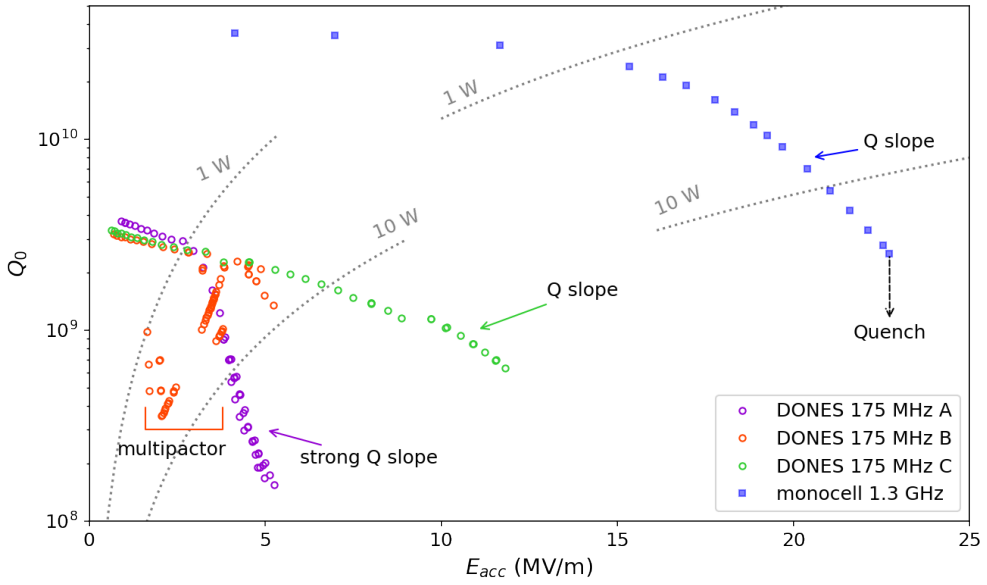

Figure 1.11: Q_0 vs E_{acc} curves for a 175 MHz IFMIF/DONES high beta cavity (T = 4.2 K) and for a 1.3 GHz monocell cavity (T = 2 K). The isopower curves are plotted for each cavity type. The figure illustrates different phenomena limiting cavity performance (multipactor, Q-slope, quench).

Figure 1.11 shows Q_0 vs E_{acc} curves, which are the usual figures of merit for cavities. These values have been measured during RF tests in a vertical cryostat at CEA. They are calculated from the incident, transmitted and reflected powers of a cavity. The three curves for the IFMIF/DONES high beta HWR were measured during three successive tests presented in section 2.4.2. The values for the monocell cavity were measured during standard tests on those type of cavities, generally used for R&D purpose.

Figure 1.11 also shows some iso-values curves for the RF losses (1 and 10 W), corresponding to the parameters of each type of cavity. These curves show that, as predicted, the cavity working at 2 K reaches much higher accelerating field values for the same level of RF losses than the cavity at 4.2 K. This graph also illustrates some characteristic phenomena limiting cavity performance.

The monocell cavity curve is interrupted by a quench. This phenomena occurs when a local increase of the electromagnetic field due to a defect results in a local heating above the niobium transition temperature (9.2 K). This drives a local area to normal conducting transition, and due to the increased heating, to the global normal-conducting state. It not possible to go beyond the accelerating field value where this quench occurs. Even small imperfections on the inner cavity surface can cause this quench. These spots can be treated once their locations are detected.

The IFMIF/DONES cavity goes through a multipactor phenomena at 2-3 MV/m. In this phenomena, secondary electrons emitted at the surface enter into resonance with the electric field lines. Multipacting consumes radio-frequency power and generates heat. This results in

"barriers" where the injected radiofrequency field is consumed by the phenomenon, preventing the accelerating field increase. These barriers can sometimes be overcome and electron emission finally stops through conditioning process. Actually, for the IFMIF/DONES cavity, the accelerating field could finally be increased after one hour conditioning. However, it can happen that the multipacting barrier permanently limits cavity performance; then a new cavity treatment becomes necessary.

Finally, all the curves in Figure 1.11 present a gradual diminution of the quality factor when the accelerating field is increased, which is usually named *Q-slope*. This may be due to dissipation around field lines (called vortex) trapped in the material, to non-linear corrections of the BCS resistance, or to electron emission at the surface of the cavity in areas of strong electric field. This latter phenomenon is called "field emission", and is associated to X-ray generation, due to the bremstrahlung of the emitted electrons when they hit the cavity walls. Actually, the strong Q-slope on the test "A" of the IFMIF/DONES cavity was associated to an increase of the measure X-rays (see Chapter 5).

Let us mention that the ultimate limit to accelerating field is the theoretical RF critical magnetic field, which is the superheating field equal to 0.23 T [PKH08]. However, the above described field limitations generally occur before this field can be reached on the niobium surface.

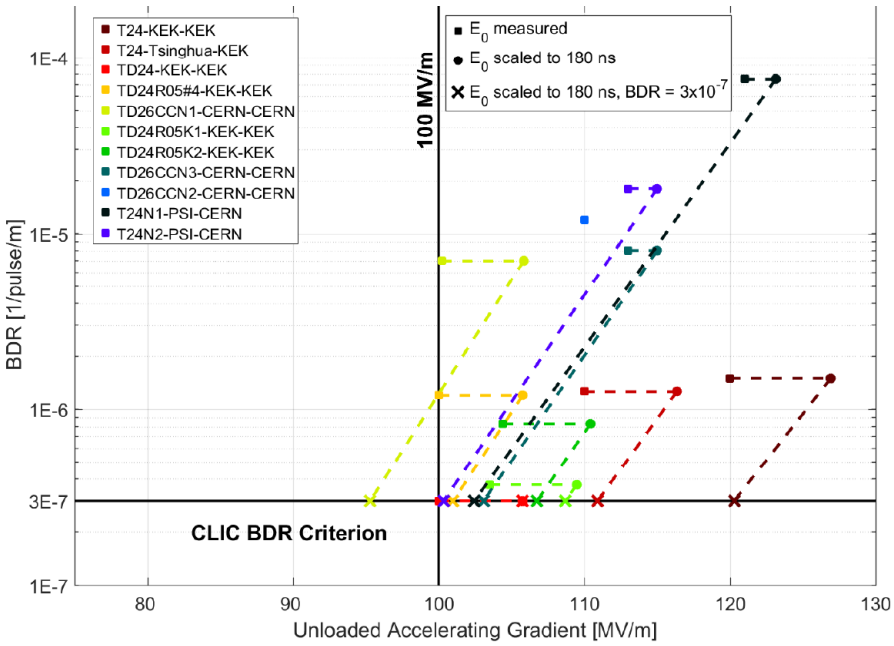

Figure 1.12: A summary of achieved performance of 3 TeV acceleration structures in tests. The vertical axis represents the breakdown rate (BDR) per meter. The final operating conditions of the tests are indicated by squares. Known scaling is used to determine the performance for the nominal CLIC pulse duration (dashed lines connecting squares to circles) and subsequently for the CLIC-specified breakdown rate of 3 $10^{-7}m^{-1}$ per pulse (dashed lines connecting circles to crosses). Ten prototype structures can be seen operating above the target gradient of 100 MV/m. (image credit: CLIC)[Rob18]

For normal conducting copper cavities, the main performance limitation arises from vacuum discharge, or breakdown. The figure of merit for copper cavities features the breakdown rate (BDR) per meter versus the accelerating field. For example, the criterion for the CLIC accelerator cavities is to get less than 3 10^{-7} breakdowns per pulse and per meter, see Figure 1.12.

For cavities aimed to equip the cooling stage of a muon collider, the breakdown phenomenon is enhanced by the presence of strong DC magnetic field (decade of teslas), and this will be detailed in 2.5. The presence of this strong magnetic field is also a reason why those cavities

are not in niobium, since they are submitted to higher levels than the RF critical magnetic field [Pal+09][SGP10].

1.4 RF field coupling with the beam

1.4.1 Accelerating mode

The RF power from the generator is transferred inside a cavity through a power coupler equipped with an antenna penetrating the cavity (see Figure 1.13) This power (P_g) is partially transferred to the cavity, and partially reflected (P_r). The power transferred to the cavity is either absorbed by the beam (P_b) or dissipated in the cavity walls (P_{cav}):

$$P_g = P_r + P_b + P_{cav} \tag{1.10}$$

In superconducting cavities the power dissipated in the walls can be neglected compared to the beam power:

$$P_g = P_r + P_b \tag{1.11}$$

The objective of an accelerating cavity is to transfer the maximal amount of RF power from the generator (P_g) to the beam (P_b).

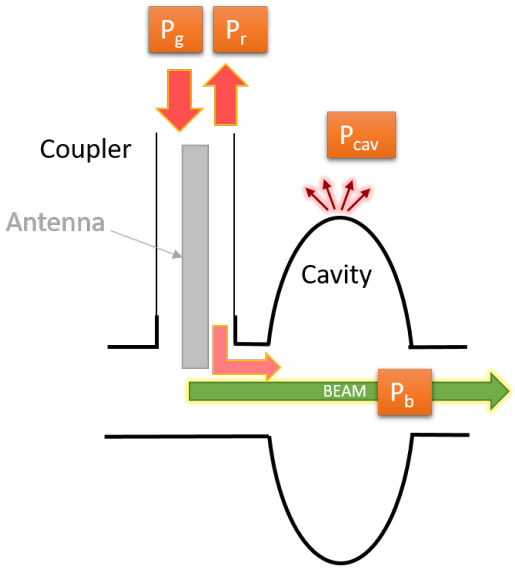

Figure 1.13: The RF power from generator (P_g) is shared between reflected power (P_r), beam power (P_b) and RF losses (P_{cav}).

As mentioned in section 1.2.4, the external coupling factor of a cavity relates the energy stored in the cavity W to the power exchange with outside P_{ext}:

$$Q_{ext} = \frac{\omega W}{P_{ext}} \tag{1.12}$$

For a single cavity, the optimal Q_{ext}, designated by Q_{opt}, corresponds to the case where whole of the power from the generator is transferred to the beam, ie $P_r = 0$ and $P_g = P_b$. In this case, $P_{ext} = P_g$ and Q_{opt} becomes:

$$Q_{opt} = \frac{\omega W}{P_g} = \frac{\omega W}{P_b} \tag{1.13}$$

In a non optimal situation, the expression of the power generated by the source is given by the following equation, involving the real Q_{ext}, the cavity shunt impedance r/Q, the cavity voltage $V_{cav} = E_{acc}.L_{acc}$, the beam current I_b and the synchronous phase Φ_s (see section 1.2.2). This equation is detailed in ref [Sch98], page 39.

$$P_g = \frac{V_{cav}^2}{4\frac{r}{Q}Q_{ext}} \left[\left(1 + \frac{\frac{r}{Q}Q_{ext}I_b}{V_{cav}} \cos\Phi_S \right)^2 + \left(2\frac{\Delta f}{f_{1/2}} + \frac{\frac{r}{Q}Q_{ext}I_b}{V_{cav}} \sin\Phi_S \right)^2 \right] \tag{1.14}$$

The quantity $f_{1/2} = \frac{f}{2Q_{ext}}$ is the bandwidth of the cavity when $Q_0 >> Q_{ext}$, condition being true for superconducting cavities. The parameter Δf is the detuning of the cavity from the resonance, which can be adjusted with a tuner system. The tuning angle, defined by $\tan\Psi = 2Q_{ext}\frac{\Delta f}{f}$ is introduced in the expression of P_g:

$$P_g = \frac{P_b}{4}\frac{Q_{opt}}{Q_{ext}} \left[\left(1 + \frac{Q_{ext}}{Q_{opt}} \right)^2 + \left(\frac{\delta\omega}{\omega_0/Q_{ext}} + \frac{Q_{ext}}{Q_{opt}} \tan\Phi_S \right)^2 \right] \tag{1.15}$$

The reflected power P_r is then given by $P_g - P_b$:

$$P_r = \frac{P_b}{4}\frac{Q_{opt}}{Q_{ext}} \left[\left(1 - \frac{Q_{ext}}{Q_{opt}} \right)^2 + \left(\frac{\delta\omega}{\omega_0/Q_{ext}} + \frac{Q_{ext}}{Q_{opt}} \tan\Phi_S \right)^2 \right] \tag{1.16}$$

The reflected power is minimized for each cavity by:

⋆ Fixing to zero the last term of P_r, by choosing the tuning angle Ψ_{opt} so that:

$$\tan\Psi_{opt} = -\frac{Q_{ext}}{Q_{opt}} \tan\Phi_S$$

⋆ Minimizing the quantity

$$(1 - \frac{Q_{ext}}{Q_{opt}})^2$$

by choosing

$$Q_{ext} = Q_{opt}$$

When both conditions are verified, the coupling between the source and the beam is perfectly adapted, and $P_g = P_b$.

The first condition is achieved during cavity operation by adjusting the cavity frequency with the tuner system. The second condition consists into fixing the external factor for a cavity. In practice, the desired Q_{ext} is adjusted by the position of the coupler antenna in the cavity. This principle is detailed in the case of a IFMIF/DONES cavity in section 2.2.2.

1.4.2 High Order Modes

In any resonator, many high order modes (HOMs) are likely to be excited in addition to the fundamental mode. This is especially true for multicell cavities, where the number of modes increases with the number of cells. If a given cavity mode can accelerate a beam, which is the principle of RF acceleration, the converse is true as well. A beam passing through a cavity can induce RF modes, which in return can lead to beam instabilities, beam loss, and additional power dissipation. The influence of high order modes can be estimated with the same parameters than the fundamental mode: quality factor Q_0 to measure the RF losses,

external quality factor Q_{ext} to measure the coupling with the coupler and shunt impedance to quality factor ration r/Q to measure the ability of providing axial component. The effect of a high order mode is maximal if its frequency coincides with a multiple of the beam bunch frequency (which is the case for the fundamental mode). Depending on the estimated danger of the HOMs, it can be necessary to equip the cavity with a dedicated HOM coupler, whose role is to extract the energy of these modes. High order modes management is illustrated for an ESS cavity in section 2.2.1.

1.5 Cryogenic and RF costs

1.5.1 Cryogenics

The role of the cryogenic setup is both to maintain a given temperature and to extract the power generated by the RF losses. In nearly all accelerators with cryomodules, the cavities are cooled down with liquid helium in a saturated bath. Considering the phase diagram of helium (Figure 1.14), this means that we stay on the saturated vapor pressure curve separating vapor from liquid. The temperature of helium at atmospheric pressure is 4.2 K, this is why many cavities are operated at this temperature. Decreasing the bath temperature from this value requires lowering the bath pressure, which is achieved by pumping operation.

The lambda point at T=2.17 K on the saturated vapor pressure curve separates normal and superfluid helium domains. Working in superfluid helium has many advantages: besides having a lower temperature, superfluid helium has nearly no viscosity [Don09]. Heat is transported by convection instead of heat conduction and this kind of heat transport is very effective, so the thermal conductivity of superfluid helium is very high.

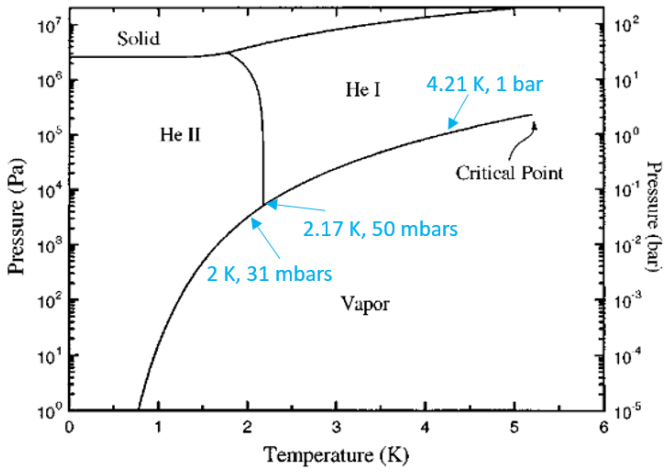

Figure 1.14: Phase diagram of helium [DB98].

However, if the production of 4.2 K helium requires energy, the production of superfluid helium requires even more. The efficiency of a cooling system working at temperature T is the product of several effects, the first being the Carnot efficiency [FLS10]:

$$\eta_c = \frac{T}{300 - T} \tag{1.17}$$

which is 0.014 at 4.2 K and 0.0067 at 2 K. In practice, helium cooling reaches less than 30 % of the theoretical Carnot efficiency. At 4.2 K, the global efficiency is then lower than 0.004. In superfluid helium, the pumping operation requires an amount of energy which increases when the vapor pressure - and thus the temperature - decreases, because the pumping becomes

less and less efficient. Usually, it is estimated that each watt of extracted power requires one kilowatt of cooling power at 2 K [Has23].

Then, working at 2 K instead of 4.2 K is generally not a matter of overall energy saving, but a matter of cavity performance. A cavity with a too low quality factor would not be able to reach the desired accelerating field. Once the choice of working at 2 K has been made, minimizing the RF losses becomes crucial to limit energy consumption.

The required DC power for an ESS cavity has been calculated with these estimations, and Table 1.1 is updated with the corresponding column in Table 1.2. Still the energy needed to use a superconducting cavity is much lower than for copper. These estimations are very important for choosing or not to use superconducting cavities. However, they are certainly not the only one. In addition to the cooling cost of helium, building an accelerator with cryomodules requires technical skills and construction costs that must be taken into account.

	R_s	Q_0	P_{diss}	$< P_{diss} >$	$\boldsymbol{< P_{DC} >}$
Copper	7 mΩ	3.5e4	20 MW	800 kW	**800 kW**
Niobium 4.2 K	166 nΩ	1.5e9	480 W	19 W	**4.8 kW**
Niobium 2 K	13 nΩ	1.8e10	38 W	1.5 W	**1.5 kW**

Table 1.2: Estimated surface resistance, quality factor, peak and average RF losses and estimated DC power for an ESS high beta cavity.

As a last point, we can also mention that the heat transportation in superfluid helium presents properties associated to its quantum nature. The heat is transported by first and second sound waves, described by the two fluids model. A method for quench localization using the dynamics of heat transportation by the second sound wave has been developed, and is presented in section 5.2.

1.5.2 RF costs

As stated in the introduction, the principle of accelerating particles consists into the transfer of energy from the electricity power grid to a particle beam. This is illustrated in Figure 1.15, in the case where the accelerator RF source is a klystron. Similar schemes could apply when using solid state power sources or other vacuum tubes [Dio+17][Job+17]. Here, the modulator transforms the DC grid power into a high voltage provided to the klystron. This high voltage is transformed into RF power by the klystron, and transferred to the RF distribution line (waveguides, circulator...). The final RF power to beam transmission is assured by the coupler and cavity. Each transmission step produces losses, which lower the overall efficiency and require cooling. While a modulator can reach efficiencies close to 90 %, usual klystrons are commonly limited around 60 %. Increasing klystron efficiency is a major issue for future accelerators, involving accelerator laboratories beside industrial manufacturers. We have contributed to this activity within the frame of the EuCARD2 and ARIES programs, as will be developed in chapter 4.

The optimization of the power transfer from the RF input power to the beam is strongly associated with the design of both cavity and RF coupler. Actually, depending on this optimization scheme, a substantial part of the RF is reflected by the cavity and then dissipated in the RF distribution lines. Such optimization will be developed for IFMIF/DONES in chapter 2.

Finally, as developed in the previous section, a part of the RF power will be dissipated in the cavity walls, which can be considerable for normalconducting cavities. In superconducting cavities, this part is very low in comparison of the total amount of RF power - but it requires energy for the cavity cooling, which is not represented here.

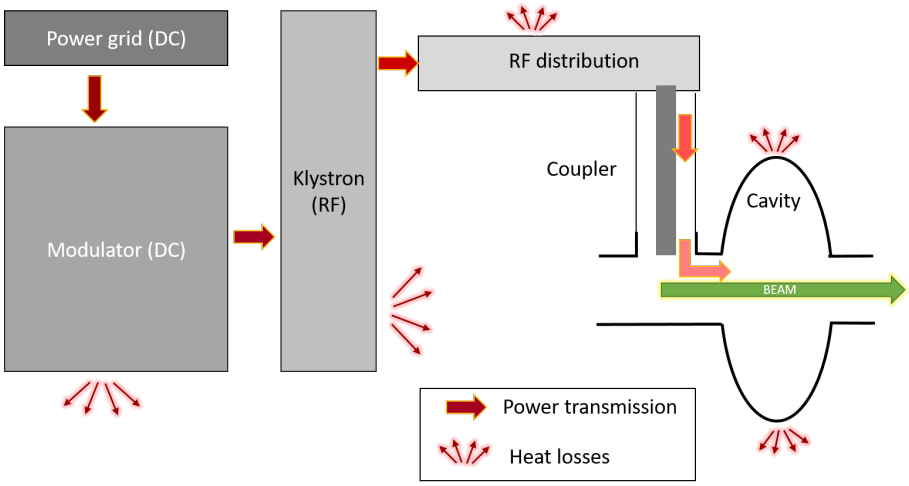

Figure 1.15: Schematic description of the power transmission from power grid to the beam.

1.5.3 Examples of overall costs for accelerators

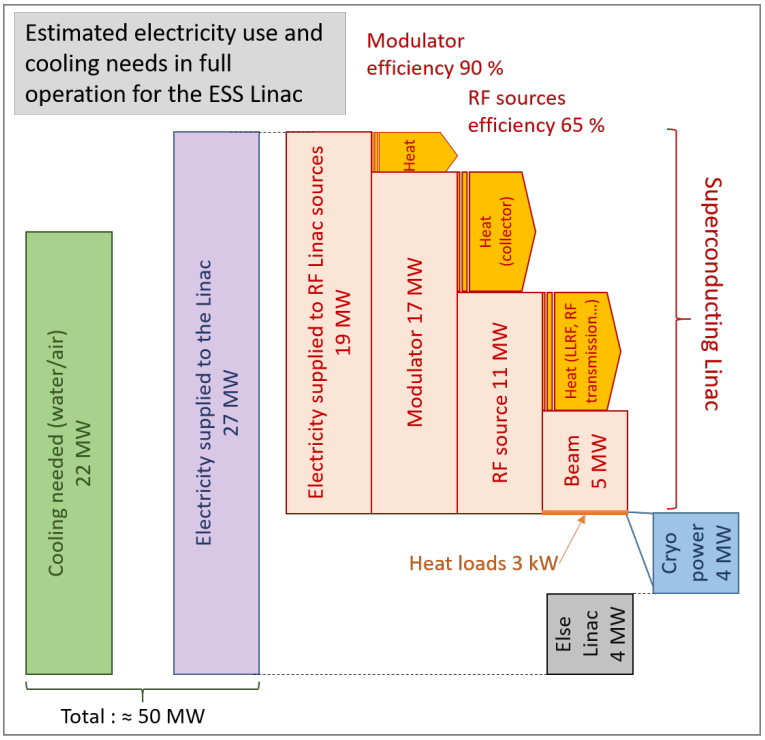

Figure 1.16: ESS RF costs orders of magnitude. Data collected in [ESS12] [Mar22] and [Yog12].

In Figure 1.16, I have represented the estimated power needs for the ESS linac, by collecting data in [ESS12] [Mar22] and [Yog12]. The total needed power for the linac is estimated to 50 MW. Nearly half of it (22 MW) is used for the water and air cooling. The electricity supplied to the linac is 27 MW. The larger part (19 MW) is used to provide RF power to the cavities, and only 5 MW are transfered to the beam. The heat load evacuation from the cavities (ca 3 kW) requires 4 MW cryopower. These values, given in the *2012 ESS energy design report* [ESS12] consider that all modulators are operated at nominal high voltage. However, an optimization of the klystron operation scheme should allow to save ca 3.7 MW on the grid power, thus the 19 MW value could be replaced by 15.3 MW [Mar22]. This graphic underlines that a large amount of the supplied power is lost because of limited efficiency of the modulator and the RF source, and also in the RF transmission process to the cavities. It also shows the important power amount needed to evacuate heat losses, and justifies the important effort to decreases the RF losses in cavities, by minimizing the surface resistance.

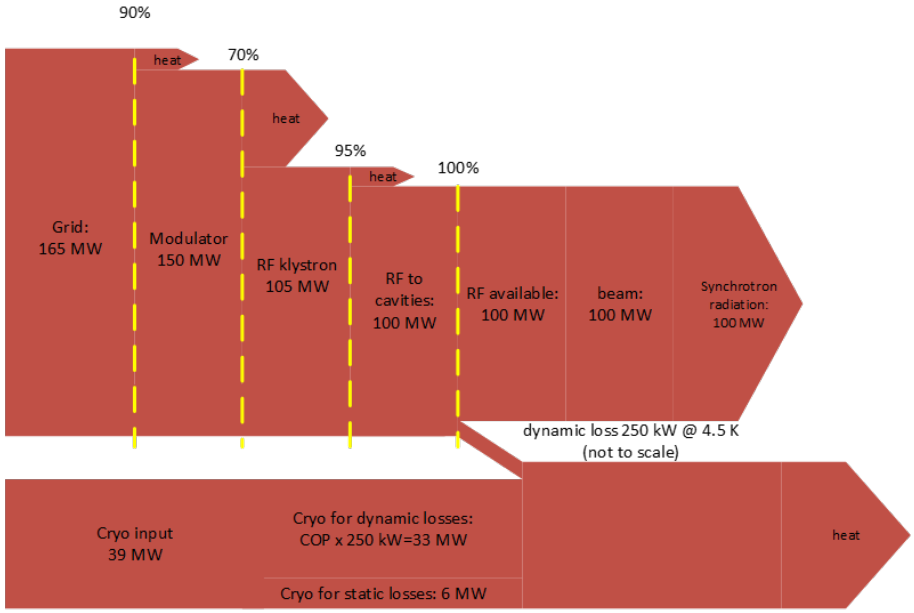

Figure 1.17: The estimated power needs for FCC-ee. From P. Lebrun, presented in [Jen19].

For the Future Circular Collidar (ee), the estimated power needs were presented in several documents, and summarized in the diagram shown in Figure 1.17. The grid power in operation is estimated to 165 MW for a final beam power equal to 100 MW, while the cryogenic power cost is estimated to 39 MW.

1.6 Conclusion

Finally, to conclude this introduction, we can come back to the figure of merit of an accelerating cavity and make the following assertions:

- ⋆ increasing accelerating gradients E_{acc} shorten the accelerator's length, and lower the construction cost.
- ⋆ increasing quality factors Q_0 decrease the RF losses and lower the operation cost.
- ⋆ lowering the overall RF power cost of an accelerator also requires the limitation of the RF losses all along the power transfer process from grid to beam.

The work presented in this dissertation is part of this general effort.

Chapter 2

Accelerating cavities: from conception to operation

2.1 Introduction

This chapter is devoted to the development of accelerating cavities, constituting the elementary components for accelerating particles. Since I have started working in the Accelerators, Cryogenics and Magnetism Division of CEA-Irfu, I have participated to the design of many cavities and ancillaries:

- ⋆ RF and mechanical design of elliptical cavities for the CARE and EuCard European programs [Bos+07; Dev+08a; Dev+08b], [PDC11; Cap+11] (major role)
- ⋆ RF and mechanical design of elliptical cavities for ESS [PD11; Dev+13; Pea+14; Cen+15; Cen+16b; Cen+16a; Bos+17; Cen+19a] (major role)
- ⋆ RF design of a half wave resonator for IFMIF [Zap+09a; Zap+09b; Ors+10; Ors+11; Dev+15] (minor role)
- ⋆ Preliminary design of an RF coupler for IFMIF [Plo+09; Jen+10; Jen+12; Gro+10; Cha+17; Baz+17] (major role)
- ⋆ Design, fabrication and tests of a half wave resonator for IFMIF/DONES [Plo+23a] (responsible)

I will focus on the high beta ESS cavity, which I have designed (2011-2012), and on the IFMIF/DONES prototype cavity, whose development is under my responsibility (2018-today). The last section will describe the future work on cavities for a muon collider, to which I contribute.

2.2 RF and mechanical design of cavities

2.2.1 ESS high beta elliptical cavity

The two last sections of the ESS accelerator are equipped with elliptical cryomodules. The high beta section is made of 21 cryomodules, each containing 4 cavities, working at 704 MHz and with a geometrical beta equal to 0.86 (Figure 2.1). They are aimed to bring the protons energy from 570 MeV to 2 GeV.

Following our experience on medium and high beta elliptical cavities developed within the CARE-HIPPI program (5 cells, $\beta = 0.5$, 704 MHz) [Bos+07], [Dev+08a], [Dev+08b] and the

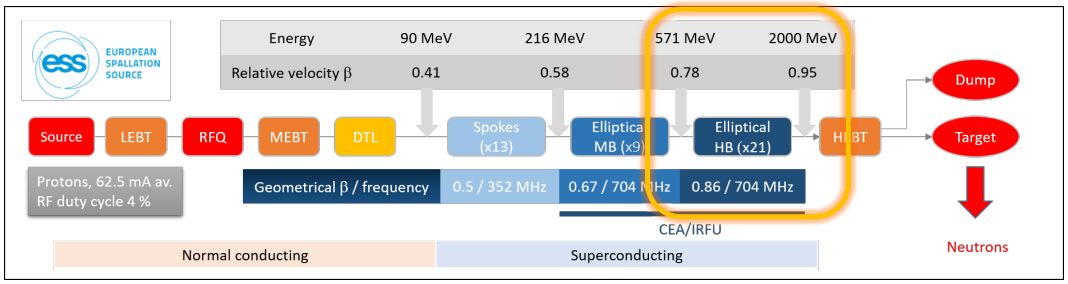

Figure 2.1: ESS high beta elliptical cavities in the linac.

EuCARD program (5 cells, $\beta = 1$, 704 MHz) [PDC11], we have been in charge of providing the design of the high beta elliptical cavities for ESS. I have developed the RF and mechanical design of these cavities.

Cavities working at high beta are operated around 2 K to minimize their surface resistance. The RF design must be optimized to limit the maximal electric and magnetic fields in the cavity walls. For this latter point, an optimal geometry was developed for the Tesla project ($\beta = 1$, 1.3 GHz) [Bri01], and resulted into multicell elliptical cavities. The rounded shape of the cells near the equator also lowers the multipacting sensitivity while the large iris radius reduces wakefield effects. In cavities constituted of n cells, each cell contributes to the acceleration, and the overall accelerating length is reduced. The number of individual RF sources (or power splitters) is also reduced by a factor n. On the other side, the energy acceptance of multicell cavities is reduced compared to monocells. Then the number of cells per cavities is the result of a compromise and the optimized cavity for Tesla has 9 cells. Since the ESS cavities operate at a nearly half of the Tesla frequency, and with higher beta, they have much larger size, and the number of cells must be reduced. The medium and high beta cavities are made of respectively 6 and 5 cells. The parameters required for the ESS high beta cavity are given in Table 2.1.

RF frequency	704.42 MHz
Geometrical beta	0.86
Accelerating length	0.916 m
Accelerating gradient	19.9 MV/m
Q_0 at nominal field	$> 6.10^9$
Mode	pulsed
Av. pulsed current	62.5 mA
Peak RF power	900 kW
Repetition frequency	14 Hz
Beam pulse length	2.86 ms
Operating temperature	2 K

r/Q	435 Ω
G	241 Ω
E_{pk}/E_{acc}	2.5
B_{pk}/E_{acc}	4.3 mT/(MV/m)
E_{pk} at nom. E_{acc}	40 MV/m
B_{pk} at nom. E_{acc}	77 mT/
Q_{ext}	7.6 10^5
HOMs freq. from machine line	> 5MHz

Table 2.1: ESS high beta cavity requirements (left) and design parameters (right).

RF design

The RF design of the high beta ESS cavity was achieved by:

- ⋆ Optimizing the coupling between cells to balance between cavity performance and field distribution homogeneity between cells.
- ⋆ Maximizing the impedance shunt to quality factor ratio r/Q.
- ⋆ Minimizing the maximal surface fields ratio. The achieved values are in Table 2.1. The maximal electric field is situated on the iris part of the cavity cells (see Figure 2.2) while the maximal magnetic field is situated on the equator part.

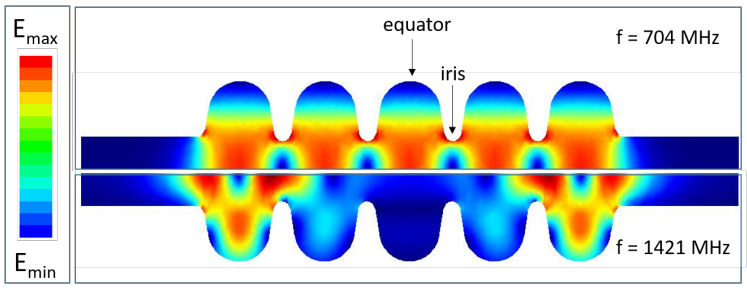

Figure 2.2: Electric field pattern in an elliptical ESS high beta cavity for the accelerating mode at 704 MHz (top) and for a high order mode at 1421 MHz (bottom). Simulations with Comsol [Com].

- ⋆ Adjusting the required external coupling for a proper RF power transfer to the beam (see section 1.4.1). The optimal coupling factor was set to $Q_{ext} = 7.6\ 10^5$ [Dev+13]. At the cavity design stage, the adjustment of the antenna (longitudinal position and distance to axis) is optimized to assess this value (see Figure 2.3).
- ⋆ Shifting monopole high order modes (HOM) frequencies far enough from any machine line (= harmonic of the beam frequency) (see section 1.4.2). It was concluded from the RF design that HOM couplers were not necessary [Dev+11][Cen+19a]. An example of high order mode is shown in Figure 2.2.

The beam aperture of the cavity plays an important role in the optimization process. A low beam aperture increases the shunt impedance for the fundamental mode, which is an advantage, but also for the high order mode, which is a drawback. In addition to HOM attenuation, increasing the beam aperture improves the field distribution homogeneity between cells and makes the coupling to the RF source easier. The maximal surface fields ratio are lowered by a delicated optimization of the elliptical shape of the cavities cells.

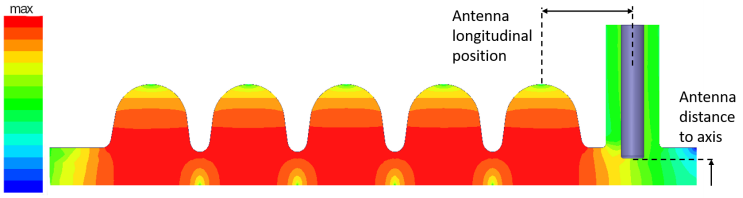

Figure 2.3: Electric field pattern (log scale) in the ESS HB cavity in presence of a coupling antenna. Simulations with Comsol [Com].

Mechanical design

The RF design of a cavity is developed by only considering the vacuum volume where the electromagnetic field is established. However, a cavity is a mechanical object subjected to many constraints, and the complete design must ensure to assure RF operation. Thus the mechanical design must be studied in parallel with the RF design to assure proper fabrication and operation of the cavity.

In operation, superconducting cavities are subjected to large temperature gradients, to pressure forces, to vibrations, and even to mechanical forces due to the RF field itself (called Lorentz forces or radiation pressure). Not only the cavity integrity must be assured during operation, but the shift in frequency due to deformations must keep manageable. The frequency adjustment into operation is assured by a tuning system, which in the case of ESS works by longitudinal cavity deformation.

The thickness of the cavity, directly related to its mechanical stiffness, is a tradeoff between several elements:

- ⋆ A thicker cavity is stiffener, which is an advantage to resist to the Lorentz forces (electromagnetic radiation pressure) and external pressure force, but can become a disadvantage for the cavity tuning.
- ⋆ A thinner cavity allows for better heat exchange, and needs less material, meaning smaller weight and price.

For the ESS cavities, aimed to work in pulsed mode, the sensitivity to the Lorentz forces is especially critical, since the frequency shift must be compensated by a fast tuning system and a low level RF system. Thus, the thickness and stiffening rings position have been optimized in order to reduce as much as possible the Lorentz force effect. This optimization has required coupled RF and mechanical calculations. For ESS, these calculations, made in 2011, were achieved using two free-license codes, Superfish [HH76] for the RF and Castem [Cas] for the mechanics, coupled together thanks to home-made algorithms developed in language C++.

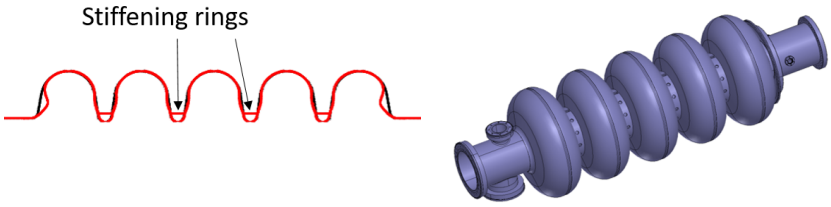

Figure 2.4: The ESS high beta cavity. Left: 2D simulation (Castem) under 5 bars internal pressure in red, without deformation in black. Right: 3D view.

The RF and mechanical design achievements have lead to the final 3D design of the cavity, then on the cavity fabrication. This work was detailed in the *ESS Technical Design Report* in 2013 [Peg13] and in conference proceedings [Dev+11][Dev+13].

2.2.2 IFMIF/DONES high beta half wave resonator

The low (0.11) and high (0.18) beta cavities for the IFMIF/DONES superconducting linac are half wave resonators (HWR), aimed to work at 4.2 K. Figure 2.5 shows the sequence of the two low beta and the three high beta cryomodules. While the low beta cavities are directly adapted from the IFMIF-Lipac [Baz+13; Ba13], the high beta cavity design is developed in the frame of the EUROfusion Workpackage WPENS (Work Package Early Neutron Source) [Pic+18; Plo+19a; Baz+20]. I am responsible of the High Beta Cavity Design and Prototyping (task 6.5.2.2) in the SRF Linac. During the last years, the whole design of the cavity has been achieved, and a prototype has been fabricated and tested in a vertical cryostat. This activity is summarized in this section (design) and in section 2.4.2 (test). It has been detailed in the EUROfusion regular reports [Plo18a; Plo18b; Plo18c; Plo20; Plo21b; Plo21a; Plo22]

RF design

The optimization of the electromagnetic geometry has been achieved according to the beam dynamics requirements (beta value, accelerating field, beam current), detailed in Table 2.2. Compared to the ESS cavities, the optimization of the maximal electric and magnetic fields is less critical, given that the accelerating field itself is rather low. Figure 2.6 shows the electric and magnetic field distribution on the cavity walls. For the IFMIF/DONES cavity, the most challenging parameters are the high current and the high RF power in continuous mode, which

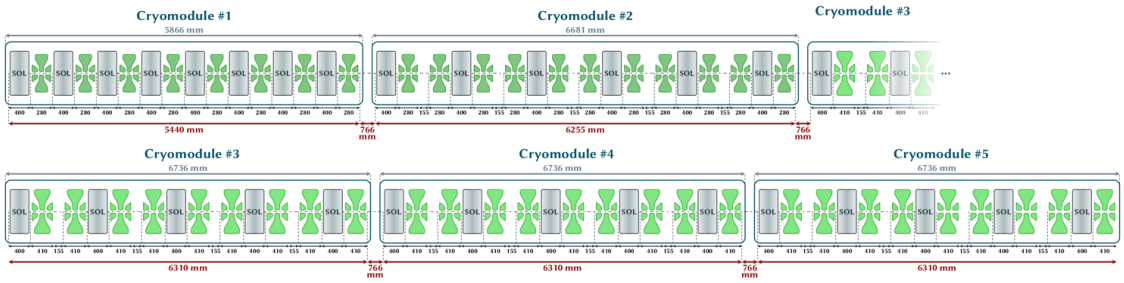

Figure 2.5: Layout of the 5-cryomodules SRF Linac. Cavities are in green and solenoids in grey.

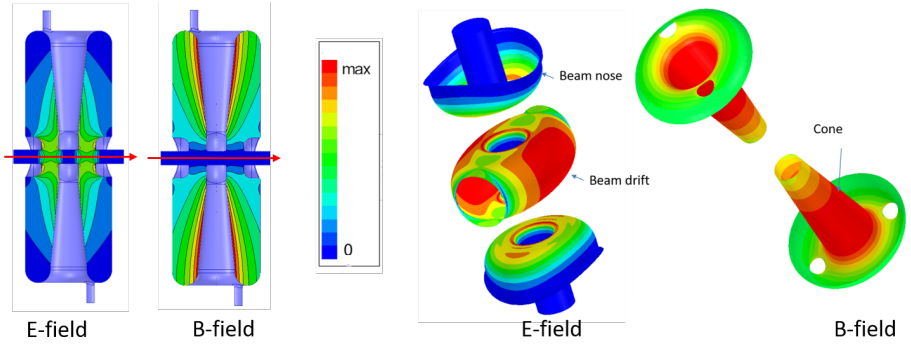

Figure 2.6: Electric and magnetic field patterns in the IFMIF/DONES high beta cavity: on cut planes (left) and on inner surface (right). Calculations with Comsol [Com] eigenmode.

lead to a high value of the external factor to allow for RF power transfer to the high current beam. The determination of an optimized Q_{ext} is detailed hereafter. The high current value also requires rather quite high beam aperture (50 cm).

RF frequency	175 MHz
Geometrical beta	0.18
Accelerating length	0.309 m
Accelerating gradient	4.5 MV/m
Q_0 at nominal field	$> 10^9$
Mode	continuous
Beam current	125 mA
RF power	200 kW
Operating temperature	4.2 K

r/Q	260 Ω
G	53 Ω
E_{pk}/E_{acc}	4.65
B_{pk}/E_{acc}	8 mT/(MV/m)
E_{pk} at nom. E_{acc}	21 MV/m
B_{pk} at nom. E_{acc}	36 mT

Table 2.2: IFMIF/DONES high beta cavity requirements (left) and design parameters (right).

Optimal Q_{ext} determination

The beam dynamics for the IFMIF/DONES SRF Linac has been optimized in the project framework [Du+18; Cha+19], and the beam power and synchronous phase evolution along the superconducting linac have been set up. Their values for the 5 cryomodules and 46 cavities are shown in Figure 2.7 (left). As described in section 1.4.1, the coupling is optimal when all the RF power is transferred to the beam, which is achieved by adjusting the external coupling Q_{ext} and the frequency detuning Δf. The optimal values for each parameter is plotted in Figure 2.7 (right): the optimal Q_{ext} varies between 4.5 10^4 and 6.5 10^4 for the 3 last cryomodules containing the high beta cavities. While each cavity can be individually tuned to its optimal frequency value, since the tuning systems are driven independently of each other, it is more complicated for the Q_{ext}, which is determined by the coupler antenna penetration.

Adjusting the quality factor for each cavity would require the adjustment of the coupler for each cavity, either by fabricating a different coupler for each cavity, or by allowing in situ adjustment of the coupler geometry. This latter solution is used in several projects, like XFEL [KM04][KMK13], where the coupler antenna position is adujstable. It is optimal for minimizing power reflection from the generators, but it is more complex to design and more fragile. Another solution is to fix the Q_{ext} value for a whole cavity set, and estimate whether the loss in RF power due to reflected power is acceptable. For IFMIF/DONES, the choice is to define two Q_{ext} values: one for the low beta cavity set and one for the high beta cavity set. The analysis leading to the determination of these values is now on going.

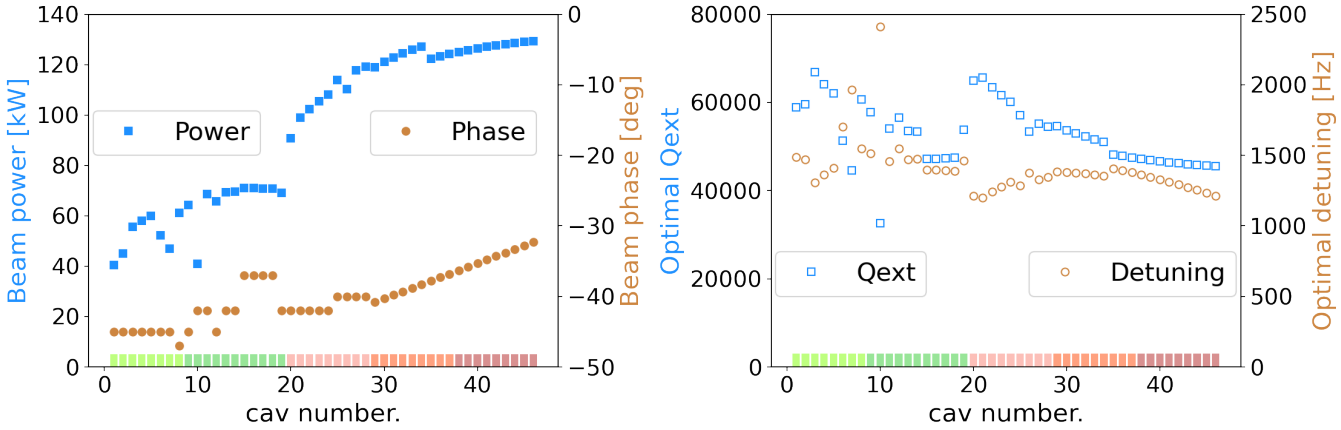

Figure 2.7: Beam power and synchronous phase (left), optimal Q_{ext} and detuning (right) along cavities. The colored bars at bottom of the plots represent the cavities in each of the five cryomodules.

Power coupler for IFMIF/Lipac and IFMIF/DONES

The power coupler designed for the IFMIF/DONES low and high beta cavities will be directly derived from the coupler designed and fabricated for the IFMIF/Lipac.

I have been in charge of the first phase of the design development of this coupler [PDC11]. The schematic view of the coupler design developed during this phase is shown in the left part of Figure 2.8 and a cavity assembled with a coupler fabricated in a following phase is shown in the right part of Figure 2.8.

The couplers have been successfully conditioned at 100 kW in continuous mode [Reg+14]. The IFMIF/Lipac cavity equipped with its power coupler was tested in a dedicated cryostat and the nominal accelerating field of 4.5 MV/m was achieved with an injected power of 14 kW [Piq+17].

Mechanical design

The mechanical design of the cavity has been realized with the multiphysics code Comsol [Com], allowing coupled RF and mechanical calculations. With the optimized shapes and thicknesses of the constituent pieces of the cavity (see Figure 2.9), the maximal stresses and deformations due to electromagnetic radiation pressure or liquid helium pressure changes remain small. The Lorentz force detuning is less critical than for ESS, since the cavities are aimed to work in continuous mode. We have also checked that only negligible frequency shifts might occur during operation in vertical cryostat or in cryomodule configuration, which is crucial to avoid instabilities leading to performance limitations and/or extra beam losses. While the cavity itself

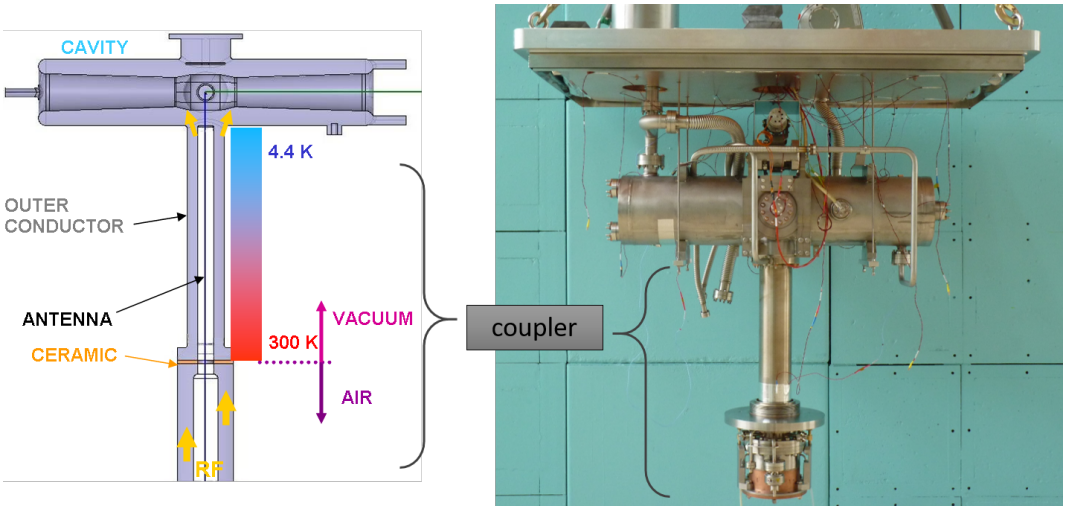

Figure 2.8: Schematic view and picture of the power coupler for the IFMIF Lipac.

is made of pure niobium, its flanges are made of niobium titanium. The mechanical design is detailed in [Plo18b].

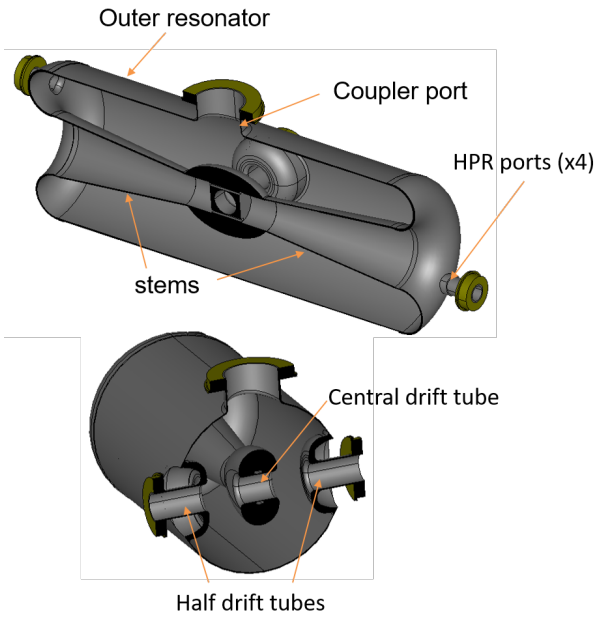

Figure 2.9: 3D view of the IFMIF/DONES high beta cavity.

2.3 Cavity fabrication and preparation

The fabrication of superconducting cavities in niobium is the role of dedicated companies. In Europe, two companies have the required expertise, Zanon R&I in Italy and Research Instruments in Germany. Cavities are not *off the shelf* objects and their fabrication involves a strong collaboration between labs and companies. The procurement of the niobium itself needs a good knowledge on materials, because the cavity performance are directly related to it. The compatibility between the mechanical design realized by the lab and the manufacturing possibilities must be carefully developed. The achievement of the cavity target frequency requires a tuning procedure, which consists into a succession of blank assembly of the cavity parts, intermediate frequency measurements, trimming and welding, realized in the manufacturer premises under the lab responsibility. These steps are developed for the ESS cavity in [Cen+15] and for

the IFMIF/DONES cavity in [Plo22]. After cavity fabrication, a tuning operation consisting in applying a plastic deformation of the cavity to reach proper frequency and electric field distribution can be realized. It has been done for the ESS cavities [Pea+14].

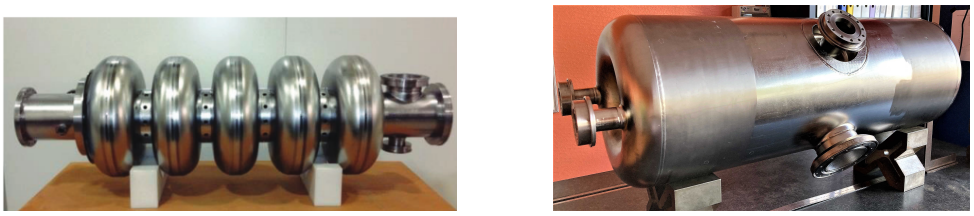

Figure 2.10: Left: picture of an ESS high beta cavity. Right: picture of the IFMIF/DONES high beta prototype.

Once the cavity is delivered by the manufacturer, it has to be prepared: to achieve expected RF performance, the surface of the niobium cavity is cleaned by chemically etching away the surface layer damaged during the fabrication. The methods used for material removal are standard buffered chemical polishing (BCP) and electropolishing (EP). In BCP, the cavity inner walls are submitted to chemical etching with an acid blend made of Phosphoric, Nitric and hydroFluoric. Since the reaction is exothermic, the temperature of acid must be actively cooled down. EP is carried out with an acid mix as an electrolyte. A cathode is inserted inside the cavity while the cavity walls serve as an anode. The assembly is rotated in an acid circulation, the device being installed horizontally or vertically [Eoz+12; Eoz+14].

The prototype [Cen+16a] and series [WAB23] high beta cavities for ESS have undergone BCP, with approximately 200 μm thickness removal. In parallel, R&D studies aim to demonstrate the superiority of vertical EP compared to standard BCP for ESS cavities [Eoz+22]. The IFMIF/DONES prototype has also undergone a 200 μm BCP.

The chemical etching of a cavity is followed by a high pressure rinsing (HPR) with ultrapure water to remove any chemical and particulate residue from the niobium surface. The cavity is then equipped with antennas and closed in a clean room. All these steps are crucial to guarantee the performance of a cavity. In particular, the field emission phenomena, one of the major reason for cavity degradation, occurs when dust particles act as emitters. The high pressure rinsing process plays a important role for dislodging the surface contaminants. For example, the first test of the IFMIF/DONES prototype presented low quality factor and high field emission; after improvement of the HPR procedure, a second test series presented good performance (Fig. 2.12).

For the ESS cavities, after a first sequence of chemical treatment, HPR and clean room assembly followed by a test in vertical cryostat, the cavities are assembled into a string in a clean room. The whole process is a main issue for the cryomodule assembly [Mad+21].

Cavities are likely to be submitted to heat treatment at several preparation steps. A lot of thermal treatment recipes have been explored and developed in many laboratories during the last decade, and have led to considerable improvements of the cavity performance. They are widely described in the book *Superconducting Radiofrequency Technology for Accelerators* by H. Padamsee [Pad23].

A standard recipe consists into baking out the cavity after clean room assembly at 120°C during 48 hours under vacuum. The BCS resistance is lowered while the residual resistance is increased. For cavities working at 4.2 K, the performance are usually improved whatever the frequency because the resistance is dominated by BCS. At 2 K, the benefit is not assured since the increase of residual resistance is likely to dominate [Lon17], and the ESS cavities have not undergone this baking. The IFMIF/DONES prototype, aimed to work at 4.2 K, was submitted to such baking, and reached good performance.

A specific thermal treatment is widely used for many decades for curing a phenomena named

Q-disease. This phenomena is caused by hydrogen absorption by niobium during chemical treatment. During the cavity cooldown, there is a temperature range, between 150 and 60 K where the formation of hydrides, Nb-H, is enhanced in the material. The presence of hydrides islands increases the RF losses and causes Q_0 drop. Baking the cavity at high temperature (600-800°C) after chemical treatments help to degas most of the hydrogen and is a well-known cure. The ESS cavities have all been submitted to such heat treatment (600°C for 10 hours) in order to vaccinate the cavity against Q-disease.

2.4 Cavity experimental characterization

The cavity performance are tested by measuring incident, reflected and transmitted power to plot the Q_0/E_{acc} curve, the cavity being cooled down by liquid helium.

Usually, a cavity is first tested in a vertical cryostat, before and/or after being equipped by its helium tank. The cavity is immersed in a helium bath and connected to an RF synthesizer delivering up to hundreds of watts. The test platform at CEA-Irfu, Supratech, is equipped with two vertical cryostats, for small and large cavities.

For a characterization closer to the configuration inside a cryomodule, a cavity can be tested fully dressed with its RF coupler and frequency tuner. A dedicated cryostat is necessary, allowing the cavity connection to cryogenic lines and its thermal insulation. The cavity is connected to a high power RF source through the RF coupler. At CEA-Irfu, several such dedicated cryostats have been build over years. The medium beta cavity developed for the CARE-HIPPI program (see p. 14) was tested in CryHoLab, the RF power being provided by a 1 MW 704 MHz test stand equiped with a DC high voltage power supply, a 50 Hz modulator and a klystron amplifier [Dev+11]. A dedicated cryostat, named SaTHoRI was build for the test of the low beta cavity for the IFMIF/Lipac [Piq+17]. The setup cavity/coupler/tuning system is shown in Figure 2.8 before insertion in SaTHoRI. In order to test both low and high beta SARAF cavities with tuner and coupler we have also designed and build the Equipped Cavity Test Stand (ECTS) [Piq+19]. Flux trapping experiments on a SARAF cavity, realized in this ECTS, are presented in section 3.4.

Finally, the cavities are tested once assembled in the cryomodule. Such characterization has been carried out at CEA-Irfu for the ESS cavities, and will be presented in the following section.

2.4.1 ESS

A set of five high beta prototype cavities for ESS have been developed and manufactured under the responsibility of CEA-Irfu, and tested in vertical cryostat at Saclay. All of them have met the specifications $Q_0 > 5 \times 10^9$ at nominal gradient $E_{acc} = 19.9$ MV/m [Cen+19a].

For the production phase, the cavities for the medium beta elliptical section are procured by INFN/LASA (Italy) and those for the high beta section by STFC/Daresbury (UK). Cryomodule assembly is performed at CEA Saclay, which receives the cavities after their successful qualification in near-critical RF coupling conditions in a vertical cryostat at 2 K.

The production and qualification of the high beta cavities is ongoing at STFC/Daresbury. The results of 86 cavities have been recently presented [WAB23], and the results are shown in Figure 2.11.

Finally, eight ESS elliptical cryomodules have been tested at CEA. All the cavities achieved the nominal voltage, except one limited by quench (but solved at ESS in nominal cryogenic condition). The dynamic heat load per cavity at nominal gradient was measured between 1 W

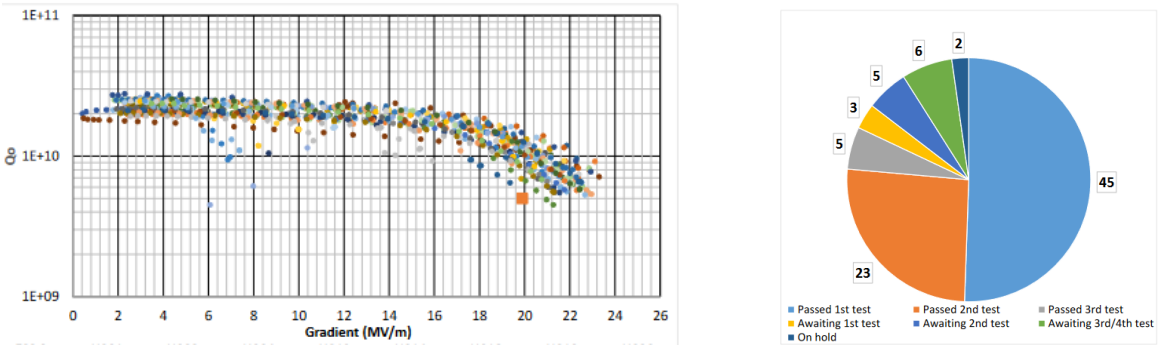

Figure 2.11: Results of 86 high ESS cavities procured and tested at STFC/Daresbury: Q_0/E_{acc} curves (left) (the orange square is the specification) and test performance. Data from [WAB23].

and 3 W with few exceptions between 4 W and 5 W (linked with strong field emission). These performance are in the ESS specifications, less than 5 W and 6. 5W, respectively for medium beta and high beta cavities [Piq+23].

2.4.2 IFMIF/DONES

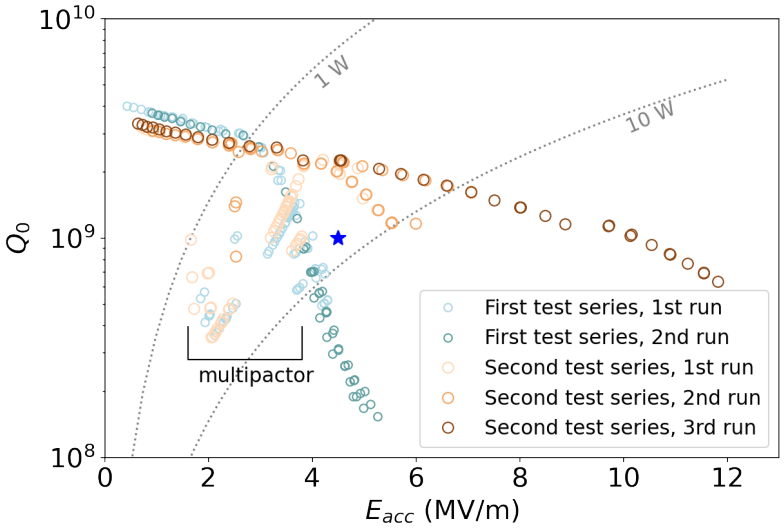

Figure 2.12: Curve $Q = f(E_{acc})$ for the IFMIF/DONES prototype. The blue star represent the specification target.

The high beta prototype cavity for IFMIF/DONES has been fabricated and first tests in vertical cryostat have been carried out on the naked cavity (without helium tank). All the process starting with the fabrication and leading to the RF tests are developed in the two successive IFMIF/DONES reports [Plo21b; Plo21a], and summarized in the paper [Plo+23a] given in annex of this chapter. A picture of the prototype is shown in Figure 2.10.

We carried out two series of tests, the first leading to results lower than the specification target and presenting Q_0 drop, typical of field emission, which was corroborated by strong X-ray emission. A new series of tests was carried out after important improvement of the high pressure rinsing process. The quality factor at nominal accelerating field (4.5 MV/m) is then 2.3×10^9, more than twice the target (10^9), and it stays above 10^9 up to 10 MV/m. The E_{acc}/Q_0 curves are shown in Figure 2.12. This prototype is qualified for the IFMIF/DONES project.

This first step opens the way to following tests and studies. First, the cavity must be equipped with a helium tank, and the whole setup must meet mechanical specifications, including cavity integrity under mechanical forces. The geometry of such HWR cavities requires

dedicated HPR ports to ensure a good rinsing and avoid field emission, and preliminary studies show that these HPR ports will endure a high level of stress when the helium tank is submitted to pressure force (in operation, the helium tank is filled up with liquid helium around 1 bar while the cavity inside and cryomodule surrounding will be close to zero bars). A delicate design development is then necessary for the helium tank. Then, the cavity must be equipped with a tuning system, able to move the frequency within some tens of kHz [Plo22]. The development of a tuning system is a challenge, since a huge force is necessary to deform such large and stiff cavities. Finally, the cavity integration in the cryomodule is to be assured.

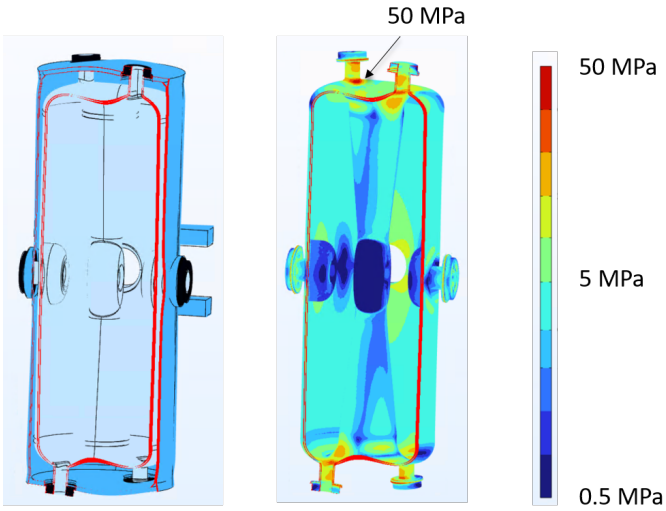

Figure 2.13: 3D view of the IFMIF/DONES cavity inside a helium tank (preliminary design), and distribution of the Von Mises (VM) stress in the cavity when the tank is submitted to 1 bar pressure. The VM stress reaches 50 MPa on the HPR ports (niobium yield stress at room temperature is around 40 MPa).

2.5 Cavities for the muon collider cooling system

Muon collider can reach center of mass energy of tens of TeV with high luminosity, offering exploration of new physics area. However, their construction faces a number of technical challenges. The MuCol program, funded by the European Community and started in March 2023, is aimed to study a facility design and explore new technologies [MuC23].

As an important stage of the high luminosity muon beam generation, a cooling system compresses the beam both transverse and parallel for decreasing its transverse components into a minimum phase-speace volume. The principle to be studied in MuCol consists into ionization cooling in presence of high DC magnetic field (a decade of teslas), where the muon beam, passing through an absorber, looses momentum through ionization. While the momentum decrease is expected in the transverse direction, the longitudinal momentum has to be restored, which is the role of an accelerating cavity. Thus, the Muon Cooling Complex (MCC) alternates absorbers and RF cavities [Col20]. The envisaged lattice involves cavities working close to 325 MHz and 650 MHz [SP15].

The Work Package 6 of MuCol consists in *"assessing crucial feasibility issues and technological challenges of the RF systems"*, and CEA is strongly involved in task 6.2 and responsible of task 6.3 [MuC]. The task 6.2 consists in *"laying out a conceptual design of the RF systems for the MCC"*, while the task 6.3 has to *"study and enhance the present comprehension of the intrinsic concepts that influence the break down rate of RF cavities submitted to strong magnetic fields."*

The breakdown in RF cavities submitted to high electromagnetic field is a well known problem encountered in normal conducting cavities. Its causes and mechanisms are being especially explored for the CLIC accelerator, aimed to provide cavities reaching a gradient close to 100 MV/m with a breakdown rate under 3 10^{-7} breakdowns per pulse and per meter [Rob18; Wue06; Mil+23]. In the case of a muon collider, the problem is accentuated by the presence of a high DC magnetic field, around a decade of teslas, which enhances the breakdown rate.

Many phenomena have been envisaged to describe the breakdown initiation, i.e. the electron current generation from an emitter, and some are detailed in [Pal+09]. They consider the mechanical properties of the cavity material (tensile stress, melting point, thermal conductivity), the dark current spectrum and the Fowler-Nordheim local enhancement factor β_{FN} [FN28] due the emitter small size.

Few of these models show the dependence on DC magnetic field. One model used to assume that the magnetic field facilitates breakdown by exerting additional forces in the form of torques $\vec{j}.\vec{B}$ on a field emitter [Mor+05]. Another model (*"beamlet"*) considers that the electrons emitted by one face of the cavity are focused by the longitudinal DC magnetic field and form a beam hitting another face (see Fig. 2.14). The impact spot size decreases with the magnetic field increase, so that the induce temperature at the collision point becomes sufficient to generate material damage [Pal+09; SGP10].

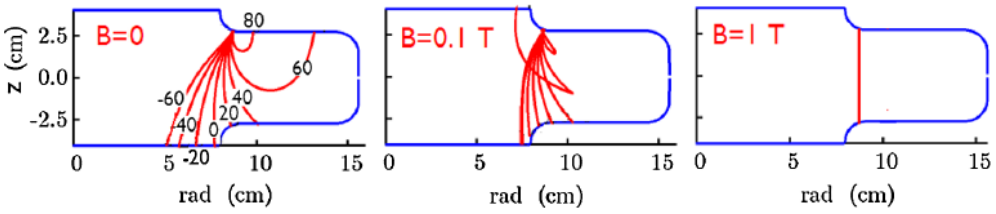

Figure 2.14: Trajectories of electrons field emitted at different phases from the highest surface field location in an 805 MHz pillbox cavity with no external magnetic field (left), an axial field of 0.1 T (center), and an axial field of 1 T (right). The axial electric field is 25 MV=m. Phases are in degrees relative to the maximum. *Figure from Palmer et. al* [Pal+09]

Several experiments have been carried out in the frame of dedicated programs (International Muon Ionization Cooling Experiment (MICE) [Col20], Muon Accelerator Program at Fermilab (MAP) [Pal15]). Higher breakdown probability and lower accelerating gradients have been observed in copper cavities operating at 805 MHz in presence of DC magnetic field [Pal+09; SGP10; Mor+05]. A model based on the *"beamlet"* principle has given good correlation with in [Bow+20]. It predicts breakdown apparition when the local temperature rise exceeds a threshold ΔT_s beyond which plastic deformation and surface damage may affect cavity behavior, and it relates the local temperature rise to the magnetic field. The same study predicts an improvement for cavities made of beryllium, which is corroborated by measurements: a maximal gradient of nearly 50 MV/m is kept in presence of 3 T, while the gradient drops to 13 MV/m with copper [Bow+20].

A simplification of this *"beamlet"* model can be applied for short pulses ($<$ 10 μs) where the heat diffusion in the cavity walls can be neglected. It provides a scaling law between the maximal allowable magnetic field and the accelerating field, $B(E_{acc})$, depending on different parameters [Mar23]:

$$B(E_{acc})^2 = K_1 \times \frac{K_2}{I(E_{acc})^{1/3}} \times \frac{1}{t_{pulse}} \tag{2.1}$$

K_1 depends on the material properties, K_2 of the cavity's geometry, $I(E_{acc})$ is the emission

current defined by the Fowler-Nordheim model and t_{pulse} the pulse duration.

Possible mitigation solutions are still to be explored, aiming to increase the allowable magnetic field:

- ⋆ testing different materials: beryllium, copper/beryllium alloy, aluminium... ($K_1 \nearrow$)
- ⋆ working with copper at cryogenic temperature ($K_1 \nearrow$)
- ⋆ optimizing cavity design ($K_2 \nearrow$)
- ⋆ working with short pulses ($t_{pulse} \searrow$)
- ⋆ working with high frequencies (decrease electron beam focusing)
- ⋆ shielding the magnetic field to protect the cavity

Dedicated test stands are needed for studying these possibilities, which must include a high power (some megawatts) RF source, one or several cavities and a strong magnet (some teslas). Among the laboratories involved in the Work Package 6 of MuCol, two tests stands in the S-Band ($\sim$ 3 GHz) are under study in the UK [Zha+23] and in Italy [GMC23], and one test stand could be implemented at CERN [GCB23]. Working at these frequencies higher than envisaged frequency domain presents advantages. In particular, smaller cavities and consequently smaller surrounding solenoid are much simpler and cheaper to develop. However, the scaling of the results to lower frequencies is not obvious. A proposition of developing a test bench at 704 MHz is under study at CEA, taking advantage of the existing klystrons in the RF platform.

2.6 Conclusion

In this section, we have detailed, for two very different types of superconducting cavities, the main issues to overcome and the implemented solutions. Tens of elliptical cavities for ESS have already been tested in dedicated cryostats and in cryomodules, and the expected gradient and quality factor value were achieved [WAB23]. The management of the Lorentz force detuning was also successfully tested [Piq+23]. The field emission was identified as the first cause of cavity failure leading to cavity reprocessing [WAB23]. Studies on the cause, the characterization and the cure of field emission are already ongoing and must be developped [Cen+21][Dev+23][Del+23][Ome+23][PGB23]. A further step for the ESS cavities will be the cryomodule operation in presence of the beam, foreseen in 2026 [Prz23]. The RF coupling to the beam will be measured, and it will be verified that the high order modes generated by the beam do not interfer with the beam acceleration.

The prototyping phase of the high beta half wave resonator for IFMIF/DONES has shown that the first RF requirements (accelerating gradient and quality factor) could be achieved without main difficulties, provided a meticulous preparation phase. Many developments are still necessary for assuring cavity operation in an accelerator. The cavity integration in a helium tank and in the cryomodule requires mechanical studies to guarantee cavity integrity, which could lead to retrofit cavity design. The frequency achievement during operation requires the development of a dedicated tuner system, adapted to such a large and stiff cavity. Then, the management of the required RF power, up to 200 kW per cavity in continuous mode, is a challenging issue. The RF power to cavity coupling scheme must be determined in accordance with the overall RF requirements and constraints. The solution must both minimize the overall lost power and protect each coupler from dangereous level of reflection. Finally, the adaptation of the power couplers for IFMIF/DONES from the IFMIF/Lipac couplers will require some development. The IFMIF/Lipac couplers have been initially designed to support 200 kW, but they will not be exposed to more than 100 kW in the Lipac phase [Reg+14]. Some upgrades

are already in development, in particular the implementation of a polarization setup, aimed to minimize the risk of multipacting[Dev22].

The study and development of normal conducting cavities for the cooling system of a future muon collider is in a very preliminary phase. Cavities reaching tens of megavolts per meters in presence of multi-teslas static magnetic field has never been achieved. Beside the development of the RF design of such cavities, including a power coupler, breakdown studies are necessary to achieve such gradients, involving theoretical, simulation and experimental activities.

ISBN: 978-3-95450-234-9 ISSN: 2673-5504 doi:10.18429/JACoW-SRF2023-TUPTB035

DESIGN, FABRICATION, AND TEST OF A 175 MHz, BETA = 0.18, HALF WAVE RESONATOR FOR THE IFMIF-DONES SRF-LINAC*

J. Plouin†, S. Chel, G. Devanz, N. Bazin, A. Madur, G. Jullien, C. Servouin, L. Maurice, M. Baudrier, Université Paris-Saclay, CEA, Département des Accélérateurs, de Cryogénie et du Magnétisme, Gif-sur-Yvette, France

Abstract

The IFMIF-DONES facility will serve as a fusion-like neutron source for the assessment of materials damage in future fusion reactors. The neutron flux will be generated by the interaction between the lithium curtain and the deuteron beam from an RF linear accelerator at 40 MeV and nominal CW current of 125 mA. The last accelerating stage is a superconducting (SRF) Linac hosting five cryomodules.

This SRF-Linac is equipped of two types of 175 MHz half wave superconducting cavities (HWRs). The first type of cavities (cryomodules 1 and 2), characterized by beta equal to 0.11, have been studied and qualified in the frame of IFMIF/EVEDA project. The development of the second type of cavities (cryomodules 3, 4, and 5), with higher beta of 0.18 is presented in this paper.

A prototype has been designed, fabricated and tested in a vertical cryostat at CEA. The measured quality factor at nominal accelerating field (4.5 MV/m) is 2.3 10^9, above the target in accelerator configuration (10^9). Moreover the quality factor stays above 10^9 up to 10 MV/m.

The next step is the fabrication of a helium vessel to be welded on the prototype, and the development of a dedicated frequency tuning system.

RF DESIGN

The SRF-Linac for IFMIF-DONES [1], represented in Fig. 1, hosts two cryomodules with low beta (LB) HWR cavities and three cryomodules with high beta (HB) HWR cavities, all the cavities working at 175 MHz [2, 3].

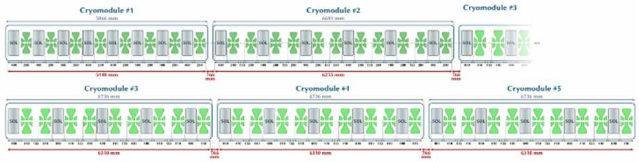

Figure 1: Layout of the 5-cryomodules SRF-Linac. Cavities are in green and solenoids in grey.

The design and qualification of the LB accelerating unit (low beta cavity equipped with its tuning system and power coupler) have been developed in the frame of IFMIF/EVEDA [4].

Table 1: RF Design Requirements

Frequency	175 MHz
Beam current	125 mA
Beam aperture	50 mm
Nominal gradient, Eacc_nom	4.5 MV/m
Optimal beta	0.18
Quality factor @ Eacc_nom	10^9

The HB cavity, with a beta equal to 0.18, is aimed to reach a nominal gradient of 4.5 MV/m with a quality factor at least equal to 10^9 (see Table 1). The RF design has been optimized to reach all requirements, while limiting the peak field (see Fig. 2), and allowing RF power transfer to the beam. Both electric and magnetic peak fields at nominal gradient remain under the ones of the low-beta cavity (see Table 2). The external coupling range for the optimization of the RF power transfer to the beam in given in Table 2. For the nominal beam current and gradient, this range corresponds to an amount of RF input power between 100 and 140 kW. Moreover, it has been checked that this external coupling range could be reached with an antenna penetrating the 100 mm coupler port.

Table 2: RF Design Parameters

Max E field @ E_{acc_nom}	21 MV/m
Max B field @ E_{acc_nom}	36 mT
External coupling	$4.5\ 10^5$-$6.\ 5\ 10^5$

The high power RF couplers were validated up to 100 kW in the IFMIF/EVEDA project [5]. In order to fulfill the needs with margin, we plan some upgrades of the couplers to reach RF power as close as possible to 200 kW.

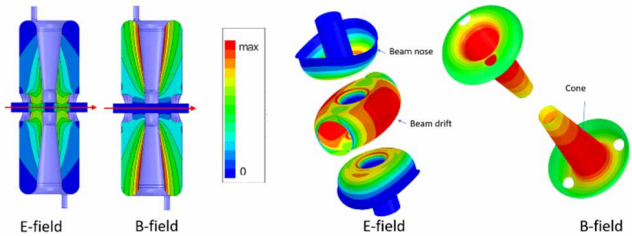

Figure 2: E and B field patterns in the DONES HB cavity: on cut planes (left) and on inner surfaces (right).

MECHANICAL DESIGN

The cavity body is made of bulk niobium (Nb), while the flanges are made of niobium/titanium (Nb/Ti) (Fig. 3). The

*This work has been carried out within the framework of the EUROfusion Consortium, funded by the European Union via the Euratom Research and Training Programme (Grant Agreement No 101052200 — EUROfusion). Views and opinions expressed are however those of the author(s) only and do not necessarily reflect those of the European Union or the European Commission. Neither the European Union nor the European Commission can be held responsible for them.
† juliette.plouin@cea.fr

Content from this work may be used under the terms of the CC BY 4.0 licence (© 2023). Any distribution of this work must maintain attribution to the author(s), title of the work, publisher, and DOI

ISBN: 978-3-95450-234-9 ISSN: 2673-5504 doi:10.18429/JACoW-SRF2023-TUPTB035

Content from this work may be used under the terms of the CC BY 4.0 licence (© 2023). Any distribution of this work must maintain attribution to the author(s), title of the work, publisher, and DOI

thickness of the cavity walls is fixed to 3 mm except for the half-torus which thickness is increased up to 4.3 mm to guarantee an adequate stiffening. Mechanical calculations have shown that with the optimized shapes, the maximal stresses due to Lorentz's forces or liquid helium pressure variation remain smaller than niobium yield stress.

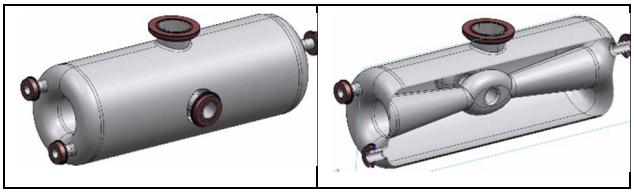

Figure 3: CAD views of the HB cavity.

The cavity walls and coupler port are made from 3.4 mm thick Nb sheets. The central drift and the beam tubes were made from Nb blocks (Fig. 4).

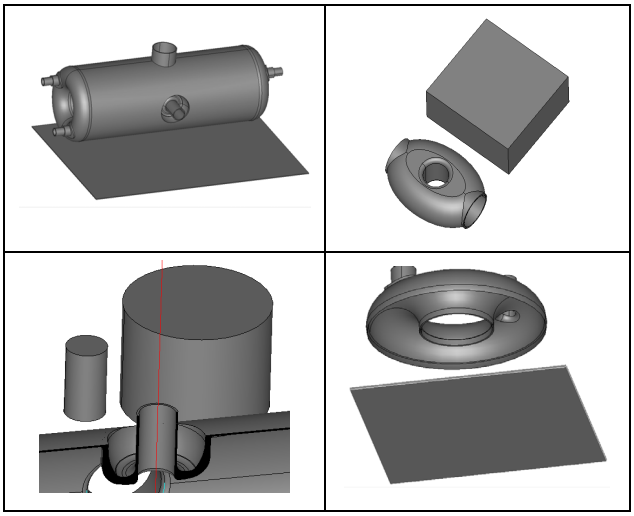

Figure 4: From left to right and from top to bottom: CAD views of cavity main body, drift tube, beam tube and half torus and corresponding Nb parts.

The Nb/Ti flanges have been designed to be compatible with the future implementation of a helium tank.

CAVITY FABRICATION

The cavity body is made out of high purity niobium (Residual Resistivity Ratio RRR > 300).

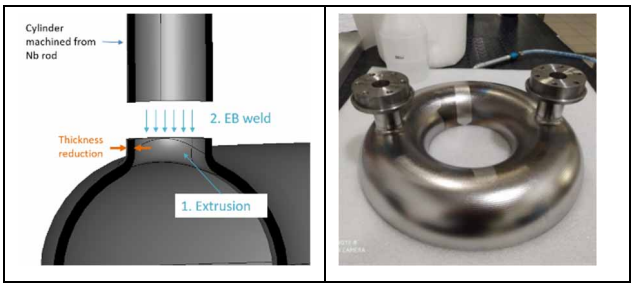

Figure 5: HPR tube and welding principle (left). Half torus with HPR ports (right).

The top and bottom half tori are manufactured by deep drawing from 4.3 mm thick Nb sheets. The welding of the High Pressure Rinsing (HPR) ports on these tori was identified as a delicate operation. The solution applied by the manufacturer (Zanon R&I) consists of extruding the basis of the HPR ports from the tori, cutting and milling to get the adequate surface and Electron Beam (EB) welding of the HPR tube (see Fig. 5).

The RF resonance frequency of the HWR is very sensitive to the internal dimensions of the resonator, and it was anticipated that fabrication tolerances could not be tight enough to reach the frequency within the required precision. To overcome this issue, a specific tuning procedure enabling to recover the cavity target frequency was implemented at the company premises. To this intend, overlengths are kept on each side of both inner and outer conductors so that some corrections can be made at intermediate steps of fabrication. The tuning procedure consists in a sequence of blank assembly and frequency measurements in different intermediate configurations in order to define the length to be cut before next welding.

The final frequency after the last weld of the manufacturing process differs from less than 30 kHz from the target frequency. The cavity after delivery at CEA is shown in Fig. 6.

Figure 6: HWR prototype.

CAVITY PREPARATION

To achieve the expected RF performances, the surface of the Nb cavity is cleaned by chemically etching away the surface layer damaged during the fabrication. For this cavity, the thickness to be removed on the inner cavity wall was estimated to 200 µm. However, the final chemical etching measured after this operation is 140 µm in average.

The cavity was then subjected to High Pressure Rinsing (HPR), to remove any chemical and particulate residue from the niobium surface. However, the HPR device was not optimized for this cavity and only one cycle could be carried out when two are usually necessary. We estimated that these surface treatments, even non ideal, should be sufficient, and after clean room assembly, the cavity was baked out at 120 °C under vacuum during 48 hours.

FIRST TESTS IN VERTICAL CRYOSTAT

The vertical cryostat is equipped with a magnetic shield to decrease the parasitic magnetic field below 2 µT. The cavity is inserted in the cryostat and cooled down to 4.2 K.

ISBN: 978-3-95450-234-9 ISSN: 2673-5504 doi:10.18429/JACoW-SRF2023-TUPTB035

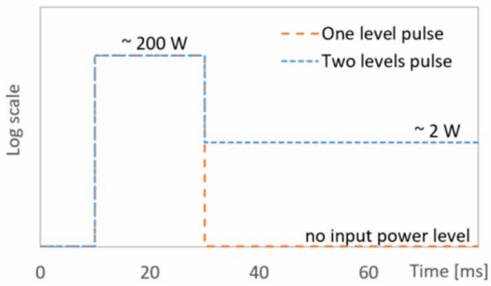

Figure 7: One and two levels pulses.

During the power ramp up of the cavity, a multipactor barrier appeared at very low field (<< 1 MV/m), which prevented the RF field from developing in the cavity. Breaking through this barrier requires injecting some hundreds of watts during tens of ms. After adjusting the power level of the pulse (Fig. 7, *one level pulse*), it has been possible to cross the multipactor barrier, but the field in the cavity dropped down immediately at the end of the pulse to values within the multipactor range. By improving the pulse shape using two power levels pulse (Fig. 7, *two levels pulse*), it became possible to keep the field above the multipactor barrier when the injected power drops down from the higher level to the lower.

During the first run (Fig. 8), a new multipactor barrier appeared between 2 and 3.5 MV/m, which could be conditioned within one hour. The Q_0 starts to drop at 3 MV/m, which is generally the signature of field emission. One Geiger-Müller (GM) detector, placed in the test area for safety control, measured an increase of the radiation rate above 3 MV/m, which could corroborate the field emission phenomenon. The cavity reached an accelerating field of 4.3 MV/m without quenching.

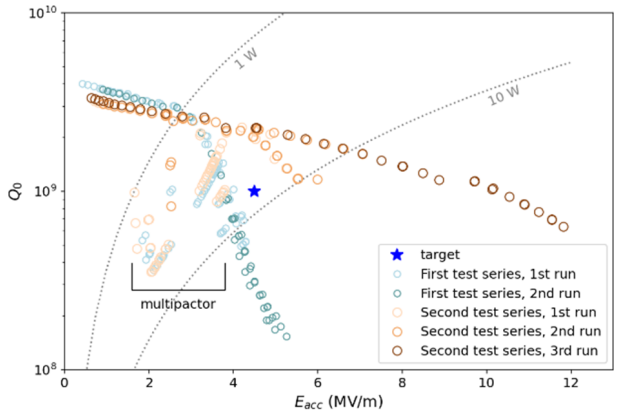

Figure 8: Q_0 vs E_{acc} curves for the two series of test.

A second run was carried out a few days later, the cavity being kept at 4 K in the meanwhile. The multipactor in the 2-3.5 MV/m range was easily processed, and the cavity field increased up to 5.25 MV/m (Fig. 8). Other values like Q_0 are unchanged with respect to the first run. However, the quality factor at 4.5 MV/m is 3 10^8, which is below the targeted value of 10^9.

IMPROVED PREPARATION AND RESULTS

The field emission at rather low field is typical of surface pollution, which is compatible with the non-optimal surface preparation (chemical etching too light, and one HPR cycle instead of two). Before a new test, two improvements are thus achieved:

- The cavity is subjected to a new chemical treatment, resulting in a total etching of 225 µm.
- A new HPR tooling is designed and fabricated, for better cavity positioning and to allow larger amplitude to the spray nozzle positions; then two complete HPR cycles are realized.

After new clean room assembly and new cavity bake-out, a second series of test in vertical cryostat is carried out.

The new Q_0 vs E_{acc} curve is shown in Fig. 8, showing three successive runs.

During the first run the multipactor barrier was conditioned. During the second run, the cavity was conditioned gradually up to 6 MV/m, resulting in Q_0 increase. Finally, during the third run, the input power was increased up to the maximum available power of 90 W, corresponding to an accelerating field close to 12 MV/m, without quench.

- The quality factor at nominal accelerating field (4.5 MV/m) is 2.3 10^9, more than twice the target (10^9).
- The quality factor stays above 10^9 up to 10 MV/m.

CONCLUSION

A cavity prototype for the high beta section of the SRF-Linac for IFMIF-DONES has been fabricated and tested in a vertical cryostat at CEA. The cavity performances have exceeded the target specifications. As a next step, the cavity will be equipped with a helium tank while a dedicated tuning system will be developed.

REFERENCES

[1] I. Podera *et al.*, "The accelerator system of IFMIF-DONES multi-MW facility", in *Proc. 12th Int. Particle Accelerator Conf. (IPAC'21)*, Campinas, Brazil, May 2021, pp. 1910-1913. doi:10.18429/JACoW-IPAC2021-TUPAB211

[2] N. Chauvin *et al.*, "Beam dynamics error studies for the IFMIF-DONES SRF-LINAC", in *Proc. 10th Int. Particle Accelerator Conf. (IPAC'19)*, Melbourne, Australia, Apr.-May 2019. doi:10.18429/JACoW-IPAC2019-WEPRB009

[3] T. Plomion *et al.*, "Preliminary design of the IFMIF-DONES superconducting LINAC", in *Proc. SRF'19*, Dresden, Germany, Jun.-Jul. 2019, pp. 311-314. doi:10.18429/JACoW-SRF2019-MOP097

[4] N. Bazin *et al.*, "Analysis of the Results of the Tests of IFMIF Accelerating Units", in *Proc. SRF'19*, Dresden, Germany, Jun.-Jul. 2019, pp. 992-996. doi:10.18429/JACoW-SRF2019-THP053

[5] D. Regidor *et al.*, "LIPAc SRF Linac Couplers Conditioning", in *Proc. 5th Int. Particle Accelerator Conf. (IPAC'14)*, Dresden, Germany, Jun. 2014, pp. 2562–2564. doi:10.18429/JACoW-IPAC2014-WEPRI039

Content from this work may be used under the terms of the CC BY 4.0 licence (© 2023). Any distribution of this work must maintain attribution to the author(s), title of the work, publisher, and DOI

Chapter 3

Magnetic flux trapping in superconducting cavities

I started to work on magnetic shields in 2008 when the elliptical CARE/HIPPI cavity has required the procurement of a magnetic shield before being tested in a horizontal cryostat [Dev+08a]. I have then being associated to the procurement of the nearly 800 magnetic shields for the XFEL cryomodules, assembled in CEA. From then I have become the expert on magnetic shielding and magnetic hygiene at CEA, associated to the design and procurement of all the magnetic shields required by the projects at CEA. I have developed this knowledge and experience through formal and informal collaboration with other labs and with material and shields manufacturers. Actually, the science of magnetic shields and magnetization, even if based on solid physical fundamentals, require some empirical knowledge about material behavior, which I learned from exchanges with many persons. In particular, the main material provider for magnetic shielding is the French company Aperam, inventor of Invar metal a hundred years ago, and I had essential discussion with its experts. I also participated to the unique Workshop on Magnetic Shielding for Cryomodules, held in March 2013 in Michigan State University [Lax13].

Moreover, my work on magnetic shields and magnetic material characterization participates to a long-term scientific collaboration with the Japanese team led by Mika Masuzawa at KEK in the frame of the TYL-FJPPL program.

I have carried out or supervised all the measurements and studies described in this chapter. A part of this work was done by a student graduating for engineer school.

3.1 Flux trapping

3.1.1 Principle

When superconducting cavities are cooled down below the critical temperature of the niobium, they transit to the superconducting state. The perfect Meissner effect is the expulsion of the whole surrounding magnetic field from a superconductor. In reality, the presence of impurities in the material produces trapping sites for the magnetic flux lines. The Meissner effect is not perfect in niobium cavities, and the flux expulsion is not complete: a part of the surrounding magnetic field is trapped inside the material [GC08]. This is illustrated in Figure 3.1.

The flux is trapped in vortices that oscillate in the RF field of the cavity, causing an increase of the surface resistance and the RF losses. Many studies are carried along the accelerators labs to limit the cause of surface resistance increase caused by flux trapping [LM21][Bal+21][DCG20][Lia+18][Kra+20]. Other studies propose methods to optimize the

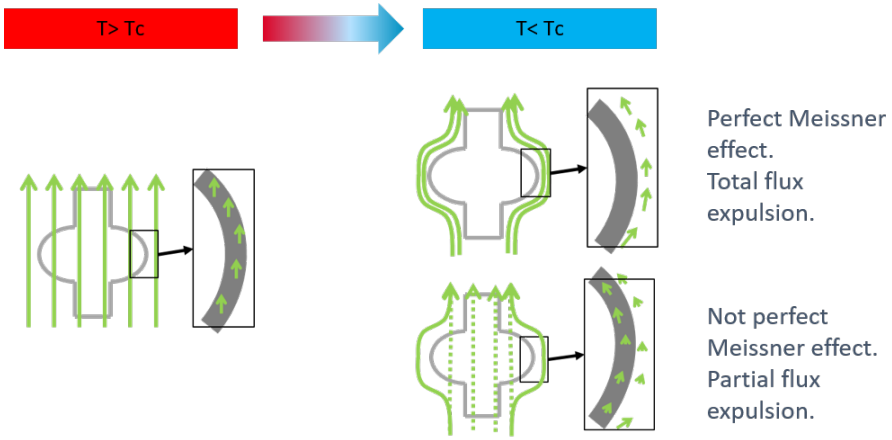

Figure 3.1: Principle of magnetic expulsion in a cavity at transition temperature.

flux expulsion, based on the cooldown dynamic control, as well as the spatial temperature gradient optimization [Rom+14][Pos+16][Kub16][VKK13]. They have been recently gathered by H. Padamsee in the book *Superconducting Radiofrequency Technology for Accelerators* [Pad23]. Besides these studies, the limitation of the magnetic field in the cavity neighborhood is a crucial point for the achievement of low surface resistance and high Q_0.

3.1.2 Magnetic field target around cavities

In the design phase of an accelerator, the estimation of the maximal magnetic field allowed around cavities in a cryomodule is a crucial point, because it conditions the technical solutions aimed to guarantee this value (magnetic shielding and control of metallic surrounding parts, see sections 3.2 and 3.3). This estimation is closely linked to the expected quality factor of the cavity in operation.

Actually, for a given cavity design, the quality factor Q_0 is inversely proportional to the RF power losses P_{diss} in the cavity walls, this latter being the product of the surface resistance R_S and the square of the RF magnetic field H integral along the walls:

$$P_{diss} = \frac{1}{2} R_S \iint_{walls} H^2 dS \tag{3.1}$$

As described in section 1.3.1, the surface resistance can be separated in two parts: the R_{BCS}, depending on the temperature, and the residual resistance, independent of temperature,

$$R_S = R_{BCS}(T) + R_{res} \tag{3.2}$$

and the BCS resistance depends on the temperature (T in K) and on the square of the RF frequency (f in GHz) with the formula [PKH08]:

$$R_{BCS}(T) = \frac{2.10^{-4}}{T} \left(\frac{f}{1.5}\right)^2 e^{-17.67/T} \tag{3.3}$$

The residual resistance becomes predominant at very low temperature, where R_{BCS} becomes smaller, and contains a contribution of the trapped flux inside niobium, which we note R_B. This component is proportional to the external magnetic field B_{ext} present during superconducting transition and depends on the niobium ability to trap the magnetic flux. This dependance was evaluated by the following coefficient involving the upper critical field H_{c2}, the niobium conductivity at room temperature σ_0 and the niobium residual resistance ration RRR [Val94]:

$$\alpha = \frac{R_B}{B_{ext}} = \frac{1}{H_{c2}}\sqrt{\frac{\pi f \mu_0}{\sigma_0 RRR}} \tag{3.4}$$

Finally, the surface resistance can be separated into three contributions, the BCS resistance, the trapped flux resistance and a remaining part of residual resistance noted R_0:

$$R_S = R_{BCS}(T) + R_0 + R_B \tag{3.5}$$

	IFMIF Lipac	IFMIF DONES	SARAF LB	SARAF HB	ESS MB	ESS HB	PIP-II LB	PIP-II HB
Freq (MHz)	175	175	175	175	704	704	650	650
Temp (K)	4.2	4.2	4.2	4.2	2	2	2	2
E_{acc}	4.5	4.5	7	8.1	16.6	19.9	15.9	17.8
Q_0	5e8	1e9	8e8	1.2e9	5e9	5e9	1.5e10	2e10

Table 3.1: Cavity frequency, operation temperature and minimum values required for the accelerating field and the quality factor. LB = low beta, MB = medium beta, HB = high beta.

The frequencies, operation temperature, target accelerating field and Q_0 are given in Table 3.1 for IFMIF/Lipac (low beta), IFMIF/DONES (high beta), SARAF (low and high beta) ESS (medium and high beta), and PIP-II (low and high beta). The left part of Figure 3.2 shows the evaluation of each contribution made during the design phase of those cavities. In all cases, the BCS contribution was evaluated by equation 3.3. The other contributions were estimated according to the target Q_0 and the state of the art possibilities and experiences with data collected in [Ba13] (IFMIF/Lipac), [Baz+20] (IFMIF/DONES), [Fer+19] (SARAF), [Cen+16b] (ESS) and [Leb15] (PIP-II). Once the R_B contribution evaluated, the corresponding magnetic field B_m was estimated from the calculation of α using equation 3.4. The results are shown in the right part of Figure 3.2. The maximal acceptable magnetic field on cavities, B_m varies between 0.5 and 2 μT. Since the coefficient α increases with frequency, the acceptable magnetic field is lower for ESS and PIP-II. The quest for very high Q_0 for PIP-II makes it even lower.

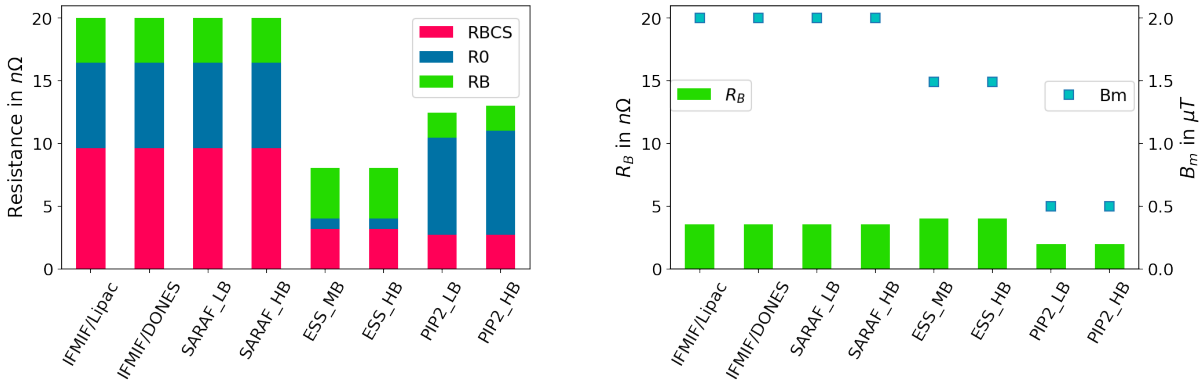

Figure 3.2: Left: contributions to the overall surface resistance, see eq. 3.5. Right: R_B contribution and corresponding B_m calculated with equation 3.4.

The ambient field is constituted of the earth magnetic field ($\sim 50\ \mu T$) and the field radiated by metallic surrounding elements, for example the steel bars inserted inside reinforced concrete walls of an accelerator facility. Moreover the cryomodules themselves contain metallic parts, possible sources of magnetic field. Lowering the magnetic field around cavity is achieved by:

- ⋆ limiting all the elements likely to generate magnetic fields in cryomodules, in particular close to the cavities. This is usually called *magnetic hygiene*, and will be developed in section 3.3.

⋆ protect the cavity from the remaining field with magnetic shields (see section 3.2).

3.2 Magnetic shielding

3.2.1 Principle

The magnetic shielding of a cavity consists into its enclosure inside a box made of high permeability material. The surrounding magnetic field lines concentrate into the walls of this box, lowering the magnetic field in the volume in the interior of the box. Figure 3.3 shows how the magnetic field lines are deviated by the presence of a magnetic shield around the cavity.

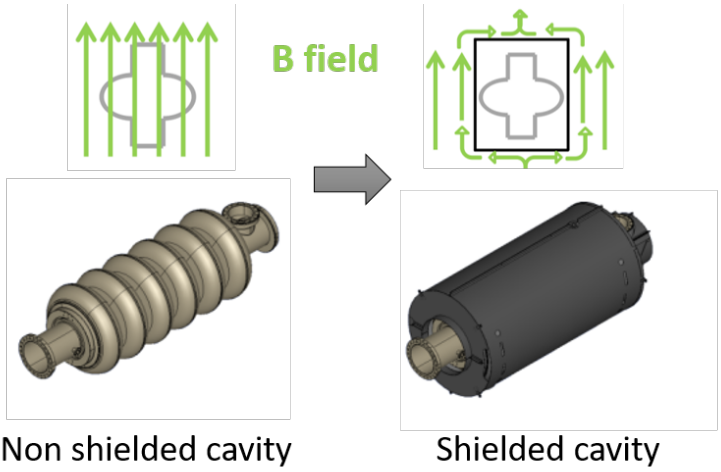

Figure 3.3: Principle of a magnetic shield.

The ratio between magnetic fields outside (B_{out}) and inside (B_{in}) the shield is called the shielding efficiency. For simple shapes, this factor is described by analytic formulas using the material relative permeability μ_r, the thickness e and the shield dimensions [Mag70]. Generally, the thickness is small compared to the main dimensions and the permeability is high compared to 1. For cylindrical shields whose length is higher than the diameter D, the transverse shielding efficiency (external field perpendicular to axis) is:

$$S_\perp = \frac{B_{out}}{B_{in}} = \frac{e.\mu_r}{D} \tag{3.6}$$

This formula shows how the shield efficiency is proportional to the permeability, this latter representing the material ability to concentrate the magnetic field lines, and thus to decrease the remaining field inside the shield. Moreover, the efficiency increases with the shield thickness, and is increased with small diameters. In a real magnetic shield, the field is generally not transverse to the cylinder axis and the shield geometry is more complicated than a simple cylinder. However, this analytic formula is useful for a very first sizing, before going into numerical calculations.

3.2.2 Magnetic shield material and efficiency evaluation

The work described in this section has been presented in three different meetings of the TESLA Technology Collaboration (TTC). This collaboration supports and encourages free and open exchange of scientific and technical knowledge, expertise, engineering designs, and equipment. These meetings do not have proceedings but the presentations are accessible on their websites [PMT14][PF18][Plo18d]. It was also partially described in a conference paper [Mas+13].

General properties

Magnetic shields are made of soft ferromagnetic materials with high permeability, mainly containing iron. For cavity shielding, the dimensions sometimes reach some meters, and require thin material sheets (1-2 mm) to limit cost and weight. Permeability higher than 10000 is needed to get one order of magnitude of attenuation. Such values are obtained with special alloys called *mumetal*, made of nickel, cobalt and iron. These materials reach their nominal values after a specific heat treatment.

In practice, the mumetal suppliers are metallurgic companies which provide both the raw material (e.g. sheets) and their associated heat treatment recipe. The heat treatment must be applied on the magnetic shield once it is completely fabricated and any plastic deformation on the material (due to sheet forming or welding) damages the microscopic structure, resulting in a local permeability drop.

The quest for optimal shield performance has led to many discussions in the Superconducting RF community, which illustrate the complexity of the problematic. A material's permeability depends on:

- ⋆ the metallurgical structure of the material itself
- ⋆ the heat treatment

but also on:

- ⋆ the shield temperature in operation (section 3.2.2)

Moreover, the response of a ferromagnetic material to an external field is a non-linear phenomena, described by a hysteresis curve, relating the magnetic field (H) and induction (B) **inside** the material (section 3.2.2).

Properties versus temperature

The dependence on temperature is a critical point since cavity shields, generally designed to be as close as possible to the cavity (to limit the diameter and increase efficiency, see formula 3.6), are used at cryogenic temperature. However, standard mumetal permeability tends to drop at low temperature. Facing adapted materials request, a first mumetal dedicated to cold temperature, named Cryoperm, was developed by the German company VacuumSchmelze in the nineteen's. At this period, the curve shown in 3.4 was usually considered as a reference. This curve represents a permeability with a maximum at cold temperature and a drop at room temperature, and it seems favorable to thermalize the magnetic shield around 4 K. However, measurements made at CEA in 1994 rather showed quite similar values for the Cryoperm at low and room temperature (Figure 3.4) .

After 2010, the French company APERAM (previously ArcelorMetal) has developed its own mumetal material for cold operation, named Cryophy [Ape], which they qualified in collaboration with CEA within the development of the XFEL magnetic shields. They provided us with ring samples of Cryophy, heat treated in their own facilities with dimensions adapted to a permeameter developed at CERN [Mon+14], in order to measure the $\mu - H$ properties of Cryophy at different temperatures. These samples have been characterized at CERN, and the $\mu - H$ curves are presented in Fig. 3.5 at cryogenic and room temperature. In the same period, Mika Masuzawa team at KEK has characterized the same kind of samples [Mas+13], and their results are also given in Fig. 3.5. This results show very good agreement between KEK and CERN measurements for the Cryophy. The permeability decreases for all materials

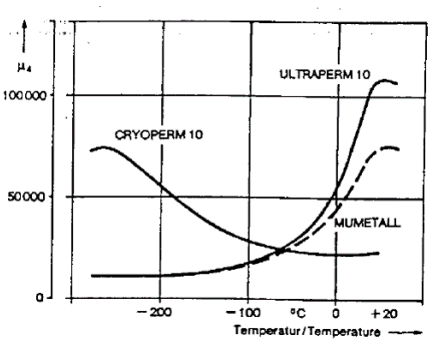

implies that the shield will be cooled at cryogenic temperatures. Measurements of μ were made at room temperature (RT) and at 4 K on cylinders of Mumetal and Cryoperm (Table 1).

	Mumetal	Cryoperm
RT	54700	10200
4K	7500	13300

Table 1. Permeability μ_1 measured on test cylinders (from M. Bork, VAC, private communication)

The μ—degradation predicted between RT and 4 K appeared indeed on Mumetal, but the expected opposite behaviour for Cryoperm was hardly observed. Altogether, it should be noted that these magnetic materials are very delicate to handle: proper annealings are required to obtain high permeabilities; moreover, shocks or strains (either thermal or plastic) can reduce μ drastically. Finally, we consider that the choice material for the passive shielding of TESLA TTF cavities is still Cryoperm, but that a realistic value for its permeability is only $\mu = 12000$. Specialists from the company VAC confirmed this view.

Figure 3.4: Left: Permeability vs temperature, shown in [Bol94], can be found in [Amu]. Right: article extract from [Bol94] (CEA measurements).

tested by KEK from room temperature to 4 K : for the standard mumetals (Tokin) and for the special cryogenic mumetals (Cryoperm, Cryophy and A4K). The results obtained for the Cryophy material, which is widely used for shielding applications in cryomodules, was confirmed by Aperam experts. They detailed during a meeting how they chose a material and a heat treatment recipe for which the permeabilty is slightly decreased at cold temperature, whilst keeping it high enough.

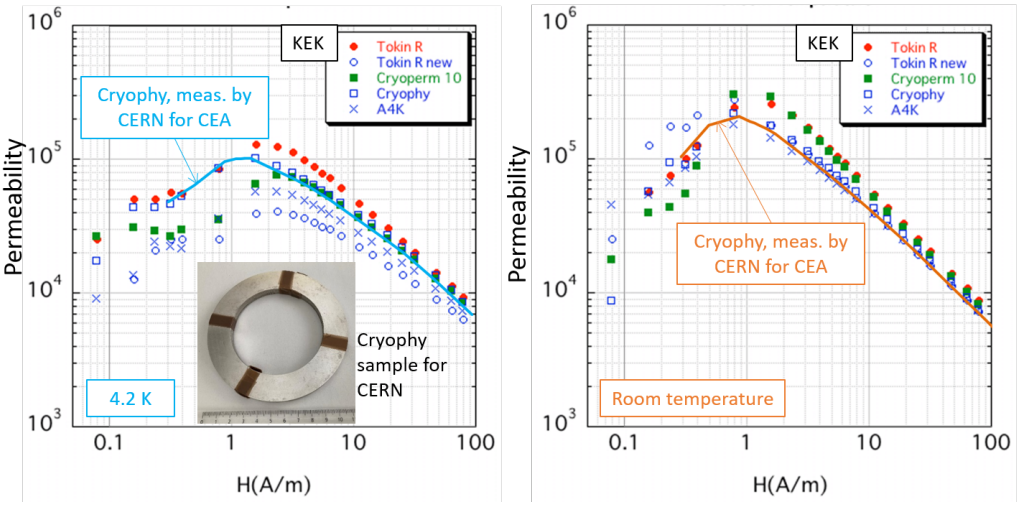

Figure 3.5: $\mu - H$ measurements on ring samples by CERN (for CEA) and KEK, at cryogenic (left) and room (right) temperature.

Dependence on the external field

Furthermore, these measurements illustrate the non linear dependence between the permeability and the magnetic field H, typical of soft ferromagnetic materials, whose $B - H$ curve presents an hysteresis. The geometry of a shield also produces a non-homogeneous distribution of the field inside the material. Magnetic shield design is carried out with magnetostatics codes [Ope][CST], where using a constant permeability value is much more suitable. We considered how to estimate an equivalent permeability, derived from the simple cylinder formula:

$$\mu_{eq} = \frac{D}{e} S_{\perp} = \frac{D}{e} \frac{B_{out}}{B_{in}} \tag{3.7}$$

We have carried out experiments with cylindrical samples especially supplied during the procurement of the IFMIF/Lipac and ESS magnetic shields and made of the same material.

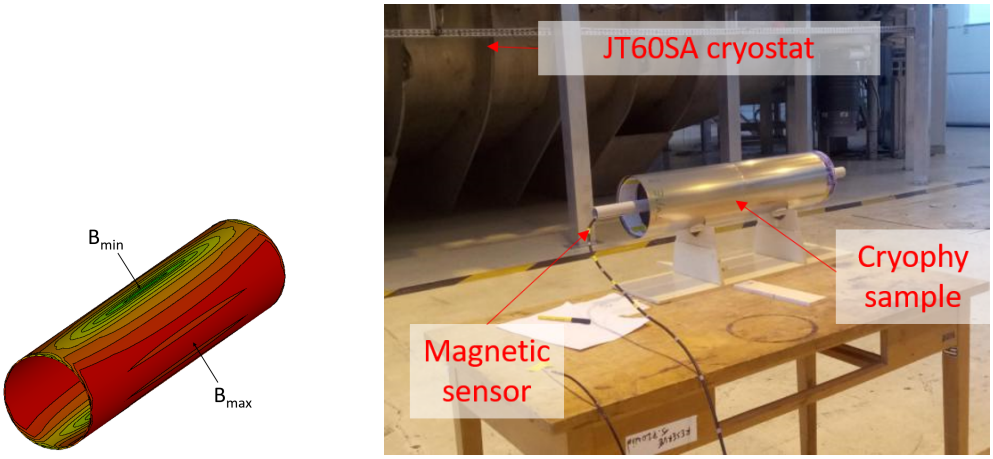

Figure 3.6: Magnetic field distribution inside the material of a cylinder shield. Experimental setup during cylinder magnetization.

One sample made of Cryophy was placed in the fringe field of a toroidal coil for fusion, JT60SA, tested in a cryostat at CEA-Saclay [Mak+18] (Fig. 3.6). The current in the coil goes from up to 27.5 kA and the magnetic field reaches 2.7 T in the coil, and 7.5 mT at the cylinder position, transverse to its axis. The measurements have been carried out during ramping up then down of the magnetic field, and the measured equivalent permeability is shown in Figure 3.7. An hysteresis effect is observed, coherent with soft magnetic materials properties.

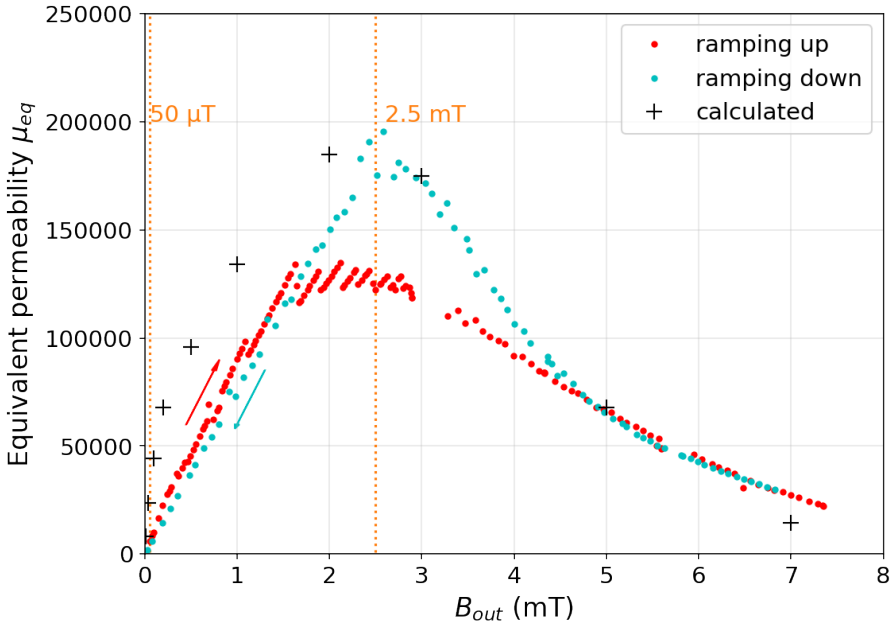

Figure 3.7: Equivalent permeability for a Cryophy cylinder in a transverse field. Measurements in increasing and decreasing field and simulations with non linear model [CST] implemented with $\mu - H$ curve corresponding to the Cryophy ring samples measured by KEK at room temperature (Fig. 3.5).

On the other hand we calculated an equivalent permeability by simulating the Cryophy cylinder with a non-linear model [CST]: the $\mu - H$ curve corresponding to the Cryophy ring samples measured by KEK at room temperature (Fig. 3.5) was implemented in the simulation model, and the equivalent permeability was calculated with equation 3.7. The results, shown in Figure 3.7 show good agreement with measurements above 2.5 mT. The discrepancy at lower field is probably due to the lack of accuracy for the field inside the shield, which drops to very low values.

The magnetic shields are destined to protect cavities again the surrounding field, usually the earth magnetic field, around 50 μT. Figure 3.7 underlines that the equivalent permeability is maximal (2.10^5) for much higher external field, around 2.5 mT. This maximal values, often given in the materials datasheet, are clearly not adapted to our application.

Finally the equivalent useful permeability must be deduced from measurement in the ambient field. Systematic measurements in both IFMIF/Lipac and ESS cylindrical shields (representing a total of 9 cylinders), resulted in equivalent permeabilities in the range [35000-55000]. These studies brought essential knowledge for the design of all the magnetic shields aimed to accelerators projects.

3.2.3 Design

Table 3.2 reminds the maximal acceptable magnetic field on cavities, B_m, for the different projects (see Figure 3.2) and gives the resulting shield efficiency ($S = B_{out}/B_{in}$) needed for a typical external magnetic field of 50 μT.

	IFMIF Lipac	IFMIF DONES	SARAF LB	SARAF HB	ESS MB	ESS HB	PIP-II LB	PIP-II HB
B_m (μT)	2	2	2	2	1.5	1.5	0.5	0.5
S	25	25	25	25	33	33	100	100

Table 3.2: Maximal acceptable magnetic field on cavities B_m and resulting shield efficiency S for the different projects.

Depending on the required shielding efficiency and the overall cryomodule design, the magnetic shield can be placed directly around the cavity or around the cryomodule. The first solution allows smaller size, and higher efficiency (see formula 3.7) but requires many openings for cables and helium circulation, and the magnetic shields are submitted to cryogenic temperature, requiring dedicated material.

On the other hand, magnetic shields can be mounted directly on the inner face of the cryomodules, which is simpler and allows for room temperature material. However, not only the efficiency is lower, but the cavity is not protected from magnetic shield radiated from inner parts of the cryomodule. This latter issue will be detailed in section 3.3.

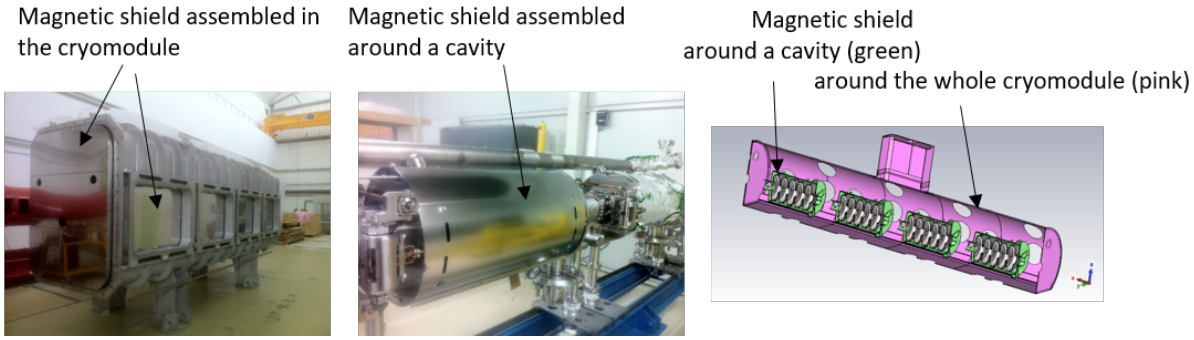

Figure 3.8: Pictures of the magnetic shields for IFMIF/Lipac (left), ESS (center) and PIP-II (right).

The IFMIF/Lipac and SARAF cryomodules are equipped by magnetic shields directly assembled on the inner side of the cryomodule [Cha+17; Cub+17], and a picture of the IFMIF/Lipac shield installed inside the vacuum vessel is shown in Figure 3.8.

For the ESS cryomodules, as was done for XFEL, which require higher shielding efficiency,

the magnetic shields are assembled around the cavity [Pea+15], and a picture is shown in Figure 3.8.

In the case of PIP-II, the very low allowable field around cavity requires an overall efficiency equal to 100, which is achieved by the addition of one magnetic shield around the module and one individual shield around each cavity [Baz+23], as shown on a 3D view in Figure 3.8.

Once fabricated and assembled, the efficiency of these magnetic shield is verified by in situ magnetic field measurements, and finally confirmed by the good cavity performance during the cryomodule testing, as for ESS [Piq+23].

3.3 Magnetic hygiene

The previous section details how magnetic shielding is used to protect cavities from ambient magnetic field. However, the protection of the cavities also requires to avoid the presence of magnetized elements, likely to radiate magnetic field, close to their position [DI67][Cha+16][Plo+15]. This concern is studied and treated by all the labs in charge of cryomodules fabrication, and is usually described by the term *magnetic hygiene*.

This point is especially crucial in some configurations:

- ⋆ when the magnetic shield surrounds the whole cryomodule, without individual cavity shields: in this case there is no protection between the elements constituting the cryomodule and the cavities,
- ⋆ when the focusing solenoids are close to the cavities, since they are likely to magnetize the surrounding elements.

The cryomodule design always takes this concern into account. For this reason, some metallic parts directly supporting the cavity are made in titanium, which is perfectly non magnetic. However the cost of this metal does not allow to fabricate all the metallic part in titanium. Many elements are then made of stainless steel (SS), and two elements are commonly made of strong magnetic material: the magnetic shield itself, made of ferromagnetic mumetal and the Invar metallic bar used as dimensional reference. We have investigated the possible issues, and we have proceeded to experimental magnetization for a set of metallic elements made of: mumetal, Invar and stainless steel. These elements were subjected to a magnetic field with amplitude 14 mT, during the tests of a toroidal coil for fusion, JT60SA, tested in Saclay cryostat [Mak+18].

Mumetal magnetic shield

As already described page 54 a cylindrical magnetic shield was subjected to the magnetic field during the JT60A experiment. The magnetic field inside the shield was not changed after this exposition. This means that even if the shield material was somehow magnetized, it has no consequence on its shielding efficiency.

Invar rod

The Invar material was developed a hundred years ago and is well known for its very low thermal shrinkage ($\sim$ one tenth of standard metals). In a cryomodule, cavities and solenoids are fixed to an Invar reference rod to limit their displacement during cool-down. The mechanical properties of Invar are associated to its ferromagnetic nature: Invar has a positive anomalous magnetostriction coefficient, and the shrinkage due to its cool-down is partially compensated

by magnetic forces [Bér+96][LS23]. Invar has a strong permeability and is likely to be starkly magnetized.

We magnetized an Invar bar (length 50 cm, diameter 1 cm) and measured the radiated magnetic field before and after magnetization. There was no significant change after magnetization, probably because the B field is not large enough to change the proper magnetization. The data after magnetization are presented in Figure 3.9. The field is still higher than 20 µT at 11.5 cm from the bar, which is a typical distance between cavity and bar in a cryomodule. The Invar rod represents a dangerous element inside the cryomodule and needs either dedicated shielding or demagnetization.

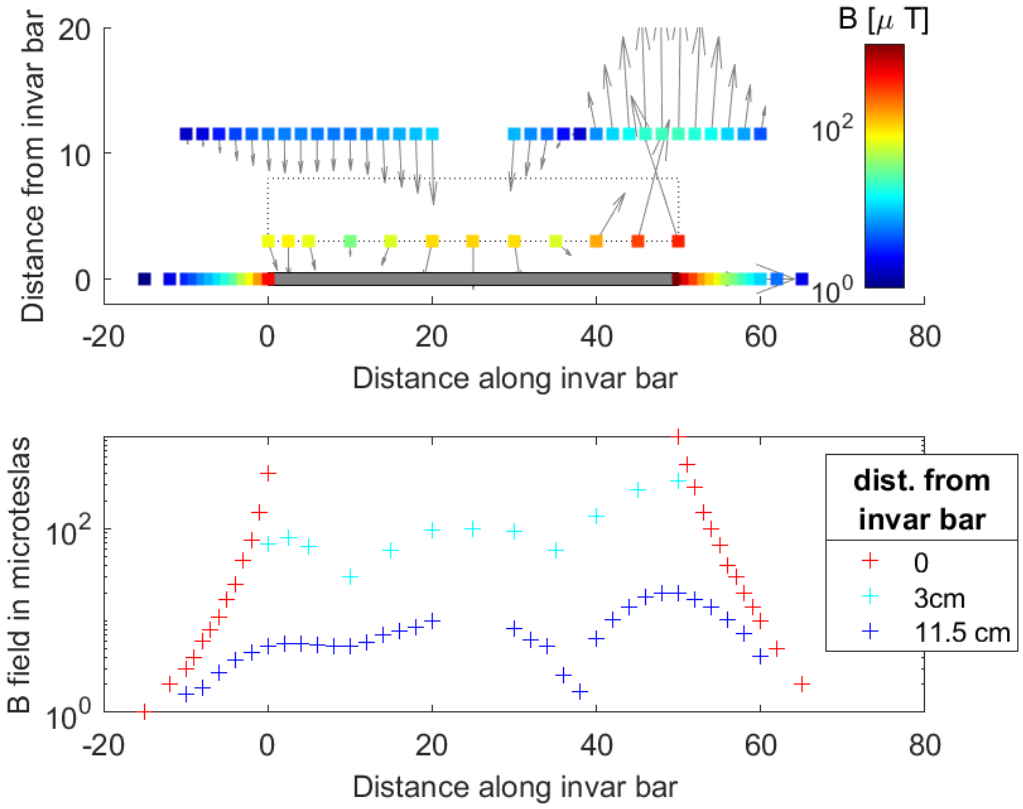

Figure 3.9: Radiated magnetic field by the magnetized Invar bar. Top: scatter plots around the Invar bar (represented in grey). Bottom: magnetic field values at several distance from bar.

Stainless steel elements

Many parts constituting the cryomodules frames and supports are made of stainless steel. Experience shows that pieces arriving from supplier often present some unexpected magnetization responsible of magnetic field radiation. It is crucial to provide proper indications to the suppliers to prevent unacceptable magnetization, and to plan control measurements. The stainless steels magnetic behavior varies considerably from non magnetic when in the full austenitic phase, named γ, to permanent magnetic state in the martensitic (named α') or ferrite (named δ) phase. The magnetic permeability increases with cold work, due to deformation-induced martensite, corresponding to the transformation $\gamma \rightarrow \alpha'$ [Mum+04][Man+08]. An apparition of ferrite phase is likely to occur during welding operation [Mic07][SBS07][CET04]. The susceptibility of a particular grade to becoming ferromagnetic when heavily cold worked depends on the stability of the austenite, which, in turn, depends on chemical composition and homogeneity.

This is illustrated in Figure 3.10: the picture on the left is extracted from the documentation of a stainless steel supplier [Car] and shows the increase of permeability due to cold

working. It also shows the huge difference between 316 SS grade, whose permeability keeps lower than 1.01 even after strong reduction, and the 304 SS grade whose permeability is likely to reach 5. Generally, the different stainless steel grades can be sorted by the tendency to the transformation $\gamma \rightarrow \alpha'$ in the decreasing order as 304>304L»316>316L>316LN [Man+08].

I plotted the graph on the right with values extracted from two publications about 304 [Mum+04] and 316LN [Man+08] stainless steel. It relates the strain on the material, the percentage of martensite and the permeability and the remnant magnetization of both stainless steel grades and shows the very low dependence of 316LN SS magnetic properties to deformation.

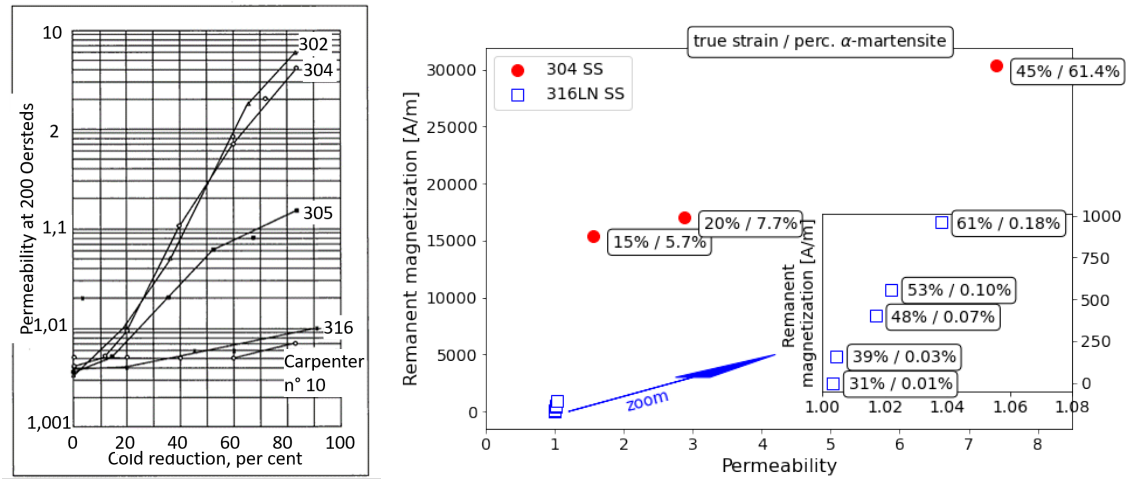

Figure 3.10: Left: permeability vs cold reduction factor for different grades of stainless steel[Car]. Right: remnant magnetization vs permeability for 304 [Mum+04] and 316LN [Man+08] stainless steel (SS) (right).

We have proceeded to the magnetization of many stainless steel components, and observed their ability to get magnetized depending on their grade and history. An example is given hereafter for mechanical supports for SARAF cavities, made of 316L SS (see Fig 3.11 left).

First, these supports present very different values of permeability depending on the measurement point (Fig. 3.11). The permeability reaches higher values in area which have endured late machining. The right part of 3.11 presents the mean value for the magnetic field at contact, before and after magnetization. The areas with higher permeability presented a pre-existing magnetization, acquired during fabrication; after magnetization the field at contact was increased up to $\sim 170\ \mu T$. We measured the magnetic field at distance from the magnetized area and observed that the field becomes lower than 5 μT at 50 mm. (see fit curve in Figure 3.11 inset). Such measurements help to estimate the danger of a stainless steel elements depending on its grade, fabrication process and distance from the cavity in the cryomodule.

Example of flux trapping limitation for the IFMIF/Lipac cryomodule

In the IFMIF/Lipac cryomodule, due to space charge associated to the high intensity beam, a short, but strong superconducting focusing magnet package is necessary between cavities [Plo+15]. During the cryomodule operation, the solenoids will only be switched on once the cavities are in superconducting state, and will not contribute directly to magnetic field trapping. However, some cryomodule components could be magnetized by some fringe field, which reaches up to $\sim$ 20 mT, and be a source of remnant field once the solenoid is switched off. This concern has led us to several adaptations in the cryomodule design. The supporting frame was initially planned to be made of stainless steel 316L C-beams welded together. The large number of welding rims with potentially higher permeability than expected represented a risk,

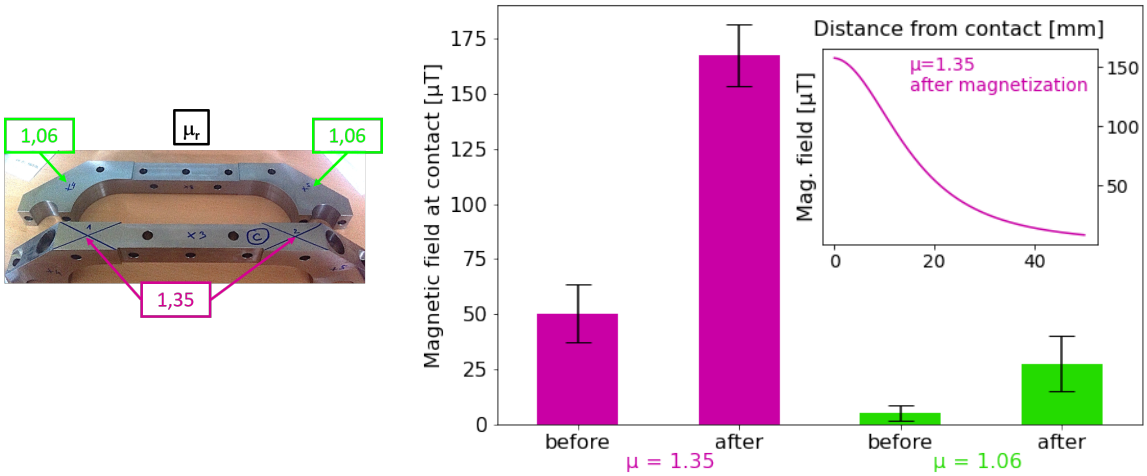

Figure 3.11: Magnetization of 316 L stainless steel supports. Permeability at several positions (left) and magnetic field at contact before and after magnetization (right). The inset shows the magnetic field vs distance from support.

that brought to the final choice of an all titanium frame. Some needle bearing, parts of the initial cavities and solenoids rolling systems, were identified as magnetized elements, and they were replaced by homemade ceramic bearing in a brass cage.

Magnetic hygiene consideration for cryomodules.

The studies presented in this section have contributed to a better global understanding of the magnetization processes of metallic elements. As a result, the criteria on material used for cryomodules elements have been refined. This is a crucial point because the issue is to:

- ⋆ assure that parts close to the cavities have a low enough permeability,
- ⋆ relax the criteria when the parts are not too close.

This last point is important. Demanding very low values (e.g. permeability < 1.02) for all the parts inside the module is attractive, but finally hardly feasible, unless requiring titanium or 316LN stainless steel for all parts, which would be excessively expensive. In reality, we often had to accept parts with higher permeability than our initial criteria because the risk of spurious magnetization was finally lower than the difficulty of requiring new parts, and it tends to discredit the importance of those criteria. Then it keeps an important issue to finely adapt the requirements on stainless steel properties to reasonable values depending on their position and size.

Finally, a demagnetization procedure can be applied to certain parts of the cryomodule before assembly, or even on the whole assembled cryomodule. This procedure consists into applying an oscillating and decreasing magnetic field to cancel the remnant magnetic field of magnetized components. This method is already used by several laboratories with good results, either with a dedicated solenoid winded around the module [CC16], or by using the solenoids present inside the cryomodule [Lax13]. We will have to develop such method in the future at CEA:

- ⋆ for the PIP-II low beta cryomodule, where such procedure is planned
- ⋆ for the IFMIF/Lipac cryomodule, where such a procedure, using the solenoids already present between cavities, is envisaged.

3.4 Flux trapping in a low beta SARAF cavity.

The last section of this chapter presents flux trapping experiments realized on a superconducting cavity during a test carried out at CEA-Saclay.

In order to test the SARAF cavities with their tuner and couplers, a dedicated cryostat has been realized, called the Equipped Cavity Test Stand (ECTS) [Piq+19]. For the purpose of carrying experiments on the effect of flux trapping on cavity performance, the test cryostat was equipped with a special aluminum sleeve allowing the positioning of a permanent magnet close to the cavity (see Fig. 3.12, left).

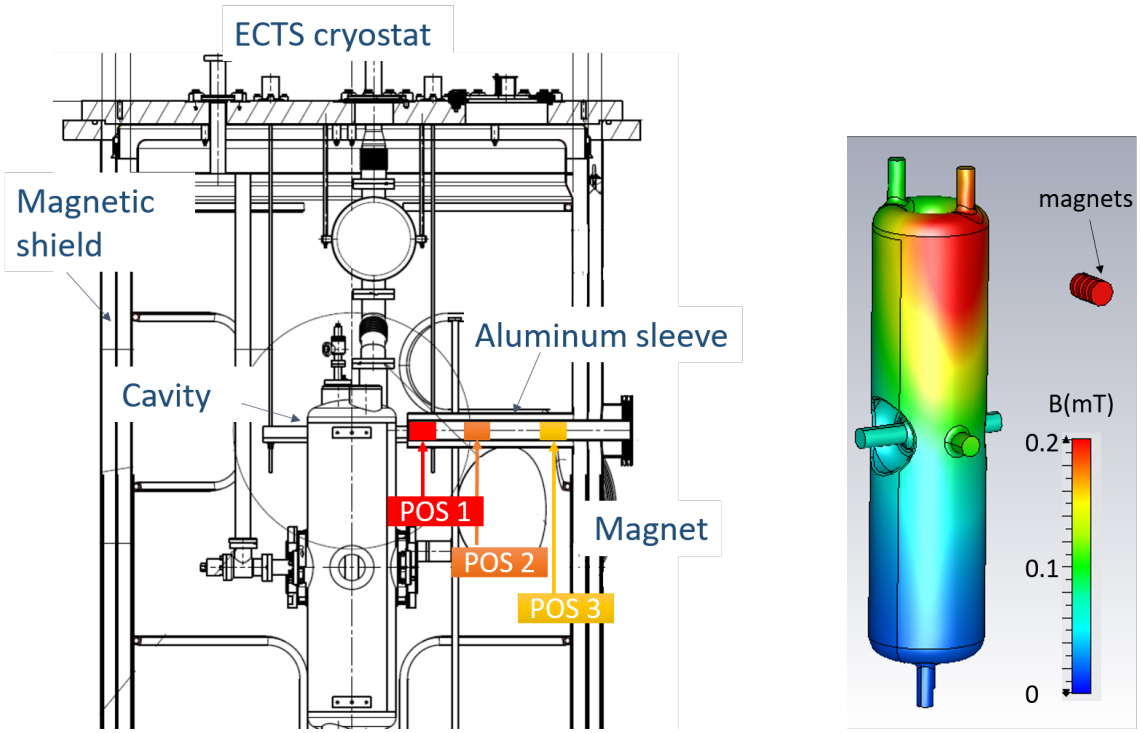

Figure 3.12: Left: section of the ECTS showing the low beta cavity, the aluminum sleeve, and the different positions of the magnet, named POS1, POS2 and POS3. Right: simulated field static field distribution (B_{ext}) on the cavity for a magnet at POS2.

The static magnetic field radiated on the closest part of the cavity varies from nearly 0.1 to 10 mT, depending on the magnet position. These values have been measured on a single point of the cavity, and some simulations [CST] were performed to estimate the magnetic field pattern on the cavity (see Fig. 3.12, right). A discrepancy of +/- 25% was observed between measurements and simulation on the single point. Two sets of experiments have been carried out.

- ⋆ While the cavity was at 4.2 K and exposed to the maximal accelerating field, the magnet was moved close to the cavity. This had no effect on either the accelerating field, nor the Q_0. This was expected, because the cavity is in the superconducting state, and its critical magnetic field is much in the order of 100 mT.
- ⋆ The cavity was heat up to the normal state, cooled down to 4.2 K in presence of the magnet, and the Q_0/E_{acc} curve was measured. This experience was repeated for three positions of the magnet, and the Q_0 dropped up to of a factor 10 for the closest magnet position (see Fig. 3.14). This demonstrates how the static field B_{ext} is trapped during cool down and thus generates an increase of the cavity surface resistance ΔR_s.

As a comparison, I have calculated the quality factor by the following equation [PKH08]:

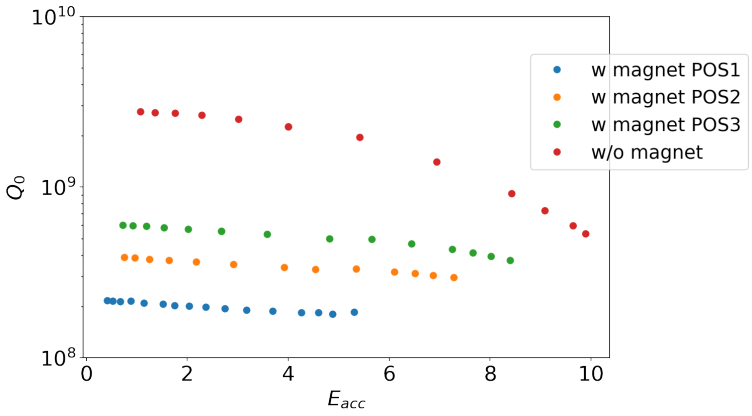

Figure 3.13: Q_0/E_{acc} curves for the low beta SARAF cavity when cooled down in presence of a magnet. The magnet positions are shown in Figure 3.12.

$$Q_0 = \omega\mu_0 \frac{\int_V |B_{RF}|^2 dV}{\int_S R_s |B_{RF}|^2 dS} = \frac{\omega W}{\int_S (R_{w/oB} + R_B)|H_{RF}|^2 dS} \tag{3.8}$$

The quantity $B_{RF} = \mu_0 H_{RF}$ is the radiofrequency magnetic field in the volume V or on the surface S of the cavity. The cavity surface resistance R_s is the sum of the contribution of the trapped flux, R_B, and the other contributions, $R_{w/oB}$, including the BCS resistance. The value of R_B is given at every cavity surface position by $R_B = \alpha B_{ext}$, B_{ext} being the static magnetic field, calculated from magnetic field simulations (Fig. 3.12, right). The coefficient α is evaluated to 0.14 nOhm/mG from equation 3.4, with $H_{c2} = 0.4$ T, $\sigma = 6.9\ 10^6$ S/m, and RRR = 300. Only the contribution normal to the cavity is considered in B_{ext}. The presence of the magnetic shield of the cryostat is taken into account in the simulations. Equation 3.8 is transformed into:

$$\frac{1}{Q_0} = \frac{1}{Q_{w/oB}} + \frac{\int_S R_B |H_{RF}|^2 dS}{\omega W} = \frac{1}{Q_{w/oB}} + \frac{\int_S \alpha B_{ext} |H_{RF}|^2 dS}{\omega W} \tag{3.9}$$

The stored energy W and the surface distribution H_{RF} were simulated (Fig. 3.14, left). I fixed the quality factor in absence of static magnetic field, $Q_{w/oB}$, to the measured value without magnet, at low accelerating field : 2.8 10^9 (see Fig. 3.13)

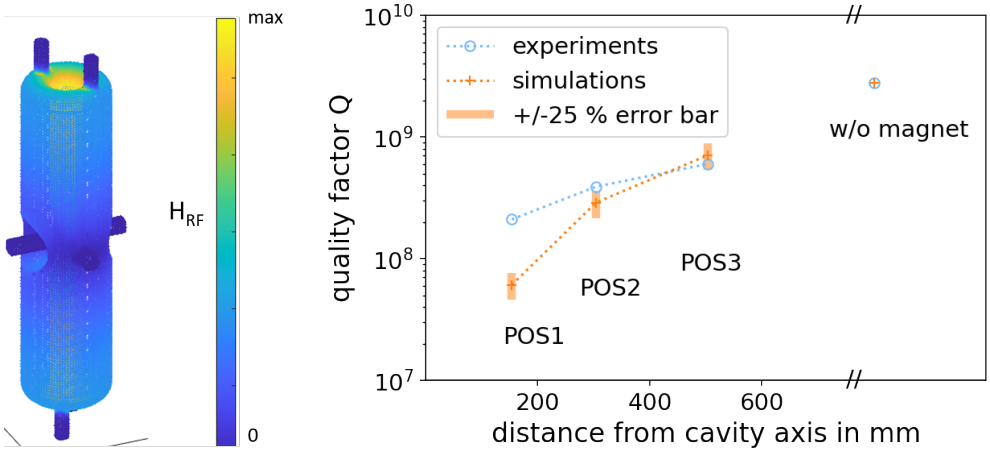

Figure 3.14: Left: surface distribution of the RF magnetic field. Right: experiments and simulations quality factors versus distance from cavity. The magnet positions are shown in Figure 3.12.)

Figure 3.14 compares the quality factor from experiments (from Fig. 3.13, values at low accelerating field) and the quality factor from simulations (equation 3.9). A large discrepancy,

up to a factor 4, is observed between both results. Several observations are likely to explain those differences:

- ⋆ the surface distribution of the static field B_{ext} on the cavity surface is strongly dependentonof the position accuracy of the different elements: cavity, magnet, and magnetic shield, and there is probably a difference between simulations and reality,
- ⋆ the magnetic field generated by the magnet on the cavity could be measured only at a single position, limiting the comparison with simulations,
- ⋆ the permeability value used for the magnetic shield also has a noticeable influence on the results, and only a rough estimation was used in the simulations,
- ⋆ the value of α is considered as uniform along the cavity surface, which is probably not true.

It was planned to carry out new measurements with a SARAF cavity in the ECTS, with better control of the magnet position relatively to the cavity. We had also planned to measure the magnetic field at several places of the cavity surface to have a better experimental characterization of the magnetic field pattern. Unfortunately these measurements could finally not be realized within the scope of the SARAF cavity characterization.

New experiments should be planned, for example during foreseen measurements of the IFMIF/DONES cavity in a horizontal cryostat.

3.5 Conclusion

The quest for high quality factors in superconducting cavities is a main issue for reaching high gradients and lowering the RF losses cost of an accelerator. It requires minimization of all the phenomena likely to weaken the superconducting properties of niobium, one of them being the magnetic flux trapping. It has led to increasing efforts limiting the static magnetic field around cavities, by both ensuring magnetic shielding and magnetic hygiene.

For the future, improvements on magnetic shields will lead to design optimization to assure proper shielding, and new solutions could consist into placing the magnetic shield inside the helium vessel for decrease their size and aperture numbers. Multiplying measurements in real magnetic shields installed in cryomodules will also help for improving the shield materials simulation. The improvement of the magnetic hygiene will require systematic anticipation of the cryomodule elements materials and their possible contribution to the magnetic field at cavity location. During fabrication and assembly, the elements likely to radiate should be detected and demagnetized, the last step being a global in situ degaussing of the cryomodule.

Flux trapping experiments allow for characterization of the cavity performance dependence to the ambient magnetic field, and have to be repeated for further cavity development. Such measurements are envisaged during the test of the IFMIF/DONES cavity in a dedicated cryostat.

The importance of magnetic measurements in test cryostats and in cryomodules, thanks to the development of dedicated sensors must be underlined, and is discussed in detail in chapter 5.

CEA EXPERIENCE AND EFFORT TO LIMIT MAGNETIC FLUX TRAPPING IN SUPERCONDUCTING CAVITIES

Juliette Plouin#, Nicolas Bazin, Patrice Charon, Guillaume Devanz,
Hervé Dzitko, Philippe Hardy, Fabien Leseigneur, Jérôme Neyret, Olivier Piquet
CEA-Saclay, Gif-sur-Yvette, France

Abstract

Protecting superconducting cavities from the surrounding static magnetic field is considered as a key point to reach very good cavity performances. This can be achieved by both limiting the causes of magnetic flux around the cavity in the cryomodule, and enclosing cavities and/or cryomodules into magnetic shields. We will present the effort made at CEA into this direction: shield design, shield material characterization, at room and cryogenic temperature, and search and attenuation of the magnetic background present in the cryomodule during the cavities superconducting transition. This last point will be especially studied for the IFMIF project where the cryomodule houses the focusing magnets.

INTRODUCTION

In low beta cryomodules with high intensity beams it is generally necessary to have solenoids close to superconducting cavities. When the cryomodule contains more than one or two cavities, the solenoids are usually inside the module, which adds a level of complexity to the cryomodule design considerations [1], because the static magnetic field can degrade the cavities performance. The static field close to a cavity must be lower than the critical field (tens of mT) when it is in the superconducting state. It has to be lower than some μT during the superconducting transition to avoid a significant increase of the surface resistance.

Then it is mandatory to prevent magnetic pollution generated by these solenoids, even when they are switched off.

Moreover the cavities must be protected from the earth magnetic field (~50 μT).

MAGNETIC SHIELD OF THE IFMIF CRYOMODULE

The IFMIF cryomodule contains all the equipment to transport and accelerate a 125 mA deuteron beam from an input energy of 5 MeV up to 9 MeV. It consists of a horizontal cryostat of about 6 m long, 3 m high and 2 m wide, which includes 8 superconducting HWRs (Half Wave Resonators) for beam acceleration working at 175 MHz and at 4.5 K, 8 power couplers to provide RF power to cavities, and 8 Solenoid packages as focusing elements [2].

A warm magnetic shield is installed on the inner walls of the vacuum vessel to protect the cavity from the earth magnetic field. Calculations have shown that with 2 mm thickness and with standard mumetal, the static magnetic field should stay lower than 2 μT inside the cryomodule, which is the design target for the HWR.

Several views (inside, outside the cryomodule, exploded) of this magnetic shield are shown in Figure 1.

The many apertures of the cryomodule are critical for the shielding, and overlap of mumetal sheets are mandatory. The tendering phase of this magnetic shield has started.

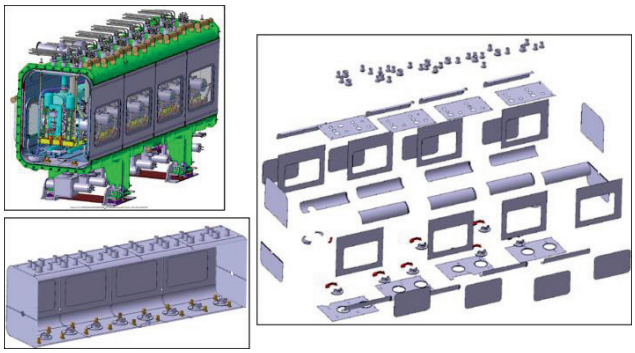

Figure 1: Magnetic shield of the IFMIF cryomodule.

MAGNETIZATION OF CRYOMODULE ELEMENTS

Due to space charge associated to the high intensity beam, a short, but strong, superconducting focusing magnet package is necessary between cavities. During the cryomodule operation, the solenoids will only be switched on once the cavities are in superconducting state. Each magnet package contains one inner solenoid, which can reach 7 T, four steerers, and one outer solenoid connected in series with the inner one with current established in opposite sense, in order to work as an active shielding. The fringe field at the cavity flange is then limited to 20 mT [3]. Figure 2 shows the magnetic field pattern generated by the solenoid package at several places in the cryomodule. Our concern is that some cryomodule components could be magnetized by this fringe field, and be a source of remnant field once the solenoid is switched off. We have focused our attention in particular on the needles bearings, the invar rod, and the magnetic shield itself.

Moreover the supporting frame was initially planned to be made of stainless steel 316L C-beams which are welded together. The large number of welding rims with potentially higher permeability than expected represented

juliette.plouin@cea.fr

Copyright © 2015 CC-BY-3.0 and by the respective authors

ISBN 978-3-95450-178-6

a risk. Thus the frame will finally be made of welded titanium I-beams which are totally non-magnetic.

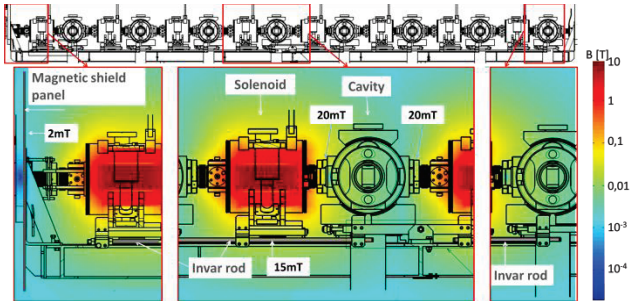

Figure 2: Static magnetic field pattern generated by the solenoid package in the cryomodule.

Needle Bearings

Cavity and solenoids supported by rolling systems similar to XFEL using needle bearings. One can see in Figure 3 that the needle bearings are close to the area of the cavities where the RF magnetic field is the highest.

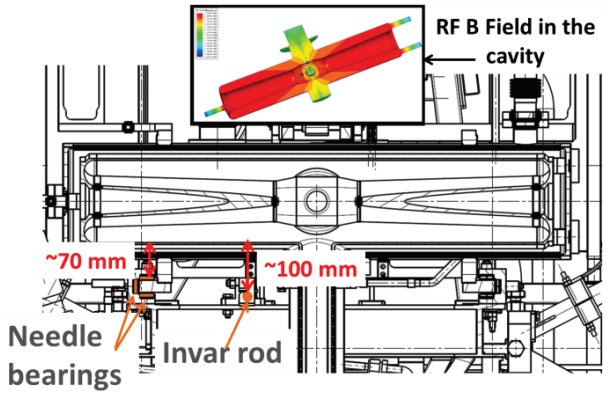

Figure 3: Position of the needle bearings and the invar rod in the cryomodule.

We observed that the bearings off the shell we had planned to use (Figure 4) were naturally magnetized [4]. We proceeded to magnetic measurements to estimate this magnetization. The magnetic field is measured with a Förster probe at several distances from the bearings. Measurements are performed inside a Cryoperm box (HIPPI magnetic shield), supported on a cardboard box instead of a table to avoid possible magnetic fields in the structure. The results are shown in Table 1 for 8 samples. The magnetic field reaches up to 400 μT at contact, and is still much higher than the 2 μT allowed on the cavity at 10 mm from the bearings. Sample 7 was dismounted and the field was measured at direct contact to each needle, reaching up to 1 mT (see Table 2).

To discard any magnetization of these elements we developed homemade bearings with brass cage and ceramic needle (Figure 5). Then these elements cannot anymore be a source of remnant magnetization.

Table 1: B Field at Different Distances from the Needle Bearing

Sample number	Average value at 10 mm (μT)	Average value at 4 mm (μT)	Average value at contact (μT)
1	5	10	25
2	25	72	220
3	60	50	140
4	42	100	215
5	34	80	135
6	5	19	39
7	42	105	440
8	16	70	235

Table 2: B Field at Contact with the Needles of Sample 7

Needle from sample 7	Field amp. at contact (μT)
1	750
2	1000
3	260
4	1000

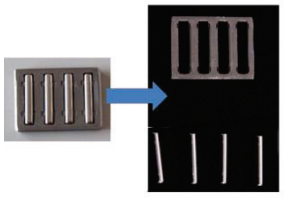

Figure 4: Off the shelf needle bearings.

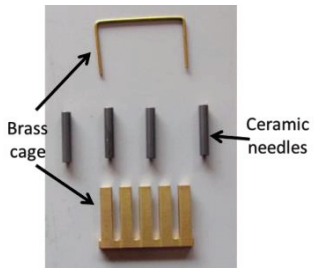

Figure 5: Home-made needle bearing.

Invar Rod Magnetization

In order to take into account the thermal shrinking of the cold mass, the cavity and solenoid will be fixed on a common specific mechanical support composed of a titanium frame to support the cold mass and of invar reference rods, to control the position along the beam axis with some sliding attachments to manage the differential thermal deformation between the frame and the invar rod. Two long invar rods will be placed in the cryomodule, each measuring half the size of the structure and the discontinuity between these two rods can be seen in Figure 2. These rods are situated at 100 mm from the cavity surface (Figure 3).

The invar material, well known for its very low thermal shrinkage at cold temperature, is also ferromagnetic, and can be magnetized. We made some tests with two invar rods (1 short, 1 long), with diameter 12 mm, like in the cryomodule, and with respective length 50 mm and 500 mm.

Copyright © 2015 CC-BY-3.0 and by the respective authors

The rods were magnetized using a board magnet (which can be seen in Figure 11) which generates a 100 mT field quite uniformly on its surface.

The short rod was magnetized in both axial and transverse direction. For the axial magnetization, while one section was placed on the magnet, the field at the other section was 25 mT, thus the whole rod is magnetized, even if non-uniformly. After each magnetization the B field is measured in different directions indicated in Figure 6.

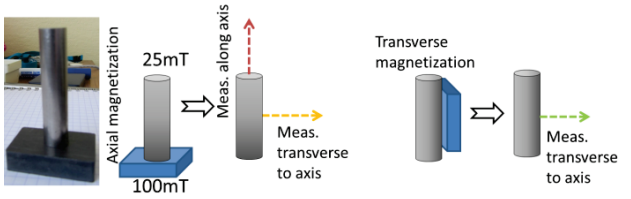

Figure 6: Magnetization of the short invar rod with a magnet.

The results presented in Figure 7 show that the field is still higher than 2 µT at 100 mm from the rod, which corresponds to the minimal distance invar/cavity in the cryomodule (see Figure 3).

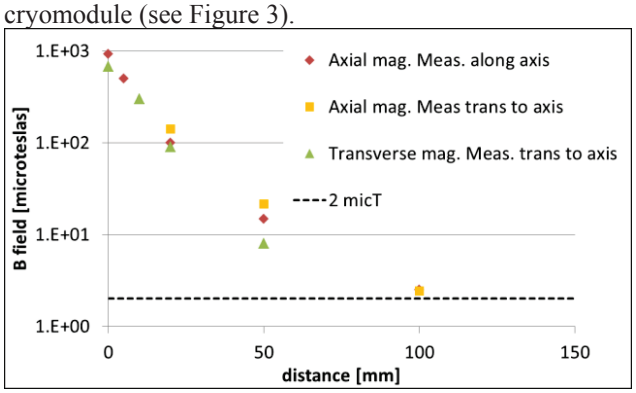

Figure 7: B field at different distances from the magnetized short invar rod.

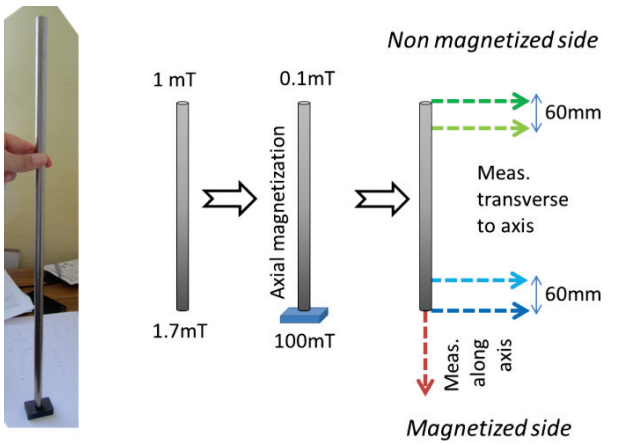

Figure 8: Magnetization of the long invar rod with a magnet.

The long rod was magnetized in the axial direction, and while one section was placed on the magnet, the field at the other section was 0.1 mT, even less that without the magnet; thus the rod is only locally magnetized. The B field is measured in different directions indicated in Figure 8. The results presented in Figure 9 show that the field is higher than 2 µT even at 100 mm from the non-magnetized side. It is even 10 times higher at the same distance from the magnetized side. One can also notice on the graph that the field is higher in the plane containing the rod end section than in a plane situated at 60 mm. Figure 2 shows that two rod extremities are situated close to a cavity (at 100 mm, see also Figure 3). It appears that this could cause the presence of a field higher than 2 µT close to the cavity, and lead to a surface resistance degradation.

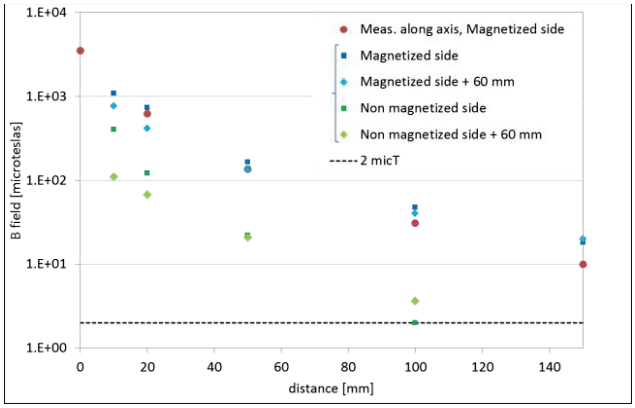

Figure 9: B field at different distances from the magnetized long invar rod.

We envisage different solutions to avoid the presence of this remnant field near the cavity. A local magnetic shield could be installed around these two invar rod extremities. An extra piece of invar could also be fixed to each extremity to deviate the magnetic flux from the cavities. Moreover, a procedure of demagnetization of the cryomodule, using the solenoids, in order to cancel all remnant static fields which could be present, in particular due to the invar rod.

In this perspective we proceeded to a demagnetization test on the short invar rod.

Invar Rod Demagnetization

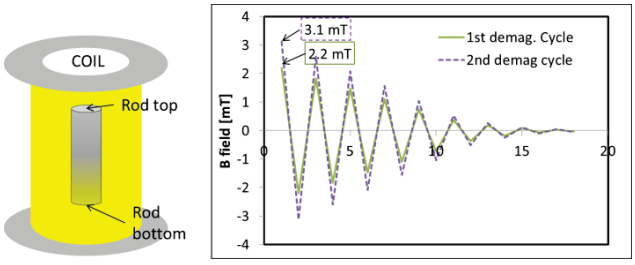

Figure 10: Demagnetization of the short invar rod placed in the centre of a coil.

The short rod was placed inside a home-made coil (see Figure 10) and subjected to a sequence defined in Table 3. The demagnetization cycles are represented in Figure 10. The abscissa represents the cycle's steps; the time constant was at least 2 s per mT.

Copyright © 2015 CC-BY-3.0 and by the respective authors

ISBN 978-3-95450-178-6

The field was measured at top and bottom of the rod (Figure 10). The results in Table 3 show that our demagnetization sequence lowers the remnant field, but is not strong enough to properly demagnetize the rod. We were limited by the current delivered by the supply connected to the coil, and we should carry out further tests with another supply.

Table 3: Magnetization/Demagnetization Cycles

Seq. #	Description	B at rod top [mT]	B at rod bottom [mT]
1	Initial	0.53	0.22
2	Magnetization +2.2 mT	0.57	0.3
3	1st demagnetization cycle	0.28	0.18
4	Magnetization -3.1 mT	0	0.2
5	Magnetization +3.1 mT	0.53	0.31
6	2nd demagnetization cycle	0.26	0.16

More demagnetization tests should also be performed with the coil described in section "SATHORI TESTS".

Mumetal Magnetic Shield

We also worried about the possible magnetization of the mumetal shield, which will be exposed up to 2 mT (see Figure 2).

We proceeded to the magnetization of a 1 mm thick ring made of Cryophy (Cryophy and mumetal have the same saturation field) (Figure 11). The applied field, given by the board magnet, is 100 mT (>>2 mT).

We observed that the remnant field at contact was the same before and after magnetization, lower than 2 μT, and for two different ring samples. In conclusion, the mumetal shield should not be magnetized by the solenoid. Our results are consistent with FRIB similar measurements [5].

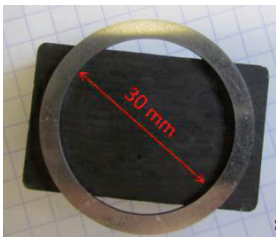

Figure 11: Cryophy ring sample on the board magnet.

SATHORI TESTS

A special horizontal test cryostat, called SATHORI ("SAtellite de Tests HOrizontal des Résonateurs IFMIF"), is under development at CEA-Saclay, in the SRF test area, and will be connected to the existing CRYHOLAB (Figure 12) [6]. This cryostat is dedicated to the IFMIF HWR performance check, fully equipped with its power coupler and cold tuning system. It will be protected from earth magnetic field by a mumetal magnetic shield with 2 mm thickness like the IFMIF shield.

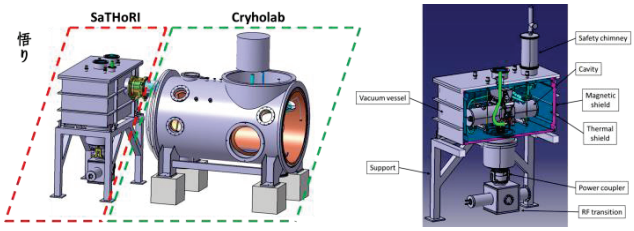

Figure 12: The SATHORI test cryostat.

Among others, it is planned to study how the presence of magnetic field from solenoid could degrade the cavity RF performances. To this intend special holes are made on the large panels of the magnetic shield to allow the penetration of the field generated by a coil placed outside the cryostat. The positioning of this coil is shown in Figure 13, left, and a schematic view of the shield with hole and coil is shown in Figure 13, right. The holes can be closed by special mumetal doors to constitute a closed shield during tests without coil.

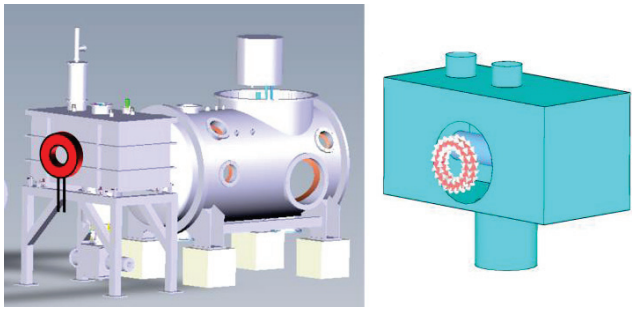

Figure 13: Positioning of a test coil in SATHORI (left). Schematic view of the magnetic shield with hole and with coil (right).

The tests foreseen with the coil are summarized hereafter:

- Cavity is in superconducting state, the coil is switched on and the current increased. The RF performances of the cavity are measured (Q-E curves) and the influence of the surrounding magnetic field is observed.
- Cavity is in superconducting state, the coil is switched on and the current increased. The cavity is forced to quench and recover. The influence of the magnetic field level on the cavity performances after recovering is studied.
- Cryogenic and RF are off. The cryostat with all elements inside is magnetized by the coil. Remnant field is measured inside the cryostat. Then a demagnetization procedure is realized. Remnant field is measured once again to check its remaining level.

The coil we plan to use for these tests is made of 144 turns and can work with 125 A. The field pattern of this coil, positioned at the outside wall of the cryostat is shown in Figure 14, in a horizontal plane crossing the cavity. The magnetic shield has been taken into account in the simulation, and the cavity has been considered either as vacuum (top) either as in Meissner state with $\mu_r \approx 0$ (bottom).

Copyright © 2015 CC-BY-3.0 and by the respective authors

ISBN 978-3-95450-178-6

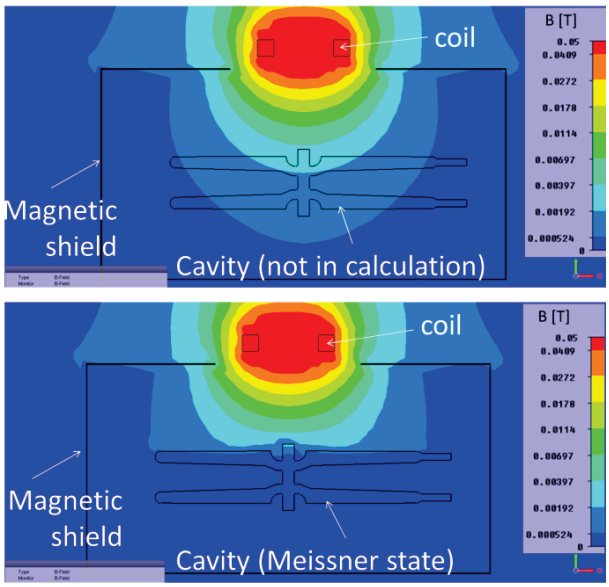

Figure 14: B field pattern given by the 144 turns, 125 A coil with magnetic shield and cavity. Cavity is in vacuum (top) or in Meissner state (bottom).

CONCLUSION

The magnetic environment of the cavities in the IFMIF cryomodule is considered in order to avoid any decrease of the superconducting cavities performance. The material of some elements (frame, needle bearings) has been changed to avoid magnetization. Solutions are under development to limit the remnant field from invar rods. A demagnetization procedure of the cryomodule is under study. Finally, the influence of the magnetic field from solenoid on the cavity performance will be observed in the SATHORI test stand.

REFERENCES

[1] R.E. Laxdal, "Review of magnetic shielding designs of low-beta cryomodules", WEIOD01, Proc. SRF'13, http://jacow.org/

[2] H. Dzitko et al., "Technical and logistical challenges for IFMIF-LIPAC cryomodule construction", FRBA01, these proceedings, Proc. SRF'15, Whistler, Canada (2015).

[3] S. Sanz et al., "Fabrication and testing of the first magnet package prototype for the SRF linac of LIPAc", WEPO030, Proc. IPAC'11, http://jacow.org/

[4] N. Bazin, "Magnetic aspect of the IFMIF cryomodule", TTC'14, Tsukuba, Japan (2014).

[5] S. K. Chandrasekaran, "Magnetic Shield Material Characterization for the Facility for Rare Isotope Beams' Cryomodules", IEEE Transactions on Applied Superconductivity **25**(3), 3500305 (2015).

[6] G. Devanz et al, "Progress in IFMIF Half Wave Resonators Manufacturing and Test Preparation", THPB045, these proceedings, Proc. SRF'15, Whistler, Canada (2015).

Copyright © 2015 CC-BY-3.0 and by the respective authors

ISBN 978-3-95450-178-6

Chapter 4

Optimization of RF sources efficiency for accelerators.

4.1 Microwave tubes

High power RF sources are essential elements for telecommunications and particle accelerators. Microwave tubes are used for more than 80 years as powerful electromagnetic waves amplifiers [Fai+08]. They have been invented and developed before the arrival of transistors and solid-state amplifiers. While traveling wave tubes (TWTs) are the major microwave amplifiers used in space telecommunication, klystrons are used for TV emission, radiotherapy and are used as RF sources for particle accelerators.

Their operating principle, based on the power transfer from a DC electron beam to an RF electromagnetic field, can be summarized as follow:

- ⋆ a monokinetic electron beam is emitted by a dedicated cathode and accelerated by an anode,
- ⋆ when subjected to RF input power the beam velocities become modulated,
- ⋆ this velocity modulation is turned into a current modulation, synchronized with the device operation frequency,
- ⋆ the coupling between the modulated current and the traveling wave (TWT) or with the output RF cavity (klystron) generates a high power microwave.

This principle is illustrated for a TWT and a klystron in Figure 4.1. In a TWT, the RF field is a traveling wave moving from input to output of the tube, and the interaction with the beam occurs all along the interaction line. The RF field amplitude grows up continuously. In

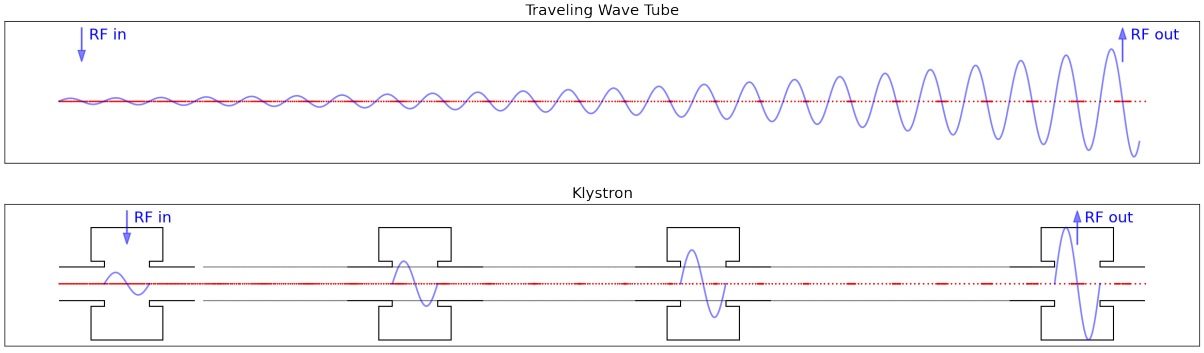

Figure 4.1: Principle of electron beam bunching and RF generation in a TWT and in a klystron.

a klystron, the RF field is located inside the oscillating cavities, and the bunching of electrons occurs in the drift tube between cavities [VV39]. When entering the output cavity, the electron beam transfers energy to an RF field. In both cases, the electron beam turns from continuous and monokinetic to a series of bunches synchronized with the device frequency.

Finally, a part of the electron beam kinetic energy has been transformed into electromagnetic energy, and the efficiency is defined as the ratio between RF power extracted from the tube and DC power provided to the beam. Optimizing the energy transfer consists into optimizing the electron bunching pattern arriving at the end of the interaction line to maximize the electron deceleration and power transfer.

This chapter presents some optimization schemes studied for TWTs and klystrons.

4.2 Improvement of output power in Traveling Wave Tubes

I started my PhD in 2000 in the Laboratoire de Physique et Technologie des Plasmas at the Ecole Polytechnique (Palaiseau, France), in collaboration with Thales Electron Devices (Vélizy, France), which is the French leader in microwaves tubes. My PhD topic was motivated by the need of improving the efficiency of traveling wave tubes used for spatial communications. The principle is to optimize the bunching pattern of the electron beam to maximize the extraction of energy from the beam. The method developed in my thesis consisted to modify the bunching pattern by the injection of an amplitude and phase controlled second harmonic wave, in order to change the resulting electromagnetic field shape.

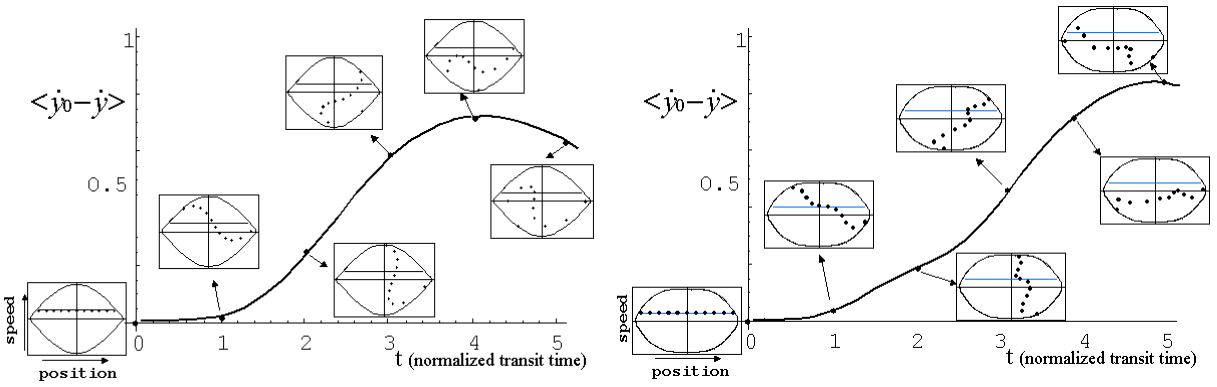

Figure 4.2: Evolution of the loss in velocity for an electron beam in a TWT, for a pure sinusoidal field $E_0 \sin(\omega t)$ (left) and for a field with harmonic injection $E_0 \sin(\omega t) + 0.5 \sin(2\omega t)$ (right). The insets show the behavior of a single bunch in a phase/velocity diagram. Figures from [Plo+05], corresponding to a low-gain Lagrangian model.

I carried out a theoretical, numerical, and experimental study of the harmonic injection, which represented an original approach of the phenomena. First, I used a low-gain Lagrangian model and showed how the beam bunching was optimized to increase extraction of energy from the beam, by using a non purely sinusoidal field. Figure 4.2 shows the average loss of beam velocity, with illustration of a single bunch behavior in a phase/velocity diagram. With harmonic injection, the maximal loss of velocity is increased.

Then I simulated harmonic injection in a TWT with the dedicated codes developed by Thales. Finally, experimental measurements with a broadband TWT manufactured at Thales gave significant results with an increase of 86% for fundamental output power with the best configuration of harmonic injection at 5 GHz and 50% at 7 GHz. The role of injection parameters has also been presented, especially the role of the input phase difference between fundamental and harmonic. Depending on the value of this parameter, harmonic injection may be favorable or unfavorable to the fundamental output power (see Figure 4.3). Results have shown that

harmonic injection allowed the optimization of energy transfer between the electron beam, the fundamental wave and its second harmonic, in order to increase the total energy extracted from the beam, and to favor the fundamental wave to the detriment of its harmonic. With good injection conditions, the improvement of the TWT's efficiency occurs with harmonic reduction.

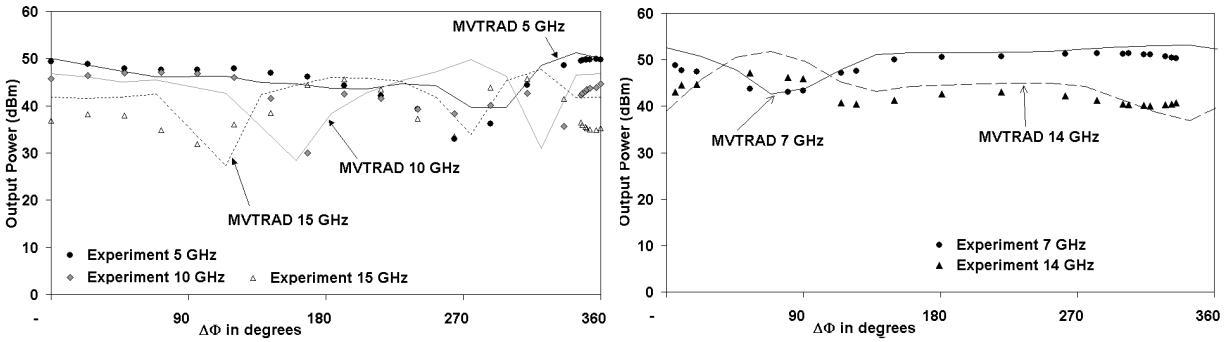

Figure 4.3: Harmonic injection at 5 GHz (left) and 7 GHz (right). Output powers versus phase difference. MVTRAD is the simulation code. Figure from [Plo+05].

These results are detailed in my PhD thesis [Plo04], and presented in conferences papers [PR02][PR03][Woh+03]and in a IEEE article [Plo+05].

Whereas I did not directly work on traveling wave tubes after my PhD, I have been reviewer for papers in IEEE, and I have been in the dissertation committee for three PhD thesis on TWTs in 2016, 2019 and 2023 (as a referee in 2016 and 2023).

4.3 High efficiency klystrons

With the emergence of new accelerator projects always more demanding concerning the amount of energy drawn from the power outlet by their Radio Frequency systems, improving energy-efficient conversion of electrical grid power into RF is becoming a key aspect in the approval process for these new facilities and ensure sustainability over the long term. This is particularly true for electrons colliders like FCC, ILC, or CLIC, which will need RF systems delivering average power of 100 MW or above [Con+16][Ger18]. Efforts have been engaged recently to stretch the efficiency of existing RF power sources to higher levels, in particular for klystrons where modern bunching techniques, described hereafter, help to improve the collection of extracted RF power. These efforts have been shared within the informal collaboration HEIKA (High Efficiency International Klystron Activity)[Syr22]

A standard klystron is made of a small number of cavities (typically 5 or 6), where one or two cavities are around the central frequency to ensure the bandwidth and two or three bunching cavities have a higher frequency. The objective is to optimize the beam current modulation in the last cavity, where the RF power is extracted, and so, increase the tube efficiency. The limit of the method is the induction of a large velocity dispersion, which limits the interaction efficiency (except for very low perveance). New bunching methods have been widely developed this last decade to increase efficiency: the Core Oscillation Method (COM) [BMS15], the Bunch Align Collect (BAC) [Guz14] method and the Core Stabilization bunching Method (CSM) [Hil+17].

The COM method consists of using a cavity highly coupled with the beam, to congregate the peripheral electrons of the bunch, while the electrons in the core of the bunch are "oscillating" through the tube [BMS15]. However, it results into a tube length increase. To solve the problem of compactness for low-frequency klystron, BAC [Guz14] and CSM [Hil+17] methods have been developed. The strategy for these methods consists into employing harmonic cavities to boost the bunching process.

These methods were applied around the world to a large range of frequencies, X-band [Wea+18][Syr+22], S-band [Guz+17], L-band [Rea+18] or below [Beu+22][Mar19][Xia+19]. Studies were applied in prototypes in some cases [Syr+22][Guz+17].

At CEA we developed another method, named kladistron, detailed hereafter.

4.4 Design, fabrication and test of a kladistron prototype

The work was developed within a PhD thesis, in collaboration between CEA and Thales Electron Devices, which is the French company specialized in klystrons. I was the CEA supervisor of the PhD student who graduated in 2017, Antoine Mollard, while Claude Marchand (CEA) was his PhD director. A prototype klystron of type *kladistron* was fabricated and tested with Thales. The kladistron method is a bunching technique, developed at CEA, [Pea14], which consists into using a large number of cavities (at least twice much as a standard klystron). Then, instead of giving a "strong" kick to the beam in a small number of cavities, the interaction line gives a "soft" kick in a large number of cavities, weakly coupled to the beam. This results in a smoother bunching process, allowing for better formation of the bunch into the last cavity.

We have decided to test this technique by transforming an existing klystron from Thales and only change the interaction line. The reference klystron is the 4.9 GHz–50 kW continuous wave (CW) TH2166 klystron, and the 6 existing cavities were replaced by 16 new cavities. All the work realized during and after the PhD thesis is presented in the conferences papers [Mol+16][Mol+17][Plo+21], the PhD thesis [Mol17] and the IEEE article [Plo+23b] given in annex to this chapter.

Figure 4.4 presents the electron velocity in the standard TH2166 klystron and in the transformed kladistron, in the whole interaction line (left) and in the last cavity (right). It shows how the bunching scheme in the kladistron turns into a higher deceleration of the electron beam than in the standard klystron.

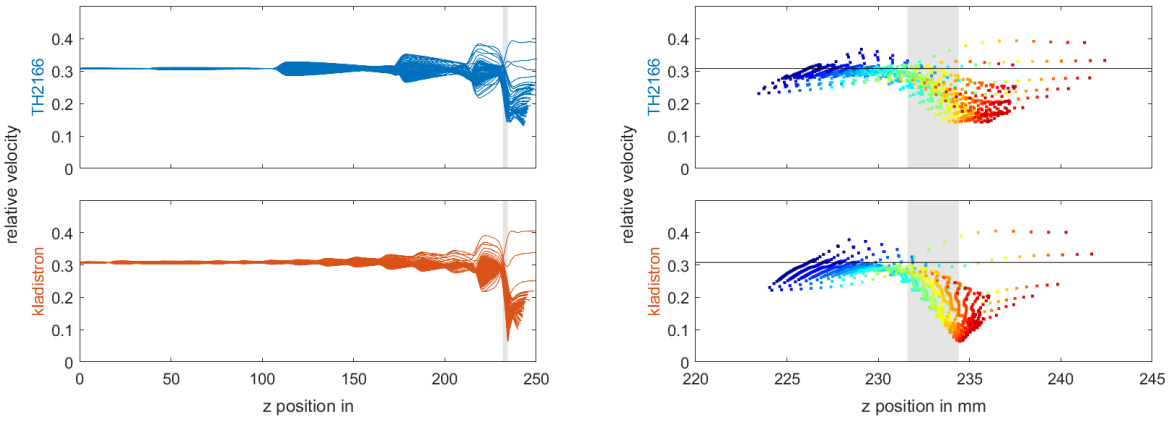

Figure 4.4: Evolution of the electrons velocity in a klystron, for the standard klystron (top) and the kladistron (bottom), for the whole interaction line (right) and in the output cavity (right). The output cavity is represented by a light grey rectangle. Simulation with KlyC [JS18].

The prototype klystron is shown at different fabrication phases in Figure 4.5. The measured efficiency was finally lower (41%) than expected (55%), and the klystron presented a spurious oscillation at 4.96 GHz. After analysis of the experimental results, it was concluded that the discrepancy between design and real frequencies was the cause for the low efficiency while the spurious oscillation resulted from a high gain peak at 4.96 GHz.

These results point out the risk of instabilities in high efficiency klystrons. It was concluded that in the future, two efforts have to be undertaken to prevent such situation. First, the tubes

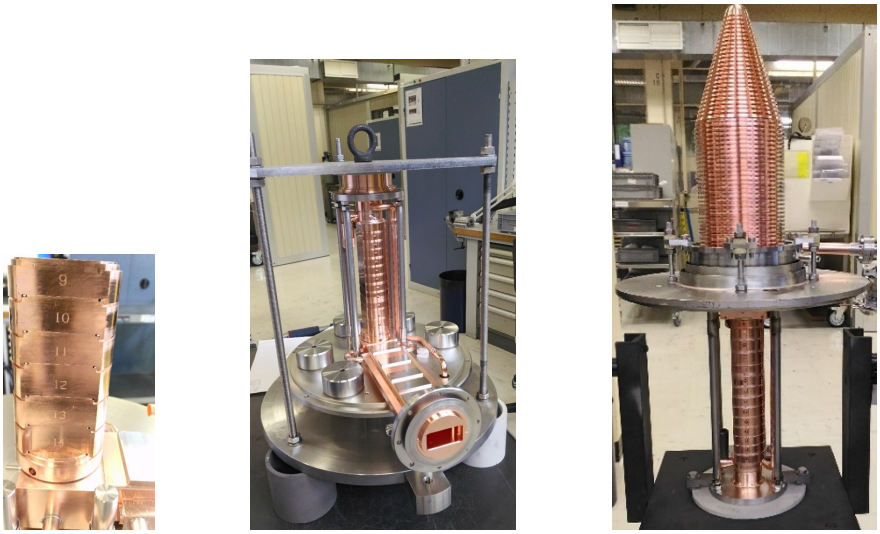

Figure 4.5: Prototype kladistron at different fabrication phases. Left: Partial cavity assembly. Center: Interaction line and output wave guide ready for brazing. Right: Tube closed.

design shall consider the risk of instabilities and, if possible, calculations should predict such instabilities. A challenging step is to predict reflected electrons and their effect on the tube performance. Some labs are now developing faster dedicated tools, with the implementation of an algorithm for the treatment of slow and reflected particles in an existing large-signal code [Che+07].

Second, our results highlight the high sensitivity of high efficiency klystrons to the accuracy of the RF parameters, especially the frequencies. For future tubes, a solution shall be developed to guarantee frequency accuracy during operation. One solution could be the implementation of in situ tuning systems, able to adjust frequency during klystron operation [SBS12]. Another solution, especially appropriate for large-scale production, is to guarantee cavity frequency by a well-controlled fabrication process. This process has been widely developed for the X-band manufacturing at CERN [SAC18].

4.5 Design of an efficient 12 GHz klystron

In 2017, the ARIES program started in the wake of EuCARD2. In the Work Package 4, "Efficient Energy Management", CEA was in charge of the task "High efficiency RF power sources", dedicated to *to deliver a complete design study of a novel RF source with at least 10 to 20% higher efficiency then the presently existing ones.*[Ars+21]. It has been decided that task 4.2 would focus on designing a high efficiency klystron operating in the X-band (12 GHz) with an electron beam power in the range 15-30 MW, that could be used for the “Compact Light” project [DAu+21].

A klystron RF design has been developed corresponding to these specifications. The cathode voltage is 240 kV and the beam current is 120 A, corresponding to an input DC power of ~ 30 MW. The bunching circuit is optimized with 8 cavities, the output cavity being a multicell cavity. The philosophy of the optimization was different from the one used for the kladistron. Instead of choosing a bunching method, a genetic algorithm was used to select an optimized configuration among thousands. A dozen of geometrical parameters are set free, and a cost function is defined:

$$cost = \nu + 1/G_s \tag{4.1}$$

The klystron efficiency ν has to be maximized, while the maximum small signal gain over

the band 11.5 GHz-12.5 GHz, G_s, has to be minimized. Actually, the experience from the EuCARD-2 kladistron results pointed out that high gain values were likely to generate klystron instabilities. Finally we obtain a klystron design with an efficiency of about 65%, well above the RF efficiency of existing klystrons in the X-band which are about 50% efficient. The overall small-signal gain is lower than 56 dB, thus ensuring the klystron robustness regarding spurious oscillations. It appears that the bunching method selected by the genetic algorithm is a hybridization between the core oscillation and the adiabatic method. The simulation results are shown in Figure 4.6.

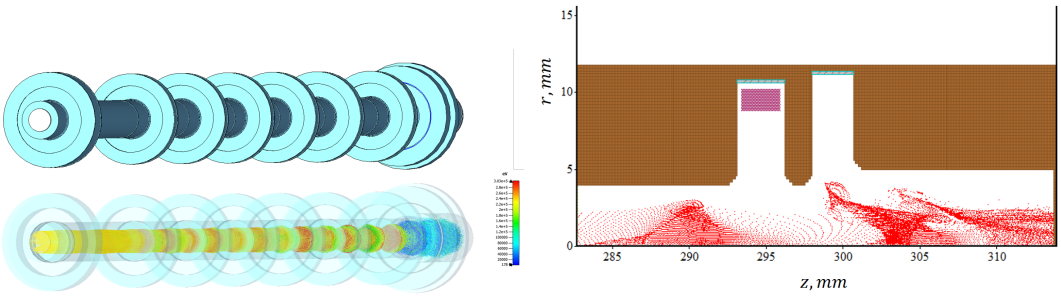

Figure 4.6: Left: Interaction line model: geometry (top) and beam particle modulation along the tube (bottom). Right: Output cavity model in a PIC code with the beam shown in red. Simulations with a Particle in Cell code.

Such study was made possible by the existence of simulation codes providing fast results like KlyC, developed at CERN [JS18]. The results could then be confirmed by the use of Particle-in-cell (PIC) simulations, Magic [Gru] and CST [Bal08] , which gives more accurate results but require much more simulation times.

This work was detailed in a specific ARIES report[Ars+21] and presented in conferences papers [Ham+19][Ham+21]

4.6 Conclusion

Today, the quest for high efficiency RF sources is an essential issue for future accelerators, and has become a major point in the R&D European and international programs: *Efficient Energy Management* Work Package in ARIES, *Sustainable concepts and technologies* Work Package in the I-Fast program (Innovation Fostering in Accelerator Science and Technology). Numbers of workshops are organized on energy sustainability and efficient RF sources. Strong collaborations are developed between vacuum tube manufacturers, like Thales in France, and research centers on accelerators like CEA, CNRS and CERN.

These developments require strong numerical tools, while the general increase in computing capacity allows and demands new optimization methods. This opens the way to efficient bunching optimization and this will lead to a general increase of the klystron efficiencies. Then, the development of dedicated codes is going on for klystrons, with the code KlyC developed at CERN [JS18], which we used for our developments, and for traveling wave tubes with the code DIMOHA [And+20], developed by the Aix-Marseille University, the CNES (Centre National d'Etudes Spatiales) and Thales. I have been referee for two thesis on the DIMOHA code [The16][Ali23].

However, such efficiency klystrons require also a large effort in the fabrication process. Our experience on the kladistron fabrication has shown that high efficiency tubes were more sensible to the fabrication process than standard tubes.

Design, fabrication and test of a 5 GHz klystron based on the kladistron principle

Juliette Plouin*†[1], Claude Marchand[1], Pierrick Hamel[1], Sergey Arsenyev[1], Antoine Mollard[2], Armel Beunas[2], Philippe Denis[2], and Franck Peauger[3]

[1]CEA, Université Paris-Saclay, Gif-sur-Yvette, France
[2]Thales MIS, Vélizy-Villacoublay, France
[3]CERN, Geneva, Switzerland

*Published in IEEE Transactions on Electron Devices, vol. 70, no. 3, pp. 1275-1282, March 2023, doi: 10.1109/TED.2023.3236590.

Date of Publication: 19 January 2023

arXiv:2404.05493v1 [physics.acc-ph] 8 Apr 2024

Abstract

A new bunching method, named "kladistron" has been developed at CEA in order to provide high efficiency klystrons. A first "kladistron" prototype was designed and realized. It was adapted from the 4.9 GHz TH2166 from Thales, where the interaction line was transformed from 6 to 16 cavities. The design and fabrication phases of this prototype are developed in this paper. The kladistron prototype was tested in Thales facility. Its efficiency is finally lower (41 %) than expected (55 %), moreover it presents a spurious oscillation at 4.96 GHz. After analysis of the experimental results, it is concluded that the discrepancy between design and real frequencies is the cause for the low efficiency while the spurious oscillation results from a high gain peak at 4.96 GHz.

Keywords— klystron, high efficiency, manufacturing process, spurious oscillation.

1 Introduction

With the emergence of new accelerator projects requiring high power from their Radio Frequency (RF) systems, improving energy-efficient conversion of electrical grid power into RF is becoming a key aspect in the approval process for these new facilities and ensure sustainability over the long term.

This is particularly true for electron colliders like FCC, ILC, or CLIC, which will need RF systems delivering average power up to 100 MW [1] [2]. Efforts have been engaged recently to stretch the efficiency of existing RF power sources to higher levels, in particular for klystrons where modern bunching techniques help to improve the collection of extracted RF power. A standard klystron is made of a small number of cavities (typically 5 or 6), where one or two cavities are around the central frequency to ensure the bandwidth and two or three bunching cavities have a higher frequency. The objective is to optimize the beam current modulation in the last cavity, where the RF power is extracted, and so, increase the tube efficiency. The limit of the method is the induction of a large velocity dispersion, which limits the interaction efficiency (except for very low perveance). New bunching methods have been widely developed this last decade which allow efficiency increase : the Core Oscillation Method (COM), the Bunch Align Collect (BAC) method and the Core Stabilization bunching Method (CSM).

The COM method consists of using a cavity highly coupled with the beam, to congregate the peripheral electrons of the bunch, while the electrons in the core of the bunch are "oscillating" through the tube [3]. However, it results into a tube length increase. To solve the problem of compactness for low-frequency klystron, BAC [4] and CSM [5] methods have been developed. The strategy for these methods consists into employing harmonic cavities to boost the bunching process.

These methods were applied around the world to a large range of frequencies, X-band [6] [7], S-band [8], L-band [9] or below [10] [11] [12]. Studies were applied in prototypes in some cases [7] [8].

Another method, developed at CEA and named kladistron, is described in this paper.

2 Kladistron principle

The kladistron, which stands for kl-adi(abatic)-stron, was inspired by the interaction mechanism in a Radio Frequency Quadrupole (RFQ) [13]. RFQs are used in proton linac injectors to bunch, focus and accelerate a continuous beam from few tens of keV to few MeV. In a RFQ, the beam bunching and acceleration are assured by the RF field generated by four electrodes, which present a longitudinal modulation all along the structure [14]. The bunching process is close to adiabatic, which means that the external forces (RF field) vary more slowly than the interaction forces in the system (space charge). The dynamics of the system is then a succession of equilibrium states and

*The work is part of EuCARD-2, partly funded by the European Commission, GA 312453.

†Electronic address: juliette.plouin@cea.fr

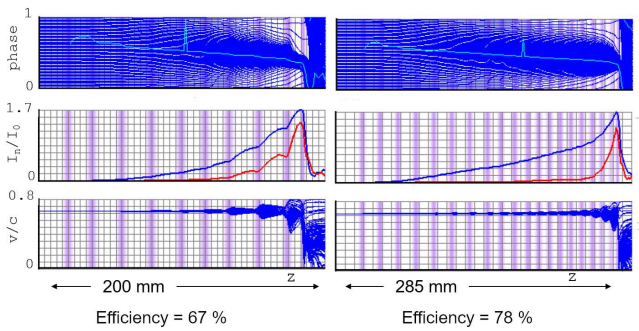

Figure 1: Figures of merit of a 10 cavities (left) and a 20 cavities (right) 12 GHz kladistron. Top : phase, medium : first (blue) and second (red) relative harmonic modulation current, bottom : normalized velocity, versus position in the interaction line. The cavities positions are represented by purple vertical lines.

the entropy increases only slightly.

In a klystron, the external forces are the beam induced bunching forces and the interaction forces are the space charge forces. The transposition of the adiabatic principle to a klystron consist into using a large number of cavities (at least twice as many as in a classical klystron). Moreover, instead of giving a "strong" kick to the beam in a small number of cavities, the interaction line gives a "soft" kick in a large number of cavities, weakly coupled to the beam, without harmonic cavities.

Very preliminary calculations made at 12 GHz showed how the number of cavities increase can lead to smoother current modulation and higher efficiency [13]. In the example shown in Figure 1 the cavities have low r/Q to be weakly coupled to the beam. Both klystrons have a microperveance equal to 1.4 $\mu A.V^{-1.5}$.

3 Design of a 5 GHz kladistron

For a first experimental validation of the kladistron principle we decided to transform an existing klystron and only change the interaction line. The chosen tube is the 4.9 GHz – 50 kW CW TH2166 klystron developed by Thales, which has an efficiency of 50 %. This tube is aimed to work with a cathode voltage of $V_0 = 26$ kV and a beam current of $I_0 = 4.3$ A, corresponding to a microperveance equal to 1.03 $\mu A.V^{-1.5}$. It is made with 6 cavities and the adapted kladistron is designed with 16 cavities. This number was chosen because it is high enough to be an example of the kladistron principle, and because a larger number of cavities would have been difficult to implement. Thus, since the tube body is kept the same, especially the focusing solenoid, the length of the interaction line is fixed. Figure 2 shows the reused TH2166 elements: the gun, the solenoid, the collector, as well as the input and output cavities. The modified elements are the 14 intermediate cavities replacing the existing 4 cavities.

This is a conservative approach, since it allows to focus only on the interaction line. However, this approach brings some constraints: the length of the interaction line is limited and the magnetic field profile cannot be modified.

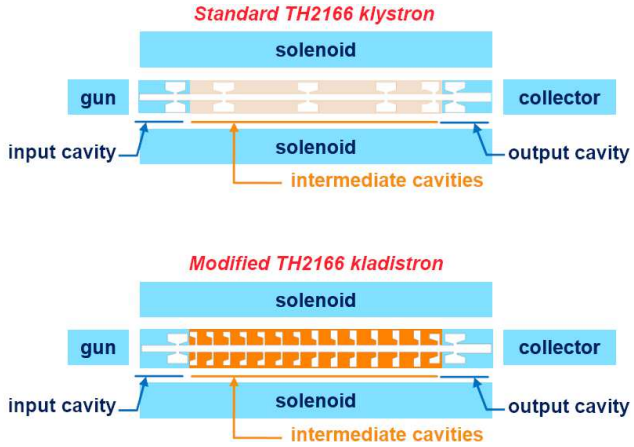

Figure 2: Principle of adaptation of the TH2166 to the kladistron. The elements in blue are kept from the TH2166 whereas the elements in orange (the intermediate cavities) are redesigned for the kladistron.

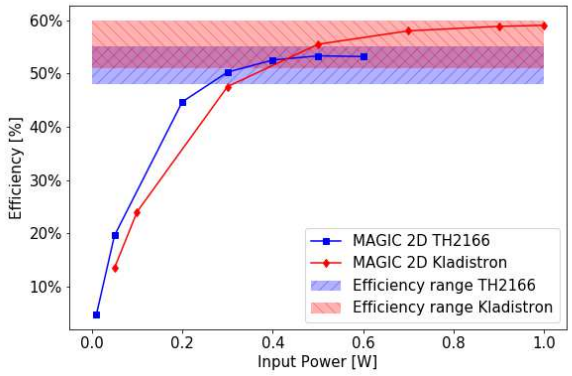

Figure 3: Efficiency comparison between the TH2166 klystron and the optimized kladistron.

3.1 Optimization of the interaction line RF parameters

The design of the intermediate cavities was realized with 2D-code Klys2D [16]: for each design, the input power is varied to find maximum output power. This is then simulated with the 2D PIC code Magic [17].

The efficiency calculated for one given design is not exactly the same within the codes, with a spread between 5 and 10 %. This is due to the difference in the RF/electrons interaction line modelisation. The result is shown in Figure 3, where the efficiency versus input power is shown for both the optimized kladistron and for the TH2166. The two curves correspond to MAGIC 2D calculations. For each tube, the range of efficiency within the different codes is represented. The gain of efficiency is thus estimated to +5 % [18].

The modulation current, shown in Figure 4 is much more regular for the kladistron, illustrating the "soft kicks" given by each cavity to the beam. The electron trajectories, simulated with MAGIC 2D are shown for both TH2166 and kladistron in

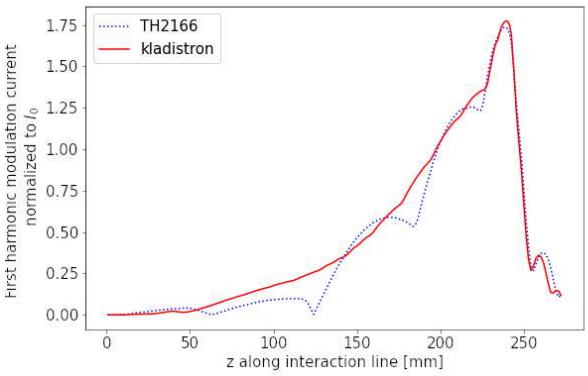

Figure 4: First harmonic modulation current vs z for the TH2166 and the kladistron. Simulations with Klys2D.

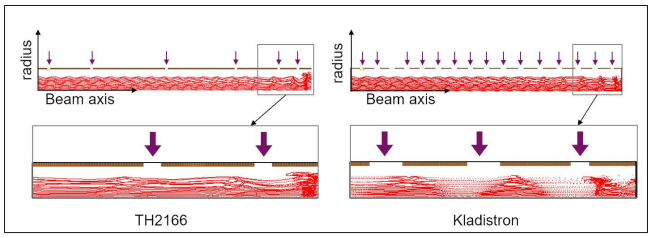

Figure 5: Electron trajectories simulated with MAGIC 2D for the TH2166 and the kladistron at their maximal efficiency. The vertical arrows show the cavities position.

Figure 5. The zoom on the last cavities shows that the bunching is more effective for the kladistron. However, it also shows a radial stratification for the kladistron beam, which could be a cause of efficiency limitation, like in COM klystrons [19].

For the kladistron RF design, the parameters for cavities 1 and 16 are kept from TH2166. The frequencies have been adjusted to maximize efficiency, and are shown in Figure 12. The r/Qs have been lowered for the intermediate cavities to decrease the coupling to the beam, to 20 Ω (cav. 2 to 8) and 33 Ω (cav. 9 to 15). The quality factors Q_0 have also been decreased (from 3000 to 1000), to limit high gain values in order to avoid oscillations.

3.2 Geometry of the cavities

The geometry of the intermediate cavities has been determined in order to fit with the chosen RF parameters. Two sets of cavities are designed whose shapes, with the electric field pattern, are shown in Figure 6. These cavities are made of copper, and their quality factor is decreased by deposition of titanium, with lower conductivity, on one of the cavity face. The asymmetric shape of the cavities was chosen to facilitate the titanium deposition in the fabrication process.

3.3 Multipacting simulations

The multipactor is an undesirable effect in RF tubes, which can lead to spurious heating in the RF structure. In the TH2166

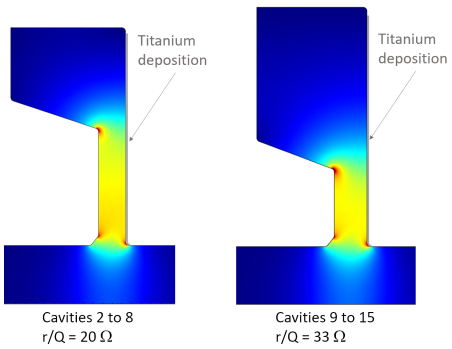

Figure 6: Geometry and electric field pattern of the intermediate cavities. The titanium deposition is shown by a thick grey line.

klystron, this phenomenon was supressed by deposition of titanium hydride, titanium having a secondary emission coefficient close to 1.

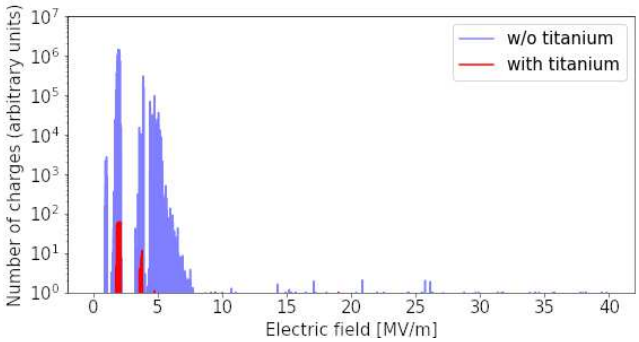

Figure 7: Multipacting simulations with MUSICC3D for cavities with or without titanium deposition.

In our kladistron, the multipactor is a problem for electric field lower than 35 MV/m, which is the maximal value expected in the cavities. Multipacting calculations were carried out in the intermediate cavities, using the MUSICC3D software from CNRS/IPNO [21]. Figure 7 shows the number of charges generated in the cavity's gaps as a function of the electric field. The simulation was carried out with 10000 electrons with the following method: one electron is extracted from a gap surface and submitted to an electric field with random phase and amplitude (between 0 and 40 MV/m). When impacting another surface, this electron is likely to extract new electrons, leading to exponential electron multiplication. The simulation is stopped once the initial electron has been either absorbed or has undergone 20 impacts. In a cavity without titanium, a single electron could extract millions of charges out of the cavity's surface whereas an electron in a cavity with titanium only generate 60 charges. Beside the need of quality factor decrease, these results show the necessity of the titanium deposition in the kladistron cavities.

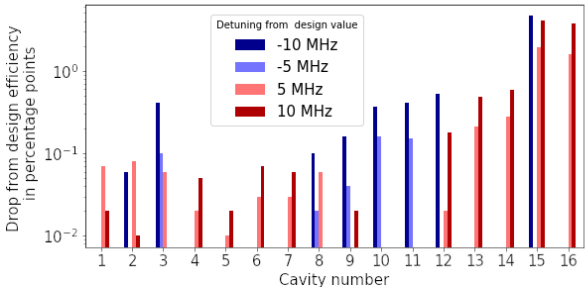

Figure 8: Kladistron efficiency variation when one cavity is detuned.

4 Manufacturing of the TH2166 based 5 GHz kladistron

The preparation of the kladistron prototype was carried out in two main phases:

- validation of innovative solutions on cavity prototypes,
- fabrication and assembly of all the elements constituting the whole klystron.

4.1 Cavities prototyping

The manufacturing of the final cavities for the kladistron was preceded by some prototyping [20], to validate:

- the achievement of the desired machining precision,
- the effect of the cavity parts brazing on the frequencies,
- the tuning system,
- the deposition of titanium.

4.1.1 Machining precision and brazing effect

Each prototype was made of two parts brazed together to form the inner cavity. It was rapidly verified that the achievement of the proper dimension was not a problem for the manufacturers, and that the difficulty to achieve the proper frequency was essentially due to the brazing operation. Several tests showed that this brazing operation could increase the frequency within 2 MHz to 8 MHz, without being easily predictable. However the kladistron's efficiency is sensitive to its cavities' frequency shifts, especially at the end of the interaction line, where a frequency shift of 10 MHz leads to an efficiency drop of 5 points. This is shown in Figure 8 where each cavity is shifted separately for a value between $-10\ MHz$ and $10\ MHz$ and the efficiency deviation from the design value is calculated.

In consequence, we could not expect the fabrication procedure to provide cavities frequencies able to guarantee the kladistron performance. A tuning system, able to recover frequency values after fabrication was thus considered necessary.

4.1.2 Design and validation of a tuning system

Each cavity is equipped with a tuning system based on cavity volume deformation to adjust the cavities' frequencies. A thick membrane between the inside and the outside of the cavity is deformed by brazed pins (four per cavity) that translate along drill holes positioned around the cavity (see Figure 9).

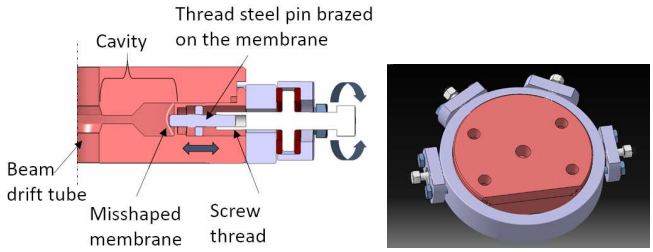

Figure 9: Tuning system on a prototype cavity. Section view of the membrane deformation principle (left) and cavity equipped with its four tuning systems (right).

Repeated measurements with these tuning systems on prototype cavities demonstrated that they could provide a reversible frequency adjustment from -6 MHz to +12 MHz and thus should be able to compensate the frequency shift due to fabrication process.

4.1.3 Titanium deposition

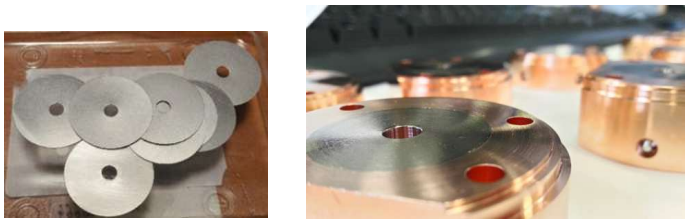

Figure 10: Left: 100 μm thick titanium disks. Right: cavity part after titanium brazing and last surface machining.

A new titanium deposition method has been developed and tested during the prototyping phase. The usual technique consists into applying a titanium hydride (TiH2) layer with a brush tool, which results in a inaccurate thickness. The new technique consists into the brazing-diffusion of a 100 micrometers thick disk onto the copper surface (Figure 10). Several tests have been achieved on dedicated prototypes and gave very good results after a last surface machining. This method was then used for the final kladistron manufacturing.

4.2 Manufacturing of the kladistron

Besides the standard klystron manufacturing procedure, the following steps have been achieved:

- All the cavities parts are individually prepared for the brazing of the titanium disk and the brazing of the tuning system pins.
- After these brazing operation, a final machining is applied on the titanium brazed cavity parts.
- Then, the whole interaction line's brazing is carried out. On Figure 11, the left picture shows the interaction line during cavity assembly and the center picture shows the interaction line with output wave guide, ready for brazing.

- At this point, some RF measurements are carried out, with two antennas inserted in the drift tube (see next section).
- Then the last elements (collector, RF gun, window and ionic pump) are welded to close the tube (figure 11, right).

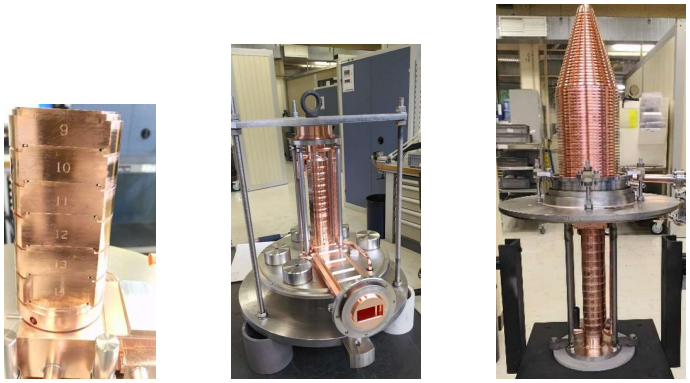

Figure 11: Left: Partial cavities assembly. Center: Interaction line and output wave guide ready for brazing. Right: Tube closed.

4.3 Measurements before final assembly

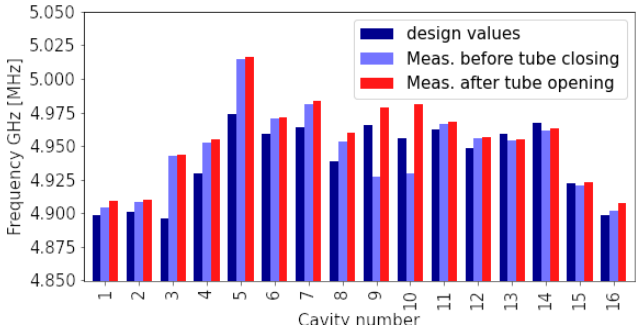

Figure 12: Cavities frequencies: design and measurements values.

The cavities frequencies are measured in the interaction line before the final assembly. A tuning operation was planned to match the design frequencies. Unfortunately, it appeared that the braze between tuner system pins and cavities was defective, and that the tuning systems were finally ineffective. However it was possible to adjust the frequencies of the two last cavities (which have the more influence on the kladistron efficiency, see Fig. 8) with the use of a mechanical tool. Those frequencies are measured in air whereas the design frequencies correspond to the tube operation under vacuum, and we have adjusted them to their corresponding values under vacuum. Those adjusted frequencies and the design frequencies are shown in Figure 12.

5 Tests of the 5 GHz kladistron

Taking the complexity of the manufacturing into account, we considered that an increase of the efficiency from 50 % to 55 % would be significant to consist into a first validation of the kladistron principle.

The kladistron was tested in Thales facilities on the test bench dedicated to the TH2166. This latter tube is aimed to work in CW. However, since the cooling system was not optimized for the kladistron, we preferred to work in pulsed mode. The duty cycle was increased up to 13.5 %, with a repetition rate of 25 Hz and a RF pulse of 5.4 ms (while the high voltage pulse was 6 ms). The nominal voltage of the TH2166 is 26 kV, and we varied the cathode voltage, V_k between 25 and 30 kV. The measured beam current always fits with a microperveance equal to 0.91 $\mu A.V^{-1.5}$. The focalisation current was set to 38 A.

The kladistron output power and efficiency were determined from RF measurements, and confirmed with calorimetric measurements.

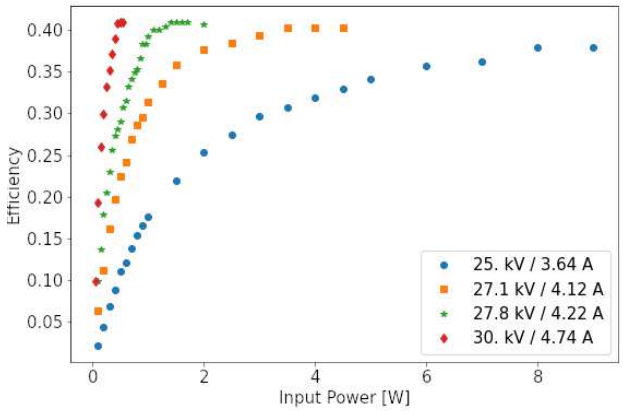

Figure 13: Measured efficiency vs input power at several values of the cathode voltage. The RF duty cycle is 13.5 %. The signal frequency is 4.904 GHz.

The efficiency versus input power measurements are shown in Figure 13. The maximal efficiency, equal to 41 %, was reached for the cathode voltages equal to 27.8 kV and 30 kV. It was not possible to reach higher values during these tests. The manufactured kladistron finally presents a maximal efficiency lower than expected, and even lower than the standard TH2166 efficiency (50 %).

During all the measurements we observed the existence of an unexpected spurious oscillation close to 4.96 GHz. When some RF power is injected into the kladistron, the oscillation and its intermodulation signals appear in the output spectrum, around the amplified input signal (see Fig. 14). Moreover, the oscillation signal is also present in pure diode mode, without input signal. An example is shown in Figure 14 (orange dots). The focalisation current was varied between 35.5 and 41 A without any effect on the oscillation signal.

The measured small signal gain is shown in Figure 15.

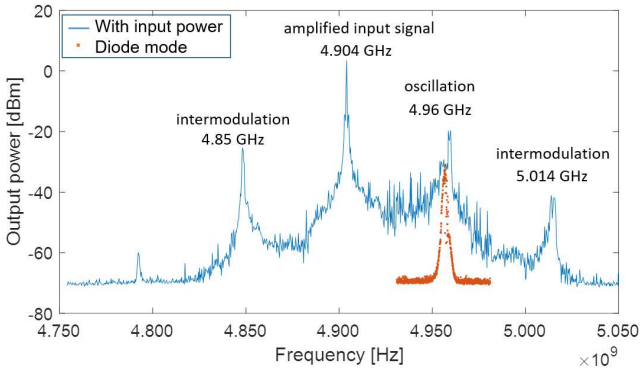

Figure 14: Output signal spectrum corresponding to $V_k = 27.8$ kV and efficiency = 41 % (blue line) and in pure diode mode (orange dots). The RF duty cycle is 13.5 %.

6 Post mortem measurements and simulations

After those measurements, the kladistron was disassembled and the frequencies, loss and external Q factors were measured. The Q factors were close to the expected values, attesting that the titanium deposition was effective. The frequencies "after tube opening" are compared to the design values in Figure 12, with the corresponding results "before tube closing". The difference "before/after" shows that the interaction line was probably slightly deformed during the manufacturing process. Although the RF parameters could be measured, the actual position of the cavities is still unknown because it could not be measured precisely.

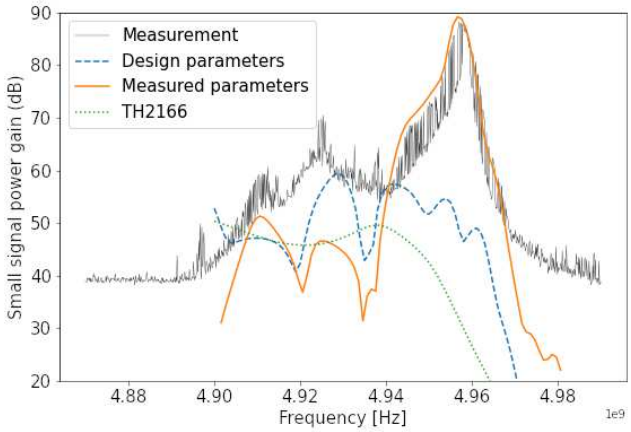

Figure 15: Measured and calculated small signal power gain of the kladistron (Meas.: RF duty cycle: 13.5 %, $V_k = 27$ kV.)

The small signal gain was calculated with code KlyC [22] using post mortem measured parameters and compared to the experimental values. Figure 15 shows that both measured and newly calculated small signal gains reach high values around 4.96 GHz, which seems to be due to the presence of several cavities frequencies around this value. This is probably the cause of the spurious oscillation, see section 7.

Furthermore, the discrepancy between design and real frequencies is probably the cause of the loss of efficiency between prediction and measurements. Figure 8 shows that with the final frequency shifts (5 MHz for the last cavity and up to 40 MHz for some intermediate cavities) the efficiency is likely to drop by several percentage points.

We have investigated this hypothesis with a set of simulations achieved with KlyC. The kladistron was modeled with both sets of design and post mortem measured parameters, and the standard figures of merit (efficiency vs input power, modulation current, beam behavior) were simulated.

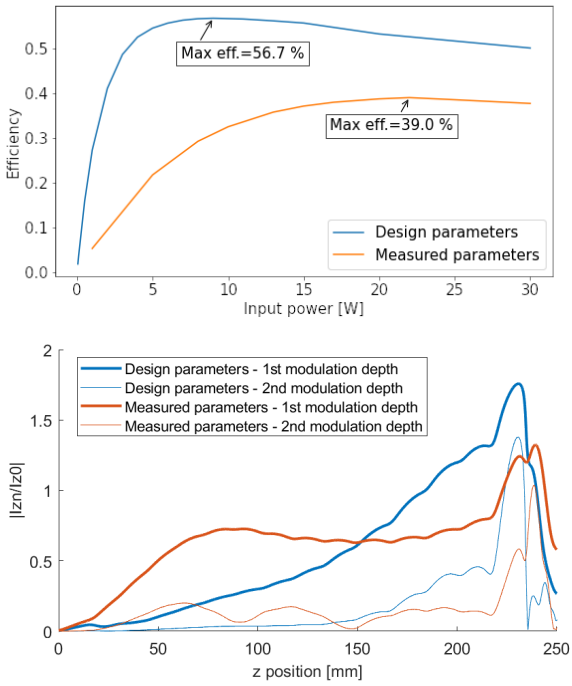

Figure 16: Calculations with KlyC for both design and measured parameters kladistrons Top: Efficiency versus input power. Bottom: 1st and 2nd modulation depth of the modulation current.

Figure 16 shows clearly how the efficiency drops when the measured parameters are used in the simulations, with a calculated maximal efficiency (39%) close to the experimental value. The modulation current profile is also dramatically decreased.

Figure 17 shows the Applegate diagram (top) and the electrons velocities (bottom). Both figures show that the electron bunching in the output cavity is degraded with the measured parameters.

In conclusion, the difference between the post mortem measured parameters and the design parameters, in particular the frequencies, appear to be the cause of the drop of efficiency experimentally observed.

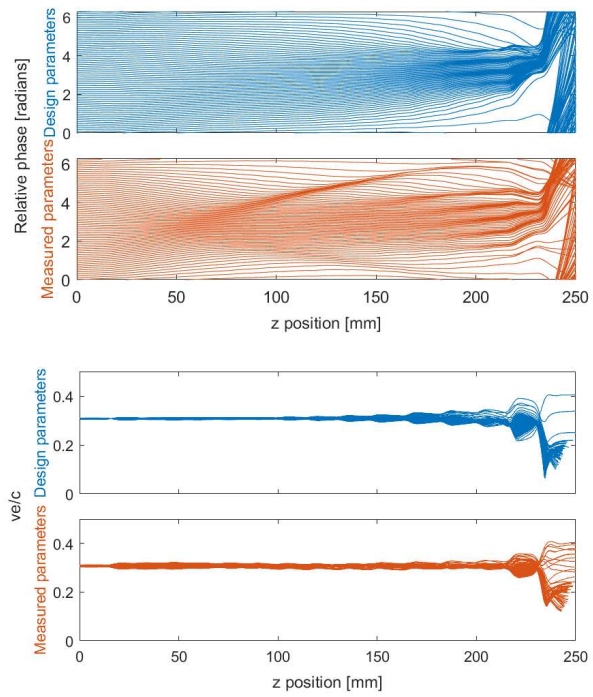

Figure 17: Calculations with KlyC for both design and measured parameters kladistrons. Top: Applegate diagram showing the electrons relative phases along the klystron. Bottom: electron velocities versus position.

7 Discussion on the oscillation origin

We have envisaged two hypothesis to explain the existence of the oscillation signal: the existence of a monotron oscillation in one of the cavities and the generation of a RF loop oscillation due to the reflection of electrons. Both hypothesis will be discussed in this section.

7.1 Monotron oscillation

When an electron beam travels along an RF cavity, the beam-loading conductance, G_b, represents the energy transfer between the beam and the cavity RF field. A negative value for G_b corresponds to an energy transfer in favor of the RF field; it can cause the excitation of the RF field in the cavity even by a non modulated beam [23] [24] [25]. We have considered whether such a "monotron" instability could arise in the intermediate cavities of the kladistron (first and last cavities, gun and collector could in principle cause oscillation, however they are shared by the TH2166 which does not present any oscillation so we discarded this possibility). The following formula [15], gives the expression of G_b:

$$\frac{G_b}{G_0} = -\frac{\beta_e}{4}\frac{\partial|M^2|}{\partial\beta_e} \tag{1}$$

G_0 being the beam conductance I_0/V_0, β_e the electron propagation constant, and M the coupling coefficient.

The criterion to discard monotron oscillation is $G_b > 0$. We have tested this criterion on the kladistron intermediate cavities, using the z-field on axis.

In the kladistron, the electron beam voltage in pure diode mode is 26 kV. The beam-loading conductance calculated at this voltage is $G_b/G_0 = 0.15$, discarding any monotron oscillation. Moreover, calculations show that the beam-loading conductance is positive at any transit angle (or beam voltage), which means that even electrons with lower energy, e.g. reflected in the structure, could not cause oscillation.

7.2 RF loop oscillation

A large gain RF structure is likely to give rise to some oscillation because even a small feedback can turn into a loop. In a klystron, the RF loop cannot be generated by some travelling waves (forward and backward) because it is a standing wave structure. The RF signal is carried out by the electron beam. However the existence of a backstreaming current, carrying some RF signal up to the input cavity, could cause some RF loop oscillation. In a klystron, backstreaming electrons are mainly generated by the strong energy decrease in the output cavity, or backscattered from the collector surface.

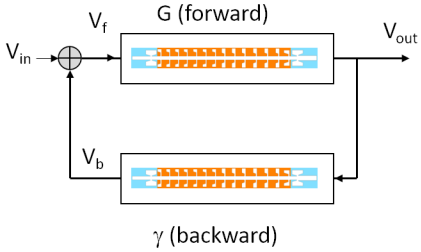

Figure 18: RF loop in the kladistron due to backstreaming electrons

Figure 18 shows the principle of such a loop. The forward electron beam generates a forward complex gain, G, defined by the output to input voltage ratio V_{out}/V_f. The backstreaming current generates a complex backward gain, γ, defined by the ratio V_b/V_{out}. The voltage V_f is the sum of V_b and V_{in} and the closed loop gain is :

$$G_{loop} = \frac{G}{1-\gamma.G} \tag{2}$$

According to the Nyquist criterion, an RF signal can be established even without input power ($V_{in} = 0$) if the amplitude of γG is equal to 1 while its phase is equal to zero modulo 2π. In this configuration, oscillations are likely to happen.

Such phenomenon has been observed and described by *Fang* [30] [31] in a 324 MHz klystron, where it is demonstrated that a spurious oscillation was generated by backstreaming electrons from the collector. *Fang* modified the shape of the collector to decrease the backstreaming current rate, and the spurious oscillation finally disappeared.

Suzuki and Okubo [29] [28] have encountered efficiency limitation on the first prototype of a high efficiency 2856 MHz klystron, due to instability in high beam power region. They have identified reflected electrons from the collector as the cause of this instability.

Roybal and Chernyavskiy [26] [27] have studied how returned electrons in a klystron can cause oscillations and lead to decreased tube efficiency.

Figure 15 shows that the maximal small signal power gain is 40 dB higher for the fabricated kladistron, compared to the TH2166. This corresponds to a factor 100 for the gain in voltage. Thus, the threshold backstreaming current rate causing oscillation is much lower for the kladistron than for the TH2166.

Both tubes have the same collector and output cavity, so in principle the rate of backstreaming electrons is the same. However, one can consider that this rate is lower than the threshold in the TH2166, which actually presents no oscillation, whereas it is higher than the threshold in the kladistron.

Finally, we think that the cause of the spurious oscillation in the experimental kladistron is due to this high gain peak around 4.96 GHz, which results from the casual presence of 4 cavities frequencies around this value.

8 Conclusion

We have developed an new bunching method for klystrons, named kladistron, based on a smooth bunching scheme. After promising simulation results predicting increase of efficiency, a kladistron prototype has been developed and fabricated by modification of an existing 5 GHz klystron. The prototype works, but presents an efficiency lower than expected and a spurious oscillation even in the diode mode.

The problem of a high gain generating oscillations was identified as a risk from the start of the study, because of the high number of cavities. This is why we had decreased the cavities quality factor with titanium deposition on copper. However, the tube finally presented such a high gain peak associated with spurious oscillation. The cause is the cavities frequencies distribution of the kladistron in operation, which results from:

- the failure of the tuning systems which prevented the frequencies adjustment of the finalized interaction line,
- the cavities frequency shift between finalized interaction line and klystron in operation.

These results point out the risk of instabilities in high efficiency klystrons. In the future, two efforts have to be undertaken to prevent such situation. First, the tubes design shall consider the risk of instabilities and, if possible, calculations should predict such instabilities. In our case, it was checked that the small signal gain was not too high. Such approach can be systematized, and for example, a limited small signal gain can be part of the figure of merit, together with the klystron efficiency [34] [35]. A further, but more challenging step is to predict reflected electrons and their effect on the tube performance. Most of frequency simulation codes do not allow such calculations, and PIC code are too time consuming for optimization. Some labs are now developing faster dedicated tools [27].

Second, our results highlight the high sensitivity of high efficiency klystrons to the accuracy of the RF parameters, especially the frequencies. Thus, the discrepancy between design and real frequencies is also the cause for the low efficiency. For a future tube, a solution shall be developed to guarantee frequency accuracy during operation. One solution could be the implementation of in-situ tuning systems, able to adjust frequency during klystron operation. Such solutions have already been studied for other klystrons [32] and could be implemented in future studies. Another solution, especially appropriate for large-scale production, is to guarantee cavities frequency by a well-controlled fabrication process. This process has been widely developed for the X-band manufacturing at CERN [33].

References

[1] D.A Constable, C. Lingwood, G. Burt, I. Syratchev, R. Marchesin, A.Y. Baikov, and R. Kowalczyk, "2-D particle-in-cell simulations of high efficiency klystrons," 2016 IEEE International Vacuum Electronics Conference (IVEC), 2016, pp. 1-2, doi: 10.1109/IVEC.2016.7561813.

[2] F. Gerigk, "Status and Future Strategy for Advanced High Power Microwave Sources for Accelerators", Conf.Proc., vol. C18-04-29, p. MOYGB1, juin 2018, doi: 10.18429/JACoW-IPAC2018-MOYGB1

[3] A. Y. Baikov, C. Marrelli and I. Syratchev, "Toward High-Power Klystrons With RF Power Conversion Efficiency on the Order of 90 %," in IEEE Transactions on Electron Devices, vol. 62, no. 10, pp. 3406-3412, Oct. 2015, doi: 10.1109/TED.2015.2464096.

[4] I. A. Guzilov, "BAC method of increasing the efficiency in klystrons," 2014 Tenth International Vacuum Electron Sources Conference (IVESC), 2014, pp. 1-2, doi: 10.1109/IVESC.2014.6891996.

[5] V. C. R. Hill, G. Burt, D. Constable, C. Lingwood, C. Marrelli and I. Syratchev, "Particle-in-cell simulation of second and third harmonic cavity klystron," 2017 Eighteenth International Vacuum Electronics Conference (IVEC), 2017, pp. 1-2, doi: 10.1109/IVEC.2017.8289626.

[6] B. Weatherford, R. Kowalczyk, V. Dolgashev, J. Neilson, A. Jensen, I. Syratchev and J. Cai, "Exploratory study of X-band Klystron designs for maximum efficiency," 2018 IEEE International Vacuum Electronics Conference (IVEC), 2018, pp. 23-24, doi: 10.1109/IVEC.2018.8391533.

[7] I. Syratchev, Z.U. Nisa, J. Cai, G. Burt, T. Anno, "DC Beam Stability issues in the first commercial prototype of a High Efficiency 8MW X-Band Klystron", CERN report CERN-ACC-2022-0007.

[8] I. Guzilov, O. Maslennikov, R. Egorov, I. Syratchev, V. Kobets and A. Sumbaev, "Comparison of 6 MW S-band pulsed BAC MBK with the existing SBKs," 2017 Eighteenth International Vacuum Electronics Conference (IVEC), 2017, pp. 1-2, doi: 10.1109/IVEC.2017.8289691.

[9] M. Read, R. L. Ives, J. Neilson and A. Jensen, "A 1.3 GHz 100 kW ultra-high efficiency Klystron," 2018 IEEE International Vacuum Electronics Conference (IVEC), 2018, pp. 25-26, doi: 10.1109/IVEC.2018.8391534

[10] A. Beunas, K.H. Khlifa, I. Syratchev and N. Catalan Lasheras, "CSM HE klystron for LHC", Workshop on efficient RF sources, Geneva, Switzerland, 2022, doi: https://indi.to/m4mW3

[11] C. Marrelli, "High Efficiency Klystrons for ESS," 2019 International Vacuum Electronics Conference (IVEC), 2019, pp. 1-2, doi: 10.1109/IVEC.2019.8745252.

[12] O. Z. Xiao, Z. S. Zhou, Zaid-un-Nisa, S. C. Wang, G. X. Pei, D. Dong and S. Fukuda, "Design Study of High Efficiency CW Klystron for CEPC," 2019 International Vacuum Electronics Conference (IVEC), 2019, pp. 1-2, doi: 10.1109/IVEC.2019.8745286.

[13] F. Peauger, "High Efficiency – High Perveance Klystron (X-band)", EnEfficiency RF Sources Workshop, CERN, 2014, doi: https://indi.to/dDvXs

[14] A. M. Lombardi. "The radio frequency quadrupole (RFQ)", CAS - CERN Accelerator School : small accelerators, 2006, pp.201-207, doi: 10.5170/CERN-2006-012.201

[15] G. Caryotakis, "High power klystrons : Theory and practice at the Stanford Linear Accelerator center". SLAC-PUB, 10620 :139, 2004.

[16] "Klys2D. Thales Internal Code for 2D Klystron Simulation", Thales Electron Devices SA, Vélizy-Villacoublay, France, 2017.

[17] B. Goplen, L. Ludeking, D. Smithe, G. Warren, "User-configurable MAGIC code for electromagnetic PIC calculations," in Comput. Phys. Commun., vol. 87, pp. 54-86, 1995

[18] A. Mollard, C. Marchand, F. Peauger, J. Plouin, A. Beunas and R. Marchesin, "High-efficiency klystron design for the CLIC project," 2016 IEEE International Vacuum Electronics Conference (IVEC), 2016, pp. 1-2, doi: 10.1109/IVEC.2016.7561812.

[19] I. Syratchev, "High Efficiency klystrons technologies", Workshop on efficient RF sources, 2022, https://indico.cern.ch/event/1138197/contributions/4821294/

[20] A. Mollard, C. Marchand, F. Peauger, J. Plouin, A. Beunas and R. Marchesin, "Development of a high-efficiency klystron based on the kladistron principle," 2017 Eighteenth International Vacuum Electronics Conference (IVEC), 2017, pp. 1-2, doi: 10.1109/IVEC.2017.8289714.

[21] T. Hamelin, J.L. Coacolo, M. Chabot, J. Lesrel, G. Martinet, "MUSICC3D: A code for modeling the multipacting", 16th International Conference on RF Superconductivity (SRF2013)

[22] J.C. Cai, I. Syratchev, "KlyC: 1.5D Large Signal Simulation Code for Klystrons", in IEEE Trans. on Plasma Science, vol.47, no.4, pp.1734- 1741, April 2019, doi: 10.1109/TPS.2019.2904125.

[23] B. Krietenstein, B. Krietenstein, K. Ko, T. Lee, U. Becker, T. Weiland and M. Dohlus, "Spurious oscillations in high power klystrons," Proceedings Particle Accelerator Conference, 1995, pp. 1533-1535 vol.3, doi: 10.1109/PAC.1995.505276.

[24] U. Becker, B. Krietenstein, T Weiland, M. Dohlus and K Ko, "Simulation of oscillations in high power klystrons", Proc. 5th European Particle Accelerator Conf. (EPAC 96), 1996.

[25] G. Nusinovich, M. Read and L Song, "Excitation of "monotron" oscillations in klystrons", Physics of Plasmas 11, 4893 (2004); https://doi.org/10.1063/1.1793175

[26] W. T. Roybal, B. E. Carlsten and P. J. Tallerico, "Dynamics of Retrograde Electrons Returning From the Output Cavity in Klystrons," in IEEE Transactions on Electron Devices, vol. 53, no. 8, pp. 1922-1928, Aug. 2006, doi: 10.1109/TED.2006.877367.

[27] I. A. Chernyavskiy, A. N. Vlasov, T. M. Antonsen, S. J. Cooke, B. Levush and K. T. Nguyen, "Simulation of Klystrons With Slow and Reflected Electrons Using Large-Signal Code TESLA," in IEEE Transactions on Electron Devices, vol. 54, no. 6, pp. 1555-1561, June 2007, doi: 10.1109/TED.2007.896697.

[28] Y. Okubo, S. Fujii, K. Suzuki, T. Tanaka, "Status OF high efficiency klystron development in TETD", 9th International Particle Accelerator Conference (IPAC2018), 2018, doi:10.18429/JACoW-IPAC2018-THPAL148

[29] K. Suzuki, T. Tanaka, S. Fujii and Y. Okubo, "High efficiency Klystron design and test result in TETD," 2018 IEEE International Vacuum Electronics Conference (IVEC), 2018, pp. 101-102, doi: 10.1109/IVEC.2018.8391586.

[30] Z. Fang and S. Fukuda, "Instability caused by Backstreaming electrons in a klystron", Proc. 2nd Asian Particle Accelerator Conf. (APAC), 2001.

[31] Z. Fang and S. Fukuda, "Analysis of spurious oscillation in klystron due to backstreaming electrons from collector", Jpn. J. Appl. Phys. 48 116501., 2009.

[32] A. Shabazian, R. Begum and B. C. Stockwell, "Design and development of 5-MW X-band klystron for medical and cargo screening applications," IVEC 2012, 2012, pp. 167-168, doi: 10.1109/IVEC.2012.6262117.

[33] J. Sauza-Bedolla, S. Atieh and N. Catalán Lasheras, "Manufacturing of X-band Accelerating Structures: Metrology Analysis and Process Capability", 29th International Linear Accelerator Conference, Beijing, China, 16 - 21 Sep 2018, pp.TUPO022, doi: 10.18429/JACoW-LINAC2018-TUPO022

[34] P. Hamel, J. Plouin, C. Marchand and F. Peauger, "Klystron efficiency optimization based on a genetic algorithm," 2019 International Vacuum Electronics Conference (IVEC), 2019, pp. 1-2, doi: 10.1109/IVEC.2019.8745162.

[35] A. Jensen, R. Ives, Jeffrey Neilson, J. Petillo and M. Read, "Single Objective Genetic Optimization of an 85% Efficient Klystron", Proceedings, 13th International Computational Accelerator Physics Conference, ICAP2018 : Key West, FL, USA, 20-24 October 2018, doi: 10.18429/JACoW-ICAP2018-SAPAF04

Chapter 5

Diagnostics for accelerating cavities

5.1 Introduction

The performance of accelerating cavities is characterized by their ability to provide large accelerating fields with small RF losses. Those performance (E_{acc} and Q_0) are deduced from the RF power measurements at the input (forward and reflected) and output (transmitted) antenna of the cavity, generally achieved with bolometers. In the previous chapters, we have seen that many phenomena could be cause or consequence of the performance degradation: ambient magnetic field, cavity surface defects, vacuum degradation, cavity surface heating, cavity quench, field emission... Detecting and measuring these phenomena is essential for improving performance but also for developing the fine understanding of the involved physical phenomena.

Many efforts have been carried out in all laboratories to develop diagnostics in cryostats dedicated to cavity testing, and in cryomodules. In this chapter I will describe some investigations to which I have directly contributed at CEA (sections 5.2 and 5.3), or which have been carried out by colleagues from my laboratory (section 5.4. I will then conclude on the further developments.

5.2 Quench detection

The work described in this section has been presented in a conference [Plo+13] and developed in a publication in the Physical Review for Accelerators and Beams [Plo+19b], given in annex of this chapter, and I will only give a short summary hereafter.

When the RF field is increased in a superconducting cavity, the presence of some defect on the cavity surface is likely to generate a local RF dissipation, responsible for a local heating. When the temperature increase becomes locally higher than the transition temperature, the niobium turns to normal conducting in this area. Consequently, the RF dissipation in this normal conducting area leads to a huge temperature increase, and the whole cavity becomes normal conducting. This phenomenon, known as thermal quench, is a limitation to the cavity performance. When such phenomena is detected during a cavity test, it can be necessary to spatially localize its origin, in order to cure the local defect and prevent future quenches.

A new technique was developed in the 2010 years for quench localization on cavities working in superfluid helium bath (temperature lower than 2.17 K). This technique is based on the detection of the second sound wave generated by heat generation in superfluid helium by dedicated sensors named Oscillating Superleak Transducers (OSTs). The time of arrival of the second sound wave on a set of sensors dispatched around the cavity is measured; the distance between sensors and quench location is estimated, leading to quench localization by triangu-

lation. However, many laboratories have observed a discrepancy between the expected and measured times of arrival, looking like a "too fast" second sound signal. We have carried on a set on experiments to participate to the phenomenon analysis.

We have collaborated with colleagues from the Cornell Laboratory for Accelerator-based Sciences and Education (CLASSE)[Con+08], who provided us a set of second sound sensors (Oscillating Superleak Tranducers, OSTs) to develop our own detection setup. We have also successively received two CERN fellows, Kitty Liao and Benedikt Peters, who participated to our experiments. Both were working on similar setups at CERN. Moreover, the study of superfluid helium properties was carried out in collaboration with the *Cryogenics Laboratory and Test Stations* (LCSE) of the DACM.

We have carried out two kind of experiments, where the "too fast" second sound signal was investigated:

- ⋆ generation and detection of a heat wave by a dedicated heater with variation of the power level and the duration of the heat pulse (see the experimental setup in Figure 5.1, left),
- ⋆ quench detection during five different RF tests of monocell cavities, with variation of the helium bath temperature during one of the tests (see the experimental setup in Figure 5.1, center).

Moreover, the heat wave propagation in the niobium and in the helium bath were modeled (see the Figure 5.1, right) and compared to measurements.

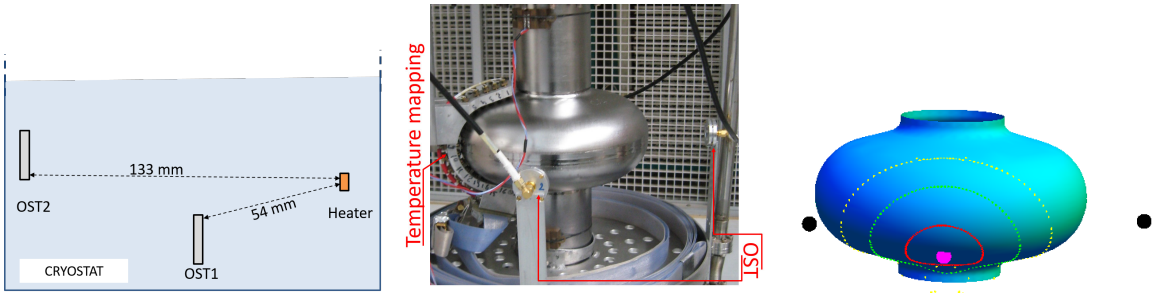

Figure 5.1: Left: experimental setup with a heater. Center: picture of the monocell cavity with OSTs. Right: representation of the heat propagation on a cavity surface. The pink dot represent the quench locations and the black dots represent the OSTs.

We have concluded that while a fast signal propagation in helium seemed very unlikely, the processes in the niobium were likely to induce the described effect. It was then assumed that the quench propagation on the inner cavity wall and the thermal diffusion in the niobium were the main cause of the "too fast" second sound signal, in the case of quenching cavities.

5.3 Magnetic field sensors

In order to achieve high performance for superconducting cavities it is necessary to control their magnetic environment during operation. The considered magnetic fields are in the order of the ambient field (50 μT) in the absence of magnetic shielding, and can be lower than one microtesla inside a magnetic shield. The measurement of such field level is commonly achieved with fluxgate sensors consisting of two coils winded around a soft magnetic core. The drive winding generates a periodical signal and the core is alternately saturated in both directions. In presence of an external field, this process becomes asymmetrical, and the resulting field and the current induced in the sensing coil are out of phase with the drive current. From the comparison between input and output currents, an electronic device calculates the external

magnetic field. Such sensors are developed by companies, and commercial solutions dedicated to cryogenic temperature have been developed by the Bartington company. These sensors work well, but they are very expensive ($\sim$ 1500 € per sensor), each sensor corresponding to a single field component.

The development of field monitoring devices in test cryostats or cryomodules, involving a large number of sensors, requires cheaper solutions. In parallel with other laboratories, we have developed AMR sensors, based on the anisotropic magnetoresistance (AMR) of a ferromagnetic material at their core. They are much cheaper than commercial fluxgates (less than 10 € per sensor) which could allow the use of tens of sensors simultaneously. Such sensors are developed and sold for room temperature application but are also resistant to cryogenic temperatures.

Their use needs a calibration step to get their sensitivity S, which is the relationship between the voltage variation ΔV measured by the sensor and the magnetic field H_{ext}, normalized by the sensor supply voltage V_{cc} and which varies with temperature. An offset value, allowing absolute determination of the magnetic field, must also be obtained.

$$S = \frac{\Delta V}{V_{cc}} \frac{1}{H_{ext}} \tag{5.1}$$

We have developed a calibration procedure detailed in [PCM21]. At room temperature, this procedure has been tested with good results and repeatability: for each sensor the sensitivity varies less than 1 % and the offset varies less than 2 %. However, at cryogenic temperature the sensitivity and offsets repeatability from one calibration procedure to the other is much more difficult to obtain, which is probably due to the increase of the permalloy's coercive field [BD02]. While we finally obtained a repeatability around 2-3 % for the sensitivity, we could not achieve an acceptable repeatability for the offsets. Consequently these sensors do not allow for the determination of an absolute value at 4 K. This has been observed by other labs, in particular at KEK (Japan) [Oa19]. A least, such sensors allow for the measurement of magnetic field variation observed during field expulsion. Our sensitivity measurements, plotted in Figure 5.2 are in good agreement with other laboratories.

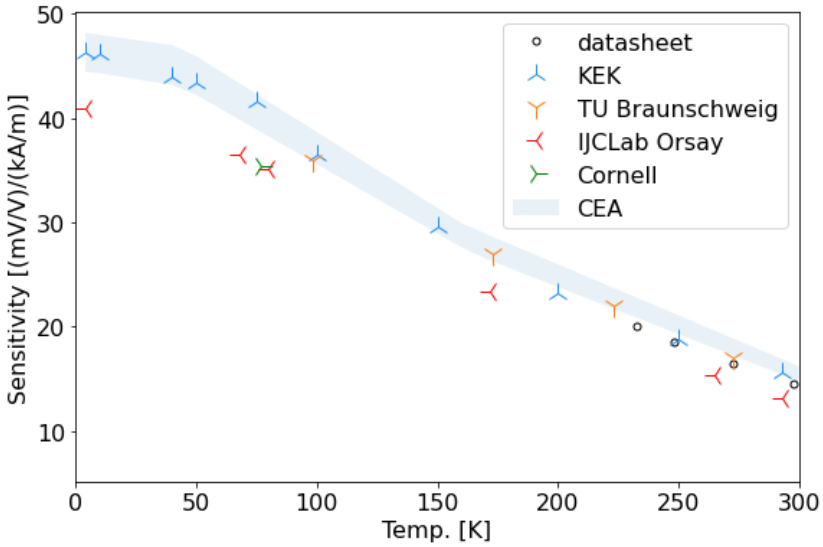

Figure 5.2: AMR sensors sensitivities versus temperature measured at CEA and comparison with KEK [Uek+20][Oa19], TU Braunschweig [Na17], IJCLab Orsay[Ma19], Cornell[La19].

Since each sensor only measures one component, we have developed a *triplet* configuration with three sensors and we are developing a rotating frame with diagnostics destined to mono-cell elliptical cavities. We have reshaped the three sensors configuration to this purpose (see Figure 5.3), to allow the implementation of nine sets of three sensors along a cavity profile. Our

aim is develop a diagnostic tool for measuring magnetic field, X-rays and temperature. This will be discussed in section 5.5.

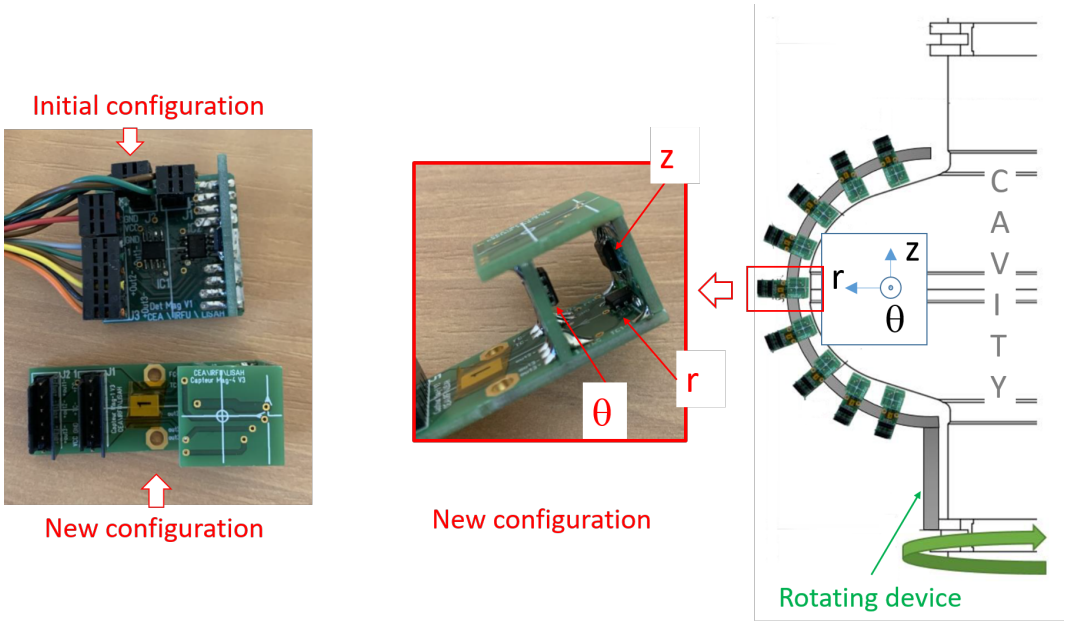

Figure 5.3: Set of three sensors, initial and old configuration (left), rotating frame with 9 sets (right).

This work has been developed under my supervision by three successive students graduating for technician level and by one student graduating for Master 2.

5.4 X-ray detection for field emission

An important limitation of the cavity performance arises from the emission of electrons from high electric field regions. The RF power is absorbed by the electrons and is deposited on the inner part of the cavity. At high electric fields, thermal breakdown can be initiated. Field emission is associated to local temperature increase and to X-ray generation, due to the bremstrahlung of the emitted electrons when they hit the cavity walls. The presence of dust particles on the cavity surface is a common source of contamination leading to field emission during cavity operation. As mentionned in chapter 2, the field emission was identified as the first cause of cavity failure leading to cavity reprocessing in ESS [WAB23]. Hence, it is essential to better understand what causes this phenomenon, how it evolves according to cavity preparation, and how it can be cured [Cen+21][Dev+23][Del+23][Ome+23][PGB23].

Some colleagues from my laboratory have developed X-ray detectors associated to the testing of ESS cavities and cryomodules at CEA [Dev+23]. First, three types of devices were used: Geiger-Mueller (G-M) probes, NaI(Tl) scintillators and PIN diodes. A simulation model was developed by means of particle tracking code which allowed an estimation of the location of the emitters [Cen+19b] [Dev+23]. Then, they have investigated the use of specific scintillator-based radiation detectors made of plastic fiber, which proved good resistance at cryogenic temperature. A detailed simulation process based on the Geant4 toolkit developed by CERN [Gea] provides a better description of the nature of the phenomenon. Further steps will include the improvement of the simulation model to interpret measurements even with limited number of monitors and to allow for measurement predictions in complex systems. A scintillator-based instrumentation is also in development to measure cavity radiation closer to the source thanks to plastic scintillators working at cryogenic temperature.

5.5 Conclusion

Improving effort on cavity diagnostics is essential for the success of all accelerators projects, with the monitoring and control of all elements from testing to final operation. Examples have been given for the quench and field emission phenomena, and for the magnetic field monitoring. Efforts have been developed in laboratories carrying out series of cavity tests to optimize the quench detection with the second sound method [Ste+19]. As stated in last section, activities are on going in several labs for X-ray detection in cryostats and cryomodules, including the use of new scintillating materials [Dev+23]. Note that X-ray detection is also a useful diagnostics for studying breakdown phenomenon in normalconducting cavities (see section 2.5) [Koc+16]. The magnetic field monitoring is being dramatically increased by the use of cheap sensors based on commercial anistropic magneto resistance, allowing for sensor arrays around cavities, adapted to field expulsion studies [Pen+19][Par+23]. Besides developing such sensors and arrays of sensors, collaboration could be envisaged with research laboratories working of new magnetic field sensor techniques [Boc+16].

In conclusion, besides ensuring successful project realization, developing diagnostics is also an inestimable tool for the development of many R&D activities. We are carrying out numbers of tests on cavities and cryomodules at CEA, and systematic diagnostics will provide a large measurement database available for many phenomena investigation.

ISBN: 978-3-95450-233-2 ISSN: 2673-5504 doi:10.18429/JACoW-SRF2021-TUPCAV009

AMR SENSORS STUDIES AND DEVELOPMENT FOR CAVITIES TESTS MAGNETOMETRY AT CEA

J. Plouin†, E. Cenni, L. Maurice, CEA, Université Paris-Saclay, Gif-sur-Yvette, France

Abstract

Studying flux expulsion during superconducting cavities test increases the need for exhaustive magnetometric cartography. The use of Anistropic Magneto Resistance (AMR) sensors, much cheaper than commercial fluxgates, allows the use of tens of sensors simultaneously. Such sensors are developed and sold for room temperature application but are resistant to cryogenic temperatures. However, they need proper calibration, which is more difficult at cryogenic temperature. Actually, this calibration uses the flip of the magnetization of the anisotropic ferromagnetic element, which coercitive field is increased at low temperature. We will present the development of method and software carried out at CEA for the use of such sensors, as well as the preliminary design of a rotating magnetometric device destined to elliptical cavities.

AMR SENSORS CHARACTERIZATION

In order to achieve high performances for superconducting cavities it is necessary to control their material behavior and their environment during operation. In our laboratory we are currently designing a suite of detectors that will focus on superconducting cavities diagnostic during their test in liquid helium bath.

The magnetic field, even if lower than the earth magnetic field, increases the Joule losses, thus it is important to control it. We are currently developing detectors able to map the magnetic field around the cavity at cryogenic temperature. The sensors are AFF755 from Sensitec. They exploit the anisotropic magnetoresistance (AMR) of a ferromagnetic material at their core. They are much cheaper than the current standard for this kind of measures (Fluxgate) and should enable to equip a cavity cryostat or even a cryomodule with more detectors.

However, they need a calibration step to get their sensitivity, which is the relationship between the voltage measured by the sensor and the magnetic field, and which varies with temperature. Our calibration procedure uses two specific coils already implemented in the sensors: the flip coil, which magnetizes the ferromagnetic material, made of permalloy, and the test coil, which generates a controlled magnetic field. This calibration can be achieved in situ, when the sensors are placed inside a cryostat, and in an unknown magnetic field.

We defined a calibration procedure that allows calibration even in an unknown ambient magnetic field. The first step is to characterize the test coil (TC) for each sensor by the relationship between the coil current and the coil generated magnetic field. To this intend, the sensor response to the test coil is compared to the sensor response to a reference Helmholtz coil and the α coefficient is deduced:

$$B_{TC} = \alpha I_{TC}$$

We have verified that α does not change at cold temperatures. Actually the only effect of the temperature change on the coil is thermal shrinkage, which is very small.

The second step is to apply a set of TC field after a positive flip coil $B_{TC}(Flip_+)$ and after a negative flip coil $B_{TC}(Flip\_)$, and to measure the corresponding voltages $U(Flip_+)$ and $U(Flip\_)$.

We get two curves with B_{TC} vs U, one for Flip+ and one for Flip-,

$$B_{TC}(Flip_+) = a_1 U(Flip_+) + B_1$$

$$B_{TC}(Flip\_) = a_2 U(Flip\_) + B_2$$

From which we extract a_1, a_2, B_1 and B_2.

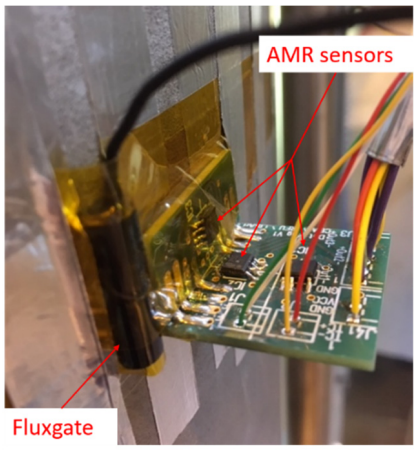

Figure 1: Set of three AMR sensors (X, Y and Z) and fluxgate installed on a cavity.

The slopes, a_1 and a_2, are opposite to each other. The offsets B_1 and B_2 contain both the electrical offset of the sensor and the ambient magnetic field, which are unknown. In order to get rid of the ambient field, we calculate the electrical offset, which is supposed to be the same for both flips:

$$B_{OFF} = \frac{B_{Flip-} + B_{Flip+}}{2} = \frac{B_1 + B_2}{2}$$

And then the real magnetic field:

$$B = a_2 U + B_2 - B_{OFF} = a_2 U + \frac{B_2 - B_1}{2}$$

† juliette.plouin@cea.fr

Content from this work may be used under the terms of the CC BY 4.0 licence (© 2022). Any distribution of this work must maintain attribution to the author(s), title of the work, publisher, and DOI

ISBN: 978-3-95450-233-2 ISSN: 2673-5504 doi:10.18429/JACoW-SRF2021-TUPCAV009

Content from this work may be used under the terms of the CC BY 4.0 licence (© 2022). Any distribution of this work must maintain attribution to the author(s), title of the work, publisher, and DOI

This procedure was tested at room temperature with good results and reproducibility (the sensitivity of one sensor varies less than 5 %). We used a flip current value equal to 200 mA.

A set of three sensors was placed on a cavity, besides a fluxgate (Fig. 1) and their sensitivity was measured during cavity cool down. The results are shown in Fig. 2 where our results are also compared with other labs [1-5]. The sensitivity is increased at low temperature. This is due to the permalloy's remnant field decrease, shown on the hysteresis curve in Fig. 3.

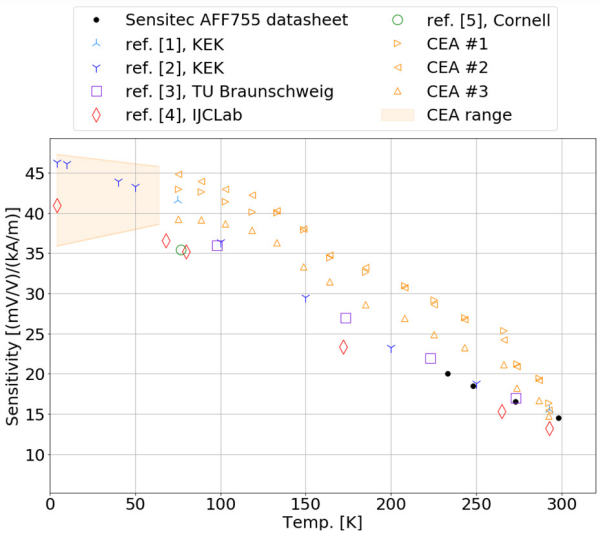

Figure 2: AMR sensors sensitivities versus temperature. CEA measurements for three sensors. For T < 60 K, only a result range is shown.

It appeared that the sensitivity reproducibility is much degraded for temperature lower than 60 K, thus only a range of results (in orange) is shown. This is probably due to the increase of the permalloy's coercive field (Figure 3). The level of flip magnetic field necessary to properly re-magnetize the permalloy material should also be increased. During this set of experiment, we could increase the flip current up to 380 mA but it was not enough to get a satisfying reproducibility. Moreover, the offset measurements, necessary for the calibration and not shown on the figure, were even less reproducible. For those reasons, it was not possible to measure the magnetic field under 60 K.

In a next set of measurements we plan to apply flip current values higher than 380 mA and observe if we can get some reproducible values.

The difficulty of measuring an accurate value for the magnetic field at 4 K is also mentioned in reference [2] from KEK, where they explain that their offset value is not reproducible after initialization. Up to now they consider using their sensors to measure relative change of the magnetic field distribution.

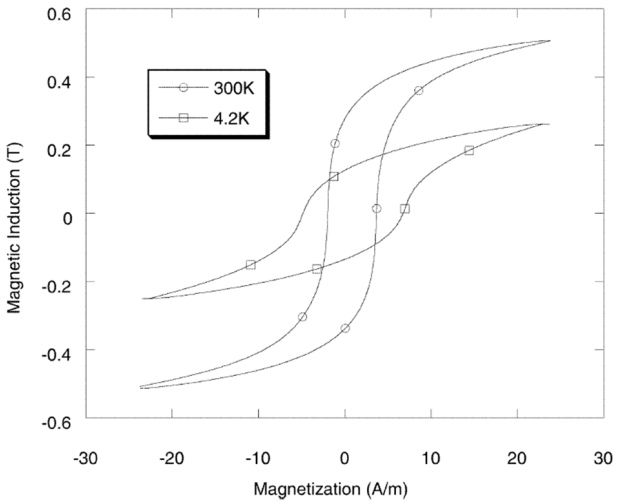

Figure 3: Mumetal torus magnetization as a function of applied field at two different temperatures [6].

MAGNETOMETRIC DEVICE

In the meantime, we are developing a rotating frame with diagnostics destined to mono cell elliptical cavities. It will support temperature, X-rays and magnetic sensors.

We have reshaped the 3 sensors (X, Y and Z) configurations to this purpose. In the new configuration, two of the three sensors (r and z) are positioned so that their distance to the cavity is 1-2 mm, allowing good detection of the flux expulsion (Fig. 4). Moreover, the size of the configuration is decreased. This allows the implementation of nine sets of three sensors along a cavity profile.

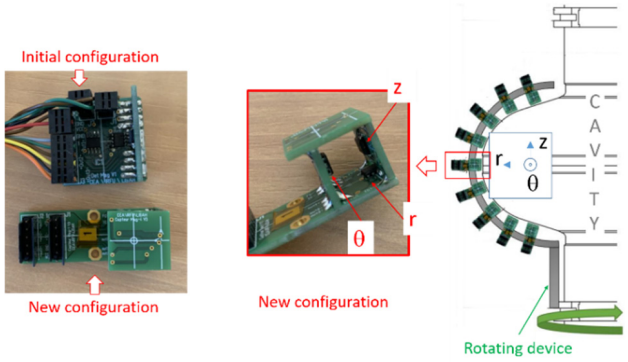

Figure 4: Set of three sensors, initial and old configuration (left), rotating frame with 9 sets (right).

The calibration and data acquisition procedure was implemented on an acquisition device (National Instrument) with the Labview software.

The electronic card allowing the operation of 27 magnetic sensors is ready (Fig. 5). It includes the flip coil generation, the sensor output amplification (x100) and decoders driven by the acquisition device.

The rotating support frame for the sensors is under development.

ISBN: 978-3-95450-233-2 ISSN: 2673-5504 doi:10.18429/JACoW-SRF2021-TUPCAV009

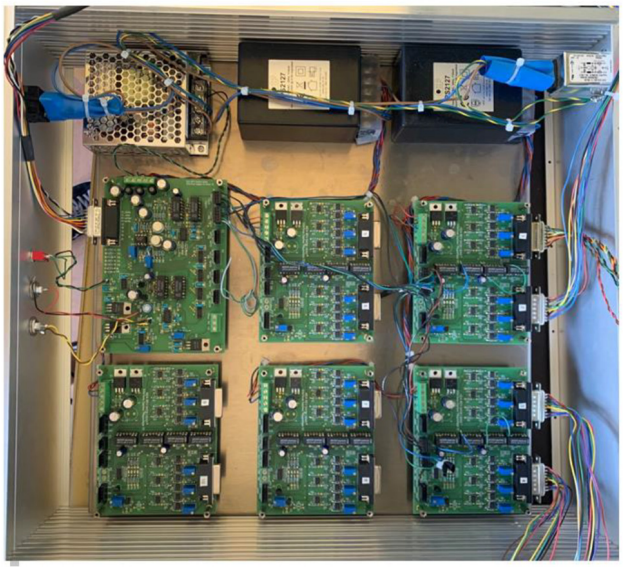

Figure 5: Electronic card for the 27 sensors.

CONCLUSION

We have developed and tested magnetic sensors based on AMR resistance destined to superconducting cavities magnetometry at 4 K. The reliability of these sensors at 4 K is still to be improved, and a rotating support frame is to be developed.

ACKNOWLEDGEMENTS

This work has been developed with the help of the following students: M. Maurice, M. Dekin, M. Deeloshan and H. Cara.

REFERENCES

[1] R. Ueki *et al.*, "Study on Magneto-Resistance Sensors for Low Magnetic Field Measurements", in *IEEE Trans. Appl. Supercond.*, vol. 30, no. 4, June 2020. doi: 10.1109/TASC.2020.2976994.

[2] T. Okada *et al.*, "Development of Temperature and Magnetic Field Mapping System for Superconducting Cavities at KEK", in *Proc. SRF'19*, Dresden, Germany, Jun.-Jul. 2019, pp. 583-585. doi:10.18429/JACoW-SRF2019-TUP060

[3] F. Nording *et al.*, "Temperature dependence of AMR and GMR sensor properties", in *Proceedings of the 14th Symposium on Magnetoresistive Sensors and Magnetic Systems*, pp. 85-92, 2017.

[4] G. Martinet, "Characterization of Small AMR Sensors in Liquid Helium to Measure Residual Magnetic Field on Superconducting Samples", in Proc. 19th Int. Conf. RF Superconductivity (SRF'19), Dresden, Germany, Jun.-Jul. 2019, pp. 576-579. doi:10.18429/JACoW-SRF2019-TUP058

[5] S. Lobo *et al.*, "Magnetic Field Mapping System for Cornell Sample Host Cavity", in Proc. 19th Int. Conf. RF Superconductivity (SRF'19), Dresden, Germany, Jun.-Jul. 2019, pp. 961-963. doi:10.18429/JACoW-SRF2019-THP046

[6] C. Berriaud and A. Donati. "Adevice for measuring high current at cryogenic temperatures", *IEEE Trans. Appl. Supercond.*, vol. 12, no. 1, 1264-1268, 2002. http://dx.doi.org/10.1109/TASC.2002.1018632

Content from this work may be used under the terms of the CC BY 4.0 licence (© 2022). Any distribution of this work must maintain attribution to the author(s), title of the work, publisher, and DOI

Experimental study of second sound quench detection for superconducting cavities

J. Plouin,* B. Baudouy, A. Four, J.P. Charrier, L. Maurice, and J. Novo
CEA Paris-Saclay, Université Paris-Saclay, Gif-sur-Yvette, France

B. J. Peters
Karlsruher Institut fur Technologie Postfach 3640 76021 Karlsruhe, Germany

K. Liao
Imperial College London and Ideabatic LTD, SW7 2AZ,
32 Lingrey Court, Cambridge, 10 CB2 9JA, United Kingdom
(Dated: Received 28 February 2019; published 26 August 2019)

Superconducting RF cavities are used in particle accelerators to provide energy to the particle beam. Such cavities are mostly fabricated in niobium and often operated in superfluid helium. One of their limits of operation is the appearance of a local quench, initiated by a local field enhancement due to a defect, which leads to a normal conducting transition of the cavity. Localizing the quench area can be achieved with temperature mapping systems. Another method is the use of second sound wave propagation in superfluid helium. Measuring the time of propagation of these waves from quench location to special sensors, called Oscillating Superleak Transducers (OSTs), and using their well-known velocity should allow trilateration. However, most of experimental measurements on cavities show "premature signals", i.e. the second sound signals arrive earlier on the OSTs than expected. This paper presents several quench experiments on cavities equipped with OSTs and temperature mapping quench detection systems. Two hypotheses can explain the observed premature signals. The first one assesses faster propagation in helium. An experimental setup has been developed for testing this hypothesis, where second sound is created by a localized heater in a controlled environment up to 4.3 kW/cm^2 and 2.8 J. Premature signals could not be verified in this setup. A second hypothesis based on a simple model including several processes in niobium and second sound propagation in helium is discussed. The model improves significantly the prediction of the times of arrival of the second sound waves. The overall study shows that the processes in niobium play a prominent role in the second sound detection for superconducting cavities.

Keywords: Superconducting cavity, Quench, Superfluid helium, Second sound

Published in Physical Review Accelerators and Beams 22, 083202 (2019)
doi: 10.1103/PhysRevAccelBeams.22.083202

arXiv:2404.06377v1 [physics.acc-ph] 9 Apr 2024

I. INTRODUCTION

Radio-frequency cavities are state of the art technology in high energy particle accelerators to increase the momentum of charged particles. The resonating electromagnetic field causes coulomb heating on the inner surfaces of these cavities. Normal-conducting cavities are usually made of copper. The generated heat can be greatly deceased by using a superconducting cavity in the Meissner state. The element with the highest lower critical field is niobium, which is thus mostly used for this purpose [1]. To generate high accelerating gradients, the cavities are operated close to their operational limit. A number of different processes are known to limit the operation of superconducting cavities [1]. The limiting process that normally occurs for very well performing cavities is the localized quench where a local increase of the electromagnetic field due to a defect drives a local area to normal-conducting transition, and due to the increased heating to the global normal-conducting state [2]. Even small imperfections on the inner cavity surface can cause this quench. These spots can be treated once their locations are detected. A number of methods has been applied for this [3, 4].

Since the 1980's temperature sensors are used to detect the temperature increase on the outer cavity surface [5]. These temperature mapping systems are based on temperature-dependent carbon sensors, mostly Allen-Bradley resistors [6]. In addition to being sensitive for temperature measurements in both normal (He I) and superfluid (He II) helium, their geometry can be customized to match the topology of the superconducting cavity. Some tests were made with temperature sensors that were glued to the cavities surface, but mechanical systems that press the sensor to the cavity surface are more common. The glued sensors are normally not reusable and a high number of sensors are presented and thus read-out systems are needed. The mechanical systems require custom-fit frame for each cavity geometry, but for elliptical cavities they can be mounted on a rotating frame, that allows moving them around the cavity

* juliette.plouin@cea.fr

in order to locate the quench spot. Another method for the detection is the utilization of the special heat transport properties in He II. In superfluid helium, heat is transported as a wave, called second sound. This wave travels with a known, temperature-dependent velocity. If at least three sensors, capable of detecting second sound with precise time information and known positions relative to the cavity were mounted, trilateration of the quench spot is possible. Conway et al. introduced this method and utilized oscillating superleak transducers (OSTs) for the detection of second sound waves [7].

For the last ten years, quench localization with 2nd sound detection has been developed in several labs. It was found that this method is cheaper and easier to implement than temperature mapping systems; however, nearly all these laboratories have observed the same kind of premature signals: the second sound signal arrives on the OSTs earlier than expected [8–13]. Efforts have been pursued to explain these premature signals and hypothesis have been envisaged. Eichhorn et al. [14] have supposed that the second sound wave could be generated before the RF system can detect the quench; they have developed a corresponding model, which could explain some tens of µs error, much lower than experimentally observed. Liu [15] and Eichhorn [16] have considered the heat diffusion in niobium, in addition to the second sound propagation, which could cause premature signals, but their models have not been systematically compared to experimental results. The possibility of other effects beside second sound propagation in He II has also been considered, and experiments have been carried out with local heaters as a source for the heat propagation. Liao et al. [17] have generated heat flux up to 200 W/cm^2, and did not observe premature signal, while Junginger et al. [12], with heat flux up to 350 W/cm^2 observed 10% faster signals in particular conditions. Very recently, a new technique using flow visualization in superfluid helium has been proposed by Bao et al. to detect quench-spot in RF cavities [18]. A prof-of-concept experiment with a miniature heater is presented for heat flows below 300 W/m^2. A ideal boiling zone model is proposed to explain the premature signal on the data obtained by [12] and [13], but no test with a RF cavity has been performed yet.

Up to now, none of these hypothesis and associated models could properly describe premature signals measured during cavity tests.

The present paper is a contribution to these efforts. We performed five tests on two single-cell superconducting cavities, with variation of the helium bath temperature for one of them, and always observed premature signals. In order to study the pure heat propagation in He II, we carried out experiments with a localized heater as a source for the second sound wave. We reached values of surface power (4.3 kW/cm^2) and global energy (2.8 J) that were never achieved in similar experiments, for these experiments no premature signal was observed.

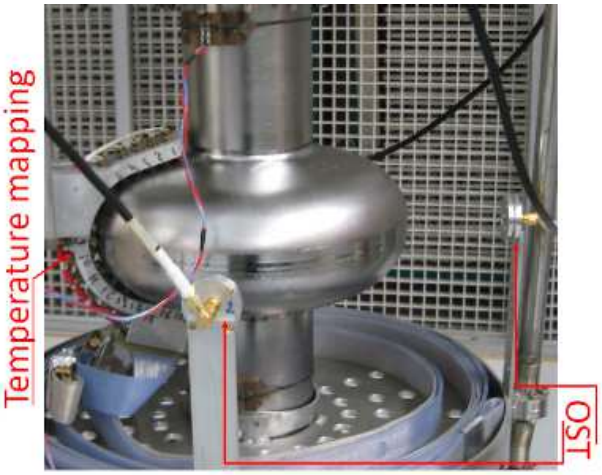

FIG. 1. 1.3 GHz single-cell cavity equipped with temperature mapping system and OSTs.

II. TESTS ON CAVITIES

A. Setup and cavities test description

At CEA Paris-Saclay, superconducting cavities are usually tested in superfluid helium in a dedicated vertical cryostat on the Supratech platform [19, 20]. For several single-cell cavities such tests could be realized with second sound sensors for quench localization. During those tests, each cavity was equipped with a temperature mapping system, and with four OSTs facing the cavity in the equator plane, placed at around 6.5 cm from the cavity. All these elements can be seen in Figure 1. Two Tesla shape single-cell cavities, C1-21 [21, 22] and 1AC3 [23] have undergone these tests; they will be named respectively A and B. These cavities have the same elliptical geometry, and thus identical RF parameters: frequency f = 1.3 GHz, shunt impedance r/Q = 104 Ωand geometrical factor G = 283 Ω. They were supplied by two different manufacturers, from niobium plates with RRR values between 250 and 300, and both of them have undergone several chemical and electropolishing treatments.

Five tests where localized quench was reached without electron emission could be realized: two tests with Cavity A and three tests with Cavity B. The Q_0 vs. E_{acc} curves are shown in Figure 2, Q_0 being the cavity quality factor and E_{acc} the accelerating field. The accelerating field is increased by injecting RF power in the cavity, until the cavity quenches, which means that the injected power is entirely reflected. The quench appearance is indicated by a vertical arrow for each test, which thus determines the maximum accelerating field allowed in the cavity (E_{max}). The test results are summarized in Table I. The differences in the Q_0/E_{acc} curve for Cavity B from one test to the another is due to the intermediate chemical/electropolishing treatments. The helium bath temperature was about 1.5 K for Cavity A and about

TABLE I. Cavity tests summary

	Cavity name	E_{max}
test 1	A	30 MV/m
test 2	A	31 MV/m
test 3	B	34 MV/m
test 4	B	35 MV/m
test 5	B	37 MV/m

1.6 K for Cavity B.

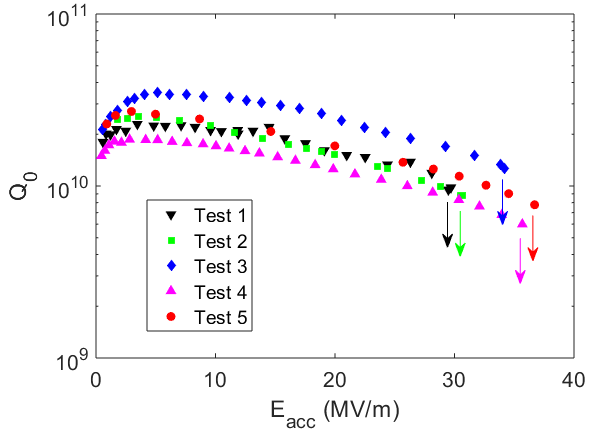

FIG. 2. Q_0/E_{acc} curves of the tested single-cell cavities. Vertical arrows show quench appearance

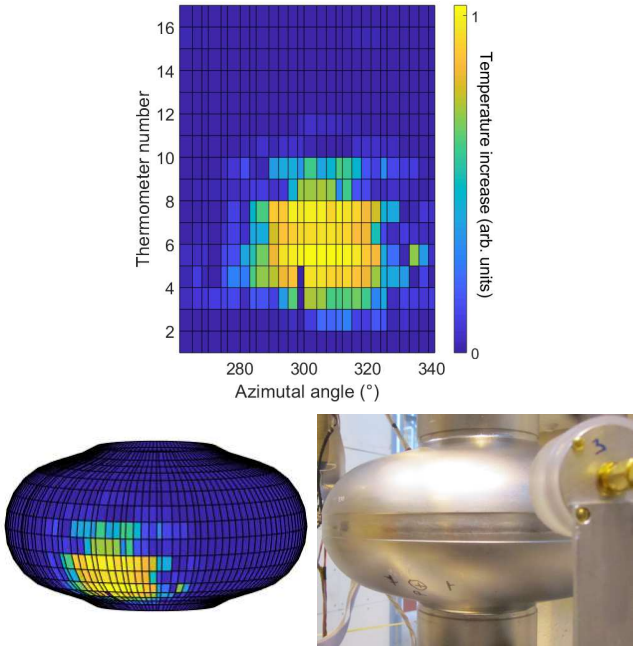

FIG. 3. Top: Thermal cartography of Cavity B during a test. Azimuthal angle gives the temperature mapping position around the cavity; thermometer number can be read in Figure 1. Bottom: Cartography projection on cavity surface (left) and identification of the quench spot on the cavity marked by $\oplus$ symbol (right).

B. Quench localization with temperature mapping system

Initially the quench position was localized by the temperature mapping system, in order to have a reference for comparison with the OSTs measurements. This system consists of 17 thermometers fixed on a structure able to rotate around the cavity axis [35]. Each thermometer is constituted of a carbon resistor placed inside a copper support which is in contact with the cavity surface. The aim of this measurement is to observe the temperature elevation when the quench occurs. The system works as follows: at each azimuthal position, the 17 thermometers are successively monitored. The duration of a single readout is long compared to the quench dynamics, so the following method is used: the sequence is repeated about twenty times while the cavity is forced to quench. For each thermometer the maximum value of this series of measurements is used, because it corresponds to the closest in time to the quench occurrence. As an example the temperature array is shown in Figure 3 around the quench location (top), and is projected on the cavity surface (bottom). The resolution is about 3 degrees in latitude and 1 cm in longitude (distance between two sensors).

This temperature mapping system is used to produce a map showing the measured temperature with respect to the bath. As the mapping system itself is immersed in the bath, the temperature given by the carbon resistors is different from the surface cavity temperature. A temperature difference equal to zero means that locally the cavity surface is at the helium bath temperature. This temperature mapping system is efficient to achieve a localization within a precision of a less than one centimeter in each direction. According to the temperature maps, the quench location of Cavity A always lands at the equator and that of Cavity B at the bottom half of the cavity (see Figure 3).

C. OST measurements at 1.7 K

An Oscillating Superleak Transducer (OST) is a sensitive sensor to detect second sound. The idea for this device originated in 1968 [24]. It consists of a capacitor like setup with one flexible membrane and a solid back electrode. The membrane is flexible and has nanometer-sized pores. For the shown measurements a metal-coated membrane with holes of about 100 nm were used. According to the two-fluid theory the superfluid component of the helium can pass through these holes while the normal fluid component cannot [25]. Thus, the arrival of a second sound wave, that has different amounts of the two components in comparison to the helium between the

two plates [25], applies a pressure on the flexible membrane, decreasing the distance between the two membrane plates. The two sides are charged with 120 V via a weakly coupled connection. For fast processes, such as a second sound arrival, the charge on the OST stays nearly constant. A decrease of the distance of the capacitor plates thus causes a drop in voltage of the membrane [26]. Each OST has its own electronic circuit which provides the polarization and amplification of the signal. For all the measurements presented in this paper, the same set of OSTs, with diameter 20 mm, was used. This set was provided by Cornell University [27].

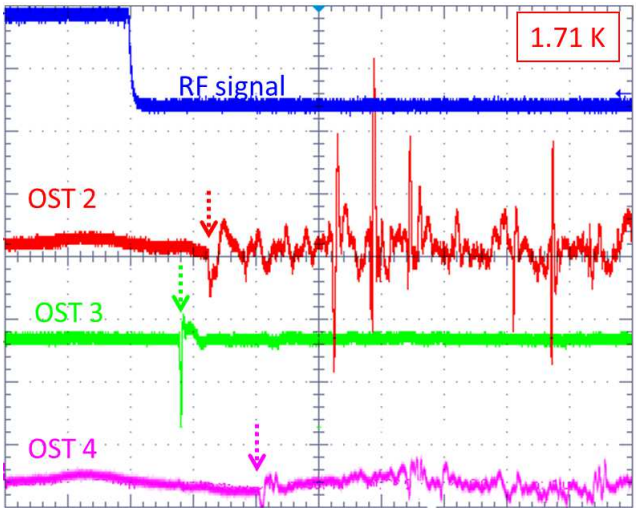

FIG. 4. Oscilloscope signals from OSTs during cavity quench. Vertical arrows show 2nd sound wave arrival on OST.

For each test, the signals from OSTs during a series of quenches were measured. The results were recorded by an oscilloscope that was triggered by the reflected RF power from the cavity, indicating a quench. A typical oscilloscope signal is shown in Figure 4. The blue curve shows the RF signal. As explained previously, the signals from OSTs always start with a sharp negative decrease. The times of arrival of the wave on each OST after quench trigger can be measured with a precision better than 100 µs, and are indicated by vertical arrows on the figure. The OSTs are ordered by their distance from the quench spot, starting with the 1st OST as the closest. During each test, the two nearest OSTs (see Figure 4) were nearly facing the quench location, and they presented a clear signal while the two others were hidden by the cavity. The signal of the furthest one was not detectable and is not shown on the figure.

The times of arrival of the second sound signal on the two nearest OSTs are represented in Figure 5 together with the corresponding times of arrival for the following hypothesis: a pure second sound wave is emitted by a point-like heat source situated at the quench location. These times are thus equal to the distance between OST and quench location (given by temperature mapping system) divided by 20 m/s, which is the second sound velocity at 1.7 K [28]. In the following, we will refer to this calculation approach as the "direct line of sight".

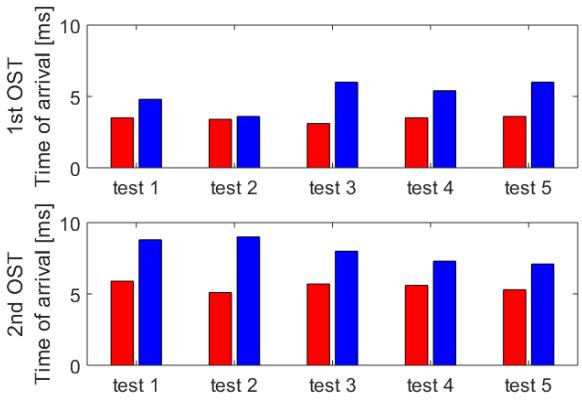

FIG. 5. Times of arrival of the 2nd sound signal on the two closest OSTs from the quench location at 1.7 K: as measured during experiment (Red) and as calculated with in direct line of sight (Blue).

The difference between measured and calculated times of arrival shows that it is not possible to consider the quench as a punctual emission of a 2nd sound wave: the heat wave reaches the OSTs faster than expected by the direct line of sight propagation.

Such premature signals have been experimentally observed by nearly all the laboratories which have used second sound sensors to localize a quench in a superconducting cavity [8, 10, 11, 14, 15]. Different hypothesis have been envisaged to explain this difference, and will be discussed later in this paper.

D. OST Measurements with varying helium temperature

During test 4 on cavity B, the helium bath temperature was varied while measuring the evolution of the OST signals during cavity quenches. The scope signals are shown on the Figure 6 for four temperature values (1.71 K, 1.9 K, 2.03 K and 2.1 K), and for the three closest OSTs.

The dotted vertical arrows show for each OST the time position taken into account for the arrival of the 2nd sound wave. While this position always stays easily detectable for the 1st OST (the closest to the quench location), one can see that for the other OSTs, the signal becomes less evident to detect with increasing temperature, and is even undetectable at 2.1 K for the 3rd OST.

The experimental results (see Figure 8) show how the time of arrival increases with temperature, which is consistent with the evolution of second sound velocity, decreasing with temperature in the [1.7-2.1 K] range, see Fig.7. For the two closest OSTs, the experimental data

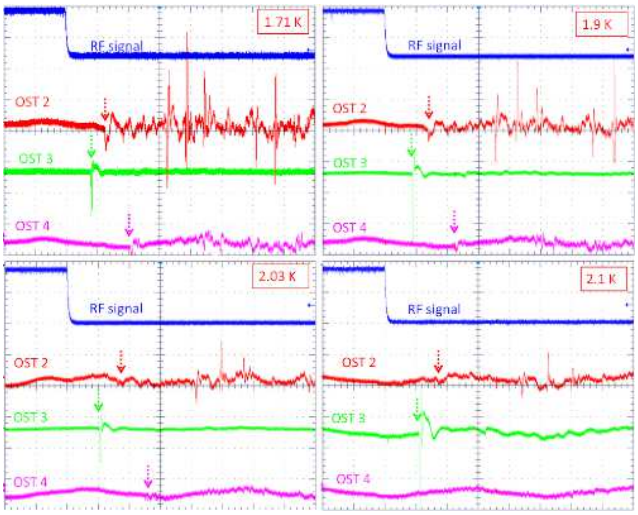

FIG. 6. Oscilloscope signals from OSTs during cavity quench at different temperatures. Horizontal: 4 ms/division. Vertical. RF Signal: 10m V/div; 2nd and 3rd OST : 100 mV/div; 1st OST: 1 V/div. (1.71 K), 500mV/div. (1.9, 2.03 K), 100 mV/div (2.1 K).

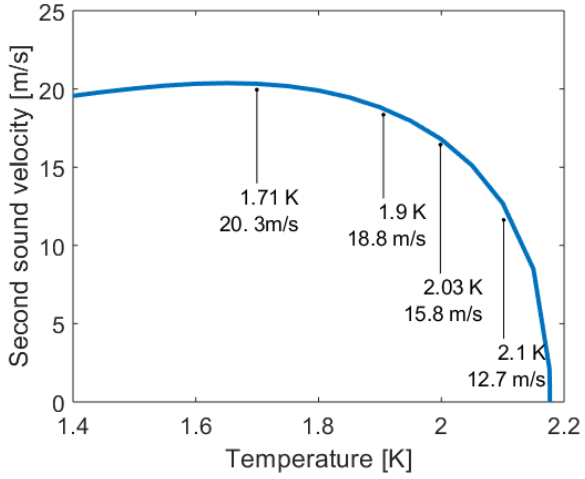

FIG. 7. Recommended values of the second sound velocity at different temperatures and values relevant for presented experiments, according to [28].

are compared to the corresponding times of arrival from the direct line of sight propagation, using the second sound velocity values between 1.7 and 2.1 K [28]. These results show that the experimental data has the same behavior as the model data when temperature is growing. However, in the whole temperature range, the heat wave reaches the OSTs faster than expected by the direct line of sight propagation. The error bars indicated in Figure 8 take into account the uncertainty on the time of arrival measurement (± 0.05 ms, error bars on points) and the uncertainty on the distance measurement between the quench spot on the OSTs (± 2 mm, shaded area on lines).

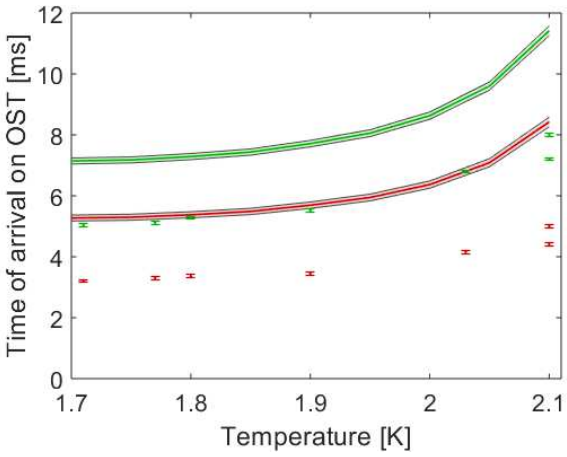

FIG. 8. Time of arrival on first (red) and second (green) OST with varying temperature: experimental data (points with error bars) and calculated data from the direct line of sight propagation (solid line). The shaded area represents the error on calculation due to geometrical measurements uncertainties.

E. Conclusions on OSTs measurement during cavity tests

The first approach considered for the quench localization with OSTs was based on the hypothesis of an instantaneously emitted heat wave by a point like source (the quench location) which travels from this source to the OSTs with the second sound velocity in superfluid helium. This hypothesis is not compatible with the experimental results during cavity quenches in the temperature range [1.7 -2.1 K].

Thus, a quench location was unable to be determined with the standard trilateration method. This is illustrated in Figure 9 for two cases (test 1 and 2) where the problem can be represented in 2D because quench occurs on the equator (and OSTs are in the equator plane). The blue plain circles have radii equal to the time propagation to corresponding OST multiplied by 20 m/s, the second sound velocity at test temperature. The circles do not intersect, showing that the localization is not possible. When the propagation velocity is arbitrarily increased, up to 28 m/s in those cases, it becomes possible to have circles intersection located on cavity equator (dashed circles). However it does not fit with the quench position measured by temperature mapping system, identified by a red region on equator as shown on the Figure 9. This situation becomes even worse if more than two OSTs are used.

To be able to allow more information sources and account for measurement errors, DESY developed an elegant method [11]. They include the information, that the heat spot will lie on the surface of the cavity. From each

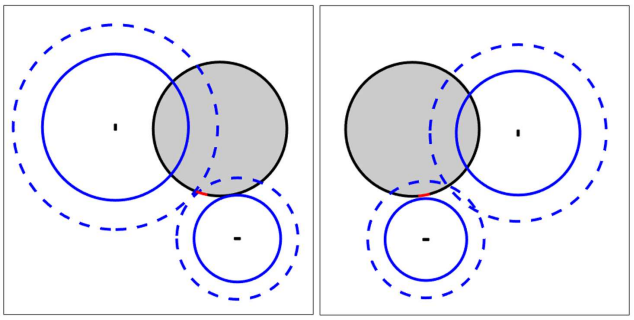

FIG. 9. 2D example of trilateration, for direct line of sight propagation for test 1 (left) and test 2 (right). Cavity is represented seen from above by a grey disk bordered by dark circle corresponding to its equator. Blue plain circles have radii equal to the time propagation for corresponding OST multiplied by 20 m/s. Dashed circles have radii equal to the time propagation for corresponding OST multiplied by 28 m/s. OSTs are represented by small dark rectangles, and quench position detected by temperature mapping system is in red.

surface point they calculate the length of the shortest path in helium to each OST. Together with the second sound velocity and the OST signal they obtain an expected distance the second sound has travelled in helium. The distance between this previous calculated propagation length $s_{z,\phi}$ and expected distance d can be used for every spot on the cavity surface and n-OSTs to determine the root mean square deviation $RSME_{z,\phi}$. The area where this deviation is smallest, can be seen as the area where the second sound was triggered.

$$RMSE_{z,\phi} = \sqrt{\frac{\sum_{i=1}^{n}(s_{z,\phi} - d_i)^2}{n}} \tag{1}$$

This method is used today by DESY to localize the quench position, and comparison with temperature method shows that it works within a few millimeters, if used in the right conditions. In practice, this method helps to localize a small area which can then be examined with some imaging system to find and cure the defect. However, the calculation results given by this method still lead to premature signals.

Discarding the first hypothesis of pure second sound direct line of sight propagation, two new hypothesis can then been envisaged:

- Considering another phenomena in helium making the overall thermal signal traveling faster than a pure second sound wave

- Considering a part of thermal signal diffusing in niobium making the overall thermal signal traveling faster than a pure second sound wave

III. PROPAGATION IN HELIUM

In this section the validity of the first hypothesis is explored.

A. Tests with a localized heater in liquid helium

A number of ideas where brought forward to explain that the information of the heat input into helium II could be transported faster than the second sound velocity. Temperley theoretically predicted a faster propagation for high heat inputs [29]. The theory was refined by Khalatnikov [30] and later experimentally proven by Dessler and Fairbank [31]. Additionally the appearance of boiling effects could also lead to a faster thermal transport. Either by the emission of a first sound wave, which is approximately ten times faster than second sound at the temperatures in question [28], or by effects concerning the gas bubble itself. Although the signals in the cavity tests arrive too late to be seen as pure first sound waves, an unproven theory by Dessler predicted an interaction between first and second sound, which could explain a faster arrival of a second sound wave [32]. The expansion of a gas bubble at the heating spot could also be faster than the second sound.

Since the premature signals were observed experimentally, an attempt was made to replicate them in a controlled environment. In order to exclude effects by the cavity itself, the heating was carried out by a small heater, whose output power and energy are regulated.

B. Heat pulse generation

The heat pulses are generated with a 50 ΩRuO_2-ZnO thick film resistor by the company Bourns, which is specified to accept up to 40 W in DC at room temperature. In the following it was used at cryogenic temperatures for pulsed heat loads of more than 1 kW. This resistor has a surface of 34 mm^2. The pulses are generated by a synthesizer at 200 MHz, driven by a function generator and are amplified by a RF amplifier able to provide more than 1 kW, with a gain around 64 dB (Bruker BLAH 1000). A directional coupler is used to control the signal injected in the resistor and to measure the reflected power (which increases abruptly if the resistor burns). The whole setup is schematized in Figure 10. The heater and sensor positions are shown in Figure 11. Two OSTs have been placed facing the heater.

C. Variation of the heat pulse power

For a set of temperatures in the range [1.3 -2.1 K] the influence of the heat pulse power level on the OSTs signals was observed. The pulse duration is kept equal to 100 µs, and the power is increased from about 150 W

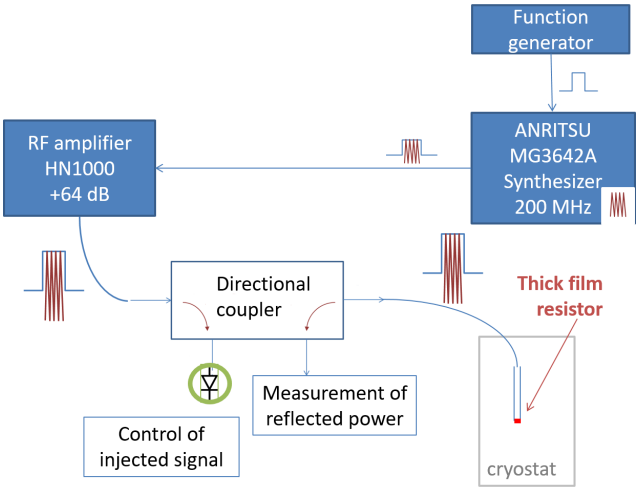

FIG. 10. Experimental setup for the generation and control of the heat pulse.

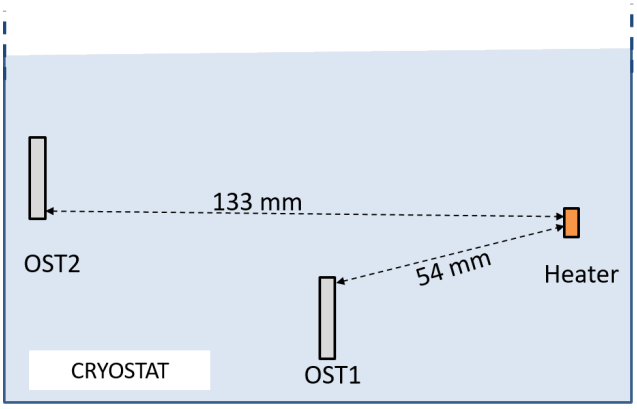

FIG. 11. Picture of the experimental setup.

to 1500 W, corresponding to a surface power from about 450 to 4500 W/cm^2. A second sound signal time of arrival has been measured for each OST, and the corresponding estimated distance from the heater to the OST has been calculated using the literature second sound velocities [28]. These calculated distances have been plotted versus heat pulse power (Figure 12), for both OSTs and for the whole set of temperatures. The results show clearly that the heat pulse power level does not have any influence on these calculated distances. For both OSTs, the mean calculated value has been plotted (dotted line), as well as the distance measured on the setup (solid line). As shown in Figure 11, these measured distances, resp. 54 mm and 133 mm, are from the heater to the closest point of each OST. In both cases, the mean calculated distances are around 3 mm lower than expected. This difference could be compatible with the inaccuracy of the distances measurements, due to the flexibility of the rods holding the OSTs. Indeed, it was observed that these rods were slightly deformed during the introduction of the setup in the cryostat.

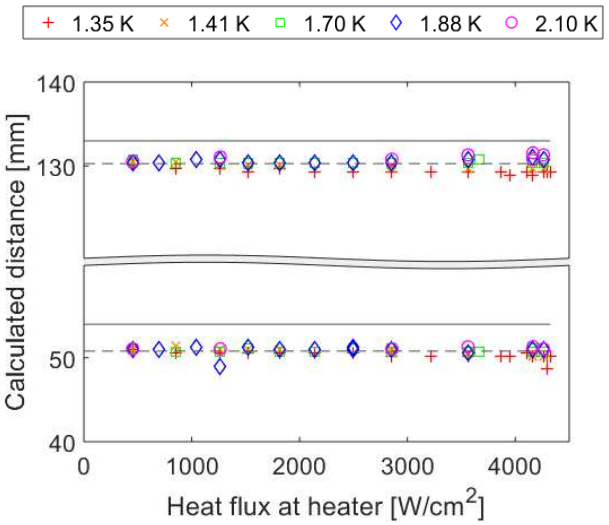

FIG. 12. Distances from heater to OSTs versus heat pulse power, calculated from times of arrival and recommended second sound velocity. For each OST, the average calculated values are shown (dashed lines) as well as the measured distances (solid lines).

However this distance difference can also be explained by a second sound velocity difference. This is shown in Figure 13 where the measured distances (54 mm and 133 mm) are divided by the times of arrivals of the OST signals ; the difference between this apparent second sound velocity and the literature values [28] is plotted versus the heat flux at heater. One can observe that the apparent velocity is between 0.1 and 2 ms higher than expected, and that the difference is higher for OST1 than for OST2. This results can be compared to the heat pulse experiments described in references [12] and [13]. The authors explore a lower level of heat flux than us: [0-700 W/cm^2] instead of [450-4500 W/cm^2]. Their results also present a higher than expected apparent velocity with a difference up to 1.5 m/s. In their measurements the velocity difference is dependent on the heating power below 200 W/cm^2. At higher heating powers the velocity difference remained constant. While this observation might explain slightly premature signals, this effect is too weak to explain the significant deviations that were observed in tests with cavities.

D. Variation of the heat pulse energy

It is possible that the heat pulse energy, rather than the pulse power, could have an influence on the heat wave propagation. Experiments have been carried out at 1.7 K, where the pulse power was varied up to 1.5 kW, the pulse duration up to nearly 2 s and thus the pulse energy up to nearly 2.8 J. The results are presented in Figure 14, and show clearly that the pulse energy does

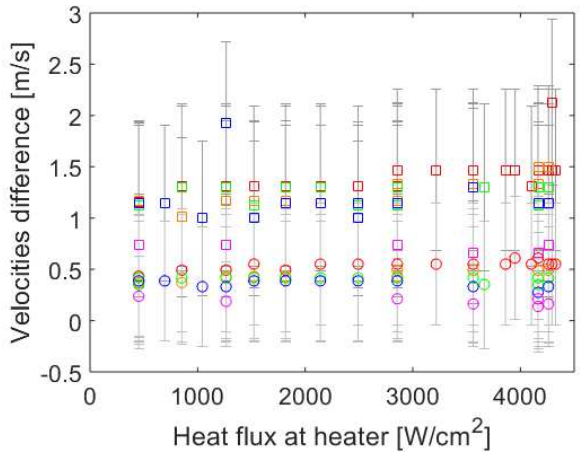

FIG. 13. Difference between the apparent second sound velocity and the literature values versus heat flux at heater. Values are given for OST 1 (squares) and OST 2 (circles), and for five sets of temperature: 1.35 K (red), 1.41 K (orange), 1.7 K (green), 1.88 K (blue) and 2.1 K (purple).

not have any effect on the heat wave propagation time.

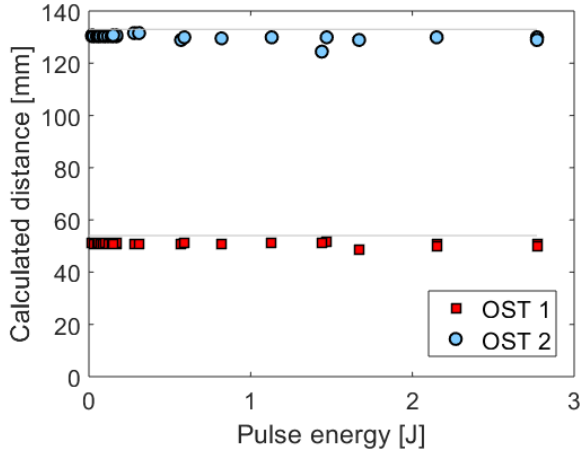

FIG. 14. Distances from heater to OSTs versus heat pulse energy, calculated from times of arrival and recommended second sound velocity. For each OST the measured distances is shown (solid lines).

E. Conclusions on heater experiments

These experiments demonstrate that the heat pulse up to 1.5 kW and 2.8 J created heat waves fully compatible with the standard second sound waves in superfluid helium.

Thus the hypothesis of a heat wave propagating significantly faster in helium than the second sound waves has to be discarded, at least until the power and energy reached in these experiments. By comparison one can estimate the overall energy dissipated during a cavity quench, which corresponds to the energy stored in the cavity just before quench occurrence (W_{stored}). This quantity is related to the accelerating field reached in the cavity E_{acc}, the cavity frequency and some geometric parameters: the coupling coefficient r/Q and the accelerating length L_{acc}[1].

$$W_{stored} = \frac{(E_{acc}L_{acc})^2}{\omega * r/Q} = 0.0141 * E_{acc}^2 \qquad (2)$$

All of the 1.3 GHz cavities tested have an r/Q coefficient equal to 115 Ω and an accelerating length of 0.115 m. The maximum accelerating field varies from 30 to 37 MV/m (see Figure 2) and thus the maximal energy from 12.7 to 19.3 J. The time to dissipate this energy during the quench was not measured but assuming a typical quench duration in the order of one millisecond, one will obtain an average heating power of 12.7 to 19.3 kW.

So the power and the energy dissipated in helium during a cavity quench is less than one order of magnitude higher than the maximal energy dissipated during the heater experiments. In contrast to the tests in the cavity no heat transfer through niobium did hinder the cooling. Taking this into account, the heating powers in the tests were even closer to the surface heat flux in the performed cavity tests. Even if the presented results cannot be directly transposed to cavity tests, at least they do not provide any argument to support the hypothesis of a heat wave propagating faster in helium than the standard second sound wave.

As additional information, during these experiments and for the highest levels of pulse energy, a cracking sound was audible, even if not recorded or measured. We identified this sound as the signature of a boiling as the highest surface heat flux were much higher than the reported literature data for the onset of boiling in superfluid helium [33]. Actually, boiling phenomena in similar conditions have already been observed and recorded [34]. Thus it seems that heat wave propagation is still compatible with the second sound velocity even if boiling in helium occurs.

IV. PROPAGATION IN NIOBIUM

As the origin of the premature signals could not be found to be caused by effects within the liquid helium, an influence of the cavity itself seems likely. Two effects come into mind to explain this. First, the quench propagation within in the cavity could be the reason. Second the heat transfer in the niobium itself could also cause this.

The quench of a cavity is generally caused by a local increase of the magnetic field on a small defect situated on the inner surface of the cavity. This spot is heated very rapidly, which causes the neighboring area to quench

as well. This process continues until the heat input by the stored energy in the cavity decreases below the value of cooling by the surrounding niobium or helium. So the heat source on the outer surface of the cavity is rather an area, with a size depending on the dynamic heating and the dynamic heat diffusion in niobium and superfluid helium. Moreover, one can consider that the temperature increase due to the heat flux diffuses faster in the niobium than in helium, both due to the additional heating as well as the high thermal diffusivity of superconducting niobium. While both processes will certainly play a role, it is likely, that the rapid signal propagation will be dominated by the occurring quench phenomena.

A. Probing fast signal propagation in niobium

The signals arriving on an OST are the combination of second sound waves arriving directly from the quench position, and second sound emitted from other positions on the cavity. The very first signal arriving on the OST will be detected, but it could be "emitted" by one of these positions rather than by the quench point itself. This situation has been discussed by Eichhorn et al. in a 2D case [16]. It is illustrated in 3D in Figure 15, with an isotropic spread of the heat flux in the niobium. The heat spot limit is represented by the dotted points, each colored set corresponding to a given time after the beginning of the quench at the niobium surface. All the points of one color are situated at the same distance, on the cavity surface, from the quench point. Figure 16 shows the different signals arriving on an OST, represented by a dark dot. The yellow line corresponds to a signal arriving directly from the quench location (large pink point) while the red and green lines show the signals arriving from two different points on the cavity surface.

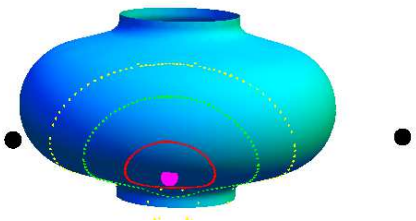

FIG. 15. Limit of the quench spot at different times (each time corresponds to a color). The large pink point is the quench position and the large dark points represent OSTs.

To obtain the time of arrival, a minimization of the propagation in helium and in niobium has to be performed. This was implemented in Mathematica code. The velocity of the heat signal was fixed to 20 m/s in helium and to 70 m/s in niobium. Using a constant propagation velocity in niobium does not capture the underlying physical processes. These are highly dynamic and include many influencing factors, mainly the quench propagation and the thermal diffusion. Using a velocity

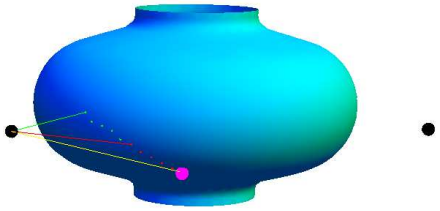

FIG. 16. Trajectory of the heat flux signal from quench spot (large pink point) to OST (large dark point) for different combination of heat transport in niobium and helium.

to describe the processes in niobium was originally meant as an example calculation [34]. It is based on simulated results in [15]. This approach was shown to match real systems surprisingly well as shown in [16].This is the reason, why the signal propagation in niobium is represented by this velocity.

This minimization was applied to the geometry of the measured cavities. The results are given in Figure 17, together with a summary of the data from Figure 5 giving results within direct line of sight propagation.

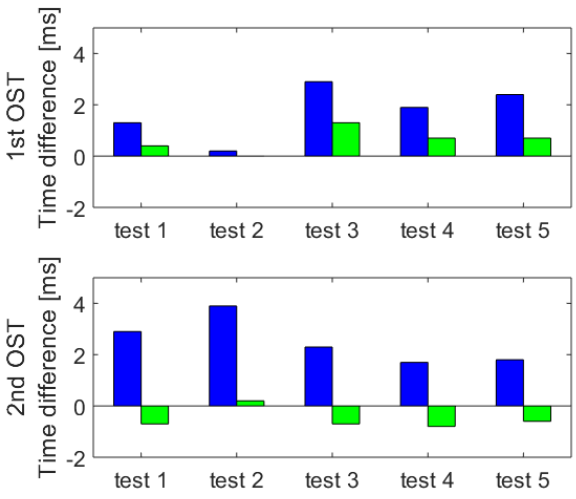

FIG. 17. Difference between calculated and measured times of arrival of the 2nd sound signal on the two closest OSTs from the quench location at 1.7 K. Calculation with direct line of sight hypothesis (blue) and calculation with the mixed niobium/helium heat propagation model (green).

It can be seen that the calculation from this niobium-helium transport model reduces the error quite considerably for all measurements. It fits particularly well for cavity A with the measurements for the first OST and with an error less than 10% for the second OST. In this case this model could describe the measured times of arrival. However, this model does not work as good for cavity B, where the difference between measurements and calculation is still quite large.

Moreover this niobium-helium transport model has

also been used for calculation with varying temperature and compared to the experimental results for test 4 with cavity B. Results are shown in Figure 18 and Figure 19. In the whole temperature range of investigation this model reduces the error compared to the direct line of sight propagation calculations, but the differences keeps quite large: around 30% for the 1st OST and around -10% for the 2nd OST.

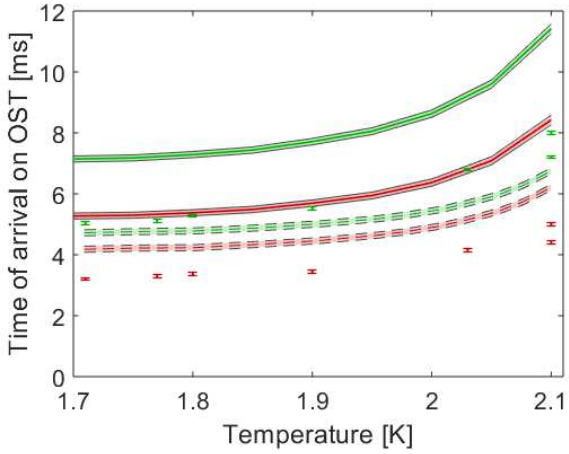

FIG. 18. Time of arrival on first (red) and second (green) OST with varying temperature for Test 4 (cavity B). Experimental data (points with error bars), calculated data with direct line of sight propagation (solid line) and with niobium-helium transport model (dashed line). The shaded area represent the error on calculation due to geometrical measurements uncertainties.

The difference between cavity A and cavity B could be explained by a number of reasons. The quench was located at different spots on the cavity. While in cavity A, the spot was on the equator, which is the region with the highest magnetic field on the inside, the spot on cavity B was in a lower field region (Figure 3). The different spots will cause different patterns of quench propagation in the cavity. Another reason could be the different accelerating field in the cavities during the quench. In cavity B it is considerably higher, corresponding to an increase of 30% of the dissipated energy for 34 MV/m and 50% for 37 MV/m. These differences will lead to different average velocity of the temperature signal in niobium. As this velocity was just based on a number of assumptions, it is not surprising that the model is not an exact fit. Nevertheless this model gives an improved prediction of the time of arrival of the temperature signal. From these calculation it seems likely that the fast signal propagation in the niobium causes the premature signals.

V. CONCLUSION

In this paper the surprising effect of premature second sound signals in quench localization studies has been described and experimentally shown. This was confirmed by the combination of OST and temperature mapping measurements on two different cavities. These measurements allowed to test different ideas on the origin of this effect. The pure second sound propagation via the direct line of sight from a localized quench spot was used as a starting point.

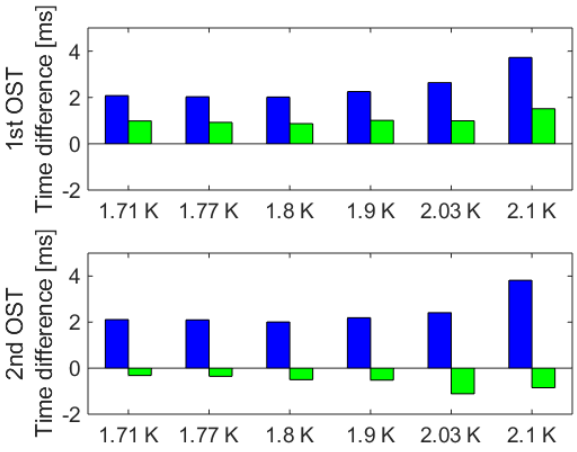

FIG. 19. Difference between calculated and measured times of arrival of the 2nd sound signal on the two closest OSTs from the quench location with varying temperature for Test 4. Calculation with direct line of sight propagation (blue) and calculation with the mixed niobium/helium heat propagation model (green). At 2.1 K the reference measured value is the average between the two real measured values shown in Figure 18

Two hypotheses were suggested to explain the early arrival of the second sound signal. A faster signal propagation in helium was probed in a dedicated experiment, where a heater with input power up to 1.5 kW, flux power to 4.3 kW/cm^2 and energy 2.8 J was used to simulate the quench spot. Such amounts of power of energy had never been reached in similar measurements. However, no faster signal propagation could be found under these conditions, which are lower than in actual cavities, but in a relevant regime. Propagation in niobium was probed by a model, which was used to evaluate the quench tests with the cavities. This model was based on a number of assumptions. Although these assumptions were quite broad, a considerable improvement on the prediction of the time of arrival for the second sound at the OSTs could be obtained. It can be concluded, that while a fast signal propagation in helium seems very unlikely, the processes in the niobium are likely to induce the described effect. It is assumed that the quench propagation on the inner cavity wall and the thermal diffusion in the niobium are the main cause, in the case of quenching cavities.

[1] H. Padamsee, J. Knobloch and T. Hays, RF Superconductivity for Accelerators, 2nd Ed., Wiley-VCH, (2008).

[2] Geng et al., Gradient limiting defects in 9-cell cavities EP processed and RF tested at Jefferson Lab, in Proceedings of International Conference on RF Superconductivity, (SRF2009), Berlin, Germany, 2009, International Conference on RF Superconductivity Vol. 14, (JACoW, Geneva, Switzerland, 2015) pp. 370-374 (2009).

[3] Y. Iwashita, H. Hayano, T. Kubo, K. Watanabe and Y. Yamamoto., Combined system of optical inspection and local grinder, Proceedings of the 27th International Linear Accelerator Conference, Geneva, Switzerland (LINAC2014), pp. 1065-1067 (2014).

[4] A. Navitski, A. Prudnikava. and Y. Tamashevich, Progress of R&D on SRF cavities at DESY towards the ILC performance goal, Proceedings of the 5th International Particle Accelerator Conference (IPAC14), Dresden, Germany, pp. 2499-2501 q(2014).

[5] Z. Conway, M. Ge and Y. Iwashita, Instrumentation for localized superconducting cavity diagnostics, Supercond. Sci. Technol. 30 (2017).

[6] H. Padamsee, C. Reece, R. Noer, W. Hartung, E. Frick, R. Kahn, Field emission studies in superconducting cavities, in Proceedings of the 1987 IEEE Particle Accelerator Conference, Washington D.C., USA, pp. 1824-1826 (1987).

[7] Z.A. Conway, D.L. Hartill, H.S. Padamsee, and E.N. Smith, Oscillating Superleak Transducers for Quench Detection in Superconducting ILC Cavities Cooled with He-II, in Proceedings of the 24th International Linear Accelerator Conference, Victoria, BC, Canada (LINAC2008), pp 863-865 (2008).

[8] Y. Maximenko and D. A. Sergatskov, Quench dynamics in SRF cavities: can we locate the quench origin with 2nd sound?, in Proceedings of the 2011 Particle Accelerator Conference, New York (PAC11), NY, USA, pp. 883-885 (2011).

[9] K. Liao, O. Brunner, E. Ciapala, T. Junginger and W. Weingarten, Second sound measurement using SMD resistors to simulate quench locations on the 704 MHz single-cell cavity at CERN, Proceedings of the 3rd International Particle Accelerator Conference (IPAC12), New Orleans, LA USA, pp. 2269-2271

[10] J. Plouin, J.P. Charrier, C. Magne, L. Maurice and J. Novo, Experimental investigations of the quench phenomena for the quench localization by the second sound wave method, in Proceedings of International Conference on RF Superconductivity (SRF2013), Paris, France, 2013, International Conference on RF Superconductivity Vol. 16 (JACoW, Geneva, Switzerland, 2013), pp. 739-742.

[11] Y. Tamashevich, Diagnostics and treatment of 1.3GHz Nb cavities, PhD thesis, University of Hamburg, http://bib-pubdb1.desy.de/record/317338, (2016).

[12] T. Junginger, P. Horn, T. Koettig, K. Liao, A. Macpherson and B Peters, High flux three dimensional heat transport in superfluid helium and its application to a trilateration algorithm for quench localization with OSTs, in Proceedings of the International Conference on RF Superconductivity (SRF2015), Whistler, BC, Canada, 2015, International Conference on RF Superconductivity Vol. 17 (JACoW, Geneva, Switzerland, 2015), pp. 201-204 (2015)

[13] Koettig, T. and Peters, B. J. and Avellino, S. and Junginger, T. and Bremer, J. (2015) Study of temperature wave propagation in superfluid helium focusing on radio-frequency cavity cooling. IOP Conference Series: Materials Science and Engineering, 101 (1). (IOP Publishing, Bristol, UK, 2015).

[14] R. Eichhorn, S. Markham, On the Mystery of using Helium's second Sound for Quench Detection of a Superconducting Cavity, Physics Procedia. 67 pp. 822–827 (2015).

[15] Z. C. Liu, M. Kelly, and A. Nassiri, New method to improve the accuracy of quench position measurement on a superconducting cavity by a second sound method, Phys. Rev. Special Topics, Accelerators and Beams, 15, 092001 (2012).

[16] R. Eichhorn and S. Markham, On quench propagation, quench detection and second sound in SRF cavities, in Proceedings of International Conference on RF Superconductivity (SRF2015), Whistler, BC, Canada, 2015, International Conference on RF Superconductivity Vol. 17 (JACoW, Geneva, Switzerland, 2015), pp. 804-808 (2015).

[17] K. Liao, C. Balle, J. Bremer, T. Junginger, W. Vollenberg and W. Weingarten, Second sound measurement for SPL cavity diagnostics, in Proceedings of International Conference on RF Superconductivity (SRF2011), Chicago, IL, USA, 2011, International Conference on RF Superconductivity Vol. 15 (JACoW, Geneva, Switzerland, 2011), pp. 767-772 (2011).

[18] S. Bao, and W. Guo, Quench-Spot detection for Superconducting Accelerator Cavities via Flow visualization in supefluid helium-4, Phys. Rev. Applied 11, 044033, (2019).

[19] E. Cenni, P. Bosland, G. Costanza C. Darve, G. Devanz, F. Eozenou, X. Hanus, L. Maurice, F. Peauger, J. Plouin, D. Roudier and C. Servouin, Vertical Test results on ESS medium and high beta elliptical cavity prototypes equipped with helium tank, Proceedings of the 8th International Particle Accelerator Conference (IPAC17), Copenhagen, Denmark, pp. 948-950 (2017).

[20] B. Baudouy, D. Bouziat, P. Bredy and P. Chesny, Cryogenics Activities at the Institute of Research into the Fundamental Laws of the Universe (Irfu), J. Cryo. Soc. Jpn. Vol. 45 No.5 (2010)

[21] F. Eozenou, S. Berry, C. Antoine, Y. Gasser, J-P. Charrier and B. Malki, Aging of the HF-H2SO4 electrolyte used for the electropolishing of niobium superconducting radio frequency cavities: Origins and cure, Phys. Rev. ST Accel. Beams 13, 083501 (2010).

[22] F. Eozenou, S. Chel, J-P. Charrier, C. Servouin, B. Visentin, Y. Gasser and Z. Wang, Development of an advanced electropolishing setup for multicell high gradient niobium cavities, Phys. Rev. ST Accel. Beams 15, 083501 (2012).

[23] F. Eozenou., Development of vertical electropolishing process applied on 1300 and 704 MHz superconducting niobium resonators, Phys. Rev. ST Accel. Beams 17, 083501 (2014).

[24] R. Williams, S.E. Beaver, J.C. Fraser, R.S. Kagiwada and I. Rudnick, "The velocity of second sound near T_λ",

Phys. Lett. A, Vol. 29, No. 5, pp. 279 - 280 (1969).
[25] R.J. Donnelly, The two-fluid theory and second sound in liquid helium, Physics Today 62, 10, 34 (2009).
[26] A. Quadt, B. Schroeder, M. Uhrmacher, J. Weingarten, B. Willenberg and H. Vennekate, Response of an oscillating superleak transducer to a pointlike heat source, Phys. Rev. ST Accel. Beams, 15 031001 (2012).
[27] Z.A. Conway, D. L. Hartill, H. Padamsee and E. N. Smith, Defect location in superconducting cavities cooled with He-II using oscillating superleak transducers, in Proceedings of International Conference on RF Superconductivity (SRF2009), Berlin, Germany, 2009, International Conference on RF Superconductivity Vol. 14 (JACoW, Geneva, Switzerland, 2009), pp. 113-116 (2009).
[28] R. J. Donelly, C. F. Barenghi , The Observed Properties of Liquid Helium at the Saturated Vapor Pressure, J. Phys. Chem. Ref. Data 27, 1217 (1998).
[29] H.N.V. Temperley, The theory of the propagation in Liquid Helium II of "Temperature-Waves" of Finite Amplitude, Proc. Phys. Soc., A64 pp. 114-125 (1951).
[30] I.M. Khalatnikov, Discontinuities and high amplitude sound in helium II, Zh. Ekspl. Teor. Fiz. [Sov. Phys. - JETP] 23 p. 253 (1952).
[31] A.J. Dessler, W.M. Fairbank, Amplitude dependence of the velocity of second sound, Phys. Rev. 104 pp. 6-12 (1956).
[32] A.J. Dessler, Interactions between First and Second Sound in Liquid Helium, Phys. Fluids, 2 pp. 5-7 (1959).
[33] S.W. Van Sciver, Helium cryogenics, 2nd Ed., Springer (2012)
[34] B.J. Peters, Advanced Heat Transfer Studies in Superfluid Helium for Large-scale High-yield Production of Superconducting Radio Frequency Cavities, Diplomarbeit, Karlsruhe Institute of Technology (KIT), http://cds.cern.ch/record/1748598 (2014).
[35] S. Berry, Topological analysis of samples and cavities: a new tool for morphologic inspection for quench site, in Proceedings of 11th Workshop on RF Superconductivity (SRF2003), Lübeck/Travemünder, Germany, 2003, 11th Workshop on RF Superconductivity Vol. 11 (JACoW, Geneva, Switzerland, 2003), pp. 591-595 (2003)

Conclusion and perspectives

In this report, I have given an overview of my research and development activities. The general purpose is to provide knowledge and solutions to improve the efficiency and performance of radio frequency (RF) structures for particle accelerators. I have participated to various activities, involving many fields of physics: electromagnetism, magnetics, mechanics, heat transfer science, solid-state physics and quantum physics, the list being non exhaustive.

A large part of my activity is related to the development of superconducting cavities, from design to tests, and involves elliptical cavities and half wave resonators, as well as associated elements, like power couplers. For the elliptical cavities of the ESS high energy linac, the design was driven by the high gradient target, leading to RF field minimization of the cavity surface, and by the operation in pulsed mode, requiring the minimization of the Lorentz force detuning by appropriate mechanical design. Those cavities were successfully tested in dedicated cryostats [WAB23] and during cryomodule operation [Piq+23]. The next milestone is the proton acceleration, foreseen at Lund in 2025, aimed to lead to the most powerful pulsed neutron source in the world.

The half wave resonator for the IFMIF/DONES high beta cryomodule was designed, aimed to accelerate a high current in continuous mode, requiring hundreds of megawatts of radiofrequency power [Kró+21]. The first prototype has demonstrated the achievement of the RF specifications. Now, mechanical studies are ongoing for ensuring cavity integrity in operation and frequency tuning [Plo22]. The power coupler must be able to transfer the large amount of radio frequency power, and upgrades are already being developed, in particular the implementation of a polarization setup for minimizing the risk of multipactor [Dev22]. The whole cavity, tuner and coupler setup, as well as the solenoid package, must also be integrated inside the cryomodule [BC21]. The IFMIF/DONES facility is aimed to provide a 125 mA deuteron beam at 40 MeV for neutron acceleration, and the construction phase has started in 2023 [IFM23].

I have dedicated a large part of my work to the design and fabrication of many magnetic shields. I have acquired an expertise in this domain which has led to the optimization of magnetic shielding development, and I have shared this experience in the SRF community in multiple occasions [Lax13][Plo+15]. I am fully associated to the general development of a strict magnetic environment management, "magnetic hygiene", which becomes more important with the search for high gradients with low losses [DI67][Cha+16]. CEA is still involved in new cryomodule developments, like IFMIF/DONES and PIP-II, where this knowledge will be applied, from the selection of materials to the degaussing of cryomodules.

Limiting trapped flux, besides decreasing the background magnetic field, is obtained by flux expulsion from the superconducting material during cavity cooldown below transition temperature. Flux expulsion is now explored in most of the SRF labs [Rom+14; Pos+16; Kub16; VKK13], aiming to provide specific cooldown time and spatial parameters for cavity operation in cryostat and in cryomodule.

Ongoing accelerator projects require improving performance for the superconducting cavities. High quality factors are expected for the PIP-II proton beam accelerator (2 10^{10} at nearly 18 MV/m [Leb15]), and for the free electron laser SHINE (2.7 10^{10} at 16 MV/m [Zon+23]). The

International Linear Collider (ILC) aims operating at nominal average gradient of 31.5 MV/m with quality factor at least 10^{10} [Tea]. In the baseline concept of a muon collider, the acceleration stage of the high energy complex requires energy gain of 10 GeV per turn, provided by very high voltage superconducting cavities.

The increase of superconducting cavity performance requires progressing in all steps from design to fabrication and preparation. Cavity design is aimed to use new optimization techniques, able to focus on accelerating field maximization or RF losses minimization, depending on the needs [SY23]. Huge progress are ongoing all around the world on niobium sheets production [Myn+23], cavity surface preparation and heat treatment [Pos+20] [Pad23]. They tend to limit the cause of radiofrequency heating in the material, and limit the phenomena of field emission by the cavity walls. These efforts are coupled with the development of dedicated diagnostics able to detect, understand and cure the phenomena leading to flux trapping, field emission or temperature increase.

The muon cooling complex of a future muon collider will require normal conducting cavities able to achieve gradients of at least 30 MV/m while being placed in magnetic fields of 13 T or more. Studies are needed for the comprehension of the intrinsic concepts that influence the breakdown rate of RF cavities submitted to strong magnetic fields and to find mitigation solutions. The coupler design and the RF distribution must allow optimization of the RF coupling from power sources to the muon beam. Strong transient beam loading effects, as well as strong wake field effects due to the very high intensity of the muon bunches will also have to be addressed in the cavity optimization and possibly requires HOM couplers.

Finally, the future accelerators projects will require high amount of power from their radiofrequency sources, and improving the energy efficient conversion from grid power into RF is a key aspect for their sustainability over the long term. While the development of solid-state high power amplifiers offers new possibilities [Mon22][Ned+23], vacuum tubes like klystrons will still play a main role. Improving efficiency requires many studies with dedicated simulation codes and optimization techniques, as well as a large effort in the fabrication process to offer reliable solution.

Bibliography

[Ali23] K. Aliane. "Méthodes pseudo-spectrales multiparticules pour les tubes à onde progressive : modèle et applications". PhD thesis. Université Aix-Marseille, 2023. URL: https://www.theses.fr/s230321.

[Amu] Amuneal. *Cryoperm datasheet*. URL: https://www.amuneal.com/storage/2016/05/AmunealDataSheet2.pdf.

[And+20] F. André, D. F. G. Minenna, K. Aliane, Y. Elskens, A. Poyé, J. Puech, and F. Doveil. "Progress with DIMOHA for fast time-domain simulations of travelingwave tubes". In: *2020 IEEE 21st International Conference on Vacuum Electronics (IVEC)*. 2020, pp. 169–170. DOI: 10.1109/IVEC45766.2020.9520629.

[AP14] C. Antoine and J. Plouin. "Cavités supraconductrices pour les accélérateurs de particules". In: *Techniques de l'ingénieur* D2706 (2014). DOI: 10.51257/a-v1-d2706.

[Ape] Aperam. URL: https://www.aperam.com/product/cryophy/.

[Ars+21] S. Arsenyev, P. Hamel, C. Marchand, and J. Plouin. *Design of an efficient klystron*. Tech. rep. ARIES, 2021. URL: https://edms.cern.ch/document/1817230/1.0.

[BMS15] A. Y. Baikov, C. Marrelli, and I. Syratchev. "Toward High-Power Klystrons With RF Power Conversion Efficiency on the Order of 90%". In: *IEEE Transactions on Electron Devices* 62.10 (2015), pp. 3406–3412. DOI: 10.1109/TED.2015.2464096.

[Bal+21] S. Balachandran, A. Polyanskii, S. Chetri, P. Dhakal, Y.-F. Su, Z.-H. Sung, and P. J. Lee. "Direct evidence of microstructure dependence of magnetic flux trapping in niobium". In: *Scientific reports* 11.1 (2021), p. 5364.

[Bal08] M. C. Balk. "Simulation possibilities of vacuum electronic devices with CST PARTICLE STUDIO™". In: *2008 IEEE International Vacuum Electronics Conference*. 2008, pp. 459–460. DOI: 10.1109/IVELEC.2008.4556402.

[Baz+23] N. Bazin, S. Berry, J. Drant, P. Fontaine Garin, H. Jenhani, A. Raut, P. Sahuquet, C. Simon, J. Belorgey, Q. Bertrand, P. Brédy, E. Cenni, C. Cloué, R. Cubizolles, S. Ladegaillerie, A. Le Baut, A. Moreau, O. Piquet, and J. Plouin. "CEA Contribution to the PIP-II Linear Accelerator". In: *Proc. of SRF2023, Grand Rapids, MI, USA*. 2023.

[Ba13] N. Bazin and al. *Engineering design report of the IFMIF-EVEDA SRF Linac*. Tech. rep. CEA and CIEMAT, 2013.

[BC21] N. Bazin and S. Chel. "Cryomodule development for materials irradiation facilities: from IFMIF/EVEDA to IFMIF-DONES". In: *Proc. of SRF2021, East Lansing, MI, USA*. 2021.

[Baz+13] N. Bazin, G. Devanz, F. Orsini, D. Roudier, P. Carbonnier, N. Grouas, P. Hardy, and G. Disset. "Cavity development for the linear IFMIF prototype accelerator". In: *Proc. of SRF2013, Paris, France*. 2013.

[Baz+17] N. Bazin, G. Devanz, S. Chel, H. Jenhani, O. Piquet, A. Bruniquel, A. Riquelme, P. Charon, G. Disset, P. Contrepois, P. Hardy, J. Chambrillon, N. N'Doye, J. Relland, B. Renard, J. Plouin, C. Boulch, D. Roudier, P. Carbonnier, F. Toral, and D. Regidor. "Manufacturing status of the IFMIF LIPAc SRF Linac". In: *Proc. of IPAC2017, Copenhagen, Denmark*. 2017, pp. 939–941.

[Baz+20] N. Bazin, K. Romieu, T. Plomion, P. Bredy, and S. Chel. *IFMIF-DONES Superconducting Linac: Design Description Document*. Tech. rep. CEA, 2020.

[Bér+96] G. Béranger, F. Duffaut, J. Morlet, and J.-F. Tiers. *The Iron-Nickel alloys*. Lavoisier Publishing, 1996, pp. 70–73.

[BD02] C. Berriaud and A. Donati. "A device for measuring high current at cryogenic temperatures". In: *IEEE Transactions on Applied Superconductivity* 12.1 (2002), pp. 1264–1268. DOI: 10.1109/TASC.2002.1018632.

[Beu+22] A. Beunas, K. Khlifa, I. Syratchev, and N. Catalan Lasheras. "CSM HE klystron for LHC". In: *Workshop on Efficient RF Sources, Geneva, 2022*. 2022. URL: https://indi.to/m4mW3.

[Boc+16] A. Bocheux, C. Cavoit, M. Mouchel, C. Ducruet, R. Fons, P. Sabon, I.-L. Prejbeanu, and C. Baraduc. "High sensitivity magnetic field sensor for spatial applications". In: *2016 IEEE Sensors Applications Symposium (SAS)*. 2016. DOI: 10.1109/SAS.2016.7479836.

[Bol94] M. Bolore. *Magnetic shielding of the TESLA TTF superconducting cavities, TESLA Report 1994-23*. Tech. rep. CEA, 1994.

[Bos+17] P. Bosland, C. Arcambal, F. Ardellier, S. Berry, A. Bouygues, A. Bruniquel, E. Cenni, J.-P. Charrier, C. Cloué, G. Devanz, F. Eozénou, X. Hanus, T. Hamelin, P. Hardy, V. Hennion, C. Marchand, F. Peauger, O. Piquet, J. Plouin, J.-P. Poupeau, T. Trublet, G. Olivier, C. Darve, P. Michelato, and G. Costanza. "Status of the ESS elliptical cryomodules at CEA Saclay". In: *Proc. of IPAC2017, Copenhagen, Denmark*. 2017.

[Bos+07] P. Bosland, S. Chel, G. Devanz, Y. Gasser, P. Hardy, J. Plouin, J. Poupeau, D. Roudier, and B. Visentin. "Stiffened Medium Beta 704 MHZ Elliptical Cavity for a Pulsed Proton Linac". In: *Proc. of SRF2007, Beijing, China*. 2007.

[Bow+20] D. Bowring, A. Bross, P. Lane, M. Leonova, A. Moretti, D. Neuffer, R. Pasquinelli, D. Peterson, M. Popovic, D. Stratakis, et al. "Operation of normal-conducting RF cavities in multi-tesla magnetic fields for muon ionization cooling: a feasibility demonstration". In: *Physical Review Accelerators and Beams* 23.7 (2020), p. 072001.

[Bri01] R. Brinkmann. *TESLA technical design report part II : the accelerator. DESY-01-011B*. Tech. rep. DESY, 2001.

[Cap+11] O. Capatina, S. Atieh, I. Aviles Santillana, G. Arnau Izquierdo, S. Calatroni, S. Chel, A. D'Elia, G. Devanz, R. Garoby, T. Junginger, J. Plouin, D. Maciocha, E. Montesinos, V. Parma, T. Renaglia, T. Tardy, and N. Valverde Alonso. "Mechanical design considerations for beta= 1 cavities". In: *Proc. of SRF2011, Chicago, IL, USA*. 2011.

[Car] Carpenter. *properties of stainless steel*. URL: https://www.carpentertechnology.com/blog/magnetic-properties-of-stainless-steels.

[Cas] Cast3M. *the Cast3M site*. URL: https://www-cast3m.cea.fr.

[Cen+15] E. Cenni, C. Arcambal, P. Bosland, G. Devanz, X. Hanus, P. Hardy, V. M. Hennion, F. Leseigneur, F. Peauger, J. Plouin, D. Roudier, C. Darve, and G. Costanza. "ESS medium beta cavity prototypes manufacturing". In: *Proc. SRF2015, Whistler, Canada*. 2015.

[Cen+21] E. Cenni, M. Baudrier, G. Devanz, L. Maurice, and O. Piquet. "Field emission studies during ESS cryomodule test at CEA Saclay". In: *Proc of SRF2021, East Lansing, MI, USA*. 2021.

[Cen+19a] E. Cenni, M. Baudrier, P. Carbonnier, G. Devanz, X. Hanus, L. Maurice, J. Plouin, D. Roudier, and P. Sahuquet. "ESS prototype cavities developed at CEA Saclay". In: *Proc. of SRF2019, Dresden, Germany*. 2019.

[Cen+16a] E. Cenni, P. Bosland, G. Devanz, F. Eozenou, X. Hanus, L. Maurice, F. Peauger, J. Plouin, D. Roudier, C. Servouin, G. Costanza, and C. Darve. "Vertical Test Results on ESS Medium and High Beta Elliptical Cavity Prototypes Equipped with Helium Tank". In: *Proc. of IPAC2017, Copenhagen, Denmark*. 2016.

[Cen+16b] E. Cenni, G. Devanz, X. Hanus, F. Peauger, J. Plouin, D. Roudier, L. Maurice, F. Eozenou, C. Servouin, S. Berry, P. Bosland, C. Darve, and G. Costanza. "Vertical test results on ESS medium beta elliptical cavity prototype". In: *Proc. of LINAC2016, East Lansing, USA*. 2016.

[Cen+19b] E. Cenni, G. Devanz, O. Piquet, M. Baudrier, L. Maurice, and D. Roudier. "Field emission studies on ESS elliptical prototype cavities at CEA Saclay". In: *Proc of SRF2019, Dresden, Germany*. 2019.

[CET04] CETIM. "Mesure du taux de ferrite en zone fondue austénitique". In: *Techniques de l'ingénieur Travail des matériaux - Assemblage* base documentaire : TIP153WEB. (2004). DOI: 10.51257/a-v1-bm7790.

[Cha+17] J. Chambrillon, N. Bazin, G. Devanz, P. Contrepois, P. Hardy, P. Charon, N. N'Doye, O. Piquet, J. Plouin, and C. Servouin. "Assembly preparation of the IFMIF SRF cryomodule". In: *Proc. of IPAC2017, Copenhagen, Denmark*. 2017.

[Cha+16] S. K. Chandrasekaran, A. Grassellino, C. Grimm, and G. Wu. "Magnetic Field Management in LCLS-II 1.3 GHz Cryomodules". In: *Proc. of LINAC2016, East Lansing, MI, USA*. 2016.

[Cha+19] N. Chauvin, N. Bazin, S. Chel, L. Du, and J. Plouin. "Beam dynamics errors studies for the IFMIF-DONES SRF-LINAC". In: *Proc. of IPAC2019, Melbourne, Australia.* 2019.

[Che+07] I. A. Chernyavskiy, A. N. Vlasov, T. M. Antonsen, S. J. Cooke, B. Levush, and K. T. Nguyen. "Simulation of Klystrons With Slow and Reflected Electrons Using Large-Signal Code TESLA". In: *IEEE Transactions on Electron Devices* 54.6 (2007), pp. 1555–1561. DOI: 10.1109/TED.2007.896697.

[Col20] M. Collaboration. "Demonstration of cooling by the Muon Ionization Cooling Experiment". In: *Nature* 578 (2020), pp. 53–59. DOI: 10.1038/s41586-020-1958-9.

[Com] Comsol. *COMSOL Multiphysics*. URL: https://www.comsol.com/.

[Con+16] D. A. Constable, C. Lingwood, G. Burt, I. Syratchev, R. Marchesin, A. Y. Baikov, and R. Kowalczyk. "2-D particle-in-cell simulations of high efficiency klystrons". In: *2016 IEEE International Vacuum Electronics Conference (IVEC)*. 2016, pp. 1–2. DOI: 10.1109/IVEC.2016.7561813.

[Con+08] Z. Conway, D. Hartill, H. Padamsee, and E. N. Smith. "Oscillating Superleak Transducers for Quench Detection in Superconducting ILC Cavities Cooled with He-II". In: *Proc of LINAC2008, Victoria, BC, Canada*. 2008.

[CC16] A. C. Crawford and S. K. Chandrasekaran. "Demagnetization of a Complete Superconducting Radiofrequency Cryomodule: Theory and Practice". In: *IEEE Trans. Appl. Supercond.* 27.1 (2016), p. 3500406. DOI: 10.1109/TASC.2016.2635803.

[CST] CST. *CST Studio Suite*. URL: https://www.3ds.com/products/simulia/cst-studio-suite.

[Cub+17] R. Cubizolles, C. Madec, N. Bazin, P. Hardy, F. Leseigneur, T. Plaisant, J. Plouin, D. Chirpaz-Cerbat, P. Bredy, and R. Bruce. "CEA preliminary design of the cryomodules for SARAF phase-II superconducting Linac". In: *Proc. of IPAC2017, Copenhagen, Denmark*. 2017.

[DAu+21] G. D'Auria, N. Thompson, J. Clarke, M. Ferrario, W. Wuensch, F. Nguyen, A. Aksoy, R. Rochow, A. Chianchi, A. Latina, and M. Aicheler. *Conceptual Design Report of the CompactLight X-ray FEL*. Tech. rep. European Union, 2021. URL: https://zenodo.org/record/6375645.

[Del+23] E. Del Core, M. Bertucci, A. Bosotti, A. Grimaldi, L. Monaco, C. Pagani, R. Paparella, and D. Sertore. "Reconstruction of Field Emission Pattern for PIP-II LB650 Cavity". In: *Proc of SRF2023, Grand Rapids, MI, USA*. 2023.

[Dev22] G. Devanz. *Design of a DC biased coaxial-T*. Tech. rep. ENS-6.5.2.2-T002-10-N1. Eurofusion IFMIF/DONES, 2022.

[Dev+13] G. Devanz, N. Bazin, M. Desmons, P. Bosland, P. Hardy, F. Leseigneur, M. Luong, F. Peauger, J. Plouin, D. Roudier, G. Olivier, and G. Costanza. "ESS elliptical cavities and cryomodules". In: *Proc. of SRF2013, Paris, France*. 2013.

[Dev+15] G. Devanz, N. Bazin, G. Disset, H. Dzitko, P. Hardy, H. Jenhani, J. Neyret, O. Piquet, J. Plouin, and N. Selami. "Progress in IFMIF half wave resonators manufacturing and test preparation". In: *Proc. of SRF2015, Whistler, Canada*. 2015.

[Dev+11] G. Devanz, D. Braud, M. Desmons, Y. Gasser, E. Jacques, O. Piquet, J. Plouin, J.-P. Poupeau, and D. Roudier. "High power pulsed tests of a beta= 0.5 5-cell 704 MHz superconducting cavity". In: *Proc. of SRF2011, Chicago, IL, USA*. 2011.

[Dev+23] G. Devanz, E. Cenni, O. Piquet, M. Baudrier, and L. Maurice. "Instrumentation for High Performance Cavities and Cryomodule Field Emission Analysis". In: *Proc of SRF2023, Grand Rapids, MI, USA*. 2023.

[Dev+08a] G. Devanz, J.-P. Charrier, S. Chel, M. Desmons, Y. Gasser, A. Hamdi, P. Hardy, J. Plouin, and D. Roudier. "704 MHz high power coupler and cavity development for high power pulsed proton linacs". In: *Proc. of LINAC2008, Victoria, Canada*. 2008.

[Dev+08b] G. Devanz, D. Roudier, J. Plouin, P. Hardy, J. Charrier, J. Poupeau, S. Chel, and Y. Gasser. "Experimental Characterization of a 700 MHz β= 0.47 5 Cell Superconducting Cavity Prototype for Pulsed Proton Linac". In: *Proc. of EPAC2008, Genova, Italia*. 2008.

[DCG20] P. Dhakal, G. Ciovati, and A. Gurevich. "Flux expulsion in niobium superconducting radio-frequency cavities of different purity and essential contributions to the flux sensitivity". In: *Phys. Rev. Accel. Beams* 23 (2 Feb. 2020), p. 023102. DOI: 10.1103/PhysRevAccelBeams.23.023102.

[Dio+17] M. Diop, J.-P. Baete, R. Cuoq, H. Dias, J. Labelle, R. Lopes, M. Louvet, C. Monnot, P. Marchand, S. Petit, F. Ribeiro, T. Ruan, R. Sreedharan, and K. Tavakoli. "Status of the SOLEIL Superconducting RF System". In: *Proc. of SRF2017, Lanzhou, China*. 2017.

[Don09] R. J. Donnelly. "The two-fluid theory and second sound in liquid helium". In: *Physics Today* 62.10 (Oct. 2009), pp. 34–39. ISSN: 0031-9228. DOI: 10.1063/1.3248499. URL: https://doi.org/10.1063/1.3248499.

[DB98] R. J. Donnelly and C. F. Barenghi. "The Observed Properties of Liquid Helium at the Saturated Vapor Pressure". In: *Journal of Physical and Chemical Reference Data* 27.6 (Nov. 1998), pp. 1217–1274. ISSN: 0047-2689. DOI: 10.1063/1.556028.

[DI67] P. Droll and E. Iufer. *Magnetic properties of selected spacecraft materials*. Technical Memorandum. NASA, 1967.

[Du+18] L. Du, N. Bazin, N. Chauvin, S. Chel, and J. Plouin. "Beam dynamics studies for the IFMIF-DONES SRF-linac". In: *Proc. IPAC18, Vancouver, Canada*. 2018.

[Eoz+22] F. Eozenou, M. Baudrier, E. Cenni, E. Fayette, H. Hayano, Y. Ida, H. Ito, G. Jullien, S. Kato, T. Kubo, L. Maurice, H. Monjushiro, K. Nii, T. Saeki, C. Servouin, and T. Yamaguchi. "Vertical Electro-Polishing of 704 MHz Resonators Using Ninja Cathode: Gradients Over 40 MV/m Achieved on ESS Single-Cell Cavity". In: *Proc. of LINAC2022, Liverpool, United Kingdom*. 2022.

[Eoz+14] F. Eozenou, Y. Boudigou, P. Carbonnier, J.-P. Charrier, Y. Gasser, L. Maurice, F. Peauger, D. Roudier, C. Servouin, and K. Muller. "Development of vertical electropolishing process applied on 1300 and 704 MHz superconducting niobium resonators". In: *Phys. Rev. ST Accel. Beams* 17 (8 Aug. 2014), p. 083501. DOI: 10.1103/PhysRevSTAB.17.083501.

[Eoz+12] F. Eozenou, S. Chel, Y. Gasser, C. Servouin, B. Visentin, J.-P. Charrier, and Z. Wang. "Development of an advanced electropolishing setup for multicell high gradient niobium cavities". In: *Phys. Rev. ST Accel. Beams* 15 (8 Aug. 2012), p. 083501. DOI: 10.1103/PhysRevSTAB.15.083501.

[ESS12] ESS. *ESS Energy Design Report*. Tech. rep. ESS, 2012.

[Fai+08] G. Faillon, G. Kornfeld, E. Bosch, and M. K. Thumm. "Microwave Tubes". In: *Vacuum Electronics: Components and Devices*. Ed. by J. A. Eichmeier and M. K. Thumm. Berlin, Heidelberg: Springer Berlin Heidelberg, 2008, pp. 1–84. ISBN: 978-3-540-71929-8. DOI: 10.1007/978-3-540-71929-8_1.

[Fer+19] G. Ferrand, P. Carbonnier, F. Eozenou, E. Fayette, G. Jullien, S. Ladegaillerie, F. Leseigneur, C. Madec, L. Maurice, N. Misiara, A. Pérolat, N. Pichoff, O. Piquet, C. Servouin, and L. Zhao. "Results of CEA tests of SARAF cavities prototypes". In: *Proc of IPAC2019, Melbourne, Australia*. 2019.

[FLS10] R. P. Feynman, R. B. Leighton, and M. Sands. *The Feynman lectures on physics; New millennium ed.* Originally published 1963-1965. New York, NY: Basic Books, 2010. URL: https://cds.cern.ch/record/1494701.

[FN28] R. H. Fowler and L. Nordheim. "Electron emission in intense electric fields". In: *Proceedings of the Royal Society of London. Series A* 119.781 (1928), pp. 173–181.

[Gea] Geant4. URL: https://geant4.web.cern.ch/.

[Ger18] F. Gerigk. "Status and Future Strategy for Advanced High Power Microwave Sources for Accelerators". In: *Proc. of IPAC 2018, Vancouver, Canada*. 2018.

[GMC23] D. Giove, G. Mauro, and L. Celona. "Test stand plans INFN ". In: *IMCC annual meeting, Orsay, France*. 2023. URL: https://indico.cern.ch/event/1250075/contributions/5343508/.

[Gro+10] N. Grouas, P. Bosland, P. Brédy, V. Hennion, H. Jenhani, J. Migne, A. Mohamed, F. Orsini, J. Plouin, J. Relland, B. Branas, I. Podadera, S. Sanz, F. Toral, and E. Zaplatin. "Mechanical and cryogenic system design of the first cryomodule for the IFMIF project". In: *Proc. of IPAC'10, Kyoto, Japan*. 2010.

[GCB23] A. Grudiev, N. Catalan Lasheras, and L. Bottura. "X-box-B RF test stand possibilities at CERN". In: *IMCC annual meeting, Orsay, France*. 2023. URL: https://indico.cern.ch/event/1250075/contributions/5343512/.

[Gru] N. Grumman. *MAGIC cod*. URL: https://www.northropgrumman.com/space/pic-code-software/.

[GC08] A. Gurevich and G. Ciovati. "Dynamics of vortex penetration, jumpwise instabilities, and nonlinear surface resistance of type-II superconductors in strong rf fields". In: *Phys. Rev. B* 77 (10 Mar. 2008), p. 104501. DOI: 10.1103/PhysRevB.77.104501.

[Guz14] I. A. Guzilov. "BAC method of increasing the efficiency in klystrons". In: *2014 Tenth International Vacuum Electron Sources Conference (IVESC)*. 2014, pp. 1–2. DOI: 10.1109/IVESC.2014.6891996.

[Guz+17] I. Guzilov, O. Maslennikov, R. Egorov, I. Syratchev, V. Kobets, and A. Sumbaev. "Comparison of 6 MW S-band pulsed BAC MBK with the existing SBKs". In: *2017 Eighteenth International Vacuum Electronics Conference (IVEC)*. 2017, pp. 1–2. DOI: 10.1109/IVEC.2017.8289691.

[HH76] K. Halbach and R. F. Holsinger. "Superfish - A computer program for evaluation of RF cavities with cylindrical symmetry". In: *Part. Accel.* 7 (1976), pp. 213–222.

[Ham+21] P. Hamel, S. Arsenyev, J. Plouin, and C. Marchand. "Optimization of a double-gap output cavity for a high efficiency klystron operating in the X-band". In: *2021 22nd International Vacuum Electronics Conference (IVEC)*. 2021, pp. 1–2. DOI: 10.1109/IVEC51707.2021.9722494.

[Ham+19] P. Hamel, J. Plouin, C. Marchand, and F. Peauger. "Klystron efficiency optimization based on a genetic algorithm". In: *2019 International Vacuum Electronics Conference (IVEC)*. 2019, pp. 1–2. DOI: 10.1109/IVEC.2019.8745162.

[Has23] N. Hasan. "Tutorial Lecture on Cryogenics". In: *Proc. of SRF 2023, Grand Rapids, Michigan, USA*. 2023.

[Hil+17] V. C. R. Hill, G. Burt, D. Constable, C. Lingwood, C. Marrelli, and I. Syratchev. "Particle-in-cell simulation of second and third harmonic cavity klystron". In: *2017 Eighteenth International Vacuum Electronics Conference (IVEC)*. 2017, pp. 1–2. DOI: 10.1109/IVEC.2017.8289626.

[IFM23] IFMIF-DONES. *International materials facility IFMIF-DONES starts construction phase*. 2023. URL: https://euro-fusion.org/.

[Jen+10] H. Jenhani, P. Bosland, P. Brédy, M. Desmons, G. Devanz, G. Disset, N. Grouas, P. Hardy, V. Hennion, J. Migne, A. Mohamed, F. Orsini, J. Plouin, J. Rellan, B. Branas, I. Podadera, S. Sanz, F. Toral, E. Zaplatin, F. Mirapeix, and C. Palacios. "Status of the CW Power Couplers for the SRF Linac of the IFMIF Project". In: *Proc. of IPAC'10, Kyoto, Japan*. 2010.

[Jen+12] H. Jenhani, P. Bosland, P. Carbonnier, N. Grouas, P. Hardy, V. Hennion, F. Orsini, J. Plouin, B. Renard, S. Einarson, and T. Treado. "Input power coupler for the IFMIF SRF Linac". In: *Proc. of IPAC2012, New Orleans, USA*. 2012.

[Jen19] E. Jensen. "Increased demand for high efficiency RF power sources". In: *Workshop on Energy Efficient RF*. 2019. URL: https://indico.uu.se/event/515/.

[JS18] C. Jinchi and I. Syratchev. *KlyC. The 1D/1.5 D large signal computer code for the klystron simulations, User manual No. CERN-ACC-2018-0050*. 2018.

[Job+17] M. Jobs, K. Gajewski, V. Goryashko, H. Li, R. Ruber, and R. Wedberg. "352 MHz Tetrode RF Stations for Superconducting Spoke Cavities". In: *Proc. IPAC2017, Copenhagen, Denmark* (2017).

[Koc+16] A. Kochemirovskiy, D. Bowring, K. Yonehara, A. Moretti, Y. Torun, and B. Freemire. "Study of RF Breakdown in 805MHz Pillbox Modular Cavity in Strong Magnetic Field". In: *Proc. of IPAC2016, Busan, Korea*. 2016.

[KM04] D. Kostin and W.-D. Moeller. "Status and operating experience of the TTF coupler". In: *Proc. of LINAC2004, Lübeck, Germany*. 2004.

[KMK13] D. Kostin, W.-D. Moeller, and W. Kaabi. "Update on the European XFEL RF power input coupler." In: *Proc. of SRF213, Paris, France*. 2013.

[Kra+20] F. Kramer, O. Kugeler, J.-M. Köszegi, and J. Knobloch. "Impact of geometry on flux trapping and the related surface resistance in a superconducting cavity". In: *Phys. Rev. Accel. Beams* 23 (12 Dec. 2020), p. 123101. DOI: 10.1103/PhysRevAccelBeams.23.123101.

[Kró+21] W. Królas, A. Ibarra, F. Arbeiter, F. Arranz, D. Bernardi, M. Cappelli, J. Castellanos, T. Dézsi, H. Dzitko, P. Favuzza, A. García, J. Gutiérrez, M. Lewitowicz, A. Maj, F. Martin-Fuertes, G. Micciché, A. Muñoz, F. Nitti, T. Pinna, I. Podadera, J. Pons, Y. Qiu, R. Román, M. Toth, and A. Zsakai. "The IFMIF-DONES fusion oriented neutron source: evolution of the design". In: *Nuclear Fusion* 61.12 (Dec. 2021), p. 125002. DOI: 10.1088/1741-4326/ac318f.

[Kub16] T. Kubo. "Flux trapping in superconducting accelerating cavities during cooling down with a spatial temperature gradient". In: *Progress of Theoretical and Experimental Physics* 2016.5 (May 2016), 053G01. ISSN: 2050-3911. DOI: 10.1093/ptep/ptw049.

[Lax13] R. E. Laxdal. "Review of magnetic shielding designs of low-beta cryomodules". In: *Proc. of SRF213, Paris, France*. 2013.

[Leb15] V. Lebedev. *The PIP-II Reference Design report*. Tech. rep. Fermilab, 2015.

[LS23] P. Lebrun and H. Schaff. "De la métrologie à la métallurgie de précision, Charles-Edouard Guillaume, prix Nobel de physique 1920". In: *Reflets de la physique* 73 (2023), pp. 28–31.

[Lia+18] D. B. Liarte, D. Hall, P. N. Koufalis, A. Miyazaki, A. Senanian, M. Liepe, and J. P. Sethna. "Vortex Dynamics and Losses Due to Pinning: Dissipation from Trapped Magnetic Flux in Resonant Superconducting Radio-Frequency Cavities". In: *Phys. Rev. Appl.* 10 (5 Nov. 2018), p. 054057. DOI: 10.1103/PhysRevApplied.10.054057.

[La19] S. Lobo and et al. "Magnetic field mapping system for Cornell sample host cavity". In: *Proc of SRF2019, Dresden, Germany*. 2019. DOI: 10.18429/JACoW-SRF2019-THP046.

[LM21] D. Longuevergne and A. Miyazaki. "Impact of geometry on the magnetic flux trapping of superconducting accelerating cavities". In: *Phys. Rev. Accel. Beams* 24 (8 Aug. 2021), p. 083101. DOI: 10.1103/PhysRevAccelBeams.24.083101.

[Lon17] D. Longuevergne. "Review of heat treatments for low beta cavities, what's so different from elliptical cavities." In: *Proc. of SRF2017, Lanzhou, China*. 2017.

[Mad+21] C. Madec, C. Arcambal, S. Berry, P. Bosland, A. Bouygues, E. Cenni, C. Cloue, G. Devanz, T. Hamelin, C. Mayri, et al. "The ESS elliptical cavity cryomodules production at CEA". In: *Proc. of IPAC2021, Campinas, SP, Brazil*. 2021.

[Mag70] A. Mager. "Magnetic shields". In: *IEEE Transactions on Magnetics* 6.1 (1970), pp. 67–75. DOI: 10.1109/TMAG.1970.1066714.

[Mak+18] W. A. Maksoud, L. Genini, D. Ciazynski, Y. Huang, and L. Vieillard. "Progress of the JT-60 SA Toroidal Field Coils Tests in the Cold Test Facility". In: *IEEE Transactions on Applied Superconductivity* 28.3 (2018), pp. 1–4. DOI: 10.1109/TASC.2017.2786687.

[Man+08] J. Manjanna, S. Kobayashi, Y. Kamada, S. Takahashi, and H. Kikuchi. "Martensitic transformation in SUS 316LN austenitic stainless steel at RT". In: *Journal of materials science* 43 (2008), pp. 2659–2665.

[Mar23] C. Marchand. "RF in strong B-field test stand motivation and requirements". In: *IMCC annual meeting, Orsay, France*. 2023. URL: https://indico.cern.ch/event/1250075/contributions/5352585/.

[Mar19] C. Marrelli. "High Efficiency Klystrons for ESS". In: *2019 International Vacuum Electronics Conference (IVEC)*. 2019, pp. 1–2. DOI: 10.1109/IVEC.2019.8745252.

[Mar22] C. Marrelli. "RF Power Generation at ESS". In: *Workshop on Efficient RF Sources*. 2022. URL: https://indico.cern.ch/event/1138197/.

[Ma19] G. Martinet and et al. "Characterization of Small AMR Sensors in Liquid Helium to Measure Residual Magnetic Field on Su-perconducting Samples". In: *Proc of SRF2019, Dresden, Germany*. 2019.

[Mas+13] M. Masuzawa, K. Tsuchiya, A. Terashima, A. Dael, O. Napoly, and J. Plouin. "Magnetic shielding: Our experience with various shielding materials". In: *Proc. of SRF2013, Paris, France*. 2013.

[Mic07] T. Michler. "Formation of martensite in 304 grade stainless steels and their welds". In: *Materialwissenschaft und Werkstofftechnik* 38.1 (2007), pp. 32–35.

[Mil+23] W. L. Millar, A. Grudiev, W. Wuensch, N. C. Lasheras, G. McMonagle, R. Zennaro, P. Craievich, M. Bopp, T. G. Lucas, M. Volpi, J. Paszkiewicz, A. Edwards, R. Wegner, H. Bursali, B. Woolley, A. Magazinik, I. Syratchev, A. Vnuchenko, S. Pitman, V. d. P. Romano, D. B. n. Caballero, and G. Burt. "High-Power Test of Two Prototype X-Band Accelerating Structures Based on SwissFEL Fabrication Technology". In: *IEEE Transactions on Nuclear Science* 70.1 (2023), pp. 1–19. DOI: 10.1109/TNS.2022.3230567.

[Mol17] A. Mollard. "Développement et réalisation d'un klystron à haut-rendement de type kladistron". PhD thesis. Université Paris Sud, 2017. URL: https://theses.hal.science/tel-01763142/.

[Mol+16] A. Mollard, C. Marchand, F. Peauger, J. Plouin, A. Beunas, and R. Marchesin. "High-efficiency klystron design for the CLIC project". In: *2016 IEEE International Vacuum Electronics Conference (IVEC)*. 2016, pp. 1–2. DOI: 10.1109/IVEC.2016.7561812.

[Mol+17] A. Mollard, C. Marchand, F. Peauger, J. Plouin, A. Beunas, and R. Marchesin. "Development of a high-efficiency klystron based on the kladistron principle". In: *2017 Eighteenth International Vacuum Electronics Conference (IVEC)*. 2017, pp. 1–2. DOI: 10.1109/IVEC.2017.8289714.

[Mon+14] G. Montenero, P. Arpaia, A. Ballarino, and L. Bottura. "A cryogenic sensing element for measurement current transformers". In: *Journal of Instrumentation* 9.03 (Mar. 2014), P03011. DOI: 10.1088/1748-0221/9/03/P03011.

[Mon22] E. Montesinos. "CERN SPS RF SSPA, from design to operation". In: *Twelfth CW and High Average Power RF Workshop (CERN)*. 2022. URL: https://indi.to/rbvZ8.

[Mor+05] A. Moretti, Z. Qian, J. Norem, Y. Torun, D. Li, and M. Zisman. "Effects of high solenoidal magnetic fields on rf accelerating cavities". In: *Physical Review Special Topics-Accelerators and Beams* 8.7 (2005), p. 072001.

[MuC23] MuCol. "MuCol, a design study for a Muon collider complex at 10 TeV centre of mass". In: *Accelerating News* (2023). URL: https://acceleratingnews.eu/news/issue-44/future-circular-collider-fcc/mucol-design-study-muon-collider-complex-10-tev-centre.

[MuC] MuCol. URL: https://mucol.web.cern.ch/wp6-radio-frequency-systems.

[Mum+04] K. Mumtaz, S. Takahashi, J. Echigoya, Y. Kamada, L. Zhang, H. Kikuchi, K. Ara, and M. Sato. "Magnetic measurements of martensitic transformation in austenitic stainless steel after room temperature rolling". In: *Journal of Materials Science* 39 (2004), pp. 85–97.

[Myn+23] G. Myneni, G. Ciovati, P. Dhakal, R. Rimmer, B. Khanal, T. Dohmae, T. Saeki, K. Umemori, M. Yamanaka, S. Michizono, M. Carl, A. Fajardo, N. Lannoy, H. Elsayed-Ali, M. O. Islam, M. N. Sayeed, A. Kumar, and A. Yamamoto. "Medium grain niobium SRF cavity production technology for science frontiers and accelerator applications". In: *Journal of Instrumentation* 18.04 (Apr. 2023), T04005. DOI: 10.1088/1748-0221/18/04/T04005.

[Nar+22] C. Narug, J. Bernardini, M. Parise, and D. Passarelli. "Design of Production PIP-II SSR1 Cavities". In: *Proc. of LINAC2022, Liverpool, United Kingdom*. 2022.

[Ned+23] M. Nedos, N. Pupeter, V. Wied, B. Keune, C. Quitmann, and G. Blokesch. "High-efficiency industrial 130 kW cw solid-state RF amplifier for 1.3 GHz". In: *Proc of IPAC2023, Venice, Italy*. 2023.

[Na17] F. Nording and et al. "Temperature dependence of AMR and GMR sensor properties". In: *Proc. of the 14th Symposium on Magnetoresistive Sensors and Magnetic Systems*. 2017.

[Oa19] T. Okada and et al. "Development of Temperature and Magnet-ic Field Mapping System for Superconducting Cavities at KEK". In: *Proc of SRF2019, Dresden, Germany*. 2019.

[Ome+23] M. Omet, H. Araki, T. Dohmae, H. Ito, R. Katayama, K. Umemori, and Y. Yamamoto. "Efforts to Suppress Field Emission in SRF Cavities at KEK". In: *Proc of SRF2023, Grand Rapids, MI, USA*. 2023.

[Ope] Opera. *OPERA Simulation Software*. URL: https://www.3ds.com/fr/produits-et-services/simulia/produits/opera/.

[Ors+10] F. Orsini, P. Bosland, B. Branas, P. Brédy, G. Disset, N. Grouas, P. Hardy, V. Hennion, H. Jenhani, J. Migne, A. Mohamed, J. Plouin, I. Podadera, J. Relland, S. Sanz, F. Toral, and E. Zaplatin. "Study and realization of the first superconducting Half Wave Resonator for the SRF Linac of the IFMIF project". In: *Proc. of IPAC'10, Kyoto, Japan*. 2010.

[Ors+11] F. Orsini, N. Bazin, P. Bosland, P. Bredy, P. Carbonnier, P. Charon, G. Disset, N. Grouas, P. Hardy, V. Hennion, E. Jacques, H. Jenhani, J. Migne, Y. Penichot, J. Plouin, J. Relland, B. Renard, D. Roudier, F. de Aragon, J. Calero, J. de la Gama, J. Gutierrez, I. Podadera, S. Sanz, F. Toral, and E. Zaplatin. "Vertical Tests Results of the IFMIF Cavity Prototypes and Cryomodule Development". In: *Proc. of SRF2011, Chicago, IL, USA*. 2011.

[Pad23] H. Padamsee. *Superconducting Radiofrequency Technology for Accelerators*. Wiley-VCH, 2023.

[PKH08] H. Padamsee, J. Knobloch, and T. Hays. *RF superconductivity for accelerators*. 2nd. Wiley-VCH, 2008.

[Pal15] M. A. Palmer. *The US muon accelerator program*. 2015. arXiv: 1502.03454 [physics.acc-ph].

[Pal+09] R. B. Palmer, R. C. Fernow, J. C. Gallardo, D. Stratakis, and D. Li. "rf breakdown with external magnetic fields in 201 and 805 MHz cavities". In: *Phys. Rev. ST Accel. Beams* 12 (3 Mar. 2009), p. 031002. DOI: 10.1103/PhysRevSTAB.12.031002.

[Par+23] I. P. Parajuli, J. R. Delayen, A. V. Gurevich, and G. Ciovati. "Magnetic Field Mapping of a Large-Grain 1.3 GHz Single-Cell Cavity". In: *Proc. of SRF 2023, Grand Rapids, Michigan, USA*. 2023.

[Pea14] F. Peauger. "High efficiency—High perveance klystron (X-band)". In: *EnEfficiency RF Sources Workshop (CERN)*. 2014. URL: https://indi.to/dDvXs.

[Pea+15] F. Peauger, C. Arcambal, S. Berry, N. Berton, P. Bosland, E. Cenni, J.-P. Charrier, G. Devanz, F. Eozenou, F. Gougnaud, A. Hamdi, X. Hanus, P. Hardy, V. Hennion, T. Joannem, F. Leseigneur, C. Loiseau, C. Madec, L. Maurice, O. Piquet, J. Plouin, J.-P. Poupeau, B. Renard, D. Roudier, P. Sahuquet, C. Servouin, C. Darve, N. Elias, and G. Olivier. "Progress in the Elliptical Cavities and Cryomodule Demonstrators for ESS". In: *Proc. of SRF2015, Whistler, Canada*. 2015.

[Pea+14] F. Peauger, P. Bosland, P. Carbonnier, G. Devanz, F. Éozénou, X. Hanus, P. Hardy, V. Hennion, L. Maurice, J. Plouin, D. Roudier, C. Servouin, G. Olivier, C. Darve, and S. Molloy. "Status and First Results of Two High Beta Prototype Elliptical Cavities for ESS". In: *Proc. of IPAC2014, Dresden, Germany*. 2014.

[Peg13] *ESS Technical Design Report*. Tech. rep. Apr. 2013.

[Pen+19] M. Peng, M. Conde, G. Ha, C. Jing, W. Liu, J. Power, J. Seok, J. Shao, E. Wisniewski, and J. Shi. "Optimization of a Single-Cell Accelerating Structure for Rf Breakdown Test With Short Rf Pulses". In: *Proc. of NAPAC2019, Lansing, MI, USA*. 2019.

[Pic+18] N. Pichoff, D. Chirpaz-Cerbat, R. Cubizolles, J. Dumas, R. Duperrier, G. Ferrand, B. Gastineau, F. Leseigneur, C. Madec, T. Plaisant, and J. Plouin. "Discussion on SARAF-linac cryomodules". In: *61st ICFA Advanced Beam Dynamics Workshop on High-Intensity and High-Brightness Hadron Beams*. 2018.

[Piq+23] O. Piquet, C. Arcambal, P. Bosland, E. Cenni, G. Devanz, T. Hamelin, P. Sahuquet, and Q. Bertrand. "Performance analysis from ESS cryomodule testing at CEA". In: *Proc. of SRF 2023, Grand Rapids, Michigan, USA*. 2023.

[Piq+17] O. Piquet, N. Bazin, P. Carbonnier, J. Chambrillon, J. Denis, M. Desmons, G. Devanz, F. Eozénou, P. Hardy, E. Jacques, et al. "First Results of the IFMIF/EVEDA-SaTHoRI Tests". In: *Proc. of SRF2017, Lanzhou, China*. 2017.

[Piq+19] O. Piquet, C. Boulch, R. Braud, P. Carbonnier, D. Chirpaz, G. Ferrand, F. Gohier, F. Gouit, P. Guiho, T. Joannem, G. Monnereau, T. Plaisant, D. Braud, L. Maurice, J. Plouin, P. Sahuquet, N. Solenne, and A. Pérolat. "SARAF Equipped Cavity Test Stand (ECTS) at CEA". In: *Proc. of IPAC2019, Melbourne, Australia*. (2019).

[Plo+19a] T. Plomion, N. Bazin, J. Plouin, K. Romieu, G. Devanz, N. Chauvin, and S. Chel. "Preliminary design of the IFMIF-DONES superconducting linac". In: *Proc. of SRF2019, Dresden, Germany*. 2019.

[Plo04] J. Plouin. "Injection d'harmonique dans un Tube à Ondes Progressives : amélioration de la puissance de sortie". PhD thesis. Ecole Polytechnique, 2004. URL: https://pastel.hal.science/tel-00007146.

[Plo18a] J. Plouin. *High beta cavity design electromagnetic design*. Tech. rep. ENS-6.5.2.2-T5-05. Eurofusion IFMIF/DONES, 2018.

[Plo18b] J. Plouin. *High beta Cavity detailed design with blueprints for the prototype*. Tech. rep. ENS-6.5.2.2-T15-04-N1. Eurofusion IFMIF/DONES, 2018.

[Plo18c] J. Plouin. *High beta cavity mechanical design*. Tech. rep. ENS-6.5.5.2-T10-05-N1. Eurofusion IFMIF/DONES, 2018.

[Plo18d] J. Plouin. "Magnetic field management in cryomodules and vertical cryostats at CEA-Saclay". In: *TTC/ARIES Topical workshop on flux trapping and magnetic shielding, CERN, Switzerland, 2018*. 2018. URL: https://indico.cern.ch/event/741615/contributions/3179883/.

[Plo20] J. Plouin. *Status of manufacturing of the high beta prototype*. Tech. rep. ENS-6.5.2.2-T20-06-N1. Eurofusion IFMIF/DONES, 2020.

[Plo21a] J. Plouin. *Additional test of the prototype of high-beta cavity*. Tech. rep. ENS-6.5.2.2-T002-09-N1. Eurofusion IFMIF/DONES, 2021.

[Plo21b] J. Plouin. *Status and lessons learned of manufacturing of high-beta cavity prototype*. Tech. rep. ENS-6.5.2.2-T26-02-N1. Eurofusion IFMIF/DONES, 2021.

[Plo22] J. Plouin. *Conceptual design of frequency tuner for high beta-cavity*. Tech. rep. ENS-6.5.2.2-T002-09-N2. Eurofusion IFMIF/DONES, 2022.

[Plo+19b] J. Plouin, B. Baudouy, A. Four, J.-P. Charrier, L. Maurice, J. Novo, B. Peters, and K. Liao. "Experimental study of second sound quench detection for superconducting cavities". In: *Phys. Rev. Accel. Beams* 22.8 (2019), p. 083202. DOI: 10.1103/PhysRevAccelBeams.22.083202.

[Plo+23a] J. Plouin, M. Baudrier, N. Bazin, S. Chel, G. Devanz, G. Jullien, A. Madur, L. Maurice, and C. Servouin. "Design, Fabrication and Test of a 175 MHz, beta = 0.18, Half Wave Resonator for the IFMIF-DONES SRF-Linac". In: *Proc. of SRF2023, Grand Rapids, MI, USA*. 2023.

[Plo+15] J. Plouin, N. Bazin, P. Charon, G. Devanz, H. Dzitko, P. Hardy, F. Leseigneur, J. Neyret, and O. Piquet. "CEA experience and effort to limit magnetic flux trapping in superconducting cavities". In: *Proc. of SRF2015, Whistler, Canada*. 2015.

[Plo+09] J. Plouin, P. Bosland, P. Bredy, M. Desmons, G. Devanz, H. Jenhani, and A. Mohamed. "Main choices and preliminary design for the IFMIF RF couplers". In: *Proc. of SRF2009, Berlin, Germany*. 2009.

[PCM21] J. Plouin, E. Cenni, and L. Maurice. "AMR Sensors Studies and Development for Cavities Tests Magnetometry at CEA". In: *Proc. of SRF2021, East Lansing, MI, USA*. 2021.

[Plo+13] J. Plouin, J.-P. Charrier, C. Magne, L. Maurice, and J. Novo. "Experimental investigations of the quench phenomena for the quench localization by the second sound wave method". In: *Proc. of SRF2013, Paris, France*. 2013.

[PD11] J. Plouin and G. Devanz. "Conceptual Design of the beta = 0.86 Cavities for the Superconducting Linac of ESS". In: *Proc. of SRF2011, Chicago, IL, USA*. 2011.

[PDC11] J. Plouin, G. Devanz, and S. Chel. "Optimized RF design of 704 MHz beta= 1 cavity for pulsed proton drivers". In: *Proc. of SRF2011, Chicago, IL, USA*. 2011.

[PF18] J. Plouin and C. Fan. "IFMIF HWR cryomodule and magnetic shield properties". In: *TTC meeting, Milano, Italy*. 2018. URL: https://agenda.infn.it/event/13791/contributions/21018/.

[Plo+23b] J. Plouin, C. Marchand, P. Hamel, S. Arsenyev, A. Mollard, A. Beunas, P. Denis, and F. Peauger. "Design, Fabrication, and Test of a 5 GHz Klystron Based on the Kladistron Principle". In: *IEEE Transactions on Electron Devices* 70.3 (2023), pp. 1275–1282. DOI: 10.1109/TED.2023.3236590.

[Plo+21] J. Plouin, C. Marchand, P. Hamel, S. Arsenyev, A. Mollard, A. Beunas, and F. Peauger. "Fabrication and test of a 5 GHz kladistron". In: *2021 22nd International Vacuum Electronics Conference (IVEC)*. 2021, pp. 1–2. DOI: 10.1109/IVEC51707.2021.9722532.

[PMT14] J. Plouin, M. Masuzawa, and K. Tsuchiya. "Magnetic shielding: material properties measurements at cold". In: *TTC meeting, KEK Tsukuba, Japan*. 2014. URL: https://indico.desy.de/event/10663/.

[PR02] J. Plouin and J.-M. Rax. "Origins of saturation in a traveling wave tube". In: *Third IEEE International Vacuum Electronics Conference (IEEE Cat. No.02EX524)*. 2002, pp. 318–319. DOI: 10.1109/IVELEC.2002.999399.

[PR03] J. Plouin and J.-M. Rax. "Influence of 2nd harmonic injection on the 1st harmonic extracted power in a traveling wave tube". In: *4th IEEE International Conference on Vacuum Electronics, 2003*. 2003, pp. 334–335. DOI: 10.1109/IVEC.2003.1286361.

[Plo+05] J. Plouin, J.-M. Rax, F. Andre, and Y. Thaler. "Improvement of the output power in TWTs by harmonic injection". In: *IEEE Transactions on Electron Devices* 52.5 (2005), pp. 783–789. DOI: 10.1109/TED.2005.845841.

[Pos+20] S. Posen, A. Romanenko, A. Grassellino, O. Melnychuk, and D. Sergatskov. "Ultralow Surface Resistance via Vacuum Heat Treatment of Superconducting Radio-Frequency Cavities". In: *Phys. Rev. Appl.* 13 (1 Jan. 2020), p. 014024. DOI: 10.1103/PhysRevApplied.13.014024.

[Pos+16] S. Posen, M. Checchin, A. Crawford, A. Grassellino, M. Martinello, O. Melnychuk, A. Romanenko, D. Sergatskov, and Y. Trenikhina. "Efficient expulsion of magnetic flux in superconducting radiofrequency cavities for high Q applications". In: *Journal of Applied Physics* 119.21 (2016).

[PGB23] T. Powers, T. Ganey, and N. Brock. "In situ plasma processing of superconducting cavities at JLAB, 2023 update". In: *Proc of SRF2023, Grand Rapids, MI, USA*. 2023.

[Prz23] H. Przybilski. "Progresses in the ESS superconducting LINAC installation". In: *Proc of SRF2023, Grand Rapids, MI, USA*. 2023.

[Rea+18] M. Read, R. L. Ives, J. Neilson, and A. Jensen. "A 1.3 GHz 100 kW ultra-high efficiency Klystron". In: *2018 IEEE International Vacuum Electronics Conference (IVEC)*. 2018, pp. 25–26. DOI: 10.1109/IVEC.2018.8391534.

[Reg+14] D. Regidor, C. De la Morena, I. Kirpitchev, P. Mendez, J. Molla, M. Weber, S. Chel, M. Desmons, G. Devanz, H. Dzitko, and H. Jenhani. "LIPAc SRF linac couplers conditioning". In: *Proc. of IPAC2014, Dresden, Germany*. 2014.

[Rob18] A. Robson. *The Compact Linear e+e- Collider (CLIC): Accelerator and Detector*. Tech. rep. CERN, 2018. DOI: 10.48550/arXiv.1812.07987.

[Rom+14] A. Romanenko, A. Grassellino, A. Crawford, D. Sergatskov, and O. Melnychuk. "Ultra-high quality factors in superconducting niobium cavities in ambient magnetic fields up to 190 mG". In: *Applied Physics Letters* 105.23 (2014).

[SAC18] J. Sauza-Bedolla, S. Atieh, and N. Catalán Lasheras. "Manufacturing of X-band Accelerating Structures: Metrology Analysis and Process Capability". In: *in Proc. of LINAC2019, Beijing, China*. 2018.

[Sch98] T. Schilcher aus Steinhöring. "Vector Sum Control of Pulsed Accelerating Fields in Lorentz Force Detuned Superconducting Cavities. s.l. : Tesla Collaboration, 1998". PhD thesis. Universität Hamburg, 1998.

[SBS12] A. Shabazian, R. Begum, and B. C. Stockwell. "Design and development of 5-MW X-band klystron for medical and cargo screening applications". In: *IVEC 2012*. 2012, pp. 167–168. DOI: 10.1109/IVEC.2012.6262117.

[SY23] V. Shemelin and V. Yakovlev. "Equidistant optimization of elliptical superconducting rf standing wave cavities". In: *Phys. Rev. Accel. Beams* 26 (9 Sept. 2023), p. 092001. DOI: 10.1103/PhysRevAccelBeams.26.092001.

[SBS07] P. Soulignac, B. Bonnefois, and E. Soutif. "Chaudronnerie en aciers inoxydables". In: *Techniques de l'ingénieur Machines hydrauliques, aérodynamiques et thermiques* base documentaire : TIP151WEB. (2007). DOI: 10.51257/a-v1-bm6570.

[Ste+19] L. Steder, B. Bein, W. Hillert, and D. Reschke. "Systematic Studies of the Second Sound Method for Quench Detection of Superconducting Radio Frequency Cavities". In: *Proc of SRF2019, Dresden, Germany*. 2019.

[SGP10] D. Stratakis, J. C. Gallardo, and R. B. Palmer. "Effects of external magnetic fields on the operation of high-gradient accelerating structures". In: *Nuclear Instruments and Methods in Physics Research Section A: Accelerators, Spectrometers, Detectors and Associated Equipment* 620.2 (2010), pp. 147–154. ISSN: 0168-9002. DOI: https://doi.org/10.1016/j.nima.2010.03.167.

[SP15] D. Stratakis and R. B. Palmer. "Rectilinear six-dimensional ionization cooling channel for a muon collider: A theoretical and numerical study". In: *Phys. Rev. ST Accel. Beams* 18 (3 Mar. 2015), p. 031003. DOI: 10.1103/PhysRevSTAB.18.031003.

[Syr22] I. Syratchev. "Summary of the high-efficiency (HEIKA) day". In: *CLIC workshop, CERN*. 2022. URL: https://indico.cern.ch/event/449801/contributions/1945347/attachments/1215636/1775110/HEIKA%5C_summary.pdf.

[Syr+22] I. Syratchev, Z. Nisa, J. Cai, G. Burt, and T. Anno. *DC Beam Stability issues in the first commercial prototype of a High Efficiency 8MW X-Band Klystron, CERN-ACC–2022-0007*. Tech. rep. CERN, 2022.

[Tea] I. I. D. Team. *ILC Technical Design Report*. URL: https://linearcollider.org/technical-design-report/.

[The16] S. Theveny. "Approches fréquentielle et temporelle de la dynamique des tubes à onde progressive". PhD thesis. Université Aix-Marseille, 2016. URL: https://www.theses.fr/2016AIXM4741.

[Uek+20] R. Ueki, T. Okada, M. Masuzawa, K. Tsuchiya, T. Kawamoto, K. Umemori, E. Kako, T. Konomi, and H. Sakai. "Study on Magneto-Resistance Sensors for Low Magnetic Field Measurements". In: *IEEE Transactions on Applied Superconductivity* 30.4 (2020), pp. 1–4. DOI: 10.1109/TASC.2020.2976994.

[Val94] C. Vallet. "Etude de la dissipation dans les supraconducteurs en regime de haute frequence". PhD thesis. Université Claude Bernard, Lyon I, 1994.

[VV39] R. H. Varian and S. F. Varian. "A High Frequency Oscillator and Amplifier". In: *Journal of Applied Physics* 10.5 (May 1939), pp. 321–327. DOI: 10.1063/1.1707311.

[VKK13] J.-M. Vogt, O. Kugeler, and J. Knobloch. "Impact of cool-down conditions at T_c on the superconducting rf cavity quality factor". In: *Phys. Rev. ST Accel. Beams* 16 (10 Oct. 2013), p. 102002. DOI: 10.1103/PhysRevSTAB.16.102002.

[Wea+18] B. Weatherford, R. Kowalczyk, V. Dolgashev, J. Neilson, A. Jensen, I. Syratchev, and J. Cai. "Exploratory study of X-band Klystron designs for maximum efficiency". In: *2018 IEEE International Vacuum Electronics Conference (IVEC)*. 2018, pp. 23–24. DOI: 10.1109/IVEC.2018.8391533.

[WAB23] A. E. Wheelhouse, A. E. T. Akintola, and A. J. Blackett-May. "Provision of High Beta cavities for European Spallation source by UKRI-STFC Daresbury laboratory". In: *Proc of SRF2023, Grand Rapids, MI, USA*. 2023.

[Woh+03] J. Wohlbier, M. Converse, J. Plouin, A. Rawal, A. Singh, and J. Booske. "LATTE/MUSE numerical suite: an open source teaching and research code for traveling wave tube amplifiers". In: *4th IEEE International Conference on Vacuum Electronics, 2003.* 2003. DOI: 10.1109/IVEC.2003.1286003.

[Wue06] W. Wuensch. "Observations About RF Breakdown From the CLIC High-Gradient Testing Program". In: *AIP Conference Proceedings*. Vol. 877. 1. 2006, pp. 15–21.

[Xia+19] O. Z. Xiao, Z. S. Zhou, Zaid-un-Nisa, S. C. Wang, G. Pei, D. Dong, and S. Fukuda. "Design Study of High Efficiency CW Klystron for CEPC". In: *2019 International Vacuum Electronics Conference (IVEC)*. 2019, pp. 1–2. DOI: 10.1109/IVEC.2019.8745286.

[Yog12] R. Yogi. "Uppsala high power test stand for ESS spoke cavities". In: *Proc. of LINAC2012, Tel-Aviv, Israel*. 2012.

[Zap+09a] E. Zaplatin, P. Bosland, P. Bredy, N. Grouas, P. Hardy, J. Migne, A. Mosnier, F. Orsini, and J. Plouin. "IFMIF superconducting β= 0.094 half-wave resonator design". In: *Proc. of PAC09, Vancouver, Canada*. 2009.

[Zap+09b] E. Zaplatin, P. Bosland, P. Bredy, G. Nathalie, P. Hardy, J. Migne, A. Mosnier, F. Orsini, and J. Plouin. "IFMIF-EVEDA SC beta=0.094 Half-wave Resonator Study". In: *Proc. of SRF2009, Berlin, Germany*. 2009.

[Zha+23] L. Zhang, G. Burt, Y. Yang, and K. Ronald. "RF in strong magnetic fields: Test stand plans in UK". In: *IMCC annual meeting, Orsay, France*. 2023. URL: https://indico.cern.ch/event/1250075/contributions/5343508/.

[Zon+23] Y. Zong, Q. Chen, X. Huang, Z. Wang, J. Chen, P. Dong, H. Hou, X. Pu, J. Shi, S. Sun, D. Wang, J. Wu, S. Xing, S. Zhao, Y. Zhao, Y. Huang, and X. Wu. "Realization of accelerating gradient larger than 25 MV/m on High-Q 1.3 GHz 9-cell cavities for SHINE". In: *Proc of SRF2023, Grand Rapids, MI, USA*. 2023.

université
PARIS-SACLAY

Title: From Radio-Frequency sources to particle beam: optimisation of RF power transfer for accelerating cavities

Abstract: Radiofrequency cavities are a fundamental element of particle accelerators, since they transfer the radiofrequency energy generated by power sources to a particle beam. This dissertation presents my contribution to the design, fabrication, preparation and operation of such cavities, destined to some of the main today and future accelerator projects in the world. The development of superconducting cavities for ESS, with elliptical shape, and for IFMIF/DONES, with half wave resonator shape, is detailed. I give a focus on the mitigation of radiofrequency losses in niobium, due to the surrounding magnetic field trapping in the material. My contribution to the power transfer optimization also resulted in studies on high efficiency klystrons, used as radiofrequency power source for cavities, with the design, fabrication and test of a klystron based on the kladistron principle. Finally, I present the work carried out on diagnostic tools, essential for cavity operation and for R&D further development.

Titre: Des sources Radio Fréquence au faisceau de particules : optimisation du transfert de puissance RF pour les cavités accélératrices

Résumé: Les cavités radiofréquence sont un élément fondamental des accélérateurs de particules, puisqu'elles transfèrent l'énergie radiofréquence générée par les sources d'énergie à un faisceau de particules. Ce mémoire présente ma contribution à la conception, à la fabrication, à la préparation et à l'exploitation de telles cavités, destinées à certains des principaux projets d'accélérateurs actuels et futurs dans le monde. Le développement de cavités supraconductrices pour ESS, de forme elliptique, et pour IFMIF/DONES, de forme résonateur demi-onde, est détaillé. Je décris également mon travail sur l'atténuation des pertes radiofréquences dans le niobium, dues au piégeage du champ magnétique environnant dans le matériau. Ma contribution à l'optimisation du transfert de puissance a également donné lieu à des études sur les klystrons à haut rendement, utilisés comme source d'énergie radiofréquence pour les cavités, avec la conception, la fabrication et le test d'un klystron basé sur le principe du kladistron. Enfin, je présente les travaux réalisés sur les outils de diagnostic, essentiels pour le fonctionnement des cavités et pour le développement futur de la R&D.